APPLICATIONS OF MATHEMATICAL MODELLING IN ONCOLYTIC VIROTHERAPY AND IMMUNOTHERAPY

ADRIANNE JENNER

A thesis submitted in fulfilment of
the requirements for the degree of
Doctor of Philosophy

School of Mathematics and Statistics
The University of Sydney
26 September 2019

ABSTRACT

Cancer is a devastating disease that touches almost everyone and finding effective treatments presents a highly complex problem, requiring extensive multidisciplinary research. Mathematical and computational modelling can provide insight into both cancer formation and treatment. A range of techniques are developed in this thesis to investigate two promising therapies: oncolytic virotherapy, and combined oncolytic virotherapy and immunotherapy. Oncolytic virotherapy endeavours to eradicate cancer cells by exploiting the aptitude of virus-induced cell death. Building on this premise, combined oncolytic virotherapy and immunotherapy aims to harness and stimulate the immune system's inherent ability to recognise and destroy cancerous cells. While both of these therapies are showing increasing success, there are still major challenges facing these therapies and the goal of this thesis is to overcome obstacles that arise from treating cancer with viruses.

Using deterministic and agent-based mathematical modelling, perturbations of treatment characteristics are investigated and optimal treatment protocols are suggested. An integro differential equation with distributed parameters is developed to characterise the function of the E1B genes in an oncolytic adenovirus. Subsequently, by using a bifurcation analysis of a coupled-system of ordinary differential equations for oncolytic virotherapy, regions of bistability are discovered, where increased injections can result in either tumour eradication or tumour stabilisation. Through an extensive hierarchical optimisation to multiple data sets, drawn from *in vitro* and *in vivo* modelling, gel-release of a combined oncolytic virotherapy and immunotherapy treatment is optimised. Additionally, using an agent-based modelling approach, delayed-infection of an intratumourally administered virus is shown to be able to reduce tumour burden.

This thesis develops new mathematical models that can be applied to a range of cancer therapies and suggests engineered treatment designs that can significantly advance current therapies and improve treatments.

PUBLICATIONS

The work in this thesis includes results from published articles and manuscripts under review.

AUTHORSHIP ATTRIBUTION STATEMENT

Chapter 4 of this thesis includes the published work in:

- Jenner, A. L., Yun, C. O., Yoon, A., Kim, P. S., & Coster, A. C. F. (2018). Modelling Heterogeneity in Viral-Tumour Dynamics: The Effects of Gene-Attenuation on Viral Characteristics. *Journal of Theoretical Biology*, 454, 41-52. https://doi.org/10.1016/j.jtbi.2018.05.030

I co-designed the study with the co-authors, conducted the analysis and wrote the manuscript.

Chapter 5 of this thesis includes the published work in:

- Jenner, A. L., Coster, A. C. F., Kim, P. S., & Frascoli, F. (2018). Treating Cancerous Cells With Viruses: Insights from a Minimal Model for Oncolytic Virotherapy. *Letters in Biomathematics*, 5(sup1), S117-S136. https://doi.org/10.1080/23737867.2018.1440977
- Jenner, A. L., Kim, P. S., & Frascoli, F. (2019). Oncolytic Virotherapy for Tumours Following a Gompertz Growth Law. *Journal of Theoretical Biology*, 480, 129-140. https://doi.org/10.1016/j.jtbi.2019.08.002.

I co-designed the study with the co-authors. I conducted the majority of the analysis with F.F creating Figs. 5.17, 5.18, 5.19 and 5.20(a). I wrote the first manuscript and co-wrote the second manuscript with F.F.

Chapter 6 of this thesis includes the published works in:

- Jenner, A. L., Yun, C. O., Kim, P. S., & Coster, A. C. F. (2018). Mathematical Modelling of the Interaction Between Cancer Cells and an Oncolytic Virus: Insights Into the Effects of Treatment Protocols. *Bulletin of Mathematical Biology*, 80(6), 1615-1629. https://doi.org/10. 1007/s11538-018-0424-4
- Jenner, A. L., Coster, A. C. F., & Kim, P. S., (2016). Mathematical Modelling of Oncolytic Virotherapy: The Effects of a PEG-modified Adenovirus Conjugated with Herceptin. *The Australian Mathematical Society*, 43(5), 297-299.

I co-designed the study with the co-authors, conducted the analysis and wrote the manuscript.

Chapter 7 of this thesis includes the published work in:

- Jenner, A. L., Yun, C. O., Yoon, A., Coster, A. C. F., & Kim, P. S. (2018). Modelling Combined Virotherapy and Immunotherapy: Strengthening the Antitumour Immune Response Mediated by IL-12 and GM-CSF Expression. *Letters in Biomathematics*, 5(sup1), S99-S116. https://doi.org/10.1080/23737867.2018.1438216

I co-designed the study with the co-authors, conducted the analysis and wrote the manuscript.

Chapter 8 of this thesis includes the publication under review:

- Jenner, A. L., Frascoli, F., Coster, A. C. F., & Kim, P. S. (submitted Nov. 7 2018). Enhancing Oncolytic Virotherapy: Observations from a Voronoi Cell-Based Model. *Journal of Theoretical Biology*.

I co-designed the study with the co-authors, conducted the analysis and wrote the manuscript.

In addition to the statements above, permission to include the published material has been granted by the co-authors.

Adrianne Jenner (PhD Candidate)

As supervisor for the candidature upon which this thesis is based, I can confirm that the authorship attribution statements above are correct.

Supervisor Peter Kim

ACKNOWLEDGMENTS

When the final sentence is written on a document that summarises all the hard work and dedication of the last four years of your life, you begin to think about all the ways you might not have made it, if not for the people who helped and supported you along the way.

First and foremost I want to thank my supervisors and mentors: Peter Kim, Adelle Coster and Federico Frascoli.

Peter, under your guidance as a supervisor I grew significantly, both as a mathematician and as a person. I learnt how to be creative and passionate about my research, and to believe in my ability.

Adelle, you have been a fantastic role model to me and I am a better academic and presenter from all that you have taught me. Without your support and enthusiasm, I would not have been able to get to the position I am in today.

Federico, I am very grateful for all the time you spent mentoring and teaching me. I learnt so much from working with you and you have made a significant impact on my academic career, for which I am very grateful.

I wish to thank my family, for their love and constant support. I feel very lucky to have such an incredible family who have always been there when I needed someone to turn to.

To Michael, thank you for everything you've done for me over the past few years. You make me a better version of myself and I could not have done this without you nuisance.

To all of my incredible and loving friends, thank you for bringing joy and friendship to my life. Lou, you got me to where I am today and Avril, thank you so much for your careful edits and amazing friendship.

A huge thank you goes to all the people who have spent hours next to me in this PhD world. To Pantea, James, Sean, Bec and Brent, thanks for being such amazing friends and your support throughout the years.

I'd also like to thank Paul Macklin for his mentorship over the last few months. I learnt so much from our time together and am very grateful for the experience.

It is thanks to all these people, that I am proud of the person I have become and this (rather large) body of work.

CONTENTS

LIST OF FIGURES

LIST OF TABLES

ABBREVIATIONS, VARIABLES AND PARAMETERS

Below is a list of abbreviations, variables and parameters that may be helpful to the reader.

ABBREVIATIONS

ODE	ordinary differential equation
PDE	partial differential equation
DC	dendritic cell
APC	antigen presenting cell
NK	natural killer (cell)
IL-12	interleukin 12
GM-CSF	granulocyte-macrophage colony-stimulating factor
VCBM	Voronoi cell-based model
SN	saddle node
HB	Hopf bifurcation
BP	branch point
GH	Generalised Hopf
PBS	phosphate-buffered saline
Ad	oncolytic adenovirus
PEG	polyethelene glycol
Ad-PEG	PEG-modified oncolytic adenovirus
Ad-PEG-HER	PEG-modified oncolytic adenovirus conjugated with Herceptin
TNF	Tumour necrosis factor
TRAIL	TNF-related apoptosis-inducing ligand
ri-Ad-stTRAIL	replication-incompetent adenovirus expressing secretable TRAIL
Ad-stTRAIL	replication-competent adenovirus expressing secretable TRAIL

VARIABLES

C	number of cells with replicating virus
Υ	number of intracellular and extracellular virus particles
V	virus population
U	uninfected cells
I	virus-infected cells
V_B	virus population in the blood
V_O	virus population in the organs
V_T	virus at the tumour site
R_S	refractory tumour cell population
R_I	infected refractory tumour cell population
K	killer immune cells
T	total tumour cell population
A	APC population
H	helper T cell population
A_I	immature APCs
A_A	active APCs
n_I	amount of intracellular virus particles
p_{VE}	density of extracellular virus in a voxel
p_{TE}	density of extracellular TRAIL in a voxel
n_I	intracellular amount of virus
T_I	intracellular amount of TRAIL

PARAMETERS

τ	start time of viral replication
l	period of time virus spends replicating
δ	time cell bursts
C_0	initial number of cells in a monolayer
k	intracellular viral replication rate
r	replication rate of tumour cells
β	virus infection rate
d_I	lysis rate
d_V	decay rate of virus particles
α	number of new viruses created through lysis
L	tumour carrying capacity
S_0	initial number of tumour cells
V_0	number of virus particles in a single injection
ϕ	Number of days between injections
d_B	decary rate of virus in the blood
τ_O	transfer rate of virus in the blood to the organs
τ_T	transfer rate of virus in the blood to the tumour site
γ	antiviral stimulation rate of tumour cells
τ_R	re-introduction rate
κ	killing rate by immune cells
β_R	infection rate of antiviral state tumour cells
d_{RI}	infected antiviral cell burst rate
s_K	stimulation rate of killer cells
d_K	decay rate of killer immune cells
V_{T0}	total viral dosage (possibly given over multiple administrations)
D_0	initial number of DCs
g_{age}	time steps taken for a daughter cell to grow to adult size
p_0	probability constant for proliferation
d	distance from a tumour cell to the nearest cell on the tumour edge
d_{max}	radial distance that nutrient reaches by diffusion from the tumour edge
r_{min}	minimum distance between neighbouring cells for proliferation to occur
p_{age}	age a cell needs to reach before it can proliferate again
d_{frac}	distance spring length of a dead cell decreases at each time step
d_{age}	time taken for a dead cell to disintegrate
p_i	probability of infection occurring
i_{age}	time steps taken from infection to when the infected cell bursts
r_μ	mean distance of viral movement per time step
r_σ	standard deviation for virus displacement
a_l	adhesion distance between two cell positions
s_v	secretion rate of virus from vein cell
c_I	rate at which cell uptakes virus
$n_{I,T}$	intracellular virus capacity
c_R	intracellular replication rate
n_{I*}	minimum virus replication threshold

1

INTRODUCTION

With more than 10 million new cases each year, cancer is one of the most devastating diseases worldwide. Cancer is the collective name given to a group of illnesses sharing one commonality: uncontrollable cell division that spreads into surrounding tissues. Progress in developing curative treatments for this disease is slow, despite the years of work by scientists and clinicians. Developing effective cancer treatments is a highly complex, multidisciplinary problem that requires extensive research and creativity.

Oncolytic virotherapy is an emerging cancer treatment that uses virus replication to destroy cancer cells. This therapy originated from observations of accidental viral infections causing remission in cancer malignancies. Competent and specific viruses which attack tumour cells but not healthy cells have been made with advancements in the field of genetic engineering. The current state of this field includes proof of feasibility for a single-shot virotherapy cure and clinical confirmation of the intratumoural herpes simplex virus therapy for metastatic melanoma (Russell *et al.*, 2012).

Oncolytic viruses are also being investigated as immunotherapy agents for cancer treatment. Combined virotherapy and immunotherapy is a new approach that uses a virus' ability to lyse tumour cells (leading to the release of soluble antigens and danger signals) to drive an antitumour immune response (Bommareddy *et al.*, 2018). This immune response then results in immune cell induced apoptosis (programmed cell death) of cancer cells. New strategies have been developed to maximise this immunotherapeutic potential through the addition of immunostimulatory cytokines to viral genes or combined injections of viruses and immune cells (Oh *et al.*, 2017).

Mathematical and computational biology is a growing field of research that is used to answer important questions in biology. Over the years, a diverse range of techniques from this field, varying from deterministic to agent-based modelling, have provided critical insight into cancer treatments. For example, chemotherapy and radiotherapy application protocols have been significantly improved through the use of mathematical modelling (Enderling and AJ Chaplain, 2014). More recently, mathematical and computational models for oncolytic virotherapy and immunotherapy have been developed (Bajzer *et al.*, 2008; Dingli *et al.*, 2009; Komarova and Wodarz, 2010; Wares *et al.*, 2015; Titze *et al.*, 2017; Powathil *et al.*, 2013; Mallet and De Pillis, 2006). These models have laid out a baseline for future modelling to be developed upon.

Unfortunately, there are still major challenges facing oncolytic virotherapy and combined virotherapy and immunotherapy. Firstly, determining which genetically engineered virus can maximise both viral spread and anticancer cytotoxicity is difficult due to the unknown correlation between the virus genomes and virus effectiveness. Additionally, optimal dosage protocols for these treatments (considering treatment length and administration protocol) are not yet universally established. Overall, significant characterisation of the virus infectivity and immune response is needed to improve future iterations of these treatments.

Experimentally, determining ways to overcome obstacles to oncolytic virotherapy and combined virotherapy and immunotherapy requires significant time and expenses. Through the use of mathematical and computational modelling, however, these challenges can be investigated efficiently. The current literature surrounding the mathematics of these therapies is still basic, and novel formulations need to be designed to investigate these therapies further.

In this thesis, a range of mathematical and computational techniques are developed to advance the current baseline of oncolytic virotherapy and immunotherapy, and investigate the challenges facing these treatments. This research aims to answer two broad questions:

1. How can mathematical and computational tools be used to improve cancer therapies?

2. In what ways can oncolytic virotherapy and immunotherapy be improved?

To answer these questions, techniques that can be applied to a range of other cancer therapies are developed in this thesis. By using these, different ways of ameliorating virotherapy and immunotherapy are able to be determined and subsequent analysis provides insight into the usefulness of mathematics in cancer modelling.

To introduce the background of this thesis, Chapter 2 is a summary of the biology behind cancer, virotherapy and immunotherapy. Chapter 3 then summarises the deterministic and agent-based models related to these fields, along with mathematical optimisation and analysis techniques employed throughout this thesis. Following this,

Chapter 4-8 are individual investigations into different oncolytic virotherapy derivatives. These are conducted at two physiological scales: intracellular and extracellular.

In Chapter 4 an integro-differential system with distributed parameters is developed to model the intracellular dynamics of the virus-tumour interactions. By optimising the model parameters to *in vitro* virus titer measurements for gene-attenuations of the E1B 19 and E1B 55 kDa proteins, specific viral characteristics and the dominant processes altered by the mutations is determined. To consider how these processes act at the extracellular level, Chapter 5 investigates the sensitivity of therapy to individual tumour cell and viral heterogeneity using a system of coupled ordinary differential equations (ODEs). Bifurcation and local stability analysis are used to establish dosage protocols that result in tumour extinction.

Chapters 6 and 7 build on the results of Chapter 5, by presenting extracellular investigations into the dynamics of specific virotherapies. To overcome the rapid clearance of viral particles by the immune system, oncolytic adenoviruses can be conjugated with Herceptin. In Chapter 6, a system of coupled ODEs is used to represent the experimental data for this specific virus and predict the response of cancer growth to other treatment protocols beyond those in the experiments. To contrast this investigation, in Chapter 7 the system of ODEs is then extended to consider a combined virotherapy and immunotherapy treatment: an oncolytic adenovirus modified with immunostimulatory cytokines interleukin-12 (IL-12) and granulocyte-macrophage colony-stimulating factor (GMCSF). A sensitivity analysis of optimised parameter values is used to investigate the characteristics of the immune response to virotherapy, and suggest treatment improvements.

To begin to establish a universal optima administration protocol, a degradable gel-release mechanism is considered in Chapter 7. Using the mathematical model developed, perturbations to the application protocol that achieve optimal treatment effectiveness are determined.

In Chapter 8 a Voronoi cell-based model (VCBM) is developed to assess the sensitivity of treatment efficacy to tumour geometry. The VCBM captures the interaction between oncolytic virus particles and cancer cells in a 2-dimensional setting by using an underlying agent-based framework, where agents are cells with edges from a

Voronoi tessellation. Simulations show that delaying the infection of cancer cells, and thus allowing more time for intratumoural treatment dissemination, can improve the efficacy of oncolytic virotherapy.

A final summary and discussion of results is presented in Chapter 9, with concluding remarks in Chapter 10. Additionally, a preliminary investigation that correlates with the results presented in Chapters 4-8, is presented in Chapter **??**. In this work, an agent-based framework similar to that of the VCBM in Chapter 8, is used to model an adenovirus expressing tumour necrosis factor (TNF)-related apoptosis-inducing ligand (TRAIL).

Fig. 1.1 presents an overview of the interactions that will be discussed in detail in this thesis and the two physiological scales: intracellular and extracellular. A subset of this diagram is included at the start of each chapter, indicating the specific interactions investigated in that chapter.

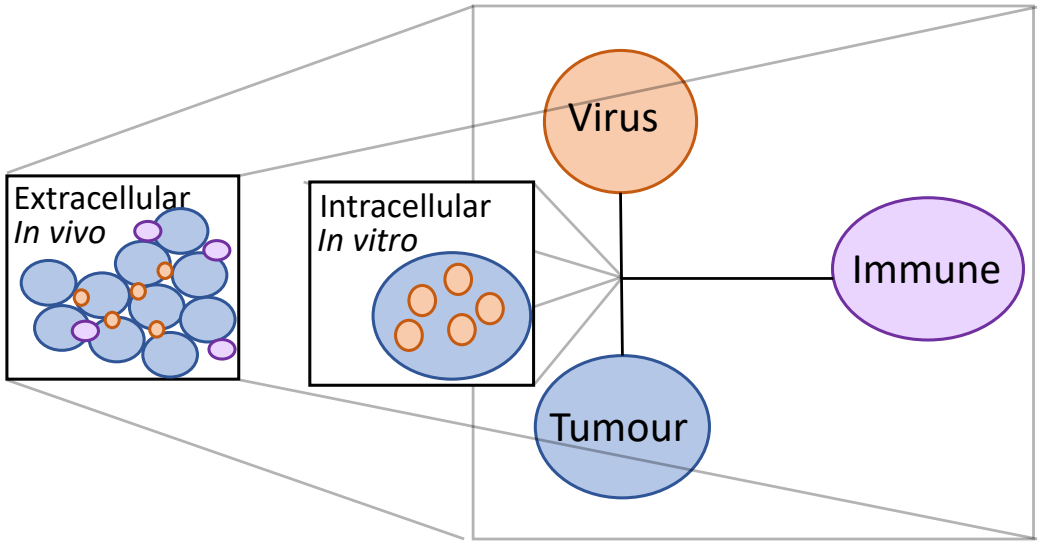

Figure 1.1: An overview of the physiological scales of the virus, tumour and immune system interaction discussed in this thesis. At the start of each chapter a subset of this diagram is presented that summaries the key concepts in that chapter.

2

BIOLOGICAL BACKGROUND

The biological background of this therapy can be summarised into three major areas: (1) cancer, (2) the immune system and (3) oncolytic viruses. The background to these areas is provided in the following sections:

1. **Cancer** - Section 2.2 presents an overview of the initial stages of cancer, cancer development, specific cancers and their attributes, and current treatments and challenges.

2. **The immune system** - Section 2.3 presents an overview of the immune response in general, the immune response to cancer, and the immune response to viruses.

3. **Viruses** - Section 2.4 introduces the adenovirus (an important oncolytic virus), followed by an overview of the virus replication cycle, the function of the E1B genes of an adenovirus, viral movement, current virotherapies and challenges, and combined virotherapy and immunotherapy.

A significant amount of published experimental data is used in this thesis and, as such, the techniques around how this data is collected are explained in Section 2.5. To understand the specific biological background in this chapter, a brief overview of biology is provided in Section 2.1.

2.1 BIOLOGICAL LEVELS: GENES/CELLS/TISSUES/SYSTEMS

Biology is the science of living organisms that exist across a large range of physiological scales. Fig. 2.1 summarises the biology at the different physiological scales considered in the interaction between an oncolytic virus and tumour cells. Genes and deoxyribonucleic acid (DNA) exist at one of the smallest possible scales in cancer biology (Kaiser *et al.*, 2007). Genes are located in the cell nucleus and are the basic physical and functional unit of heredity. Genes are made of DNA, a double helix carrying genetic instructions for the development, function, growth and reproduction of organisms and viruses. A genome is an organism's complete set of DNA, including all of its genes. In humans, a copy of the entire genome is contained in all cells that have a nucleus (Kaiser *et al.*, 2007).

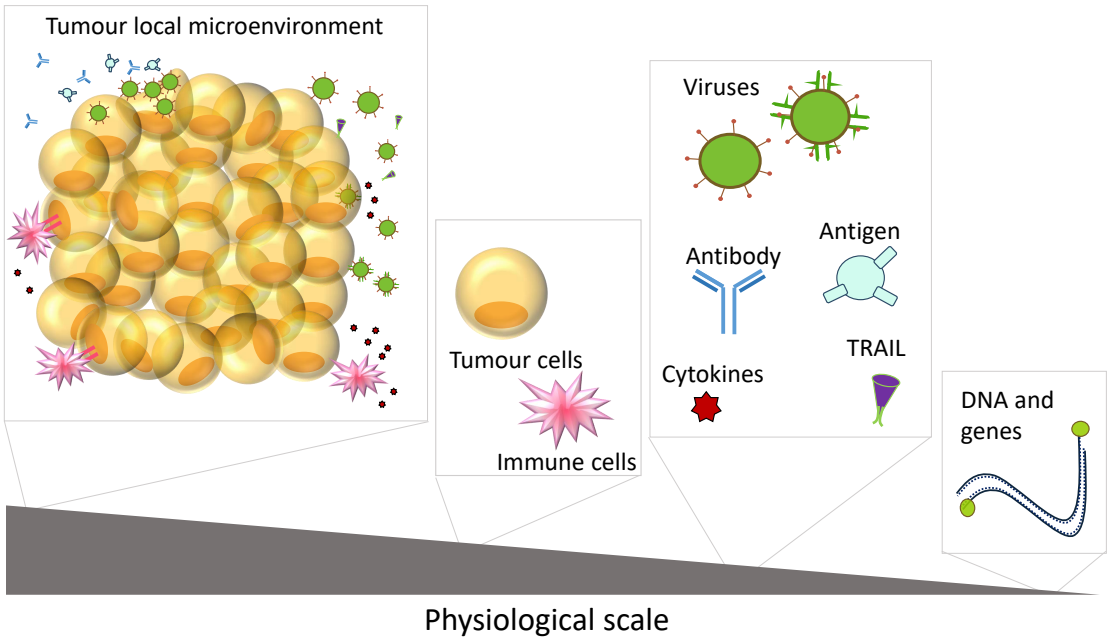

Figure 2.1: Overview of the physiological scales of the biology presented in this thesis.

Building up in scale, there are large classes of molecules and proteins that are crucial to the immune system. Antibodies are large, Y-shaped proteins produced mainly by plasma cells. They are used by the immune system to neutralise pathogens, such as bacteria and viruses (Janeway *et al.*, 2005). Monoclonal antibodies are made by identical immune cells that are all clones of one parent cell. Monoclonal antibodies can have monovalent affinity, meaning that they bind to the same part of an antigen that is recognised by the antibody. Antigens are any substance that stimulate the immune system to produce antibodies and cytokines. Cytokines are signalling molecules that control cell activities. They allow immune cells to communicate and generate a coordinated, robust response to a target antigen (Janeway *et al.*, 2005).

Viruses are microscopic packages of DNA (Kaiser *et al.*, 2007). They are classified as non-living as they are unable to reproduce without a host cell. The exterior protective of a virus is called a capsid. For some viruses, the capsid is surrounded by an additional envelope which is used to help viruses avoid the host immune system (Kaiser *et al.*, 2007). Through infection of cells, virus antigen (or viral genome) is released into the microenvironment were it can be detected by immune cells and induce an immune response (Janeway *et al.*, 2005).

Cells are the basic structural, functional, and biological unit of living organisms (Alberts *et al.*, 2013). Cells provide structure for the body, absorb nutrients and carry out important functions. Cells that group together form tissue and then organs. Other cells, such as immune cells, scavenge the body for possible threats and protect humans from infection and disease. At the tissue and tumour level, all of the biological scales interact to promote or inhibit tumour growth.

2.2 CANCER

2.2.1 *Initial formation*

Cancer begins at the genetic level and starts from the mutation of a single gene (De Pillis and Radunskaya, 2001). These mutations occur due to an array of lifestyle, environment and hereditary factors. Genetic mutations that cause cancer lead to accelerated cell division and inhibition of programmed cell death (O'Connor *et al.*, 2010). These genetic mutations then result in large populations of contiguous damaged cells known as tumours.

Tumours are heterogeneous and are made up of many different cells (De Pillis and Radunskaya, 2001). Due to over proliferation and space limitations, cancer cells are able to push out normal cells in the surrounding tissue and form densely packed groups. Normal tissue, lymphocytes, macrophages, and other types of cells can either grow at the tumour site or are recruited to the tumour through chemotaxis (De Pillis and Radunskaya, 2001). These cells ends up forming part of the tumour and become known as the tumour stroma.

2.2.2 *Development and growth*

Excessive cancer cell proliferation, spatial limitations and interstitial pressure all influence the shape of a tumour. Furthermore, the location of the initial tumour (e.g. which organ the tumour starts in or the tumour's proximity to the bone) can have

significant effects on the geometry and shape that the tumour forms. If there are no spatial limitations for proliferating cancer cells, then a roughly spherical tumour will form, similar to that of a hanging drop tumour spheroid (Weiswald *et al.*, 2015), see Fig. 2.2(a). When there is an obstruction above and below a growing cancer cell population, the tumour will form a more cylindrical shape. This obstruction, for example, could be stiffer stromal tissue, similar to that seen in breast ductal carcinomas in situ (DCIS) (Kim *et al.*, 2011d), see Fig. 2.2(b). Additionally, in certain cancers, the cells on the periphery of the tumour can become invasive cells, allowing them to degrade the surrounding extra-cellular matrix (the structure and support of cells) and invade the space of nearby cells (Jiao and Torquato, 2011). These tumours form invasive branches that can spread into surrounding tissue, see Fig. 2.2(c).

The cell cycle is the series of stages that occur when a cell duplicates and divides. If a healthy cell in the tissue enters the proliferative stage of the cell cycle, it will only divide if there is sufficient surrounding space. Cancer cells, however, ignore the spatial requirement and divide uncontrollably, forming regions of densely packed cells.

Pressure from over proliferating cancer cells restricts the diffusion of oxygen and nutrients (such as glucose) from the blood vessels. As the tumour grows larger, insufficient nutrients reach cells within the centre of the tumour and the tumour reaches a diffusion-limited steady state. The cells towards the centre then form a quiescent tumour cell population (Folkman and Hochberg, 1973; Sherar *et al.*, 1987).

Quiescent cells enter into a state of dormancy, whereby their growth is arrested in the non-proliferative phase of the cell cycle (Zhang *et al.*, 2016). To counteract this, tumours release tumour angiogenesis factor (a growth factor) that stimulates the creation of new capillaries so as to provide nutrients to the necrotic and hypoxic regions. This process is known as vascularisation. If the nutrient supply to quiescent cells increases then cell proliferation may resume (Potmesil and Goldfeder, 1980).

The later stage of a tumour's life cycle can be the most difficult to treat. At late stages, the inner core of a tumour will be necrotic tissue, surrounded by a shell of quiescent cells, and an outermost layer of live, proliferating cells (Folkman and Hochberg, 1973; Sherar *et al.*, 1987). Individual or small groups of cancer cells may then break away from

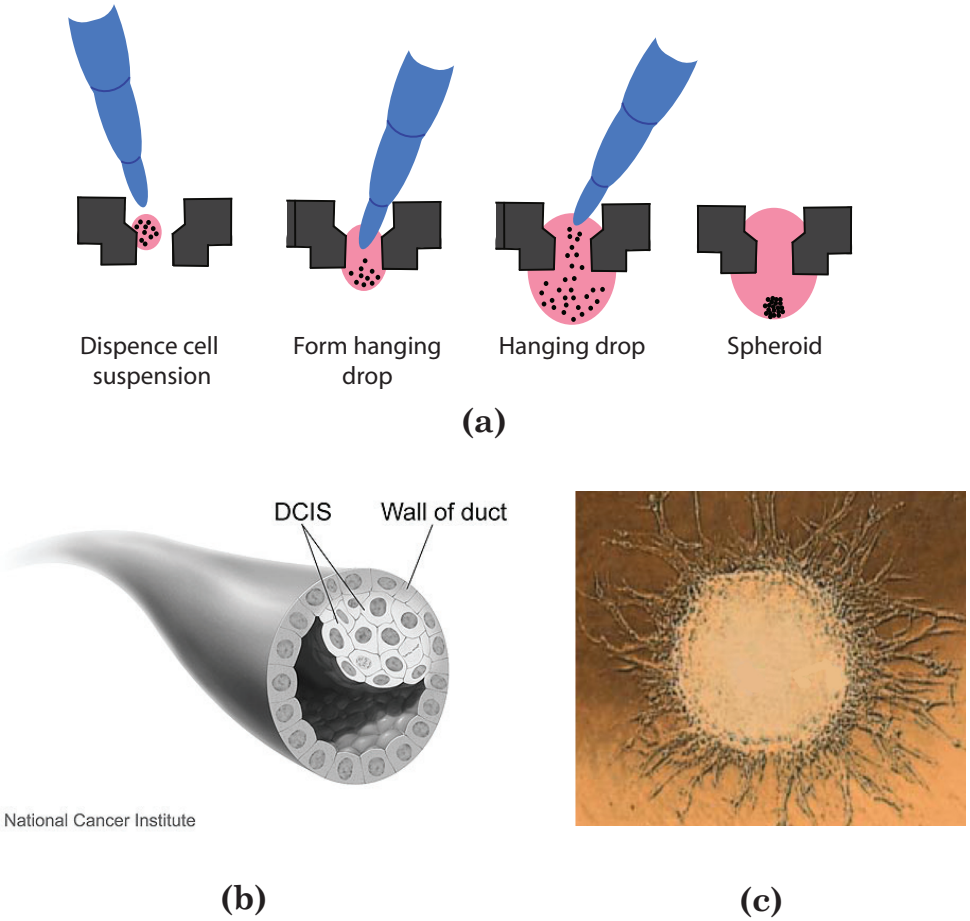

Figure 2.2: Different shapes seen in cancer experiments and treatments. In (a) is an illustration of the hanging drop tumour spheroid (inspired by image published in Horman *et al.* (2013)). In (b) is an illustration of the ductal carcinomas in situ (DCIS) growth (Image source: National Cancer Institute (http://www.cancer.gov)). In (c) is an image of invasive tumour branches (first published in Jiao and Torquato (2011)).

the primary tumour and initiate a new tumour in another location called a metastasis (Chaffer and Weinberg, 2011).

Apoptosis and necrosis are the primary modes of cell death. Apoptosis plays an essential role in the homeostasis of multicellular organisms (Kim *et al.*, 2006a). Failure of cells to undergo apoptosis allows cells to grow unchecked, resulting in the initial stages of cancer (Kim *et al.*, 2006a). Apoptosis is a mode of cell death where the cell is an active participant. It can be induced by immune cells, such as killer T cells and natural killer cells. In comparison, necrosis is associated with premature death of cells in living tissue. It can be caused by viral infection or from cells receiving insufficient

nutrients (such as oxygen and glucose). When a cell undergoes necrosis, it swells and then ruptures and the contents leak out.

2.2.3 *Specific cancers and their attributes*

The treatment strategy and prognosis for a cancer patient will often differ based on the type of initiating cell. Cancer cells have access to different levels of nutrients and space to grow depending on where they are located in the body. This can significantly influence the growth rate of a tumour. In this thesis, treatments for four types of cancer are presented: breast cancer, melanoma, lung cancer and cervical cancer.

2.2.3.1 *Breast cancer*

Breast cancer results from abnormal growth of cells lining the breast lobules or ducts. There are several different types of breast cancer and in this thesis the MDA-MB435 type is considered. This is because this breast cancer is known to express high levels of the the monoclonal antibody Her2/neu+. This monoclonal antibody is found over-expressed on the surface of 20-30% of breast cancer cells (Slamon *et al.*, 1987). Herceptin is a Her2/neu-specific monoclonal antibody that is used regularly in breast cancer treatment as it recognises and binds to Her2 (Kim *et al.*, 2011a) (see Fig. 2.3). In this thesis, an oncolytic virus modified to express Herceptin is examined for its effectiveness on MB435 breast tumours.

2.2.3.2 *Melanoma*

Melanoma is a type of skin cancer which develops from the pigment-containing cells known as melanocytes. The primary cause of melanoma is over-exposure to ultraviolet light (UV). To measure melanoma growth under treatment, experimentalists often use B16-F10 melanoma tumours, as this cell line grows aggressively and cures have rarely been reported (Choi *et al.*, 2012a).

2.2.3.3 *Lung Cancer*

Lung cancer begins in the lungs and the mutations causing this type of cancer are often linked to smoking (Gibbons *et al.*, 2014). Lewis lung carcinoma (LLC) is the only reproducible syngeneic lung cancer model (i.e. can be grown in mice). As such, experimentalists regularly use LLC cells to predict the effectiveness of treatments on lung cancer.

2.2.3.4 *Cervical cancer*

Cervical cancers grow in lining of the cervix. SK-OV3 cervical cancer cell lines are used in mice to test treatment effectiveness for cervical cancer. These cells form adenocarcinoma, a less common and more difficult to diagnose cervical cancer. Experimentalists use SK-OV3 cells as they express Her2/neu+, a monoclonal antibody which, like MDA435 breast cancers, responds to treatment with Herceptin (Kim *et al.*, 2011a).

2.2.4 *Current treatments*

The most commonly used cancer treatments are chemotherapy, radiotherapy and surgery. Chemotherapy is a type of cancer treatment that uses anti-cancer drugs that target and destroy over-proliferating cells in the body. Radiotherapy uses targeted ionizing radiation to kill malignant cells. Surgery is the process of physically cutting out the cancer, and is sometimes used in conjunction with chemotherapy or radiotherapy. While all these therapies are effective, they do not always result in complete tumour eradication and can be dangerous for the patient.

A phenomenon of current interest to clinicians is tumour dormancy. There is clinical evidence that a tumour mass may disappear for a period of time, or at least become no longer detectable, and then reappear, growing to a lethal size (De Pillis and Radunskaya, 2001). In some cases, this phenomenon is seen experimentally under oncolytic virotherapy, where approximate eradication is achieved, and then tumour regrowth occurs, see Choi *et al.* (2012a) and Kim *et al.* (2006a).

2.3 THE IMMUNE SYSTEM

The immune system is the body's defence against infectious organisms and cancerous cells. The immune system is made up of a complex network of cells, tissues and organs that work collectively to eradicate invading pathogens and damaged cells. Immunotherapy is a field of oncology that investigates ways to stimulate an immune system that is targeted towards cancer. As viruses naturally instigate an immune response, combined virotherapy and immunotherapy is a promising therapeutic area.

2.3.1 *The immune response*

The immune system is divided into the innate immune system (the first response) and the adaptive immune system (the second response). There are three primary cells in the innate immune system: macrophages, natural killer (NK) cells and dendritic cells (DCs). Macrophages and DCs form a special subgroup of immune cells called antigen presenting cells (APCs). These cells are a critical part of the immune system as they have class II major histocompatibility complexes (MHCs). Almost every cell has class I MHC and uses it to present antigen. This is essential for the function of killer T cells (CTLs), as they use the class I MHC on cells to determine whether to induce apoptosis in a particular cell. However, only cells with class II MHC molecules (e.g. macrophages and DCs) are able to activate immature helper T cells and immature killer T cells(Sompayrac, 2008; Janeway *et al.*, 2005).

DCs can be activated by macrophages, infected cells or cancerous cells. When a DC encounters a dangerous antigen, it travels to the lymph node to activate immature T cells. At the lymph nodes, it produces interleukin-12 (IL-12) which instructs helper T cells to produce the cytokines: tumour necrosis factor (TNF), interferon (IFN)-γ and interleukin 2 (IL-2) (Sompayrac, 2008; Janeway *et al.*, 2005).

Both TNF and IFN-γ help to keep NK cells activated and IL-2 is a growth factor which stimulates the proliferation of killer T cells, NK cells and helper T cells. NK cells are also activated by signals from macrophages. In return, activated NK cells release

cytokines that promote macrophage activation. The primary function of NK cells is to kill tumour and virus-infected cells by forcing them to undergo apoptosis (Sompayrac, 2008; Janeway *et al.*, 2005).

Immature helper T cells are activated by DCs expressing their cognate antigen. This takes between four and ten hours. Once activated, the helper T cell proliferates (Sompayrac, 2008). To activate an immature killer T cell, also known as cytotoxic T lymphocyte (CTL), an activated DC presents the CTL with the dangerous antigen (Sompayrac, 2008). The activated killer T cell (or CTL) then goes on to kill cells which are presenting this antigen. Also helper T cells are suppliers of interleukin-2 (IL-2) which is required for killer T cells to proliferate (Sompayrac, 2008).

2.3.2 *The immune response and cancer*

Cancer cells are known to suppress the immune system by the induction of anergy or tolerance in the host (Janeway *et al.*, 2005). There are, however, ways to overcome this suppression with administration of immature DCs or immunostimulatory cytokines. Intratumoural administration of DCs increases the probability of tumour antigen recognition and subsequent activation of helper T cells and killer T cells. Administration of immunostimulatory cytokines, such as IL-12 or granulocyte-macrophage colony-stimulating factor (GM-CSF), has been shown to provoke the antitumour immune response by instigating the proliferation and activation of local immune cells (Choi *et al.*, 2012a).

2.3.2.1 *Effects of interleukin IL-12*

IL-12 is an interleukin naturally produced by DCs and macrophages in response to antigen stimulation. It promotes the immunity of helper T cells and activation of CTLs (Choi *et al.*, 2012a). In the presence of IL-12, helper T cells are stimulated to produce TNF, IFN-γ and IL-2, which in turn stimulates the proliferation of CTLs (Janeway *et al.*, 2005). IL-12, accompanied with TNF, stimulates NK cells to produce IFN-γ which is protein that activates macrophages.

2.3.2.2 *Effects of GM-CSF*

GM-CSF is a molecule that functions like a cytokine. It is secreted by macrophages, T cells and natural killer cells. GM-CSF stimulates stem cells to produce monocyte (a type of white blood cell) that exit the circulation and migrate into tissue, whereupon they mature into macrophages and dendritic cells. Thus, it is part of the immune cascade, by which activation of a small number of macrophages can rapidly lead to an increase in their numbers. GM-CSF also enhances the processing and presentation of antigen on APCs (Heystek and Kalthoff, 2000). Studies by Choi *et al.* (2012a) found that GM-CSF expressed in the tumour tissue strongly recruited APCs to the tumour site.

2.3.3 *The immune response and viruses*

Human immune systems have a very powerful and effective way of eliminating viruses. Macrophages and DCs are activated by virus-infected cells through the presentation of virus antigen. Additionally, virus-infected cells undergo lysis, the process by which the membrane of a cell breaks down, compromising its integrity. Cytokines and antigens released during lysis then activate DCs and macrophages (Janeway *et al.*, 2005). These activated cells then stimulate helper T cells and killer T cells to the presence of the virus. Helper T cells also secrete specific cytokines for a virus invasion (specifically type Th1), that provide continual stimulation of killer T cells.

2.4 ONCOLYTIC VIROTHERAPY

Oncolytic viruses are genetically engineered viruses that selectively infect and lyse cancerous cells without causing harm to normal cells (Russell and Peng, 2007). For some time now, viruses have been investigated as a treatment for cancer. The antitumour potency of viruses comes from their inherent ability to induce lysis in infected cells (Kumberger *et al.*, 2016). Additional interest in oncolytic virotherapy arises from the ability to deliver anti-cancer drugs or immunostimualtory cytokines to the tumour site using viruses (Lawler *et al.*, 2017; Myers *et al.*, 2007). This allows for high dose and

localised long-term expression of a drug to be achieved efficiently (Kim *et al.*, 2006a). It reduces the risk of ineffective dosing and nonspecific toxicity (damage of nearby healthy cells) (Kim *et al.*, 2006a). In this form, viruses are known as therapeutic vectors. Viruses can also be engineered to fuse infected cells with neighbouring cells, forming syncytia (multinucleated cells) that ultimately die (Bajzer *et al.*, 2008).

2.4.1 *Adenovirus*

Adenoviruses are non-enveloped viruses with an icosahedral capsid that contains a double stranded linear DNA (Alemany, 2014). The adenovirus is a commonly investigated virus that is showing increasing oncolytic potential. Adenoviruses are known to deliver transgenes most effectively and has widely been used in clinical applications (Kim *et al.*, 2006a). Additionally, adenoviruses can bind to a specific carbohydrate over-expressed on certain types of cancer cells. Genetic modifications of adenoviruses aim to improve the ability of the virus particles to selectively infect, replicate and lyse cancer cells.

2.4.2 *Replication cycle*

The fundamental function of viruses is to infect and replicate within cells. While the replication of every oncolytic virus differs slightly, they follow essentially the same cycle. Once inside a cell, viruses undergo the molecular processes of transport, disassembly, integration, transcription, translation, assembly and, finally, export (Kumberger *et al.*, 2016), see Fig. 2.3.

The adenovirus enters the cell via receptor-mediated endocytosis (Wagner *et al.*, 1999), whereby the genome is maintained inside the virus particle in a highly condensed form. Once inside the cell, the adenovirus exploits active transport by the host cell to get from the cell periphery to the nucleus, (Kumberger *et al.*, 2016). As it is being transported through the cell cytoplasm, the virus is unpacked and the DNA is released from inside the capsid.

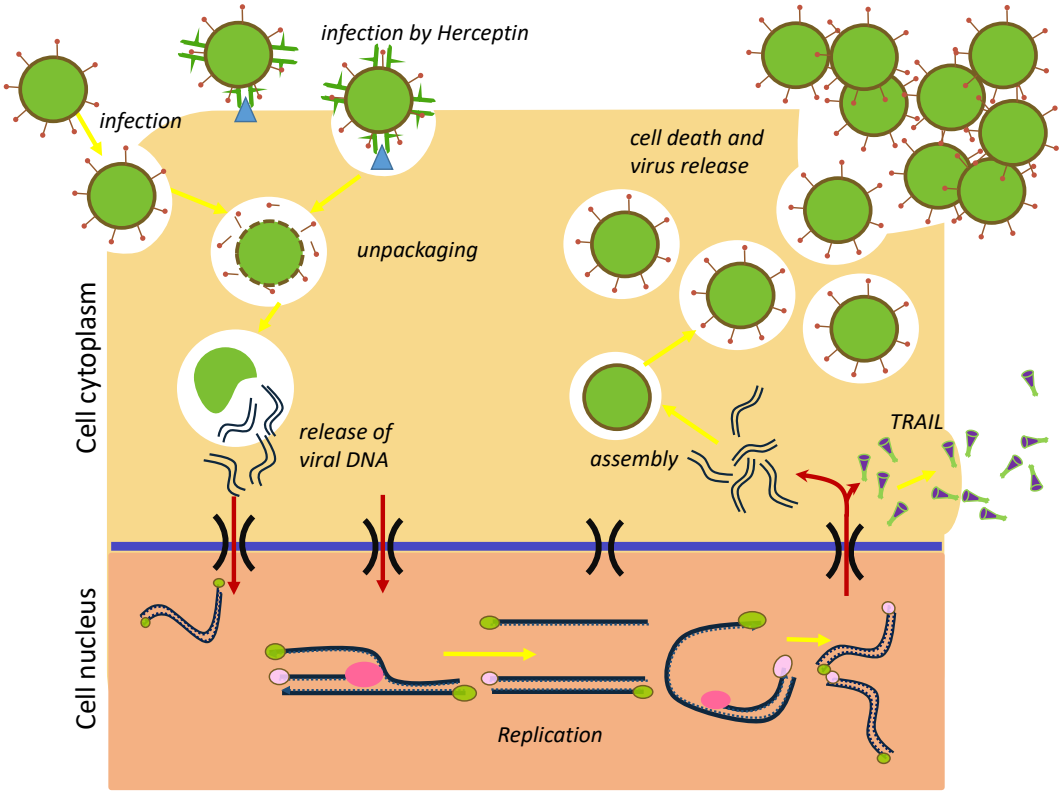

Figure 2.3: The replication process of an oncolytic adenovirus. Viruses can either enter the cell by receptor mediated endocytosis or, if they have been modified to express Herceptin, they will bind to the Her2/neu receptors on the cell membrane and enter that way. The virus is unpacked in the cytoplasm and the DNA is released and enters the nucleus. The DNA then undergoes strand-displacement replication where only one strand is replicated at a time. This synthesis releases a single stranded DNA, which is in turn copied into double strand DNA. These new double stranded DNA then exit the nucleus and are repacked in the cytoplasm before leaving the cell through lysis. If the virus has been genetically engineered to express secretable trimeric TRAIL, then as the virus replication new TRAIL molecules will be released from the nucleus and exit the cell.

Once inside the nucleus, the adenovirus' DNA stimulates the infected cell to transcribe and replicate its genes (Liu *et al.*, 2003; Wagner *et al.*, 1999). The infected cell's transcription machinery cleaves the DNA in a strand displacement mechanism. This is the process by which an initial strand of the DNA is removed and simultaneously copied. Then the single strand that was removed is reprocessed into a double stranded DNA (Hoeben and Uil, 2013; Wagner *et al.*, 1999). The progeny DNA is subsequently packaged into virus particles. After a certain number of virus particles have been gen-

erated, the cell reaches a maximal capacity and bursts open, undergoing lysis and consequently dying. All the new virus particles are then released from the cell.

2.4.3 *The function of the E1B genes in adenoviruses*

Gene-attenuated adenoviruses are emerging as a promising new modality for cancer treatment. Gene-attenuation is the process by which particular genes of the virus are deleted or removed (Kim *et al.*, 2002). With the motivation of improving adenoviruses for cancer gene therapy, genetic attenuation of the E1B gene in adenoviruses has been investigated for enhanced oncolytic and replication effects. Replication-incompetent adenoviruses can also be created through gene-attenuation. These are viruses which are unable to replicate or lyse a cell, and are primarily used as a drug delivery vector.

The E1B gene encodes two distinct tumour antigens, the *19* kDa and *55* kDa proteins, which are both independently capable of influencing the behaviour of the adenovirus (Kim *et al.*, 2002; Rao *et al.*, 1992). Oncolytic adenoviruses with perturbations on the E1B genes have been tested in a range of human clinical trials on throat cancer, glioma, ovarian cancer, sarcoma, pancreatic cancer and more, see Chiocca *et al.* (2004); Galanis *et al.* (2005); Xu *et al.* (2003); Vasey *et al.* (2002); Nemunaitis *et al.* (2001, 2007).

Experimental studies in mice have shown that the *E1B 55* kDa protein could be responsible for viral potency and non-selective replication (Kim *et al.*, 2002). The potency of the *E1B 55* kDa protein likely derives from a physical association with the p53 tumour suppressor gene (Rao *et al.*, 1992). During the early phase of infection, *E1B 55* kDa counteracts stabilisation of p53 and, therefore, the induction of cell apoptosis. Apart from interfering with the p53 function during viral infection, the *E1B 55* kDa protein is also required for efficient cytoplasmic accumulation and translation of adenoviral DNA. Lee *et al.* (2000) showed that *E1B 55* kDa-deletion promoted tumour-selective replication, however, with reduced cell killing. This reduced potency is likely due to the loss of efficient cytoplasmic accumulation and translation.

The *E1B 19* kDa protein has been shown experimentally to be correlated with the rate of cell lysis. The loss of *E1B 19* kDa enhances adenoviral lytic potency. In infected cells, the *E1B 19* kDa protein blocks DNA fragmentation (i.e. separation of DNA into

pieces) and premature death of the host cells induced by expression of the E1A proteins (Kim *et al.*, 2002; Rao *et al.*, 1992). Kim *et al.* (2002) showed experimentally that U343 glioblastoma brain cancer cells infected by an *E1B 19* kDa deleted adenovirus exhibited obvious cell lysis by 2 days post infection *in vitro*. They concluded that deletion of *E1B 19* kDa increased the rate of cell death by infection.

2.4.4 *Viral movement*

Intratumoural virus transport is governed by the molecular structure of the tumour (Wang and Yuan, 2006). At the periphery of a tumour, convection is the dominant mode of transvascular transport of viral vectors. As such, viral vectors preferentially accumulate at the border of tumours (Wang and Yuan, 2006). Extracellular transport once inside a tumour, in the interstitium, is then significantly hindered by the cells and extracellular matrix (Jain, 1988, 1997; Wu *et al.*, 1993; Yuan *et al.*, 1994). The extracellular matrix is a network of macromolecules, such as collagen and enzymes, that provide structural and biochemical support of surrounding cells.

Within the interstitial space, viruses move by diffusion and convection as they cannot move in a self-directed manner (McKerrow and Salter, 2002). Homogeneous diffusion of viral vectors through the extracellular matrix is difficult as the size of these vectors is close to or larger than the space between fibres in the extracellular matrix (Wang and Yuan, 2006). Additionally, viral vectors may bind to cells and extracellular matrix, either with the intent to infect or by accident, which further hinders the interstitial transport (Jain, 1997; Juweid *et al.*, 1992).

2.4.5 *Typical treatment application protocol*

Treatment application protocols are characterised by their method of administration and the dosage protocol. For the most part, in tumour treatment, therapy is either administered intravenously (injected into the blood) or intratumourally (injected into the tumour). The dosage protocol then defines the magnitude and systemic nature of

the treatment. For the most part, viruses are administered in discrete injections, as this is the easiest and most controllable way to administer treatment. Continuous treatment injections are possible when using materials such as degradable hydrogels (Oh *et al.*, 2017). Treatment loaded gels can be injected adjacent to a tumour and release the treatment as the gel degrades.

2.4.6 *Current oncolytic virotherapies and challenges*

The success and capability of adenoviruses as a cancer treatment is evident from a range of clinical trials: see for examples Chiocca *et al.* (2004); Galanis *et al.* (2005); Nemunaitis *et al.* (2001, 2007); Vasey *et al.* (2002); Xu *et al.* (2003). For example, Chiocca *et al.* (2004) conducted a dose-escalation trial of injections of an *E1B 55* kDa attenuated oncolytic adenovirus as a treatment for malignant glioma. None of the 24 patients treated experienced serious adverse effects; however, only one patient experienced remission. Galanis *et al.* (2005) undertook a clinical trial of the same virus, but simultaneously administered with a chemotherapy drug called MAP. For one patient, antitumour activity was seen that lasted 11 months after the injection. While their clinical investigations were promising, they also did not achieve complete remission in their patients.

There have been recent advances of other genetically modified cancer-killing viruses, for example herpes simplex virus, measles, reovirus and vesicular stomatitis Virus (Russell *et al.*, 2012). These viruses are currently being tested in clinical trials for a range of cancer types such as glioma, ovarian cancer, sarcoma, pancreatic cancer, prostate cancer and bladder cancer (Prestwich *et al.*, 2008; Russell *et al.*, 2012). However, while research has progressed and is advancing, oncolytic virotherapy is still at an early stage in its development. Challenges for the field are to select viruses that transiently suppress but then unleash the power of the immune system to maximize both virus spread and anticancer immunity. Additionally, more universally effective treatment protocols need to be developed to overcome the barriers imposed by viral clearance and tumour structure (Russell *et al.*, 2012).

Until recently, most studies of oncolytic viruses have focused on the direct antitumour properties of these vectors, (Kim *et al.*, 2007, 2011a; Lun *et al.*, 2005; Martuza *et al.*, 1991; Thorne *et al.*, 2006); however, there is now an increasing body of evidence suggesting that the host immune response may be critical to the efficacy of oncolytic virotherapy, (Choi *et al.*, 2013a, 2012b; Elsedawy and Russell, 2013; Huang *et al.*, 2010; Melcher *et al.*, 2011). Oncolytic viruses can also be used as cytokine delivery and generating vectors. On this basis, oncolytic viruses represent a promising novel immunotherapy strategy, which may be further combined with existing therapeutic modalities to create an effective cancer treatment.

2.4.7 *Combined virotherapy and immunotherapy*

Immunotherapy is a cancer treatment that uses the body's immune response to target and destroy cancer cells. The focus of immunotherapy is to overcome cancer's ability to suppress the immune system. Novel anticancer immunostimulatory therapies harnessing pre-existing (ineffective) immune responses have shown remarkable clinical results across several tumour types (Velcheti and Schalper, 2016). However, not all patients benefit from these agents, and this is likely due to the heterogeneity in the immune response (Velcheti and Schalper, 2016).

Oncolytic virotherapy can be easily integrated with tumour immunotherapies in the hope of improving their efficacy (Bommareddy *et al.*, 2018). Oncolytic viruses are useful in immunotherapy, as they directly lyse tumour cells, leading to the release of soluble antigens and danger signals, which drive the antitumour response (Bommareddy *et al.*, 2018). In addition, some oncolytic viruses can be engineered to express therapeutic genes. An example of a successful combined virotherapy and immunotherapy experiment can be seen in the results of Chard *et al.* (2015). Using the Vaccinia virus, modified with a gene that can modulate the patient's immune system, they found that the time for which the treatment was effective was longer than without the modification. The immune protein they inserted was able to reduce the intensity of the immune response against the virus, allowing it to perform its function for a longer period of time.

2.5 EXPERIMENTAL TECHNIQUES AND DATA COLLECTION

In vitro and *in vivo* experiments are a way of measuring the validity and efficacy of new oncolytic therapies. *In vitro* experiments are performed on cells or biological molecules outside their normal biological context, whereas, *in vivo* experiments measure the effects on living organisms. The protocols of the experiments for data that is used in this thesis are outlined below.

2.5.1 *Virus titer and plaque assay*

To determine the concentration of a particular virus stock, *in vitro* experiments are performed. In these, aliquots of different dilutions of the stock are prepared, and applied to susceptible cells in mono-layers. The cells are incubated for a period and then covered with a nutrient rich gel. During the incubation period the infected cells release the replicated viruses (progeny). These new viruses are restricted in movement by the gel, resulting in each infectious particle producing a circular zone of infected cells, called plaque.

The plaques are counted for each dilution case, focused on those cases with between 10 and 100 plaques. By assuming that each plaque formed is representative of one infective virus particle, the titre (a measure of the concentration) of the applied solution can be determined. This is most accurate if there are very few plaques, with those with 100 plaques determining the original stock concentration to within approximately $\pm 10\%$. The titre is determined as

$$[\mathrm{titre}] = \mathrm{pfu/mL} \tag{2.1}$$

$$\frac{\mathrm{pfu}}{\mathrm{mL}} = \frac{\#\mathrm{plaques}}{\mathrm{Vd}} \tag{2.2}$$

where pfu is the plaque forming units, d is the dilution and V is the volume. PFU/mL represents the number of infective particles within the sample unit volume (Baer and Kehn-Hall, 2014).

2.5.2 *Cell viability (%)*

Cell viability is the quantification of the number of live cells at a point in time usually in an *in vitro* experiment. It is expressed as a percentage of the total cell population, measured as the sum of both live and dead cells.

2.5.3 *Tumour growth measurements*

Changes in tumour volume are used for therapy response monitoring in *in vivo* experimental studies. Experimentalists can measure tumour growth in non-invasive ways using image technologies such as MRI or x-rays, however, these are costly. Although less accurate, many experiments on mice or rats use calipers to measure the size of the tumour through the skin of the animal. This technique is convenient, cost-effective and non-invasive (Lee *et al.*, 2015). Assuming an elliptical spheroid shape for a tumour, the volume can be estimated from the measurements of tumour length and width using $0.523 \times \mathtt{length} \times \mathtt{width}^2$.

2.5.4 *Polymerase chain reaction (PCR) of viral genomes*

Polymerase chain reaction (PCR) is a technique primarily used to measure the amount of a specific DNA in a sample. Real-time PCR is an assay that monitors the accumulation of a DNA product from a PCR reaction in real time. Experimentalists use real-time PCR to monitor the amount of viral genome in the blood stream of mice. This is done by collecting whole blood from the retro-orbital plexus and conducting quantitative real-time PCR of the sample. Similarly, to assess the distribution of virus within the mouse after injection, organs are harvested and the number of viral genomes in each sample is assessed by real-time quantitative PCR.

2.5.5 *Dendritic cell release profile*

To investigate the release profile of dendritic cells from a gel by enzymatic degradation, the supernatant is obtained and viable dendritic cells are counted by trypan blue staining. Trypan blue is a dye that is cell membrane impermeable and therefore only enters cells with compromised membranes. Upon entry into the cell, trypan blue binds to intracellular proteins rendering the cell a blue colour and allowing for direct identification and enumeration of live and dead cells in a given population.

3

MATHEMATICAL BACKGROUND

The mathematical work in this thesis can be divided into four areas: (1) deterministic and distributed-parameter models, (2) agent-based models, (3) techniques for model optimisation and (4) model analysis. This chapter summarises the literature in following sections:

1. **Deterministic and distributed-parameter models** - Section 3.2 provides examples of relevant mean-field models and distributed-parameter models for cancer growth, oncolytic virotherapy, and combined oncolytic virotherapy and immunotherapy.

2. **Agent-based models** - Section 3.3 presents published cellular automata and off-lattice agent-based models used in cancer therapy.

3. **Model optimisation** - Section 3.4 provides an overview of the numerical implementation of the fitting algorithm used to analyse oncolytic virotherapy data and the goodness of fit statistical calculations.

4. **Model analysis** - Section 3.5 summarises the Routh-Hurwitz stability criteron, and the theory behind the parameter sensitivity analysis.

The motivation behind the modelling techniques for cancer growth and oncolytic virotherapy is given in Section 3.1.

3.1 MODELLING TECHNIQUES IN CANCER GROWTH AND ONCOLYTIC VIROTHERAPY

Mathematical models are designed to distill the essential behaviour of a biological system. The biological context and purpose of the interaction determines whether a system should be modelled deterministically or stochastically. Deterministic (or mean-field) models are chosen when randomness is not a critical part of the dynamics. Whereas random-parameter models or agent-based models (ABMs) can be insightful when stochastic relationships and interactions in the system can have a significant effect.

Mean-field models assume that the interaction of a group of individuals can be approximated by an averaged response. These models are useful in modelling biological

systems where interactions between well-mixed populations can be taken as an average rate, for example, when the rate at which cancer cells proliferate can be taken as an average rate across the entire population. The two most common deterministic frameworks in cancer research are ordinary differential equations (ODEs) and partial differential equations (PDEs).

ODEs are used when the biological interaction considered depends primarily on a single variable, time. In this way, tumour geometry or viral movement are considered insignificant. However, if the spatial aspect of cancer treatment modelling is important, PDEs are able to account for this. In addition, age-structured PDEs have been shown to be very useful in modelling cancer growth by accounting for the time a cell spends in the cell cycle (Crivelli *et al.*, 2012).

If the heterogeneity in a biological system is important, distributed (random)-parameter models or agent-based models can be useful. In this thesis, distributed-parameter models are those that have one or more parameters drawn from a random distribution. These are useful in oncolytic virotherapy as viral infection and replication rates can be heterogeneous across a population of cells and viruses (Miyashita *et al.*, 2015). ABMs can also be useful in virotherapy, as they allow for the interactions of a population of cells and viruses to be modelled individually.

A collection of models that represent a scaffold for this thesis are detailed below. There are many other deterministic and stochastic models that have been used in cancer therapies, but they will not be reviewed here.

3.2 DETERMINISTIC MODELS

3.2.1 *Models for cancer*

ODE models can be used to describe a growing population of tumour cells. These models are well-mixed and predominantly do not include any geometric effects. Exponential growth is one of the simplest cancer ODE models, Eq. (3A), and is useful for describing tumour growth in its initial stages (Laird, 1964). Another formulation of tumour growth is the logistic model, Eq. (3B). This model is used when considering

tumour growth over a longer time as it allows the population to reach a carrying capacity. The Gompertzian tumour growth model, Eq. (3C), captures a similar dynamic, albeit with the addition of a ln term. See the formulations of these models below:

$$\frac{dU}{dt} = rU, \quad (3A) \qquad \frac{dU}{dt} = rU\left(1 - \frac{U}{L}\right), \quad (3B) \qquad \frac{dU}{dt} = rU\log\left(\frac{L}{U}\right), \quad (3C)$$

where U is the tumour population, r is the growth rate, L is the carrying capacity, and t is time.

Both logistic and Gompertz functions model qualitatively similar tumour growth rates and are known to accurately reproduce experimentally observed proliferating tumours (Laird, 1964; Dingli *et al.*, 2009; de Pillis *et al.*, 2005). The primary difference between the two is that the Gompertz function will have a more rapid growth at smaller values of the dependent variable (Laird, 1964), which is time in Eq. (3B). This initial growth is what makes the Gompertz function a good approximation for tumour growth, as tumours are known to grow rapidly early on.

There are many mathematical models that consider tumour growth as a more complicated dynamical process, where spatial interactions, multiple cell types and cytokines are considered, see for examples Adam (1986); Anderson *et al.* (2000); Byrne *et al.* (2003); Chaplain *et al.* (2006); Delgado-SanMartin *et al.* (2015). In this thesis, the emphasis is placed more heavily on the modelling of the interaction between tumour cells and treatment, and as such, this level of cancer modelling is beyond the scope of the research.

3.2.2 *Models of viral dynamics*

Mean-field models can be used to add insight into the dynamics of viral-based therapies or the treatment of viral-based diseases. In these models, the viral infection and replication processes are modelled as average rates across the population. When modelling the interaction between uninfected cells, U, and virus particles, V, the populations are considered well-mixed and spatial dynamics are neglected.

Human Immunodeficiency Virus (HIV) causes the development of AIDS (Acquired Immune Deficiency Syndrome, or Acquired Immunodeficiency Syndrome). HIV targets cells that carry the CD4 cell-surface protein, and the major target of HIV is the helper T cell (Perelson and Nelson, 1999). After becoming infected, helper T cells produce new HIV particles. This is similar to what occurs after a tumour cell is infected by an oncolytic virus (see Section 2.4.2). Perelson and Nelson (1999) developed a system of mass-action equations to model the important features of HIV pathogenesis:

$$\frac{dU}{dt} = s + rU\left(1 - \frac{U}{L}\right) - d_T U - \beta UV, \tag{3.1}$$

$$\frac{dI}{dt} = \beta UV - d_I I, \tag{3.2}$$

$$\frac{dV}{dt} = \alpha d_I I - d_V V. \tag{3.3}$$

where U is the population of uninfected helper T cells, I is the population of infected cells, s is the rate at which new uninfected cells are created from sources within the body, d_T is the death of T cells cells, β is the infection rate, d_I is the rate of cell lysis, α is the number of new cells created through lysis and d_V is the decay rate of the virus. The proliferation of uninfected T cells is modelled using the logistic function, Eq. (3B). Perelson and Nelson (1999) used their system to help guide future treatment strategies of HIV.

While HIV and oncolytic viruses are different, they both undergo infection and replication in a similar manner. As such, there is a large cross-over between mean-field models in oncolytic virotherapy and HIV. There are many other mean-field models of HIV (e.g. (Li and Shuai, 2010; Bonhoeffer *et al.*, 1997)) that share similar features to the models for oncolytic virotherapy detailed in the following section.

3.2.3 *Models for oncolytic virotherapy*

Mathematical models have been used to describe the interaction between an oncolytic virus and a tumour, either on a theoretical basis or applied to data. Predominantly, these models are ODE systems (similar to Eqs. (3.1)-(3.3)) where the interactions

between cancer cells and virus particles are assumed to occur at average rates across the population.

Komarova and Wodarz (2010) developed a simple base model for virotherapy:

$$\frac{dU}{dt} = Uf(U, I) - \beta I g(U, I), \tag{3.4}$$

$$\frac{dI}{dt} = \beta U f(U, I) - d_I I, \tag{3.5}$$

where $f(U, I)$ governs the cancer growth and death processes and $g(U, I)$ is the rate of infection. In this model, the viral population and its corresponding dynamics are assumed to be constant and not modelled explicitly. Komarova and Wodarz (2010) analysed this general system and found that if the viral spread (i.e. $g(U, I)$) was sufficiently fast, the tumour could be eliminated.

An example of a more complex model for oncolytic virotherapy can be seen in the work by Wodarz (2003). Wodarz (2003) studied the conditions under which virotherapy could lead to tumour remission for a non-replicating versus replicating virus. Wodarz (2003) found that for replication-competent viruses, the efficacy was optimal when the rate of virus-induced cell killing was kept small. In contrast, for replication incompetent viruses the optimal antitumour effectiveness occurred when rate of virus-induced cell killing was maximised.

One of the first models that explicitly accounted for the viral population was developed by Bajzer *et al.* (2008). Conducting a bifurcation analysis of their system, these authors discovered stable oscillations in the tumour population emerging from a Hopf bifurcation. While the concept of an oscillating tumour may seem unusual, such behaviour has been observed experimentally (Titze *et al.*, 2017).

Titze *et al.* (2017) developed a model, analogous to Bajzer *et al.* (2008)'s, for treatment of glioblastoma growth with an oncolytic adenovirus:

$$\frac{dU}{dt} = rU - dU - \beta UV, \tag{3.6}$$

$$\frac{dI}{dt} = \beta UV - \delta(V)I, \tag{3.7}$$

$$\frac{dV}{dt} = pI - d_V V, \tag{3.8}$$

where p is the release rate for new virions and δ is the infected cell death function. Matching their model to data, Titze *et al.* (2017) found that the treatment was predicted to give long-term tumour recurrence, similar to the original oscillating tumour behaviour suggested by Bajzer *et al.* (2008).

Some extensions to the basic oncolytic virotherapy models above can be seen in the works by Dingli *et al.* (2006, 2009); Novozhilov *et al.* (2006); Karev *et al.* (2006). Dingli *et al.* (2009) developed a system of ODEs that modelled the process of syncytium (virus-infected cells fusing together):

$$\frac{dU}{dt} = rU \ln\left(\frac{L}{U+I+s}\right) - \beta UV - \rho UI, \tag{3.9}$$

$$\frac{dI}{dt} = \beta UV - d_I I + \lambda \rho UI, \tag{3.10}$$

$$\frac{dV}{dt} = \alpha(I+s) - \omega V - \beta UV, \tag{3.11}$$

$$\frac{ds}{dt} = (1-\lambda)\rho UI - d_I s, \tag{3.12}$$

where s is the number of syncytia, ρ is the rate at which additional syncytia are created and $1-\lambda$ is probability of syncytia fusing. Dingli *et al.* (2009) found that tumour eradication could only occur if the population of uninfected cells decayed faster than the cells incorporated in syncytia. By analysing their framework through a bifurcation and stability analysis, they discovered stable oscillations in the tumour cell population emerging from a Hopf bifurcation. Note that in this model, a variation of the Gompertz function (Eq. (3C)) model was used to model tumour growth.

As illustrated in the results of Bajzer *et al.* (2008) and Dingli *et al.* (2009), bifurcation analysis can be fundamental in finding conditions for successful oncolytic virotherapy. Novozhilov *et al.* (2006) showed using a bifurcation analysis that there is a region of the parameter space where trajectories form a family of homoclinics to the origin. A homoclinic orbit is a trajectory which joins a saddle equilibrium point to itself and yields an orbit of infinite duration. This finding was reinforced again by Berezovskaya *et al.* (2007), who showed how certain models possess a dynamical regime of deterministic extinction through the presence of homoclinics. From the biological point of view, the

existence of homoclinic orbits suggests that tumour cells can be eliminated with time and complete recovery is possible.

3.2.4 *Models for the immune response to cancer*

For many years, researchers have turned to mathematical modelling as a way of understanding the complex interactions of immune cells in the tumour microenvironment. One of the first mathematical models of immunotherapy was a system of ODEs developed by De Boer *et al.* (1985) to model the activation of macrophages and subsequent antitumour immune response. Their model formed the basis for the development of many other models of the tumour-immune interaction, such as the model developed by de Pillis *et al.* (2005) to describe the role of natural killer (NK) cells, N, and killer T cells, K, in tumour surveillance:

$$\frac{dU}{dt} = rU\left(1 - \frac{U}{K}\right) - cNU - D, \tag{3.13}$$

$$\frac{dN}{dt} = \sigma - fN + \frac{gU^2}{h + U^2}N - pNU, \tag{3.14}$$

$$\frac{dK}{dt} = -mK + \frac{jD^2}{k + D^2}K - qKU + rNU, \tag{3.15}$$

$$\text{where } D = d\frac{(K/U)^\lambda}{s + (K/U)^\lambda}U \tag{3.16}$$

where the tumour growth was modelled logistically (Eq. (3B)), and both NKs and killer T cells were able to kill tumour cells. Using a parameter sensitivity analysis, de Pillis *et al.* (2005) suggested that the model can predict which patients may positively respond to treatment. Computer simulations of their model also highlighted the importance of killer T cell activation in cancer therapy.

Additionally, there has been recent work on developing models that consider the immune response to combined immunotherapy and virotherapy, such as the work of

Wares *et al.* (2015) and Kim *et al.* (2015). The work of Kim *et al.* (2015) looked at the effect of an oncolytic virus expressing 4-1BBL and IL-12 on the immune response:

$$\frac{dU}{dt} = rU - \beta\frac{UV}{N} - k(I)\frac{UT}{N}, \tag{3.17}$$

$$\frac{dI}{dt} = \beta\frac{UV}{N} - d_I I - k(I)\frac{IT}{N}, \tag{3.18}$$

$$\frac{dV}{dt} = u_V(t) + \alpha d_I I - d_V V, \tag{3.19}$$

$$\frac{dT}{dt} = s_T(I) + pA - d_T T, \tag{3.20}$$

$$\frac{dA}{dt} = s_A(I) - d_A A, \tag{3.21}$$

where T is the number of T cells at the tumour site, A is the number of APCS at the tumour site, N is the number of cells, $u_V(t)$ is the rate at which new virus particles are injected into the system, $s_T(I)$ is the activation rate of T cells by infected cells, p is the activation rate of T cells by APCs, and T cells and APCs die at rates d_A and d_T. Conducting a parameter sensitivity analysis of their model, Kim *et al.* (2015) found that combinations of specialist viruses that express either IL-12 or 4-1BBL might initially act more potently against tumours than a virus that expresses both.

A major difference between the model of Kim *et al.* (2015) and de Pillis *et al.* (2005) was the use of frequency-dependent infection terms, $\beta UV/N$, in place of mass action, βUV. Frequency-dependent terms are common in epidemic modelling as they allow for interactions to occur at a rate dependent on the frequency of the constituents as opposed to the total number. The primary difference between these two modelling terms is that mass action assumes that the infection rate increases with either an increase in the pathogens or host. Whereas, the frequency-dependent infection rate assumes that the infection rate increases with the prevalence (freuqency) of infection.

Wares *et al.* (2015) then extended the model of Kim *et al.* (2015) in Eqs. (3.17)-(3.21) to include discrete DC injections and subsequent interactions. Through perturbing the dosage strategy, Wares *et al.* (2015) found that it is more effective to treat a tumour with immunostimulatory oncolytic viruses first followed by a sequence of DCs than to alternate virus and DC injections. While insightful, there is still a considerable amount of development needed for these models. For example the effects of the helper T cell

were not modelled explicitly by Kim *et al.* (2015) and the immature and active states of the DCs were not considered by Wares *et al.* (2015).

3.2.5 *Models with distributed (random) parameters or delays*

Time delays are intrinsic to the viral infection and replication processes. Most mathematical models of viral dynamics account for the intracellular delay between viral infection and the appearance of new viral progeny using a constant delay parameter, see Herz *et al.* (1996); Nelson *et al.* (2000); Nelson and Perelson (2002); Pawelek *et al.* (2012); Wang *et al.* (2009); Zhu and Zou (2008). For example, Herz *et al.* (1996) developed the below model to account for the intracellular phase of the hepatitis B viral life cycle:

$$\frac{dU}{dt} = \lambda - dU - \beta UV, \tag{3.22}$$

$$\frac{dI}{dt} = \beta(t-\tau)U(t-\tau)V(t-\tau)e^{-\bar{a}\tau} - aI(t), \tag{3.23}$$

$$\frac{dV}{dt} = kI - uV, \tag{3.24}$$

where λ is the influx of cells, d is the death rate, τ is the delay in viral production, $\bar{a}$ is the death rate for infected cells that have not started producing virus, a is the death rate of virus-producing infected cells, k is the rate of virus production and u is the rate that free virus particles are cleared. Herz *et al.* (1996) incorporated a constant delay into the equivalent mass-action and frequency-dependent infection terms (seen in the models above). Using their model, Herz *et al.* (1996) illustrated that frequent early sampling of plasma virus would provide more reliable estimates of the hepatitis B virus free virus half-life.

While constant delays are an elegant way to account for the delay in viral production, they remove the possibility of heterogeneity within the cellular population. Viral infection, replication and evolution can be stochastic events dependent on the behaviour of viral genome molecules in each cell (Miyashita *et al.*, 2015). Distributed delays can be used effectively to model both the delay in viral replication and the heterogeneous nature of a population of viruses and cells, see for example Banks *et al.* (2003); Culshaw

et al. (2003); Elaiw (2012); Li and Shu (2010); Nakata (2011); Shu *et al.* (2013); Yuan and Zou (2013).

One of the first mathematical models to use distributed delays to model viral replication was introduced by Mittler *et al.* (1998) for HIV-1 (a type of HIV). To model the dynamics of the virus, Mittler *et al.* (1998) introduced a time delay between initial infection and the formation of productively infected cells, assuming that the variation among cells with respect to this intracellular delay could be approximated by a gamma distribution:

$$\frac{dI}{dt} = \int_0^\infty kUf(t')V_I(t-t')e^{-mt'}dt' - \delta I(t), \tag{3.25}$$

$$\frac{dV_I}{dt} = [1-H(t)](1-\eta)pI(t) - cV_I(t), \tag{3.26}$$

$$\frac{dV_{NI}}{dt} = H(t)\eta pI(t) - cV_{NI}(t), \tag{3.27}$$

where V_I and V_{NI} are the populations of infectious and non-infectious viruses, k is the infection rate constant, U is the constant density of uninfected target cells, f is the probability distribution for the delay t', t' is delay from infection to the time infected cells begin producing virus, e^{-mt} accounts for the loss of infected cells between the time of initial infection and the release of the first virus particles, δ is the rate of productively infected cell death, h is the Heaviside function, η is the drug efficacy, p is the rate at which productively infected cells release, and c is the clearance rate of plasma virus particles. Using their model, Mittler *et al.* (1998) demonstrated that it is possible to incorporate distributed delays into existing models for HIV dynamics and from these estimate the half-life of free virus from data.

Following on from the work of Mittler *et al.* (1998), many mathematical modellers introduced distributed delays to account for the intracellular viral delay, see for example Culshaw *et al.* (2003); Nakata (2011); Shu *et al.* (2013); Yuan and Zou (2013). However, distributed-delay models have not been employed in oncolytic virus modelling. Additionally, none of the previous work has considered the effects of stochasticity in the length of time viruses spend replicating (Miyashita *et al.*, 2015).

3.3 AGENT-BASED MODELS

Agent-based models are a class of computational models for simulating the actions and interactions of a population of programmed agents within a controlled environment. Cell-based computational models are a subset of agent-based models that simulate individual cells as they interact in tissue (Metzcar *et al.*, 2019). Generally speaking, agent-based models used in cancer research are split into two classes: lattice-based (cellular automata) and off-lattice models, see Fig. 3.1.

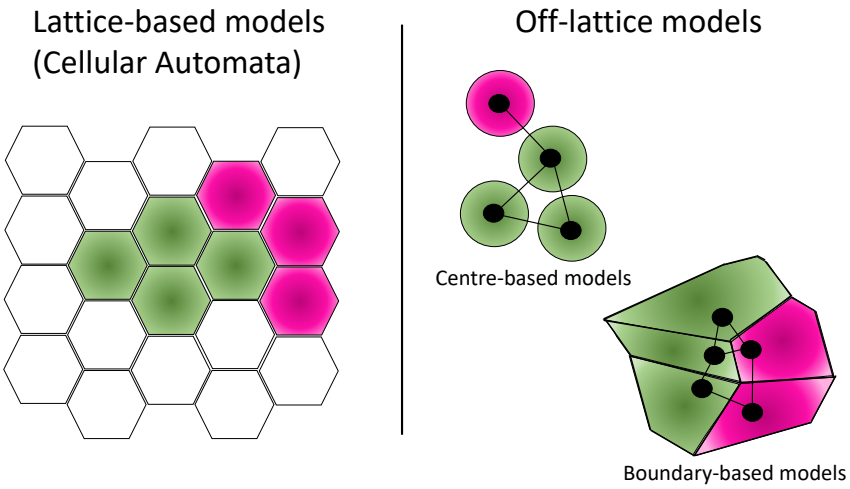

Figure 3.1: An illustration for lattice-based (cellular automata) models and off-lattice models.

3.3.1 *Cellular automaton*

In cellular automata (CA) or lattice-based models, each lattice site in a structured mesh can hold a single cell (Metzcar *et al.*, 2019). At each time step, each cell is updated with discrete lattice-based rules: remain, move to a neighbouring lattice site, die (vacating the current lattice site), or divide to place a daughter cell in a nearby site (see Fig. 3.1). Cellular automata allow individual population interactions to be modelled explicitly and probabilistically. In this way, heterogeneity and variability in biology can be captured and simulated.

A common mesh, or tessellation, used in cellular automata is the Voronoi tessellation. This is regularly used by researchers to model tumour cell sheets, (Lobo, 2014; Kansal *et al.*, 2000a; Schaller and Meyer-Hermann, 2005). A Voronoi tessellation is a partitioning of a space into regions based on where the lines of the tessellation are the points equidistant to centre points in the space. The hexagonal lattice in Fig. 3.1 is an example of a Voronoi tessellation. The first use of the Voronoi tessellation to study the dynamics of tumour growth in a cellular automaton was undertaken by Kansal *et al.* (2000a). Since then, researchers have used Voronoi tessellations successfully in tumour histopathological image analysis (Kiss *et al.*, 1995; Haroske *et al.*, 1996).

Recently, cellular automata have been derived to explain oncolytic virotherapy in a more realistic setting. Wodarz *et al.* (2012) developed a lattice-based stochastic computational model to understand the principles underlying virus spread in spatially structured target cell populations. Their model used a two-dimensional grid where each spot was either occupied by a cell or empty. They defined a set of rules that determined the interaction between viruses and tumour cells and predicted which pattern of virus growth (hollow ring, filled ring or dispersive) would occur based on different parameter values. They showed that long-term only hollow ring structured viral patterns resulted in treatment success.

A hybrid PDE-CA approach can also be useful in oncolytic virotherapy modelling. Paiva *et al.* (2009) used partial differential equations and cellular automata rules to describe the multiscale dynamics of tumour growth. Reaction-diffusion equations were defined for the tissue dynamics of nutrients and viruses. In these equations, cells acted as sinks and sources of nutrients and viruses depending on their internal states. On top of this, the cell dynamics were modelled using a stochastic process controlled by the local concentration of nutrients and free virus at the tissue level. Paiva *et al.* (2009) found that successful virotherapy requires a strong inhibition of the host immune response and high virus mobility.

A more detailed summary on cellular auatomaton models of tumour development can be found in the reviews by Moreira and Deutsch (2002) and Boondirek *et al.* (2010). For more examples of cellular automata in oncolytic virotherapy and immunotherapy, see the work of Alarcón *et al.* (2003); Jiao and Torquato (2011); Frascoli *et al.* (2016);

Ghaffarizadeh *et al.* (2018); Kim and Lee (2012); Dormann and Deutsch (2002); Powathil *et al.* (2013); Mallet and De Pillis (2006). The disadvantage of lattice-based modelling is that cell movement is restricted to a pre-defined grid, and over time, this can restrict the formation of spatial heterogeneity. Using an underlying off-lattice model reduces grid-based artefacts that can occur when using a fixed lattice model (Ghaffarizadeh *et al.*, 2018), producing a more realistic representation of the biological system.

3.3.2 *Off-lattice agent-based modelling*

Off-lattice agent-based models can be used effectively to simulate mechanical and physiological phenomena in cells and tissues (Van Liedekerke *et al.*, 2015). In off-lattice agent-based models, interactions between cells are usually described by forces or potentials, and position changes in cells can be obtained by solving an equation of motion (Metzcar *et al.*, 2019; Van Liedekerke *et al.*, 2015). A range of frameworks have been developed to model cellular interactions as centre-based models (Frascoli *et al.*, 2013; Ghaffarizadeh *et al.*, 2018) or boundary-based models (Meineke *et al.*, 2001). The general difference between the two styles of off-lattice models, is that boundaries of cells play a role in boundary-based models, see Fig. 3.1.

PhysiCell is an example of a centre-based off-lattice agent-based model (Ghaffarizadeh *et al.*, 2018). It is an open source physics-based multicellular simulator with a robust, scalable C++ code for simulating large systems of cells. It allows for biologically realistic modelling of cell cycling, apoptosis, necrosis and cell volume changes. PhysiCell is an example of a hybrid PDE-ABM model, but unlike the work of Paiva *et al.* (2009), PhysiCell combines a PDE framework for substrate diffusion with an off-lattice cell-based model.

Similar to the majority of off-lattice ABMs, PhysiCell models the cell-cell adhesive, cell-cell "repulsive" forces, drag forces and locomotive forces of a cell i using

$$m_i \frac{d\mathbf{v}_i}{dt} = \sum_{j \in N(i)} (\mathbf{F}^{i,j}_{cca} + \mathbf{F}^{ij}_{ccr}) + \mathbf{F}^{i}_{drag} + \mathbf{F}^{i}_{loc}, \tag{3.28}$$

where $\mathbf{F}_{cca}$ and $\mathbf{F}_{ccr}$ are cell-cell adhesive and "repulsive" forces, $\mathbf{F}_{drag}$ collects dissipative, drag-like forces, and $\mathbf{F}_{loc}$ is the locomotive forces. This equation is used to calculate the cell's velocity $\mathbf{v}_i$ given a mass m_i. The explicit formulations for the force terms $\mathbf{F}_{cca}, \mathbf{F}_{ccr}, \mathbf{F}_{drag}$ and $\mathbf{F}_{loc}$ can differ between off-lattice models, depending on the model's assumptions.

Frascoli *et al.* (2013) developed their own computational framework for the migration of groups of cells in three dimensions. The model focused on the forces acting at the microscopic scale and the interactions between cells and the extracellular matrix (ECM). They developed equations of motion and velocity functions by calculating the total cell-cell and cell-ECM interactions, similar to that of Eq. (3.28). Frascoli *et al.* (2013) modelled cell-cell forces by assuming that cells had a compactable outer ring with a solid core.

Building on these frameworks, off-lattice ABMs have been used effectively in modelling tumour elimination by the killer-T-cell response. Kim and Lee (2012) formulated a hybrid PDE-ABM model of the dynamics of an anti-cancer killer-T-cell response in the vicinity of a developing tumour. Their work demonstrated the importance of tumour geometry in determining killer-T-cell effectiveness and the likelihood of eliminating the tumour.

A boundary-based off-lattice ABM was developed by Meineke *et al.* (2001) to model cell movement and arrangement in the intestinal crypt using a Voronoi tessellation. Unlike a Voronoi tessellation in a cellular automaton, the Voronoi tessellation in Meineke *et al.* (2001)'s model changed at every time step based on the interaction forces felt by a cell, given by a similar formulation to Eq. (3.28). The advantage of this style of modelling is that cells do not have to retain a fixed circular shape as is evident by the illustration in Fig. 3.1.

The different off-lattice ABM approaches mentioned above would be useful for modelling oncolytic virus dynamics; however, up until now, these models have yet to be applied in oncolytic virotherapy.

3.4 MODEL OPTIMISATION

3.4.1 *Simultaneous and hierarchical fitting*

Simultaneous and hierarchical parameter optimisation (or fitting) methods are useful ways of obtaining parameters that match a system of ODEs to data. For the hierarchical optimisation technique, the different dominant processes in a model that relate to each data set are first determined and the parameters relating to those processes are fit individually. For the simultaneously fitting algorithm, multiple parameters are fit to multiple data sets simultaneously and the full collection of data is used to optimise each parameter in the model. There are examples of hierarchical optimisations in the work by Kim *et al.* (2015) (Eqs. (3.17)-(3.21)), where they used they used the algorithm to optimise a set of tumour time-series measurements under treatment with an oncolytic virus expressing variations of 4-1BBL and IL-12. One of the earliest illustrations of the simultaneous optimisation algorithm, can be see in Brewer *et al.* (2014)'s work on modelling the trafficking kinetics of insulin-regulated glucose transporter Glut4. Gray and Coster (2016) also employed the simultaneous fitting algorithm in their work on modelling Akt, a key mediator of glucose transport in response to insulin.

3.4.2 *Numerical implementation*

A least-squares fitting method can be used to optimise model parameter values to data. This is a common technique used to optimise parameters in many different ODE systems, see the work by de Pillis *et al.* (2005) and Kronik *et al.* (2008). The least-squares fitting method determines an optimal value for the model parameters $\mathbf{p}$ to approximate data $d(\mathbf{t})$. The vertical distance between a data point and a models approximation to that point $y(\mathbf{t}, \mathbf{p})$ is known as the residual, i.e. $d(t_i) - y(t_i, \mathbf{p})$. The least-squares fitting algorithm looks to minimise the L-2 norm of the residual of data to the model evaluated

for a particular set of parameters, where $\mathbf{t} = [t_1, t_2, ..., t_n]$ is the discrete time points measured for the data, i.e.

$$\min_x \|y(\mathbf{t}, \mathbf{p}) - d(\mathbf{t})\|_2^2 = \min_x \left(\sum_{i=1}^{n} (y(t_i, \mathbf{p}) - d(t_i))^2 \right).$$

An extension on the least-squares formulation above is weighted least squares. This is a method used when the response data might not be of equal quality and, therefore, does not have constant variance. If this is the case, the fit might be unduly influenced by data of lesser quality. To account for this, a weighted-least squares formulation can be used. This is where an additional scale factor, the weight, is included in the fitting process, i.e.

$$\min_x \|w(\mathbf{t})(y(\mathbf{t}, \mathbf{p}) - d(\mathbf{t}))\|_2^2,$$

where $w(\mathbf{t})$ is the weights. These weights are determined by how much each data point should influence the final parameter estimates.

In this thesis, the least-squares nonlinear fitting algorithm in Matlab (R2018b, Mathworks 2018) called *lsqnonlin* was used. The maximum number of function evaluations was $100 \times N$, where N is the number of parameters, and the maximum number of iterations for each fit was 400. If the value of the objective function crossed 1×10^{-6}, the iterations stopped. Each mathematical model was numerically solved using a combination of the inbuilt ODE solver *ode45* or the integral solver *integral2*.

3.4.3 *Goodness of fit statistics*

Goodness of fit statistics are used regularly to confirm that an optimisation of parameter values in a model to data has produced a reliable representation. The most basic measure for how well the model approximates the data is through the norm of the residuals, or residual norm. This is this the squared norm of the vector of residuals:

$$\sum_{i=1}^{n} (y(t_i, \mathbf{p}) - d(t_i))^2. \tag{3.29}$$

A low residual norm represents a close fit to the data.

The ability of a model to represent data accurately is also reaffirmed by the coefficient of determination (R-squared or R^2). This is a measurement of the proportion of the variance in the data that is predictable from the model. In other words, how well the fit approximates the data. It is calculated using

$$R^2 = 1 - \frac{\sum_{i=1}^{n}(y(t_i, \mathbf{p}) - d(t_i))^2}{\sum_{i=1}^{2}(d(t_i) - \overline{d})^2} \tag{3.30}$$

where $\overline{d}$ is the mean of the observed data:

$$\overline{d} = \frac{1}{n}\sum_{i=1}^{n} d(t_i). \tag{3.31}$$

An R^2 value close to 1 represents a good fit.

Lastly, a Pearson's r correlation coefficient can also be used to determine whether the model is a reliable representation for the data. It is calculated using

$$r = \frac{\sum_{i=1}^{n}(d(t_i) - \overline{d})(y(t_i, \mathbf{p}) - \overline{y})}{\sqrt{\sum_{i=1}^{n}(d(t_i) - \overline{d})^2}\sqrt{\sum_{i=1}^{n}(y(t_i, \mathbf{p}) - \overline{y})}} \tag{3.32}$$

where $\bar{y}$ is the mean of the model values corresponding to the observed data points using the formula in Eq. (3.31). Again a value close to 1 represents a good approximation to the data.

A confidence interval is an interval which might contain the true parameter estimate and has an associated confidence level. A 95% confidence interval means that given 100 different samples and computing a 95% confidence interval for each sample, then approximately 95 confidence intervals will contain the true mean value. In other words, the 95% confidence interval contains the population mean 95% of the time. The confidence intervals for the parameters were calculated using the inbuilt *nlparci* function in Matlab (R2018b, Mathworks 2018). This function uses the Jacobian from *lsqnonlin* in conjunction with optimised parameter values and corresponding residuals to calculation the 95% confidence intervals for a parameter.

3.5 MODEL ANALYSIS TECHNIQUES

A range of analytical techniques can be used to obtain useful information from models similar to those described above. Bifurcation and local stability theory are useful ways to study long-term dynamics of an ODE system. A review of bifurcation and local stability theory is not provided in this thesis. We recommend the reader to the works of Guckenheimer *et al.* (1984) and Kuznetsov (2013) for a revision of the theory neccessary. The Routh-Hurwitz stability criterion is revised in detail below. Once parameter values that match experimental data have been obtained, a parameter sensitivity analysis is a useful way to analyse local stability and relative sensitivity for a given metric.

3.5.1 *Routh-Hurwitz stability criterion*

The Routh-Hurwitz stability criterion provides a necessary and sufficient condition for the stability of a linear time-invariant control system (Routh, 1877; Hurwitz, 1895). It is used in bifurcation theory and control theory to determine whether all the roots of the characteristic polynomial of a linear system have negative real parts Shinners (1998). In that way, the criterion determines if the equations of a linear system have only stable solutions without solving the system directly. Consider an nth order polynomial

$$D(s) = a_n s^n + a_{n-1} s^{n-1} + ... + a_1 s + a_0$$

the Routh array has $n+1$ rows and is given by the following structure:

$$\begin{array}{cccc} a_n & a_{n-2} & a_{n-4} & ... \\ a_{n-1} & a_{n-3} & a_{n-5} & ... \\ b_1 & b_2 & b_3 & ... \\ c_1 & c_2 & c_3 & .... \\ ... & ... & ... & ... \end{array}$$

where the elements b_i and c_i can be computed as follows:

$$b_i = \frac{a_{n-1} \times a_{n-2i} - a_n \times a_{n-(2i+1)}}{a_{n-1}}$$
$$c_i = \frac{b_1 \times a_{n-(2i+1)} - a_{n-1} \times b_{i+1}}{b_1}$$

and the number of sign changes in the first column determines the number of non-negative roots.

3.5.2 *Parameter sensitivity*

Sensitivity analysis is a commonly used technique to quantify the dependency of the output of a mathematical system on the variables or parameters of the model (Saltelli *et al.*, 2008). It is a useful way of studying the robustness of the results in the presence of uncertainty. One of the simplest and most common approaches is to change one input variable, keeping others at their baseline values, and measure the effect on the output (Murphy *et al.*, 2004). More generally, in a sensitivity analysis a metric is defined to measure the change in the model value $f(t, \mathbf{p}, \mathbf{f_0})$ for a set of parameters $\mathbf{p}$ and initial conditions $\mathbf{f_0}$ from the original case denoted $f(t, \mathbf{p}^*, \mathbf{f_0}^*)$. This technique has been in a large majority of the models previously discussed, such as de Pillis *et al.* (2005); Kim *et al.* (2015); Wares *et al.* (2015).

4

THE EFFECTS OF GENE-ATTENUATION ON THE INTRACELLULAR VIRAL-TUMOUR DYNAMICS OF THE ONCOLYTIC ADENOVIRUS

OVERVIEW

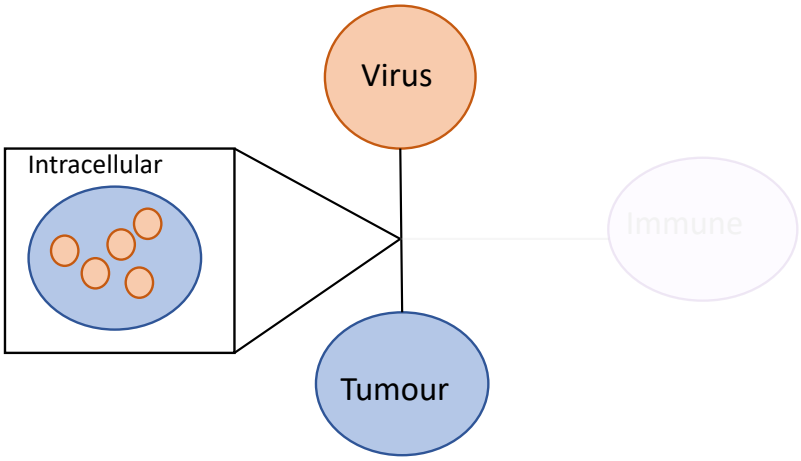

Figure 4.1: Subset of Fig.1.1, summarising the investigation of the virus-tumour interaction in this chapter

One major challenge in the field of oncolytic virotherapy is to determine which virus, out of a burgeoning number of engineered derivatives, can maximise both viral spread and anticancer cytotoxicity. To solve this problem, an in-depth understanding of the virus-tumour interaction generated by the genetic material of the virus is crucial. The intracellular dynamics of the virus-tumour interaction can, however, be extremely heterogeneous and difficult to model. In this chapter, an integro-differential system with distributed parameters is developed to model the intracellular dynamics of the virus-tumour interaction. Modifications to the viral E1B 19 and E1B 55 genome are then mapped to specific viral characteristics, and the dominant processes altered by the mutations determined. This allows for a thorough investigation into which genetic attenuation would produce the optimal viral vector for cancer therapy.

Some of the work in this chapter was previously published in Jenner *et al.* (2018a).

The adenovirus is a virus that has been investigated extensively for its potential as an oncolytic virotherapy vector, see Section 2.4.1. Due to the popularity of adenoviruses as a modality for cancer treatment, it is imperative that a way to understand the effects of gene-attenuation of this virus is developed.

Traditionally, oncolytic virus dynamics are modelled using mean field systems of ordinary differential equations (ODEs), in which the infection time and replication time period are set at the average value across the populations, see Section 3.2.3. In contrast to those assumptions, it is likely that the proportion of uninfected cells encountering a virus is initially low, and over time the probability that any uninfected cell has encountered a virus particle increases until the population of uninfected cells has been exhausted. Similarly, life spans of cells, especially infected cells, need not necessarily be exponentially distributed (Althaus *et al.*, 2009; Dowling *et al.*, 2005). Thus assuming a common likelihood of cell death can result in biologically inaccurate models. Previously, modellers have developed ways to take a distributed parameter approach to modelling viral dynamics of HIV, see Section 3.2.5, and these approaches now need to be integrated into a model designed to probe the effects of viral genetic variations.

Developing a biologically accurate model that describes the interaction between gene-attenuated viruses and cell monolayers *in vitro* is challenging as the viral replication process is complex, see Section 2.4. With the motivation of improving adenoviral vectors for cancer gene therapy, Kim *et al.* (2002) constructed genetically attenuated adenoviruses and investigated the possibility of enhanced oncolytic and replication effects. Each gene-attenuated virus constructed differed slightly, depending on the presence or absence of the *E1B 55* and *E1B 19* genes.

Due to the nature of the experiments few measurements could be taken by Kim *et al.* (2002) during their investigations. Model parameter inference when the data is sparse is difficult. In this chapter, a parsimonious approach is taken to determine the effects of the genetic mutations, focusing on the variations to the dynamic processes rather than determining precise parameter values, using a multi-layer model investigation. In Section 4.2, a model that considers heterogeneity in the virus-cell interaction is developed using an integro-differential equation system. The relationships between the *E1B 19* and *E1B 55* genes and the downstream characteristics they control in the

viral-tumour interaction is then determined by applying the model from Section 4.2 to the results from Kim *et al.* (2002).

4.1 GENE-ATTENUATION OF AN ONCOLYTIC ADENOVIRUS

Gene-attenuated replication-competent adenoviruses are emerging as a promising new modality for cancer treatment. The E1B gene of the adenovirus encodes two distinct tumour antigens, the *E1B 19* kDa and *E1B 55* kDa proteins, which are both independently capable of significantly influencing the adenoviruses behaviour, see Section 2.4.3. Experimental studies have shown that the *E1B 55* kDa protein could be responsible for viral potency and non-selective replication (Kim *et al.*, 2002; Lee *et al.*, 2000). The *E1B 19* kDa protein on the other hand, is correlated with the rate of cell lysis (Kim *et al.*, 2002; Rao *et al.*, 1992).

Kim *et al.* (2002) evaluated the possibility of improving the adenovirus for cancer gene therapy by constructing genetically attenuated adenoviral vectors with different combinations of *E1B* genes. Four viruses were constructed: three *E1B* mutant adenoviruses, Ad-ΔE1B19, Ad-ΔE1B55 and Ad-ΔE1B19/55, and one control virus Ad-wt. The Ad-ΔE1B19 virus was designed to be deficient in the *E1B 19* gene, whereas the Ad-ΔE1B55 virus lacked the *E1B 55* gene. The AdΔE1B9/55 virus was designed as a form of negative control, expressing neither the *E1B 19* nor the *E1B 55* genes. The final virus, Ad-wt, is the wild-type version of the gene-attenuated viruses. A wild-type virus is the naturally occurring, non-mutated strain of a virus. The Ad-wt was, therefore, used as a positive control for the experiments as it contained both the *E1B 19* and *E1B 55* genes (Kim *et al.*, 2002). A summary of the different viruses and their commonalities is illustrated in Fig. 4.2.

To investigate how the attenuation of the *E1B 19* and *E1B 55* genes affect the system performance, Kim *et al.* (2002) performed an *in vitro* experiment using virus titer and plaque assays (see Section 2.5.1). Replication competency of the four viruses was determined by comparing virus titer measurements on two cell monolayers: a Human embryonic kidney cell line (HEK293) and a brain cancer cell line (U343). Approximately $2-8\times10^4$ HEK293 and U343 cells were plated onto a 6-well plate for each experiment.

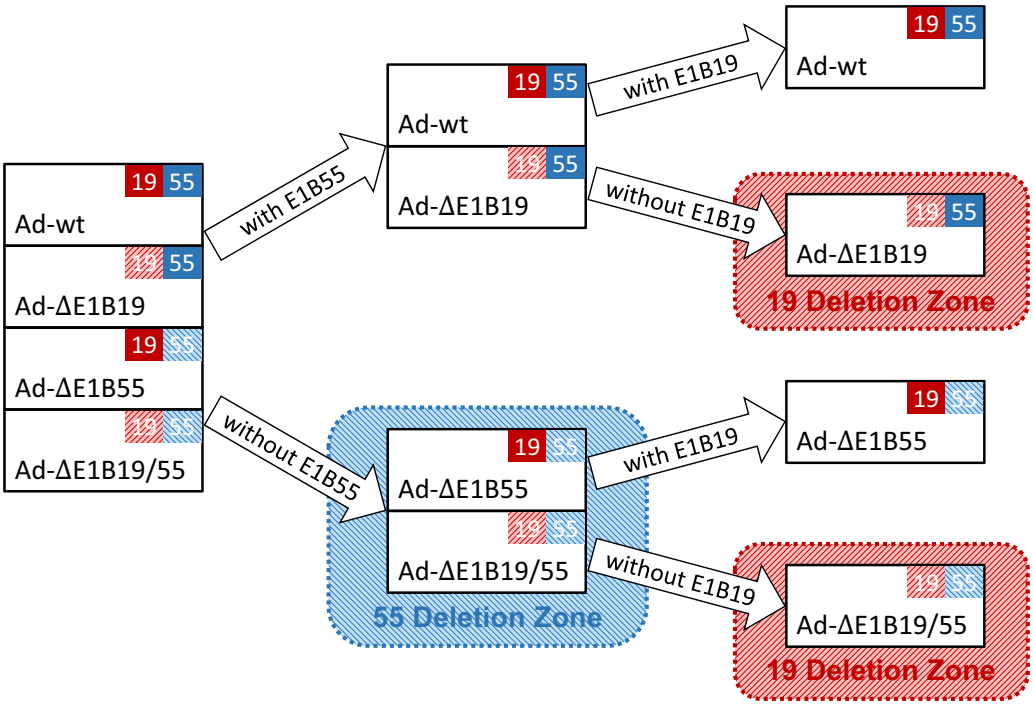

Figure 4.2: Gene tree diagram. The tree diagram above displays the presence or deletion of the *E1B 19* and *E1B 55* genes in each of the four viruses engineered by Kim *et al.* (2002). First published in Jenner *et al.* (2018a).

To assay for viral growth, the cells were infected with either Ad-ΔE1B19, Ad-ΔE1B55, Ad-ΔE1B19/55 or Ad-wt at a multiplicity of infection (MOI) of 1. The MOI is the average number of virus particles infecting each cell, i.e., the ratio of the number of virus particles to the number of target cells in a defined space. Supernatant and monolayer samples were assayed by plaque assay at various times of incubation to determine the virus titer. Virus titer measurements were calculated as the sum of viral particles within the pellet and supernatant. The sum of these quantities is assumed to be a proxy for all intracellular and extracellular virus in the plate at the specific time points.

4.2 DISTRIBUTED-PARAMETER MODEL OF INTRACELLULAR VIRAL-TUMOUR CELL DYNAMICS *in vitro*

One of the key mechanisms that ensure cancer robustness is tumour heterogeneity (Karev *et al.*, 2006). Different tumour cells can show distinct morphological and phenotypical properties, leading to a variety of responses to treatment. Additionally, the

ability of viral particles to infect and replicate within a cell can differ substantially from cell to cell even within the one culture. Timm and Yin (2012) measured virus production from single cells and found that production rates and virus yields spanned values over a 300-fold range, highlighting an extreme diversity in virus production for cells from the same population (Timm and Yin, 2012).

Using distributed delays, mathematicians have made some progress in investigating heterogeneity in the viral replication process, see Section 3.2.5 and Eqs. (3.25)-(3.25). To model heterogeneity in the virus-tumour interaction, this chapter considers that the distribution of viral replication start times and lengths of replication for a population of viruses can each be drawn from a probability distribution. To derive the model, the interaction of a single virus and a single cell is first considered. The bold line in Fig. 4.3 depicts a schematic of the virus population over time in a single infected cell in the population, clearly accounting for the three stages of the viral replication process: infection, transport and disassembly; replication; and cell death (see Section 2.4.2).

In the initial stage of infection, the virus is yet to enter the nucleus of the cell, no replication occurs and the virus population remains unchanged. This period of time is denoted by τ. After τ it is assumed that the viral DNA arrives in the nucleus and commences replication at a linear rate k. Replication occurs for a period l after which the cell will be full to capacity with viral progeny, causing it to burst. After this time no new viral particles are created by that cell, as the cell has died at time $\delta = \tau + l$. The viral replication hijacks the usual protein replication machinery of the cell, which is assumed here to work at a constant average rate. The processes that govern extracellular and intracellular transport of the virus to the nucleus are independent of the replication machinery of the cell (Tokarev *et al.*, 2009). As such, the length of time the viruses spends replicating is independent of the time it takes for the virus to enter the nucleus and start replicating.

It is plausible that there may be more than one viral infection per cell. In this case, the rate of replication may vary depending on how many virus particles are within one cell. In the current model, the rate of replication can be thought of as the mean rate over all possible multiplicities of infection experienced by the cell during the replication

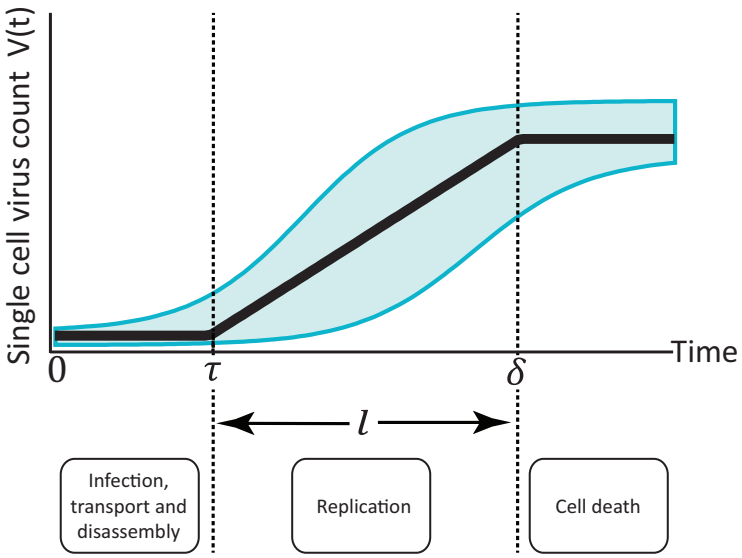

Figure 4.3: Illustration of the single virus-single cell dynamics. After the initial infection, the virus particle undergoes transport and disassembly (see Fig. 2.3). In this time period τ, no new virus particles are created. After time τ the virus has arrived in the nucleus and undergoes replication at a rate k for a period l, after which the cell bursts at time $\delta = \tau + l$. The solid line depicts the process for a particular cell in the population. The shaded region is illustrative of the spread due to the heterogeneity of the processes across a population of viruses and tumour cells. Note the replication rate, k, is taken to be constant for a given cell, and can be thought of as the average replication rate (at all MOI experienced by that cell during the replication period). First published in Jenner *et al.* (2018a).

process. This is an approximation to what is, in reality, an infection and reinfection process.

To derive a model for a group of cells infected by virus particles, consider a population of the single virus-single cell interactions, all following the same replication process represented in Fig. 4.3. Heterogeneity is assumed to exist within the cell and virus populations and to relate directly to the start time of replication, τ, and the period of time spent replicating, l. To model the delay between viral infection and the production of virus particles, let τ be the random variable that describes the time between the start of the experiment and the first replication with a probability distribution f_τ. Let l be the random variable that depicts the replication period of the virus particles with a probability distribution f_l.

To calculate the total number of virus particles (intracellular and extracellular) at any point in time, an expression for the proportion of the initial number of cells C_0

that contain replicating virus particles is derived. This is equivalent to determining the probability that the time t is in the random interval $[\tau, \tau + l]$, i.e. $\{t > \tau\} \cap \{t < \tau + l\}$. This gives the number of cells with replicating virus particles as

$$C(t) = C_0 \int_0^t \int_t^\infty f_{\tau,\tau+l}(x, y) dy dx,$$

where $f_{\tau,\tau+l}(x, y)$ is the joint density function for τ and $\tau + l$. Due to the independence of τ and l, the joint distribution, and hence $C(t)$ becomes

$$C(t) = C_0 \int_0^t \int_t^\infty f_\tau(x) f_l(y - x) dy dx,$$

where this can be derived using either the law of total probability or the Jacobian matrix transformation. For more detail see Appendix A.

The change in the total virus (both intracellular and extracellular), Υ, at any point in time t, is the cumulative number of cells actively producing virus multiplied by the rate at which the virus replicates:

$$\frac{d\Upsilon}{dt} = kC = kC_0 \int_0^t \int_t^\infty f_\tau(x) f_l(y - x) dy dx, \tag{4.1}$$

where k is the mean viral replication rate, taken to be common across the cell population of C_0 cells. It is assumed each cell is not actively producing virus until time τ, chosen from the distribution f_τ, and that they then produce for a period, l, chosen from the distribution f_l. At time t, the number of cells with virus replication within the nucleus is equal to the proportion of cells that have reached time τ minus the proportion that have reached time $\tau + l$.

4.3 CHOOSING A BIOLOGICALLY REASONABLE DISTRIBUTION

To examine how the overarching model dynamics depends on the choice of underlying distribution, Eq. (4.1) has been simulated for a range of distributions. Assuming f_τ and f_l are uniform distributions gives

$$f_\tau(x;\bar{\tau},s) = \begin{cases} \frac{1}{s} & \text{for } x \in [\bar{\tau}-\frac{s}{2},\bar{\tau}+\frac{s}{2}] \\ 0 & \text{otherwise} \end{cases}$$

$$f_l(x;\bar{l},s) = \begin{cases} \frac{1}{s} & \text{for } x \in [\bar{l}-\frac{s}{2},\bar{l}+\frac{s}{2}] \\ 0 & \text{otherwise} \end{cases}$$

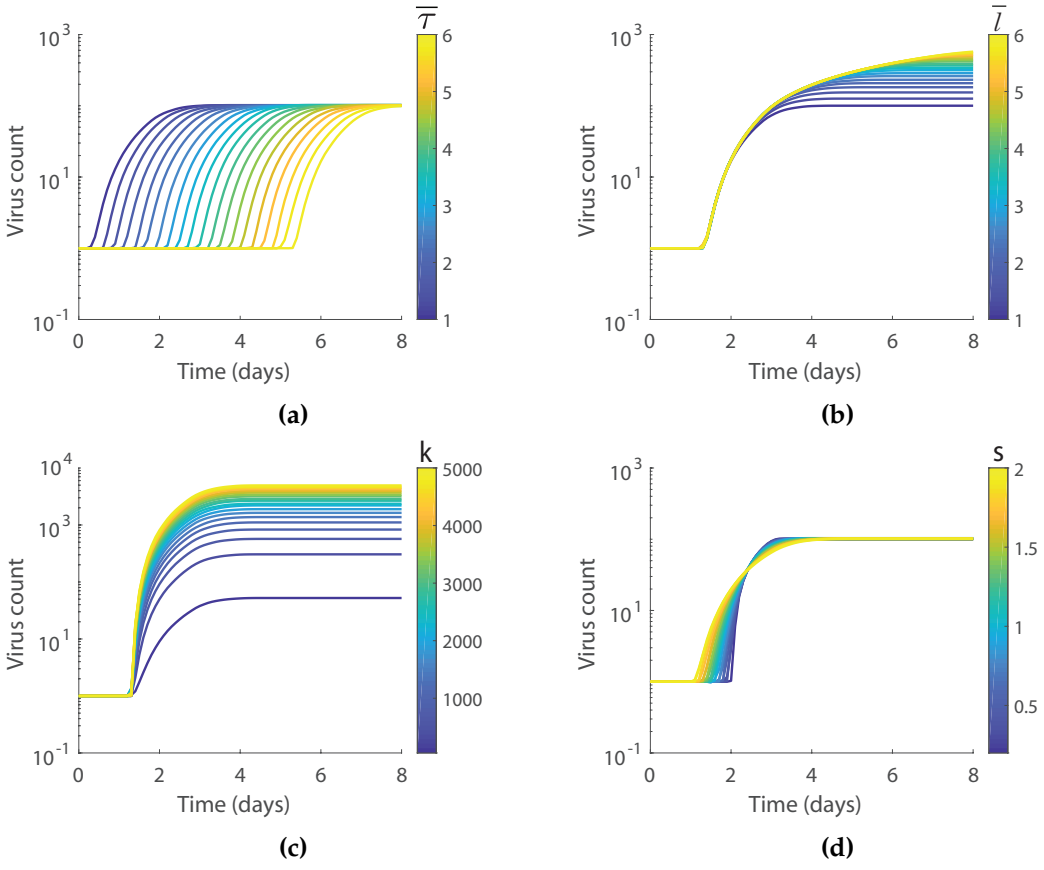

Figure 4.4: Model simulations based on the uniform distribution. The effects of individually varying (a) average replication start time $\bar{\tau}$; (b) average replication period $\bar{l}$; (c) replication rate k; and (d) width of the support s, are shown with the colour indicating the varied parameter value. First published in Jenner *et al.* (2018a).

where the width of the support of f_τ and f_l has been fixed as s and the mean of each distribution is denoted by $\bar{\tau}$ and $\bar{l}$ respectively. Simulations with uniform distributions are shown for a range of parameter values in Fig. 4.4. It is clear that each parameter controls a unique dynamic of the virus count from the model.

To compare this then to the dynamics of the model when the distribution is a triangular distribution, Eq. (4.1) was also simulated with f_τ and f_l as triangular distributions:

$$f_\tau(x;\bar{\tau},s) = \begin{cases} \frac{4}{s^2}(x-\bar{\tau}+\frac{s}{2}) & \text{for } x \in [\bar{\tau}-\frac{s}{2},\bar{\tau}] \\ \frac{4}{s^2}(\bar{\tau}+\frac{s}{2}-x) & \text{for } x \in [\bar{\tau},\bar{\tau}+\frac{s}{2}] \\ 0 & \text{otherwise} \end{cases}$$

$$f_l(x;\bar{l},s) = \begin{cases} \frac{4}{s^2}(x-\bar{l}+\frac{s}{2}) & \text{for } x \in [\bar{l}-\frac{s}{2},\bar{l}] \\ \frac{4}{s^2}(\bar{l}+\frac{s}{2}-x) & \text{for } x \in [\bar{l},\bar{l}+\frac{s}{2}] \\ 0 & \text{otherwise} \end{cases}$$

where the width of the support for f_τ and f_l has been fixed as s and the mean of each distribution is denoted by $\bar{\tau}$ and $\bar{l}$. The results of the simulations are shown in Fig. 4.5. The triangular distributions were also fixed to have symmetric shape, thus allowing the re-parameterisation of the distributions in terms of their mean and support.

Eq. (4.1) is also simulated with f_τ and f_l as Lévy distributions, see Fig. 4.6. For this distribution, the variance could not be fixed as Lévy distributions have infinite variance. Similarly, since Lévy distributions have an infinite mean, the parameter perturbations cannot be linked in this example to the mean replication start time $\bar{\tau}$ and mean replication period $\bar{l}$ in the previous examples. Instead, the location, δ_1 and δ_2, and scale γ_1 and γ_2, give the form of the Lévy distribution:

$$f_\tau(x,\delta_1,\gamma_1) = \sqrt{\frac{\gamma_1}{2\pi}}\frac{e^{-\frac{\gamma_1}{2(x-\delta_1)}}}{(x-\delta_1)^{3/2}}$$

$$f_l(x,\delta_2,\gamma_2) = \sqrt{\frac{\gamma_2}{2\pi}}\frac{e^{-\frac{\gamma_2}{2(x-\delta_2)}}}{(x-\delta_2)^{3/2}}$$

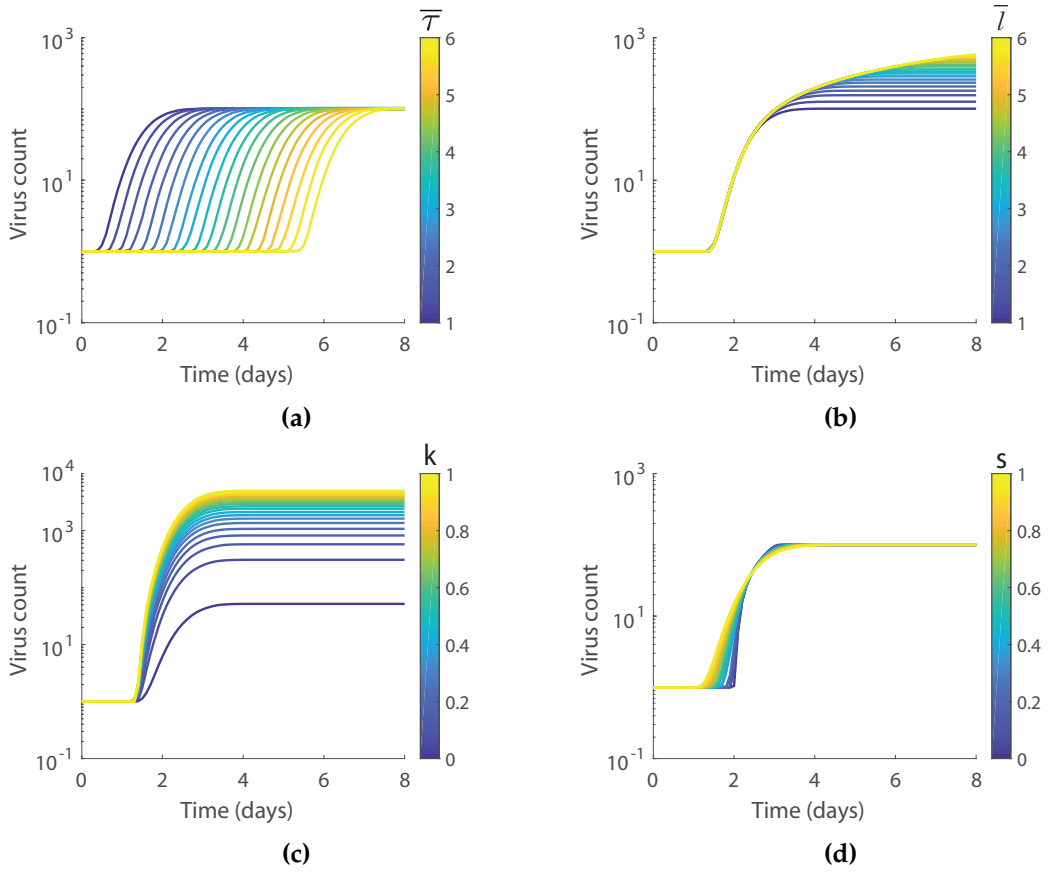

Figure 4.5: Model simulations based on the triangular distribution. The effects of individually varying (a) average replication start time $\bar{\tau}$ (b) average replication period $\bar{l}$ (c) replication rate and (d) width of the support s, are shown with the colour indicating the varied parameter value. First published in Jenner *et al.* (2018a).

The overall model behaviour does not depend significantly on the underlying distribution being a uniform, triangular or Lévy distribution (see Fig. 4.4, 4.5 and 4.6). When f_τ and f_l are Levy distributions (Fig. 4.6), the model behaviour for the shape and scale of these distributions reflects the behaviours of the model when the underlying distribution was the uniform or triangular distribution, albeit with different parameters. The parameters for the processes of replication - start time and period - are, therefore, not overly dependent on the nature of the underlying distribution.

Gamma distributions are widely used in engineering, science and business to model continuous variables that are always positive. These distributions are commonly used throughout the literature to model biologically plausible delays, see for example Banks *et al.* (2003); Blythe *et al.* (1984); Chattopadhyay *et al.* (2002); Culshaw *et al.* (2003); Cush-

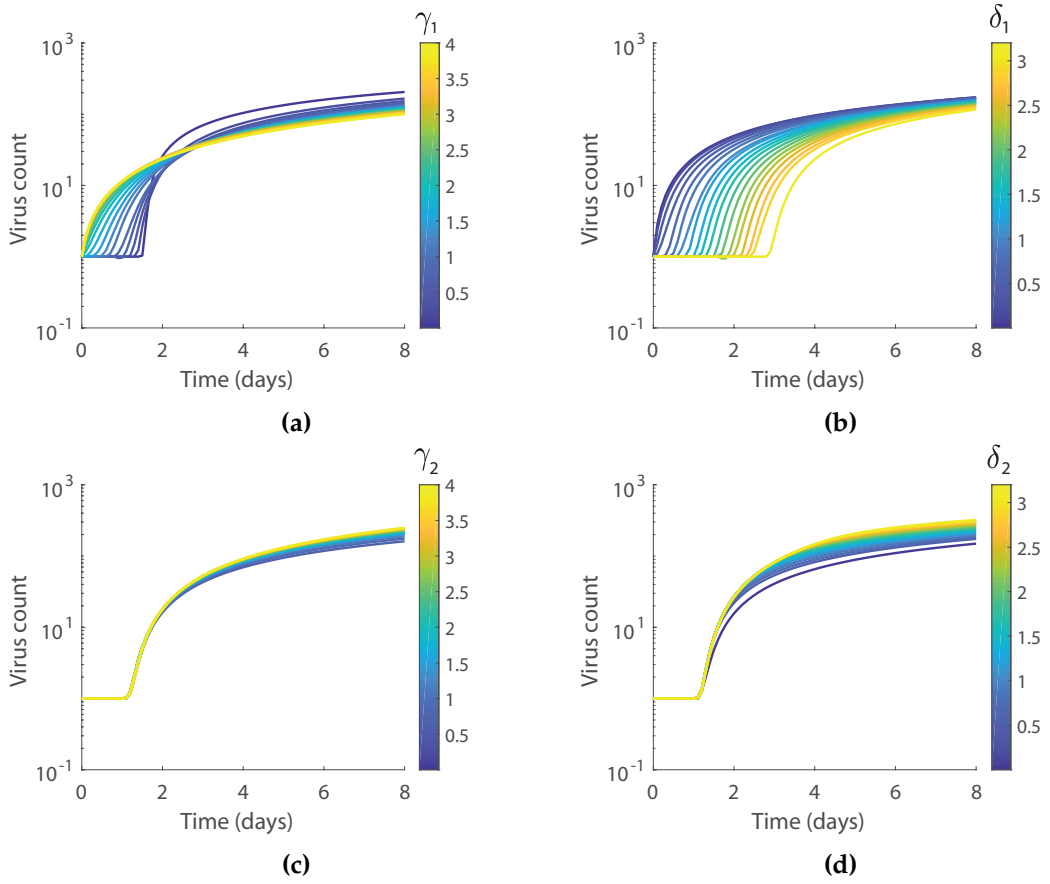

Figure 4.6: Model simulations based on the Lévy distribution. The effects of individually varying (a) the scale of f_τ, γ_1 (b) the location of f_τ, δ_1 (c) the scale of f_l, γ_2 (d) the location of f_l, δ_2, are shown with the colour indicating the varied parameter value. First published in Jenner *et al.* (2018a).

ing (1977); Mittler *et al.* (1998); Nelson and Perelson (2002). Their popularity in the field of biological modelling is due to their 'tunable' distribution that can mimic both exponential declines and general bell-shaped distributions. Since a gamma random variable is simply the sum of independent exponential random variables, the gamma distribution is a natural choice when modelling biological events, such as delay in viral replication. In this case, the waiting time before replication commences is a random event occurring in a Poisson process with some mean time between the events.

While the Lévy distribution is commonly used in biological modelling, there are advantages to choosing the gamma distribution over the Lévy distribution. The gamma distribution has a finite mean and finite variance, both of which a biological system is expected to contain, whereas the Lévy distribution does not. Numerically simulating the Lévy distribution is also costly.

For the purposes of this study, the distribution of replication start times f_τ and the distribution of replication time lengths f_l are set as gamma distributions; although as discussed above, other distributions of similar character, such as the Lévy distribution, can also be employed. The two distributions were also reduced to a three-parameter family by linking the variances of f_τ and f_l giving the resulting forms below:

$$f_\tau(x;\bar{\tau},s) = \frac{s^{\bar{\tau}s}}{\Gamma(\bar{\tau}s)e^{sx}}x^{\bar{\tau}s-1}, \tag{4.2}$$

$$f_l(x;\bar{\tau},\bar{l},s) = \frac{\left(\bar{l}s/\bar{\tau}\right)^{\bar{l}^2s/\bar{\tau}}}{\Gamma\left(\bar{l}^2s/\bar{\tau}\right)e^{\bar{l}s/\bar{\tau}x}}x^{\bar{l}^2s/\bar{\tau}-1} \tag{4.3}$$

where $\bar{\tau}$ is the average replication start time, $\bar{l}$ is the average period the virus particles spend replicating, and s describes the shape of the distributions. The linking of the variances could be relaxed, however, the parameter reduction was undertaken here due to the sparsity of the data that is optimised in the following section.

4.4 OPTIMISATION OF THE VIRUS TITER MEASUREMENTS

Due to the limited number of experimental time points compared to the degrees of freedom in the model, a tiered optimisation was employed to improve the efficiency of the search of the parameter space, and to identify the dominant processes affected by each mutation of the E1B gene. Kim *et al.* (2002)'s virus titer measurements for the E1B gene-attenuated adenovirus were undertaken on two cell types: human embryonic kidney cells (HEK293) and brain cancer cells (U343). Based on the assumption that these cells will have different sizes and cellular machinery, it was hypothesised that the cell type will predominantly affect the mean replication period $\bar{l}$. This accounted for cell differences causing variation in the length of time virus particles spend replicating in a cell. Leading on from this, it was also hypothesised that the viral replication rate k was cell type dependent. These hypotheses were then investigated in the primary tier optimisation below.

4.4.1 *Primary tier optimisation*

To reduce the degrees of freedom in the model, the initial number of cells C_0 was assumed to be common across all cell types as the wells were filled to 70% confluence. The data from Kim *et al.* (2002) was then normalised by dividing through by the mean of the first data point of the experiments.

Given the underlying differences in the genetic make-up of each of the oncolytic viruses, two subgroups in the virus titer measurements for U343 cells were evident, see Subgroup 1 and Subgroup 2 in Fig. 4.7. Subgroup 1 is comprised of the viral titer measurements for Ad-wt and Ad-ΔE1B19, and Subgroup 2 of the viral titer measurements for the Ad-ΔE1B55 and ΔE1B19/55. Based on the experimental work of Kim *et al.* (2002), the differences in the gene attenuation of the viruses should largely influence the replication rate of the virus k. Therefore, the optimisation of the model parameters allowed for there to be a different replication rate for each subgroup.

To investigate the major cause of the different behaviour between the cell types, all parameters in the system were initially linked across the cell types. Then, this assumption was relaxed for a single parameter at a time. When the replication rate alone was decoupled between cell types, leaving the other parameters linked, it was insufficient to produce an accurate approximation to the data for the first 4 days. In this case, the model was unable to determine a replication period $\bar{l}$ that was suitable for both the HEK293 and U343 cells simultaneously. As seen in Fig. 4.7, the virus production of these two cell types had very different extremes, 4 days in comparison to 8 days. This led to the introduction of an average replication period, $\bar{l}$, that differed with cell type.

A cell-specific mean replication start time $\bar{\tau}$ (with all other parameters linked) was then investigated to be sufficient to explain the dynamics across the three sub-groups of data. In keeping the mean replication period distribution common across the cells, the different steady state virus populations could not be modelled. The best result under this restriction produced an overly quick growth in virus for U343 cells compared to the HEK293 cells to compensate for the lack of time the system had to reach the viral steady state before cell death.

A summary of the parameter values that represent the broad features of the data is shown in Table 4.1 and a comparison of the model and data in Fig. 4.7. Some of these parameters were unique to the individual experiments but others were linked between the classes of experiments. To optimise the data, the numerical implementation described in Section 3.4 was followed.

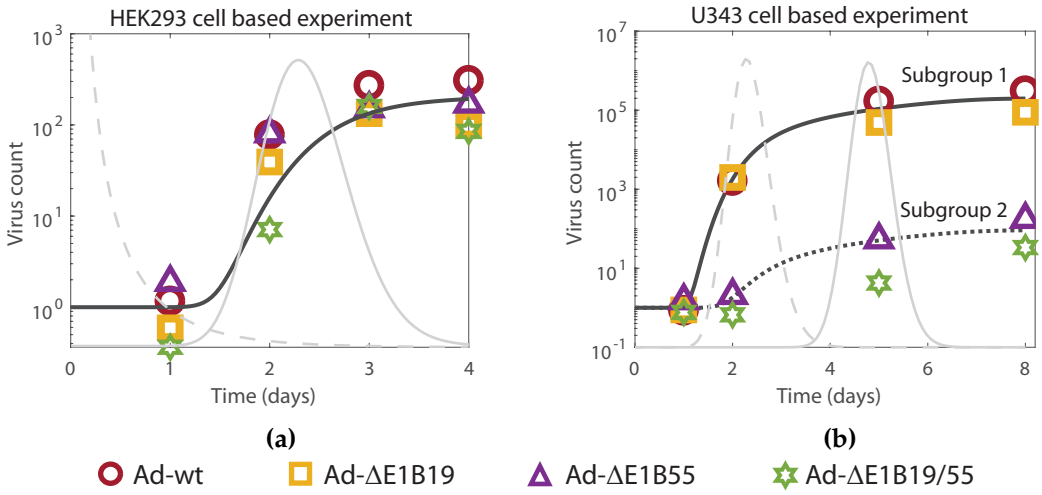

Figure 4.7: Results of the optimised model, Eq. (4.1) representing the main features of the virus titer of Kim *et al.* (2002) for (a) HEK293 cells and (b) U343 cells. The data is represented as large coloured shapes and the model's approximation is a solid or dotted black line. The solid grey line represents the gamma distribution of start times f_τ and the dashed grey line represents the gamma distribution for the replication period f_l. The parameter values are listed in Table 4.1. Note the two distinct groups of dynamics in the U343 cell based experiments: Subgroup 1 comprises of Ad-wt and Ad-ΔE1B19, and Subgroup 2 comprises Ad-ΔE1B55 and Ad-ΔE1B19/55. First published in Jenner *et al.* (2018a).

Table 4.1: Parameter values for Eq. (4.1) representing the main features of the virus titer of Kim *et al.* (2002) for Fig. 4.7. Some parameters were linked across the different experiments as indicated in the table.

Parameter		HEK293	Subgroup 1 U343	Subgroup 2 U343
mean replication start time	$\bar{\tau}$	2.4		
mean replication period	$\bar{l}$	0.27	4.8	
replication rate	k	760	41000	19
shape parameter	s	12		

The purpose of this optimisation is not to obtain a perfect representation of the data. Instead, by doing the primary tier optimisation, the parameter values are placed in the correct region of the parameter space. Due to the sparse nature of the data it is

not possible to obtain the parameter values with any certainty, but it is possible to demonstrate the suitability of the model.

It is worth noting the dominance of the AdΔE1B55 data in the fit for Subgroup 2. This indicated that an additional mechanism was needed to explain the difference between the Ad-ΔE1B55 and Ad-ΔE1B19/55 virus titer measurements, leading to the secondary tier optimisation below.

4.4.2 *Secondary tier optimisation investigation*

While the primary tier optimisation in the previous section provided an overall understanding of the key dynamical differences between the two cell types and the two subgroupings of the U343 cells, it did not explain all the differences within the subgroups. Considering Subgroup 2 of the U343 cells, it is clear that there exists a difference in the viral genome population generated by these two gene attenuated viruses: Ad-ΔE1B55 and ΔE1B19/55. To examine whether any parameters could capture the characteristic differences between these results, $\bar{\tau}$, $\bar{l}$, k and s were individually perturbed about the values obtained in the primary tier optimisation, see Fig 4.8.

The ranges of parameters explored were dependent on the relative change of the solution compared to the virus titer data measurement. The fan of model solutions produced for the perturbations in the parameters shows how effective the model can be at producing a variety of dynamics. From the model solutions based on the parameter perturbations, Fig. 4.8, the key differences in the effects of the genes on the virus titer of Subgroup 2 were inferred.

Perturbations in the average cell replication period $\bar{l}$, Fig. 4.8(b), resulted in a peel-off of the virus titer measurements from the steady state. In the case of the shape parameter s, Fig. 4.8(d), there was no long-term effect on the virus titer measurement, but rather a displacement of the initial take-off time of the virus titer. This indicates that changes in neither $\bar{l}$ nor s were sufficient to describe the main mechanistic differences between the Ad-ΔE1B55 and Ad-ΔE1B19/55 viruses. The range of solutions produced when these parameters are varied, however, still gives insight into their influence on the model behaviour.

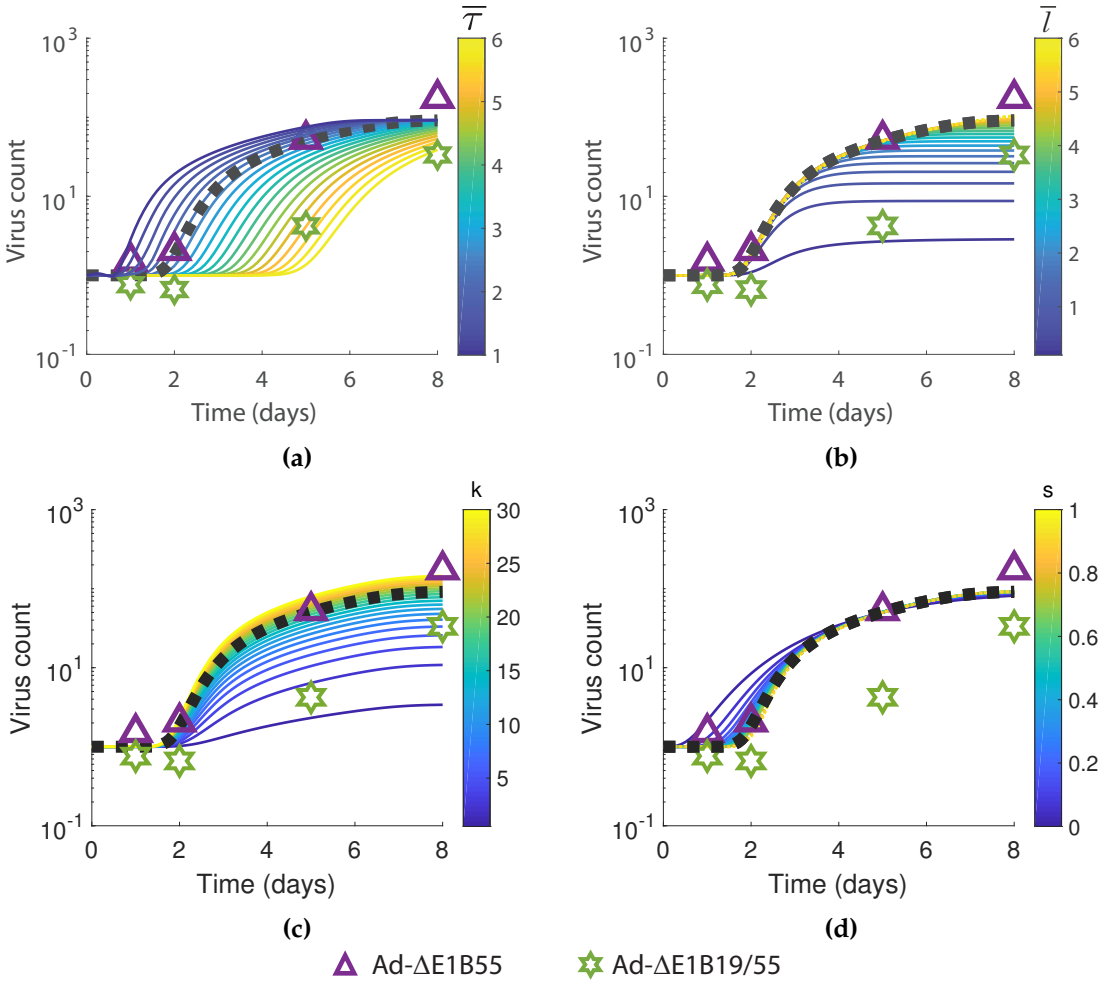

Figure 4.8: Model simulations for the Ad-ΔE1B55 and Ad-ΔE1B19/55 viral dynamics on U343 cells (Subgroup 2). The optimal model parameter dynamics are indicated as a dotted black line overlaid on the data, represented by coloured shapes. The effects of individually varying (a) average replication start time from 0.5 to 5.5, $\bar{\tau}$ (day^{-1}), (b) average cell replication period 0.1 to 6, $\bar{l}$ (day^{-1}), (c) replication rate from 0.5 to 30, k (day^{-1}) and (d) distribution shape from 0.01 to 20, s, are shown with the colour indicating the varied parameter value. First published in Jenner *et al.* (2018a).

Changes in the steady-state value of the virus titer were observed under perturbations in the replication rate of the virus, k, Fig. 4.8(c), with minor influence on the gradient of the virus titer measurement. The average replication start time $\bar{\tau}$, Fig. 4.8(a), appeared to be the major determinant of the difference between the two virus titer measurements. Not only did it affect the steady state of the model, but also the time at which viral replication took off. From Fig. 4.8, it can be seen that changes in the average replication start time alone were sufficient to explain the differences between the Ad-ΔE1B55 and Ad-ΔE1B19/55 viruses.

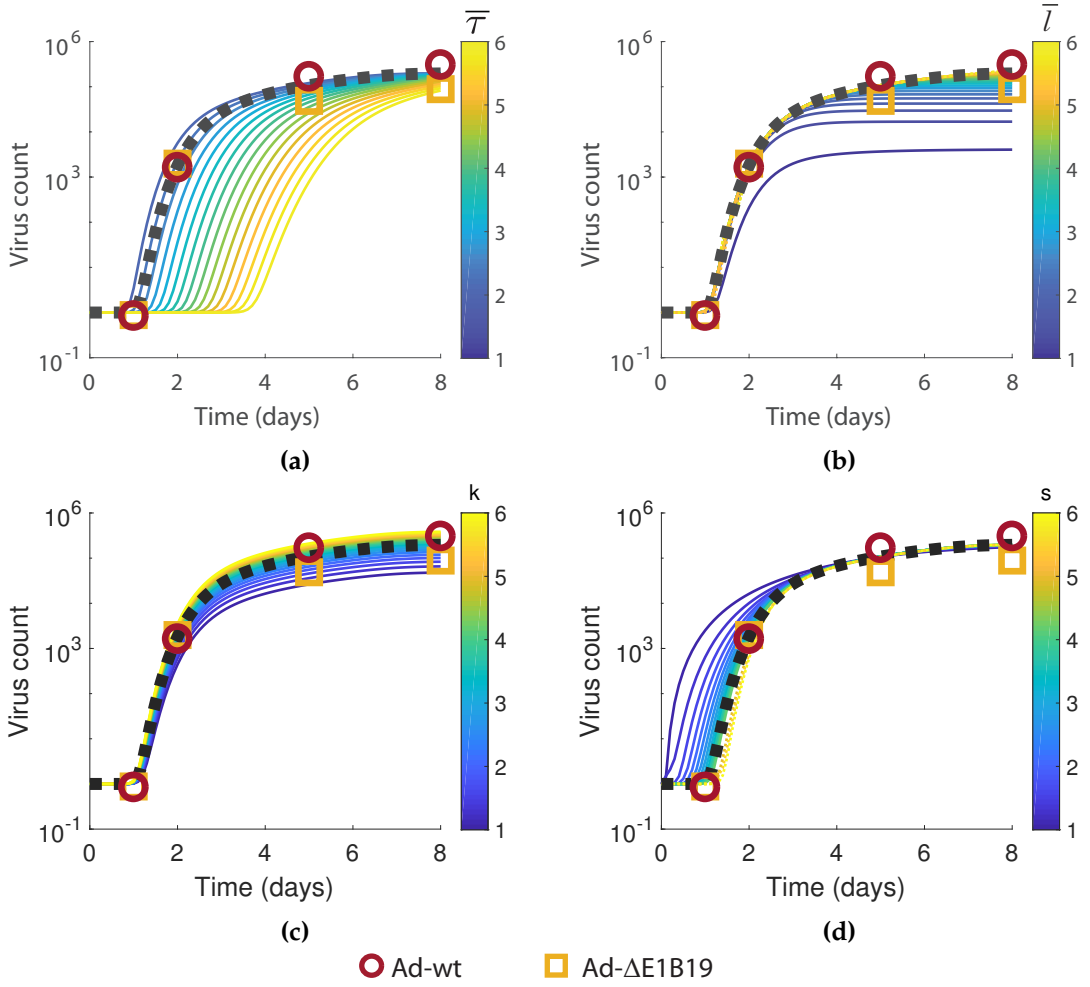

Figure 4.9: Model simulations for the Ad-wt and Ad-ΔE1B19 viral dynamics on U343 cells (Subgroup 1). The optimal model parameter dynamics are indicated as a dotted black line overlaid on the data, represented by coloured shapes, and the effects of individually varying (a) average replication start time from 0.5 to 5.5, $\bar{\tau}$ (day^{-1}), (b) average cell replication period from 1 to 6, $\bar{l}$ (day^{-1}), (c) replication rate from 10000 to 50000, k (day^{-1}) and (d) distribution shape from 0.01 to 20, s, are shown with the colour indicating the varied parameter value. First published in Jenner *et al.* (2018a).

The two virus titer time-series measurements of Subgroup 2, Ad-ΔE1B55 and Ad-ΔE1B19/55, were more dissimilar in their initial levels than the members of Subgroup 1. Examining the virus titer measurements on U343 cells, Fig. 4.7(b), clear differences can be seen for each gene attenuated virus. Recall that the mean start time and replication period, $\bar{\tau}$ and $\bar{l}$ respectively, for Subgroups 1 and 2 of the U343 cells were different. To identify the processes that could determine the differences within Subgroup 1, again $\bar{\tau}, \bar{l}, k$ and s were perturbed individually about the Subgroup 1 values to explore the effects on the dynamics, see Fig. 4.9.

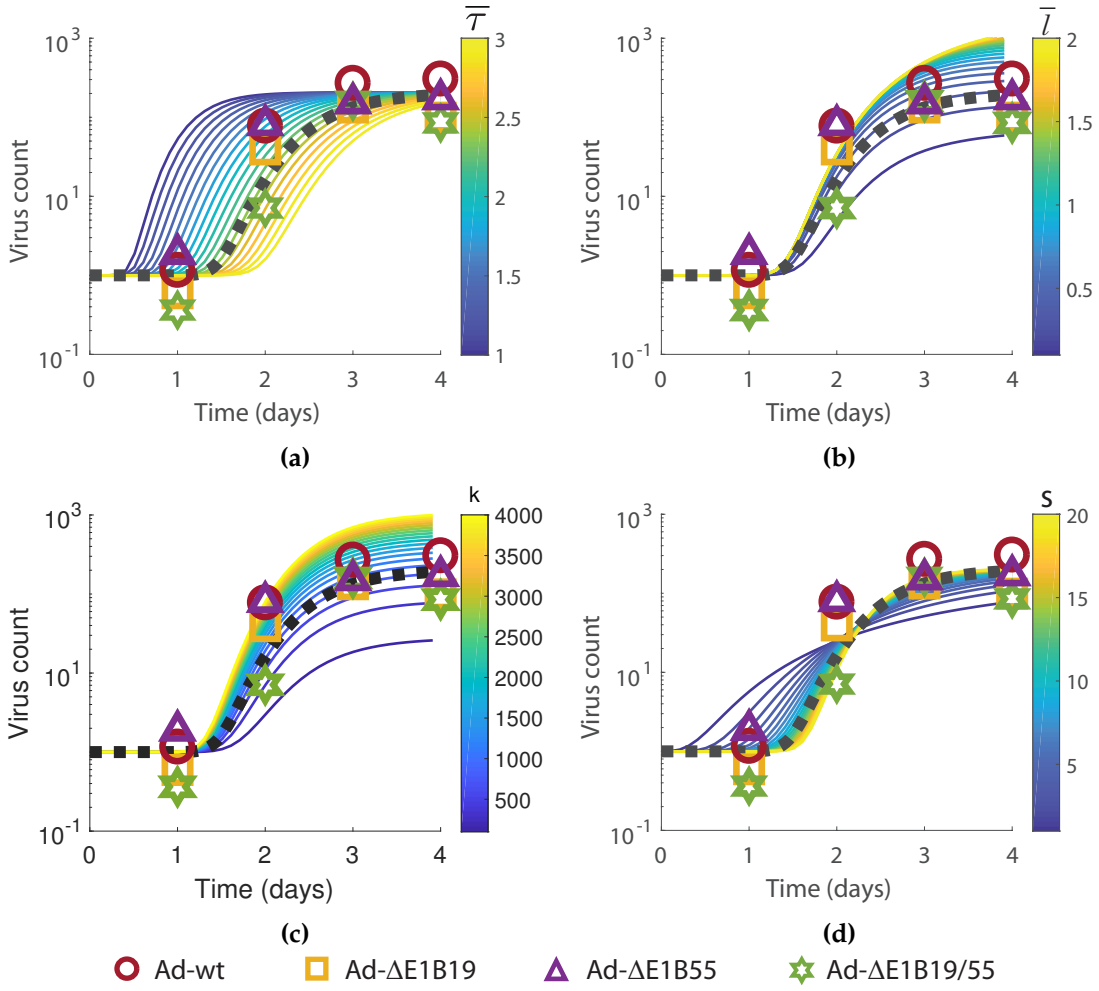

Figure 4.10: Model simulations for the HEK293 cell viral dynamics. The optimal model parameter dynamics are indicated as a dotted black line overlaid on the data, represented by coloured shapes. The effects of individually varying (a) average replication start time from 1.5 to 2.5, $\bar{\tau}$ (day^{-1}), (b) average cell replication period from 0.1 to 2, $\bar{l}$ (day^{-1}), (c) replication rate from 50 to 2500, k (day^{-1}) and (d) distribution shape from 0.01 to 20, s, are shown with the colour indicating the varied parameter value. First published in Jenner *et al.* (2018a).

In the case of the differences in virus titer measurements of Subgroup 1, it was less clear which parameters could be influencing the changes in viral dynamics. Parameters $\bar{\tau}, \bar{l}$ and k, Fig. 4.9(a), 4.9(b) and 4.9(c), were all possible determinants of the relatively small virus titer differences in this subgroup. As the average replication rate k was key to explaining the differences between Subgroups 1 and 2, it would seem a likely candidate to be the dominant parameter that described the differences within Subgroup 1 as well.

To examine how the variation in the model parameters could describe the effects of gene attenuation on virus particles infecting HEK293 cells, this analysis was repeated for the virus titer measurements on HEK293 cells, Fig. 4.10. Note that in this case, it was more challenging to determine the major differences between the four viruses, as there was significant overlap in their virus titer measurements. It is possible that all four parameters varied slightly to produce the minor variability observed between these four viruses. Kim *et al.* (2002) intentionally designed the experiments on HEK293 (non-cancerous) cells as a way of showing the antitumour specific potency of the oncolytic adenovirus. The primary motivation of the current investigation was to determine the specific effects of deletion of the *E1B 55* and *E1B 19* genes on the adenoviruses antitumour potency. The analysis on the HEK293 cells is included for completeness, and as expected, the differences between the virus titers for gene-attenuated forms of the adenovirus were less significant in HEK293 cells, compared to U343 cells.

To generate the parameter perturbation model solutions seen in Fig. 4.8, 4.9 and 4.10 a Monte Carlo simulation was employed as a cross check for the numerical approximations using *ode45* and *integral2*.

4.4.3 *Compatibility map summary*

To summarise the effects of parameter perturbations in the model, a compatibility map is presented in Fig. 4.11. This maps parameter values to three specific dynamics of the model: "Steady state", "Start time" and "Rapidity". Each parameter $\bar{\tau}$, s, $\bar{l}$ and k has been perturbed individually and the corresponding increase or decrease on the dynamics of the model are grouped into two levels: dominant or secondary. In this way, the models dynamics and parameters can be directly linked so that hypothesises may be drawn on future improvements on this virus or other viral therapies.

The steady state of the model's predicted virus titer measurement decreases with increases in the mean replication start time $\bar{\tau}$. In other words, if the average virus starts replicating later, then there will be less virus produced overall. Increasing the mean replication start time also has the obvious effect on the models start time, or take of time, as the virus titer will start increasing later if $\bar{\tau}$ is larger.

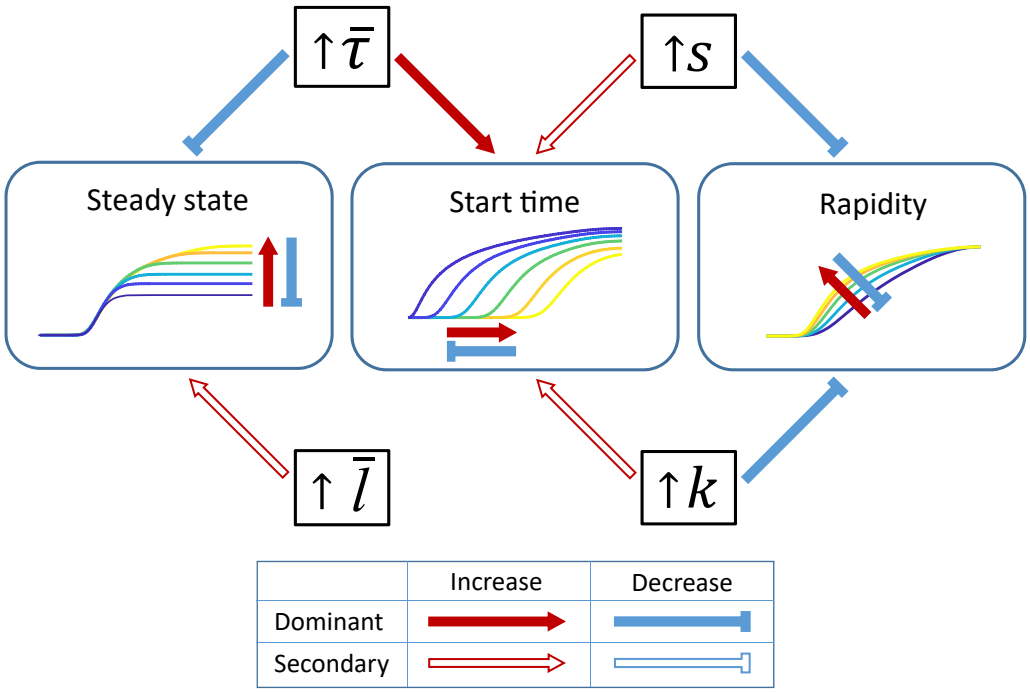

Figure 4.11: Compatibility map. In this figure, the parameters $\bar{\tau}, s, k$ and $\bar{\delta}$ are linked to the Steady state, Start time and Rapidity of the dynamics. The level and nature of the effect of the parameter changes on the processes is also indicated.

Increasing the variance and shape s of the distributions f_τ and f_l results in the rapidity of the virus titer population growth decreasing. This indicates that the larger the variance of the distribution s, the slower the population of viruses grows over time. Increasing s has a secondary effect of increasing the start time of replication. This can be interpreted as the distribution of virus particles approaching the same mean-field behaviour, similar to what was examined in Section 3.2.3.

The replication rate k also has a dominant and secondary effect on the model. Increasing k decreases the rapidity of virus titer growth while increasing the start time of virus titer growth. Increasing the mean time between replication onset and lyse of cells $\bar{l}$, increases the virus titer steady state measurement. This is intuitive, since the longer a virus spends replicating, the more virus will be obtained overall.

Categorising the dynamics of the model with the compatibility map in Fig. 4.11, allows for the the virus titer measurements in Figs. 4.8, 4.9 and 4.10 to be linked to specific processes in the model that can be linked to viral characteristics.

An identifiability analysis of the model parameters has not been conducted in this chapter; however, the compatibility map in Fig. 4.11 and the parameter perturbations in Figs. 4.8-4.10 can be used to deduce the identifiability of the model. For a model to be identifiable, different parameters must generate different probability distributions of the observable variables. It is clear that all parameters, apart from s, are identifiable in Figs. 4.8-4.10 as each parameter controls a very specific dynamic which is summarised by the compatibility map in Fig. 4.11. It is, therefore, unlikely that there will be any identifiability issues for the data and the model. Future work will consider a method such as those published by Little *et al.* (2010) as a way of confirming the identifiability of the model.

4.5 SUMMARY

Using the model presented in this chapter, the mechanisms controlled by the presence or deletion of *E1B 19* and *E1B 55* genes can be inferred. First, by considering how the cell type affects the overall virus titer, it is likely that cell type heavily influences the average cell replication period $\bar{l}$ and replication rate k. This can be seen by examining the results of the optimisation of the three distinct groupings of experiments: HEK293 cells and Subgroups 1 and 2 of the U343 cells, Fig. 4.7 and Table 4.1. By allowing the replication rate k and replication period $\bar{l}$ to vary between cell types, the model was able to capture the dynamic differences between the three groupings. Furthermore, allowing the viral replication rate k to be subgroup specific was sufficient to capture the major differences in the virus titer measurements on U343 cells. All other parameters could be linked and identical across the different experiments. From this it would appear that cell type primarily affects the average replication period and viral replication rate.

To reinforce the conclusion that the average replication period in a cell, $\bar{l}$, solely depends on the cell type, perturbations about the optimal values for the three groups of experiments, Fig. 4.8(b), 4.9(b) and 4.10(b) were examined. Perturbing the replication period alone was insufficient to capture the variation in each case, except perhaps the case of Subgroup 1 for U343 cells, Fig. 4.9(b), where the dynamics between the viruses

were already quite similar. Overall, the average replication period, $\bar{l}$, was able to reproduce the major observed differences (i.e., the primary tier of the optimisation), leading to the conclusion that this is solely a cell-specific parameter. Allowing for changes in $\bar{l}$ between the cell types then enabled the discovery of the specific effects of gene attenuation on the viral dynamics.

The replication rate was suggested by the experiments of Kim *et al.* (2002) to be a key factor in describing the differences in virus titer measurements of the four viruses. It was clear from Fig. 4.7 that the replication rate, k, of the HEK293 and U343 cells was different. However, the replication rate was also dissimilar in the optimal fit to Subgroups 1 and 2 of the U343 cells. As shown in the parameter values, Table 4.1, changes in k allowed a much higher virus titer measurement to be attained by the Ad-wt and Ad-ΔE1B19 viruses (Subgroup 1) compared to that of Ad-ΔE1B55 and Ad-ΔE1B19/55 (Subgroup 2). This leads to the idea that the replication rate, k, is heavily affected by the presence of the *E1B 55* gene, as, unlike Subgroup 2, both viruses in Subgroup 1 have their *E1B 55* gene intact.

Analysing further the results of the tiered hierarchical optimisation, the differences between the individual viruses and the effects of certain gene combinations were determined, indicating which combination of genes that may be optimal for viral production and cell death. First considering the results of the parameter perturbations for Subgroup 2, Fig. 4.8, the difference in the two virus titer measurements for the Ad-ΔE1B55 and Ad-ΔE1B19/55 was clearly explained by changes in the average replication start time, $\bar{\tau}$. It would appear that deletion of both *E1B 55* and *E1B 19* delays the average start of replication of the virus but the deletion of *E1B 19* without the deletion of *E1B 55* does not, as the difference in the Ad-ΔE1B55 and Ad-ΔE1B19/55 is the presence of the *E1B 19* gene.

Thus the presence or absence of the *E1B 55* gene changed the effect of the deletion of the *E1B 19* gene. When both *E1B 19* and *E1B 55* were deleted, the start time of viral replication, $\bar{\tau}$ was delayed. However, in the presence of the *E1B 55* gene, deletion of the *E1B 19* gene reduced the replication rate, k, as seen in Fig. 4.9 for the Ad-wt and Ad-ΔE1B19 viruses.

Linking the two sets of model simulations on Subgroups 1 and 2 (Fig. 4.8 and 4.9) the modelling indicates that combined gene deletion may give effects beyond the sum of the parts: deletion of both the *E1B 19* and *E1B 55* genes compounds the effect of the deletion the single genes alone. While reducing the replication start time, $\bar{\tau}$, appears to be sufficient to describe the differences in the Ad-ΔE1B55 and Ad-ΔE1B19/55, it is likely a combination of both the replication rate and replication start time that is reduced and delayed in the deletion of the *E1B 19* gene from a virus deficient in the *E1B 55* gene.

Examining the virus titer measurements of the four viruses on HEK293 cells, Fig. 4.10, it is less evident how the gene attenuation affects the viral characteristics. There is no clear connection to conclude regarding how the gene attenuation affects the viral characteristics in the HEK293 cell experiments. However, note that varying the viral replication start time, $\bar{\tau}$, and the viral replication rate, k, as in Fig. 4.10(a) and 4.10(c), would be sufficient to explain the small differences between the data sets in this cell type.

The results of the study are not unique to the choice of distribution. While the underlying heterogeneity in the current study is derived from a gamma distribution, many other distributions can be used and produce similar results as mentioned in Section 4.3. The dynamics of Eq. (4.1) with the underlying distributions either uniform, triangular or Lévy distribution, results in similar qualitative dynamics to those presented in Fig. 4.8, 4.9 and 4.10.

By creating a compatibility map, Fig.4.11, the dynamics of 'Steady state', 'Start time' and 'Rapidity' can be linked to viral characteristics. From this, hypothesis for the effects of genetically engineering a virus with particular characteristics can be tested. For example, if the aim was to increase the overall virus titer, then the most effective way to do this would be to increase the average start time and increase either the shape of the variance or the replication rate k, as a secondary effect.

By modelling the virus titer measurements for different genetic attenuations of the oncolytic adenovirus, an understanding can be developed for which viral characteristics ultimately drive treatment efficacy. In Chapter 5, this idea is investigated further by developing an *in vivo* extracellular modelling framework for an oncolytic virus treat-

ing a growing tumour. In this way the viral characteristics of infectivity and lysis rate, which have been linked in this study to genetic markers, may be investigated for their influence in the overall efficacy of treatment.

5

USING A DYNAMICAL SYSTEMS APPROACH TO UNDERSTAND ONCOLYTIC VIROTHERAPY IN VIVO

OVERVIEW

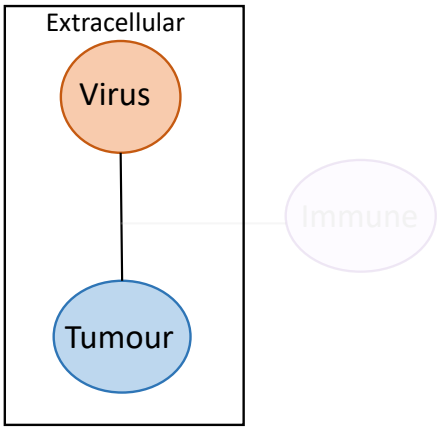

Figure 5.1: Subset of Fig.1.1, summarising the investigation of the virus-tumour interaction in this chapter

While in vitro investigations into oncolytic viruses and their lytic and replication competency reveal important details about their efficacy, it is only by considering the in vivo nature of treatment that further understanding of this therapy may be obtained. Currently, much is still unknown about the sensitivity of oncolytic virotherapy to individual tumour and viral heterogeneity. Additionally, optimal protocols detailing dose and treatment lengths are not yet universally established. In this chapter, a set of hierarchically developed models focusing on the interaction between tumour cells and virus particles engineered to infect and destroy cancerous tissue are presented. A local stability analysis and bifurcation analysis of these models quantifies the effectiveness of oncolytic virotherapy in vivo in an extracellular context. From this, conditions driving tumour extinction or survival are determined for a generic tumour-virus interaction.

The work in this chapter was previously published in Jenner *et al.* (2018c) and Jenner *et al.* (2019).

Over the past decade, hundreds of patients with cancer have been treated in clinical trials with oncolytic viruses, see Section 2.4. Unfortunately, due to the heterogeneous nature of cancer, success has been elusive, and there is a growing need to quantify the dependency of treatment outcome on cancer characteristics. Chapter 4 provided an in-depth understanding of the virus-tumour interaction as a function of a virus' genetic material. However, to improve therapy at the clinical level, an extracellular *in vivo* understanding is crucial.

A number of mathematical models have been constructed to understand the *in vivo* dynamics of proliferation and diffusion of oncolytic viruses in cancerous and healthy tissues (Section 3.2.3). The two hierarchically developed models of oncolytic virotherapy outlined in this chapter are extensions of the work by Wodarz (2001) and Titze *et al.* (2017) (Eqs. (3.6)-(3.8)). The models presented in this chapter focus on determining which aspects of virus-tumour interactions drive the success of oncolytic virotherapy both mathematically and biologically. The outcomes of oncolytic virotherapy predicted by the models are analysed using a range of mathematical techniques. A complete local stability analysis and bifurcation analysis of the system are used to find that stable equilibria only exist in the absence of tumour growth or viral decay, and further modelling shows the dependence of tumour size as a function of injection profile, in the case of intratumourally administered viral loads. In this chapter, parameter values and initial conditions are simulated over biologically reasonable intervals. These were determined primarily from the experimental conditions and model optimised performed in the following Chapter 6 (see Table 6.1).

5.1 A BIFURCATION AND LOCAL-STABILITY ANALYSIS OF A MINIMAL MEAN-FIELD ONCOLYTIC VIROTHERAPY MODEL

To model the interaction between an oncolytic virus and a growing tumour, a system of three ODEs is used. While ODE models do not address spatial spread, they do provide a mathematical framework within which the mean-field interactions between tumour

cells and viral particles can be explored. The state variables in the model are

- $u(\tau)$ - uninfected tumour cells,
- $i(\tau)$ - virus-infected tumour cells,
- $v(\tau)$ - free virus particles,

where τ represents the number of days.

In this section, an aggressive form of tumour is modelled, assuming that uninfected tumour cells replicate at a rate r proportional to their population. This unbounded exponential tumour growth is not biologically realistic in the long-term due to nutrient and space limitations. However, given the short time frame of the interaction between virus particles and tumour cells, exponential growth is considered a sufficient approximation for the tumour growth under treatment with an oncolytic virus.

The rate of infection of the uninfected tumour cell population is assumed to be proportional to the product of the virus and tumour cell populations (Novozhilov *et al.*, 2006) and occurs with rate constant β. Once infected, it is assumed that tumour cells are incapable of division as the virus particle within the cell takes control of the cellular machinery for self-replication (Section 2.4.2). Virus-infected tumour cells will then burst due to lysis at a rate d_I, releasing α new virus particles.

Fig. 5.2 shows a schematic of the interaction between the uninfected tumour cell population u (or U in non-dimensional form), infected tumour cells i (or I in non-dimensional form) and the virus population v (or V in non-dimensional form). The corresponding system of equations describing the interaction is given below:

$$\frac{du}{d\tau} = ru - \beta uv, \tag{5.1}$$

$$\frac{di}{d\tau} = \beta uv - d_I i, \tag{5.2}$$

$$\frac{dv}{d\tau} = -d_V v + \alpha d_I i. \tag{5.3}$$

This model complements other oncolytic virotherapy models in the literature discussed in Section 3.2.3. The model above differs to the one developed by Titze *et al.* (2017) (see Eqs. (3.6)-(3.8)) as tumour cell death due to factors unrelated to treatment are neglected. In this thesis, unrelated tumour cell death is considered negligible in

comparison to virus-induced tumour cell death. The model above also resembles some previous modelling work by Baccam *et al.* (2006) on the kinetics of influenza in humans, i.e. the so called TIV model (see Section 3.2.2). Baccam *et al.* (2006) derived a model for target-cell limited influenza infection, which is equivalent to Eqs. (5.1)-(5.3) when $r = 0$. The minimal and adaptive nature of the results in this chapter can be easily translated to influenza and infectious disease modelling.

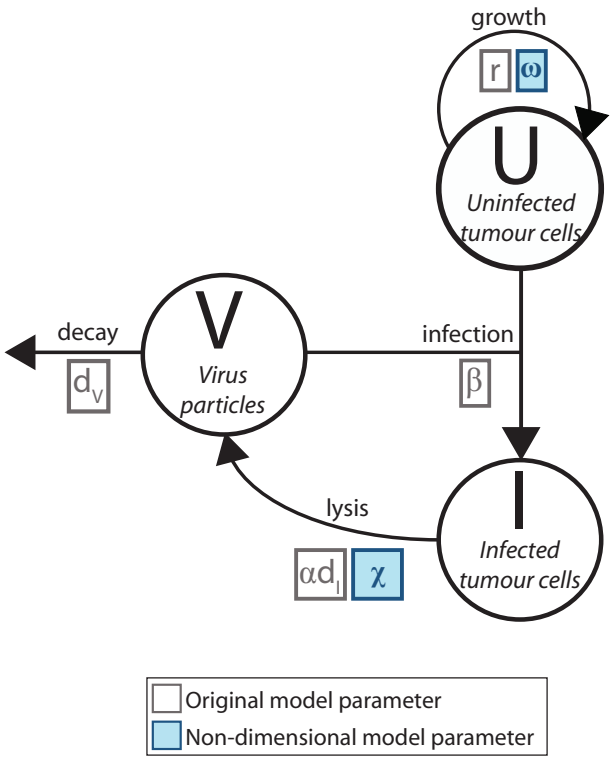

Figure 5.2: Flow diagram for the interaction between a population of uninfected tumour cells, U, virus-infected tumour cells, I, and virus particles, V. The diagram lists parameters relating to the original model, Eqs. (5.1)-(5.3), in grey boxes and parameters relating to the non-dimensionalised form of the model, Eqs. (5.4)-(5.6), in blue boxes. First published in Jenner *et al.* (2018c).

A bifurcation and local stability analysis allows for quantification of the success of oncolytic virotherapy as a function of the viral and tumour characteristics. To simplify this mathematical analysis while preserving the essential properties of the model let

$k_1U = u$, $k_2I = i$, $k_3V = v$ and $k_4t = \tau$, in the original system of Eq. (5.1)-(5.3). Rearranging gives

$$\begin{aligned}\frac{dU}{dt} &= rk_4U - \beta k_3k_4UV,\\ \frac{dI}{dt} &= \beta\frac{k_1k_3k_4}{k_2}UV - d_Ik_4I,\\ \frac{dV}{dt} &= -d_Vk_4V + \alpha d_I\frac{k_2k_4}{k_3}I,\end{aligned}$$

then letting $k_1 = k_2 = d_I/\alpha\beta, k_3 = d_I/\beta$ and $k_4 = 1/d_I$ gives the non-dimensional system of equations

$$\frac{dU}{dt} = \omega U - UV, \tag{5.4}$$

$$\frac{dI}{dt} = UV - I, \tag{5.5}$$

$$\frac{dV}{dt} = -\chi V + I, \tag{5.6}$$

where $\omega = r/d_I$ and $\chi = d_V/d_I$, and the scaled variables are

$$\begin{aligned}U &= \frac{u}{k_1} = \frac{\alpha\beta}{d_I}u,\\ I &= \frac{i}{k_2} = \frac{\alpha\beta}{d_I}i,\\ V &= \frac{v}{k_3} = \frac{\beta}{d_I}v,\\ t &= \frac{\tau}{k_4} = d_I\tau.\end{aligned}$$

For all numerical simulations, the state variables are scaled by the initial conditions: i.e. $U/U(0), I/I(0)$ and $V/V(0)$.

This model pertains to an idealised situation of homogeneous tumour properties and virus spread. It is well documented that oncolytic virotherapy can fail due to intratumoural obstructions (such as the extracellular matrix) pressure and impermeable veins (Ariffin *et al.*, 2014). To investigate conditions driving tumour extinction based solely on the mean-field virus-tumour interaction, spatial obstacles that may inhibit treatment efficacy are ignored. In Chapter 8 these obstacles are modelled and discussed in more detail.

5.1.1 *Local stability analysis*

While parameter estimates for tumour cell replication, viral decay, and viral infectivity are readily available in the literature, see Komarova and Wodarz (2010); Titze *et al.* (2017), they represent only one adaptation of the tumour-virus interaction. In this section, a detailed local stability analysis is used to quantify how the system behaves under various tumour and virus characteristics and determine the possible treatment outcomes.

5.1.1.1 *Equilibrium solutions*

The equilibria for the non-dimensionalised system Eqs. (5.4)-(5.6) is given by

$$U = 0, \quad I = 0, \quad V = 0, \quad \text{and} \tag{5.7}$$

$$U = \chi, \quad I = \chi\omega, \quad V = \omega. \tag{5.8}$$

For the specific case of $\chi = 0$ or $\omega = 0$, two more equilibria exist. For χ to be equal to zero, $d_V = 0$, i.e. viral particles are not decaying. Biologically, this represents the case when the virus is not cleared by the immune system. The resulting equilibrium for $\chi = 0$ is $U = 0$, $I = 0$ and $V \in \mathbb{R}$.

Similarly, when $\omega = 0$, $r = 0$, i.e. tumour cells are not replicating. This can be thought of biologically as a stagnant or non-growing tumour. The oncolytic viruses will, therefore, only be removing existing tumour cells. The resulting equilibrium at $\omega = 0$ is at $I = 0$, $V = 0$ and $U \in \mathbb{R}$. Therefore, there are four equilibria in total, two of which only exist for the specific cases $\chi = 0$ or $\omega = 0$.

5.1.1.2 *Stability of the equilibrium at the origin:* $U = 0, I = 0, V = 0$

To achieve complete tumour eradication in the model, the equilibrium at the origin must be stable. Evaluating the Jacobian of the non-dimensionalised model at the equilibrium at the origin gives the following eigenvalues:

$$\lambda_1 = \omega, \quad \lambda_2 = -1, \quad \lambda_3 = -\chi.$$

Thus, the equilibrium is a stable node for $\chi \geqslant 0$ and $\omega \leqslant 0$ and a saddle point for all other regions in the parameter space, as summarised in Fig.5.3.

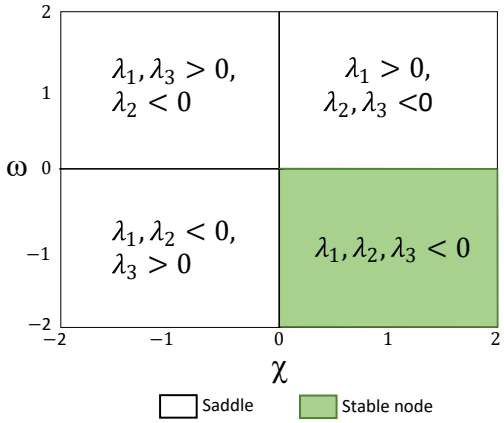

Figure 5.3: Stability of the equilibrium at the origin as a function of the (ω, χ)-parameter space. The shaded region of the parameter space represents the (ω, χ)-parameter set corresponding to a stable node at the origin. First published in Jenner *et al.* (2018c).

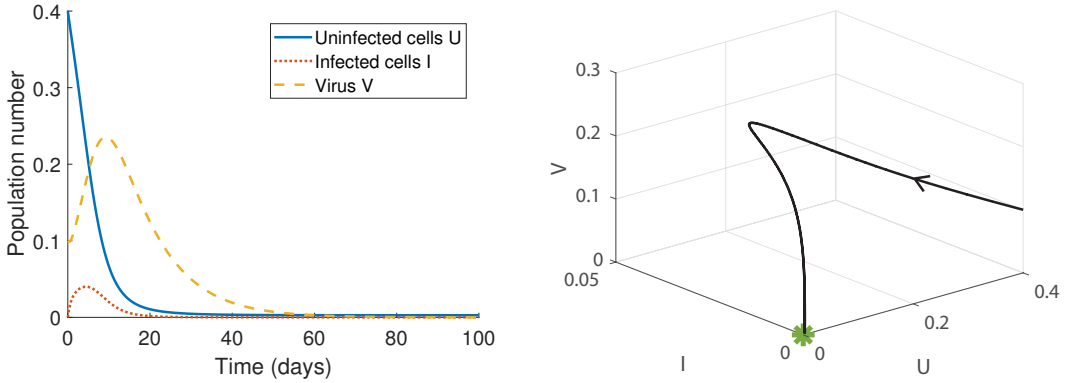

(a) **(b)**

Figure 5.4: Numerical simulation of the non-dimensionalised model, Eqs. (5.4)-(5.6), for the parameter regime where the equilibrium at the origin is stable. The time-series model solution, (a), and 3-D model curve, (b), are plotted for parameter values $\omega = 0$ and $\chi = 0.1$, and initial conditions $U = 0.4$, $I = 0$ and $V = 0.1$. The green asterisk represents the stable equilibrium at the origin. First published in Jenner *et al.* (2018c).

Biologically, both ω and χ need to be non-negative real numbers. As such, the reasonable parameter values resulting in a stable node at the origin are $\omega = 0$ and $\chi \geqslant 0$. When $\omega = 0$, there is no tumour growth, i.e. $r = 0$, and there is a benign tumour or a

malignant tumour growing at a negligible rate. Fig. 5.4 shows a numerical simulation of Eqs. (5.4)-(5.6) for typical parameter values that result in a stable node at the origin: all tumour cells and virus particles die out over time, achieving complete tumour eradication.

5.1.1.3 *Stability of the non-zero equilibrium:* $U = \chi, I = \chi\omega$ *and* $V = \omega$

Evaluating the Jacobian for the non-dimensionalised model at the non-zero equilibrium $U = \chi, I = \chi\omega$ and $V = \omega$, gives the characteristic equation:

$$\rho(\lambda) = -\lambda^3 - (1+\chi)\lambda^2 - \chi\omega. \tag{5.9}$$

The eigenvalues corresponding to the non-zero equilibrium are the roots of the characteristic equation, Eq. (5.9). The position and nature of the stationary points of the characteristic equation are used to deduce the sign and number of real roots of Eq. (5.9). See Fig. 5.5 for a more detailed explanation.

Stationary points of the characteristic equation, Eq. (5.9), occur for two values of λ:

$$\lambda_1^* = 0, \qquad \lambda_2^* = -\frac{2}{3}(1+\chi).$$

The first stationary point listed, λ_1^*, is fixed on the vertical axis $\lambda = 0$. The corresponding value of the characteristic equation at the stationary point λ_1^* is $\rho(\lambda_1^*) = -\chi\omega$. The second derivative at the stationary point λ_1^* is $\rho''(\lambda_1^*) = -2(1+\chi)$. Therefore the stationary point at λ_1^* is a minimum for $\chi < -1$ and a maximum for $\chi > -1$. This is summarised in Fig. 5.6(a) along with the sign of $\rho(\lambda_1^*)$.

The location of the second stationary point, λ_2^*, depends solely on the value of χ, i.e. for $\chi < -1$ it is positive and for $\chi > -1$ it is negative. The value of the characteristic polynomial at λ_2^*:

$$\rho(\lambda_2^*) = -\frac{4}{27}(1+\chi^3) - \chi\omega,$$

determines the nature of the stationary point, summarised in Fig. 5.6(b).

The Routh-Hurwitz criterion (for details see Section 3.5.1) is used to determine whether there exists a ω, χ combination resulting in stable solutions, i.e. all roots of

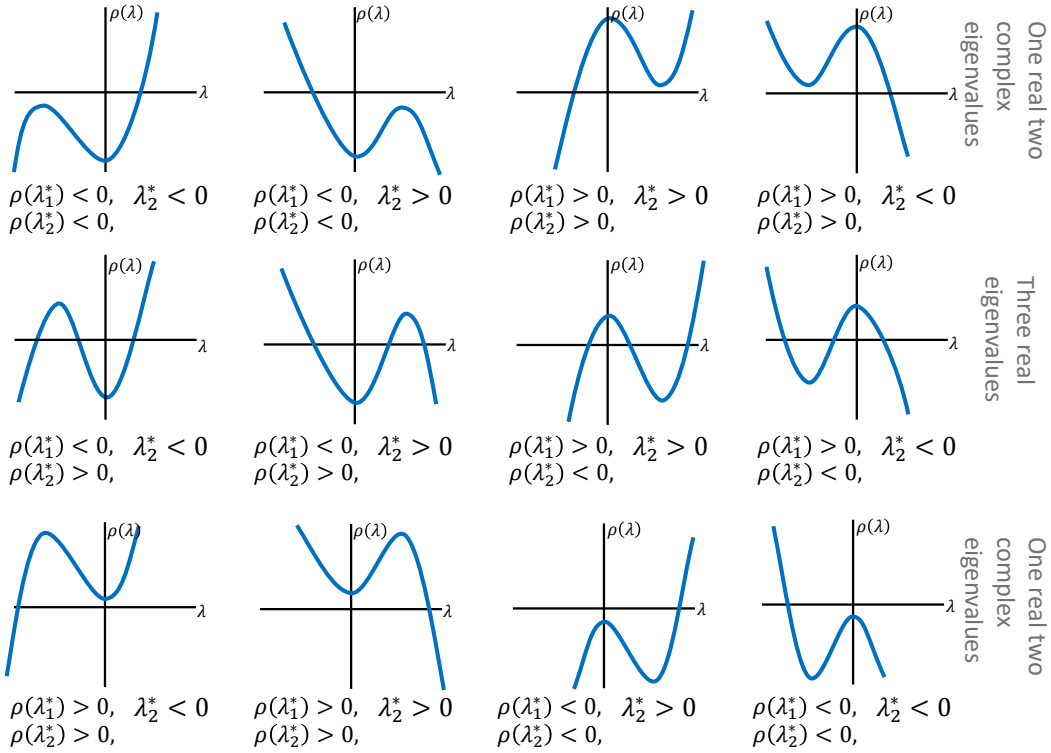

Figure 5.5: All possible cubics for the characteristic function in Eq. (5.9). Collection of the possible shapes displayed by the cubic determining the sign and nature of the eigenvalues for the non-zero equilibrium: $U = \chi, I = \chi\omega, V = \omega$. The values of λ for which the characteristic function has stationary points are λ_1^* and λ_2^*. First published in Jenner *et al.* (2018c).

the characteristic equation having negative real part. The Routh-Hurwitz stability criterion is a necessary and sufficient condition for the stability of a linear time invariant control system. For the Routh-Hurwitz criterion to be satisfied $\chi\omega$ needs to both less than and greater than zero, which gives a contradiction. As such, there is no set of χ and ω that will result in all roots of the characteristic equation where the real parts are negative and, therefore, the non-zero equilibrium will always be unstable.

The sign of the eigenvalues for the non-zero equilibrium, and hence the nature of the non-zero equilibrium, are determined by the position of the two stationary points λ_1^* and λ_2^* in the $(\lambda, \rho(\lambda))$-plane, refer to Fig. 5.5. The nature of the equilibrium for each region of the (ω, χ)-parameter space is plotted in Fig. 5.7. There are three possible values of the non-zero equilibrium: an unstable focus node, a saddle focus and a saddle. For biologically reasonable parameters, $\omega > 0$ and $\chi > 0$, there is a saddle focus,

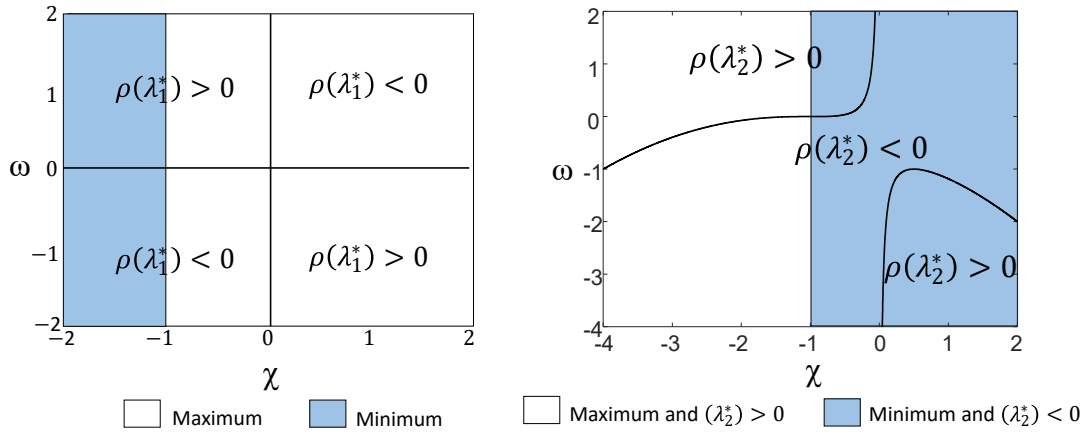

(a) **(b)**

Figure 5.6: The nature of the stationary points λ_1^*, (a), and λ_2^*, (b), as functions of the (ω, χ)-parameter space. In all figures the shaded regions represent a maximum and the white regions represent a minimum. The sign of the characteristic equation $\rho(\lambda)$ is noted as a function of the (ω, χ)-parameter space at the stationary point λ_1^*, (a), and λ_2^*, (b). Additionally, in (b), positive λ_2^* occurs in the white shaded and negative λ_2^* occurs in the blue shaded regions. First published in Jenner *et al.* (2018c).

which consists of one negative real eigenvalue and a pair of complex eigenvalues with positive real parts.

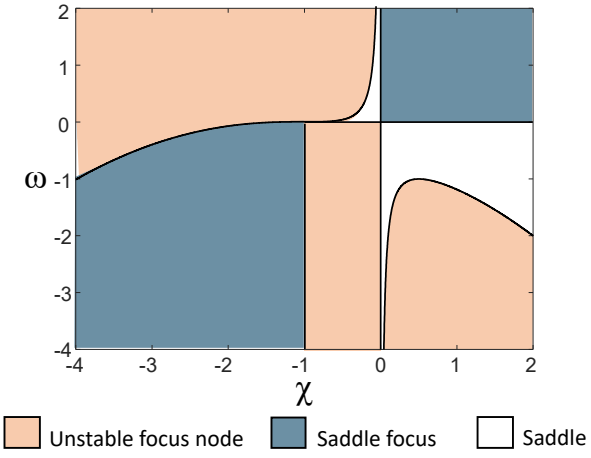

Figure 5.7: The nature of the non-zero equilibrium as a function of the (ω, χ)-parameter space. The three shaded regions correspond to the three possible equilibrium stabilities: unstable focus node, saddle focus and saddle. First published in Jenner *et al.* (2018c).

To illustrate the behaviour of the saddle focus, the numerical solution to the model, Eqs (5.4)-(5.6), is plotted in Fig. 5.8 for initial conditions close to the non-zero equilibrium. For biologically reasonable parameters there are growing oscillations in all of the

variables for the first 30 days of the oncolytic virus tumour interaction, illustrating that this regime of the virus-tumour interaction does not result in tumour eradication.

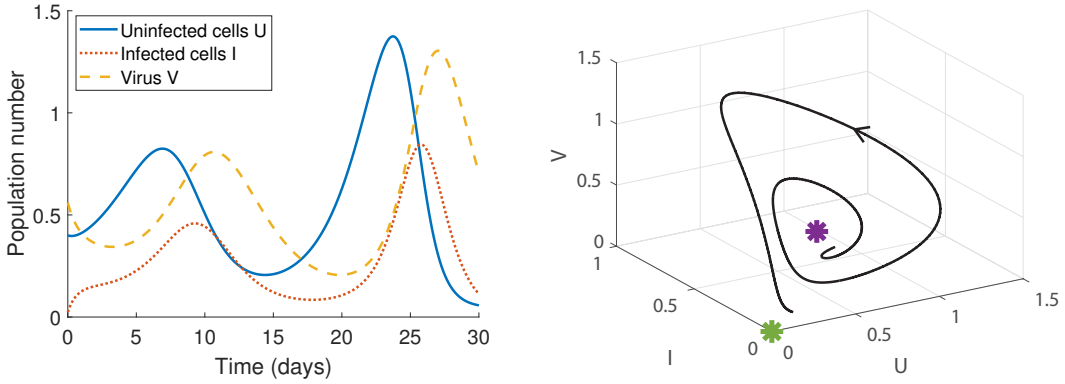

(a) **(b)**

Figure 5.8: Numerical simulations of the non-dimensionalised model, Eqs. (5.4)-(5.6), for $\chi = \omega = 0.5$. The time-series, (a), and 3-D solution curve, (b), are plotted for initial conditions $U = 0.4$, $I = 0.0243$ and $V = 0.56$. The asterisks represent the equilibrium at the origin (green) and the non-zero equilibrium (purple). First published in Jenner *et al.* (2018c).

Note that the choice of scaling for U, I and V corresponds to the proportion of the initial amount of those populations. As such $U = 1, V = 1$ and $I = 1$ indicates the cell and virus amounts present initially in the dimensional system of Eqs. (5.1)-(5.3).

5.1.2 *One-parameter bifurcation analysis*

To determine how the value of the equilibrium solutions change to variations in the virus and tumour characteristics, a bifurcation analysis of the non-dimensionalised model was conducted. In Fig. 5.9, the branches of equilibria were plotted for $\chi = 0.1$. Given that $\omega > 0$, both equilibria are unstable, as previously illustrated in the local stability analysis. The effect of changing χ is that as χ approaches zero from above, the non-zero equilibrium value for U and I decreases and the value for V remains constant, while the stability of the equilibria stays the same (not plotted).

In Fig. 5.9(a), at $\omega = 0$ there is a zero eigenvalue on the branch of equilibria labelled B2 (i.e. the axis $U = 0$). As such, between the two branch points (BP1 and BP2) and below the branch point at the origin (i.e. BP1), there are two eigenvalues with negative

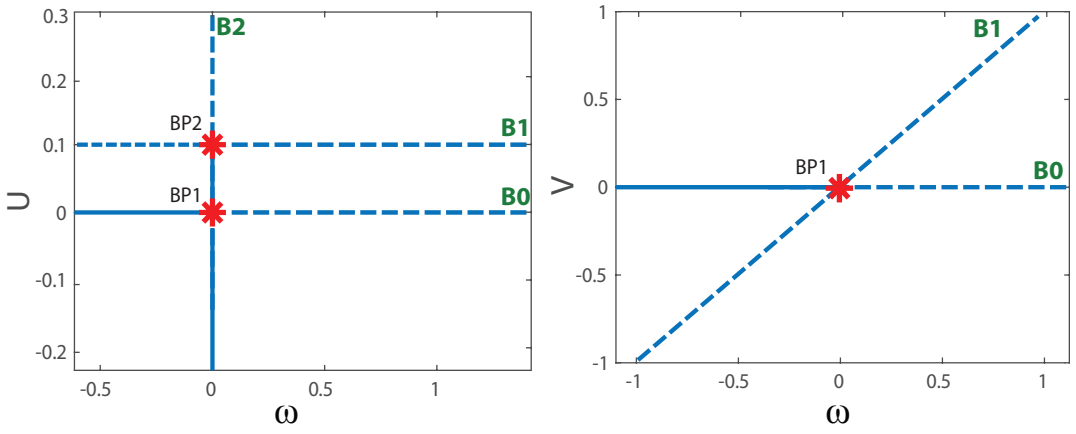

(a) **(b)**

Figure 5.9: One-parameter bifurcation plot for (a) U and (b) V as functions of ω with $\chi = 0.1$. A solid line represents a stable branch and a dotted line represents an unstable branch. A branch point is labelled BP. The equilibrium branches have been labelled B0, B1 and B2 for referencing. First published in Jenner *et al.* (2018c).

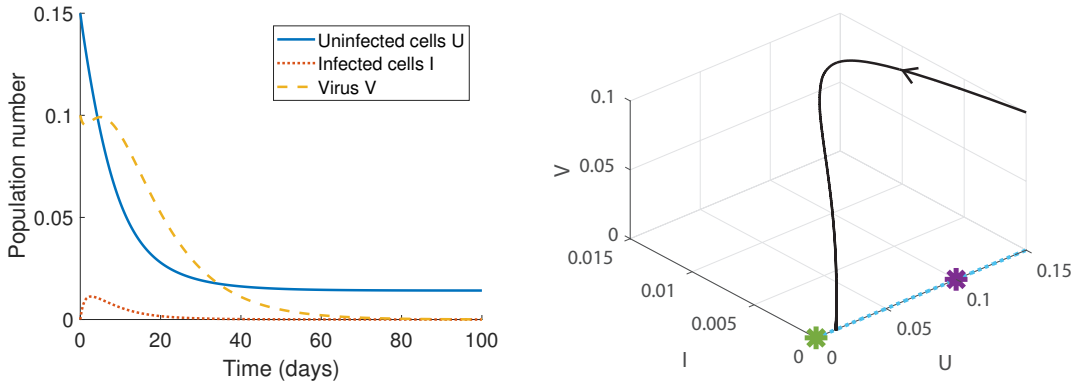

(a) **(b)**

Figure 5.10: Numerical simulations for the non-dimensional model for $\chi = 0.1$ and $\omega = 0$. The time-series, (a), and 3-D solution curve, (b), are plotted for initial conditions $U = 0.15$, $I = 0$ and $V = 0.1$. The green asterisk represents the equilibrium at the origin and the purple asterisk represents the non-zero equilibrium $U = \chi, I = \chi\omega, V = \omega$. First published in Jenner *et al.* (2018c).

real part and one zero eigenvalue. Above BP2 there is one eigenvalue with negative real part, one eigenvalue with positive real part and one zero eigenvalue. Therefore branch B2 has a two dimensional manifold that is stable below BP2 and a one-dimensional stable manifold above BP2. To illustrate the behaviour of this branch, in Fig. 5.10 a numerical simulation was presented for Eqs. (5.4)-(5.6) when $\omega = 0$ and $\chi = 0.1$.

Recall that this case represents a non-growing tumour so treatment will only amount to eradicating already existing cells. The model solution tends to a stable fixed point where $I = V = 0$ and $U \approx 0.02$.

From the analysis in Fig. 5.3 and 5.4, for $\omega = 0$ (i.e. a static tumour) the equilibrium at the origin is also stable. This means, in general, that there is a set of initial conditions that will tend to the origin and a set of initial conditions that will tend to a non-zero fixed point for $\omega = 0$ and $\chi \geqslant 0$ (the case when the tumour cells are not replicating). In Fig. 5.11, the solution curves for the model were plotted for a fixed $\chi = 0.1$ and $\omega = 0$, and a range of initial conditions. For a subset of initial conditions in the parameter space, the resulting stable equilibrium is non-zero for the uninfected tumour cells. This occurs for small vales of initially infected cells, I, and virus particles, V, and is a subset of the (larger) basin of attraction of the portion of branch B2 between BP1 and BP2. .

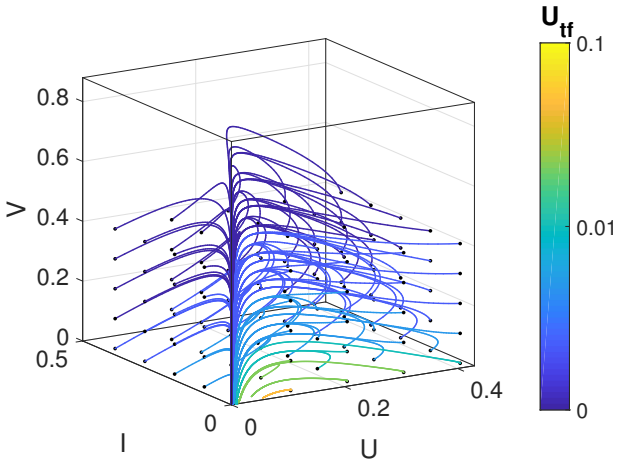

Figure 5.11: Numerical solution curves for the non-dimensional model for a range of initial conditions. The colour of the line corresponds to the equilibrium value for U, labelled U_{tf}. First published in Jenner *et al.* (2018c).

An interesting case occurs when $\chi = 0$, representing a virus decay rate of zero, i.e. the virus is not cleared from the tumour site. In Fig. 5.12, the numerical model solution for $\chi = 0$ and $\omega \geqslant 0$ is shown. Note that the uninfected and infected tumour populations are quickly eradicated whilst the virus population tends to a non-zero fixed point. This corresponds to the branch of stable equilibria at $U = I = 0$ and $V \in \mathbb{R}$ (see Section 5.1.1.1). While the virus population is still non-zero in this situation, the tumour populations have been eradicated and, therefore, this is a positive outcome for oncolytic virotherapy. This result is interesting, as it says that if it were possible

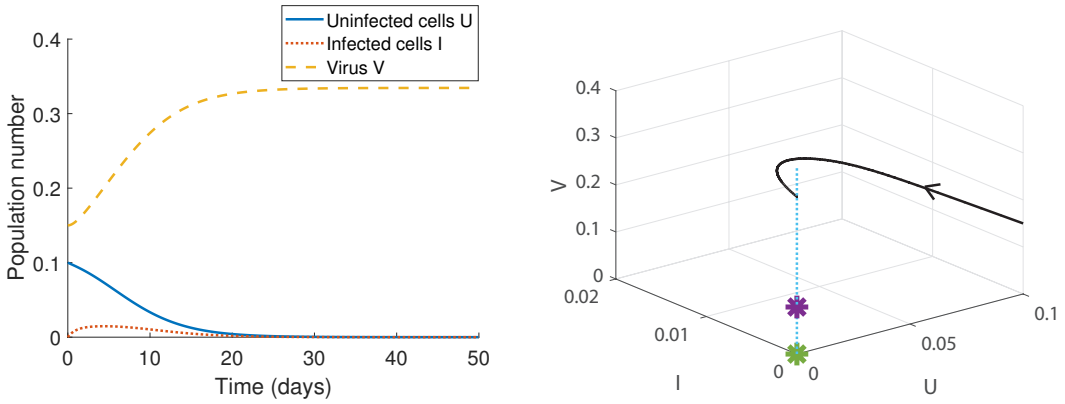

(a) **(b)**

Figure 5.12: Numerical simulations for the non-dimensional model for $\chi = 0$ and $\omega = 0.1$. The time-series (a), and 3-D solution curve (b), are plotted for initial conditions $U = 0.5$, $I = 0.05$ and $V = 0.2$. The green asterisk represents the equilibrium at the origin and the purple asterisk represents the non-zero equilibrium $U = \chi, I = \chi\omega, V = \omega$. First published in Jenner *et al.* (2018c).

to avoid viral clearance, treatment could be more effective irrespective of the tumour growth rate.

5.1.3 *Incomplete eradication and long-period orbits*

The goal of the previous section was to determine whether there was a parameter regime that would result in complete tumour eradication. Unfortunately, since the equilibrium at the origin is unstable for $\chi > 0$ and $\omega > 0$, tumour eradication cannot be achieved for a growing tumour and decaying virus. However, numerically simulating Eqs. (5.4)-(5.6) for a long time period shows the existence of stable long-period orbits, see Fig. 5.13. These orbits could be indicating that, in the limit for $\chi \to 0^+$, the system shows a quasi-homoclinic state. By simulating the non-dimensionalised system for three biologically reasonable initial conditions, time-series and phase portraits were produced for a range of parameter values. It is clear from Fig. 5.13 that the lower the value of χ or ω, the closer the orbit gets to the long-period orbit state.

To quantify the dependence of the orbits on the parameter values, the amplitude and period were numerically calculated as a function of χ and ω in Fig. 5.14. The period

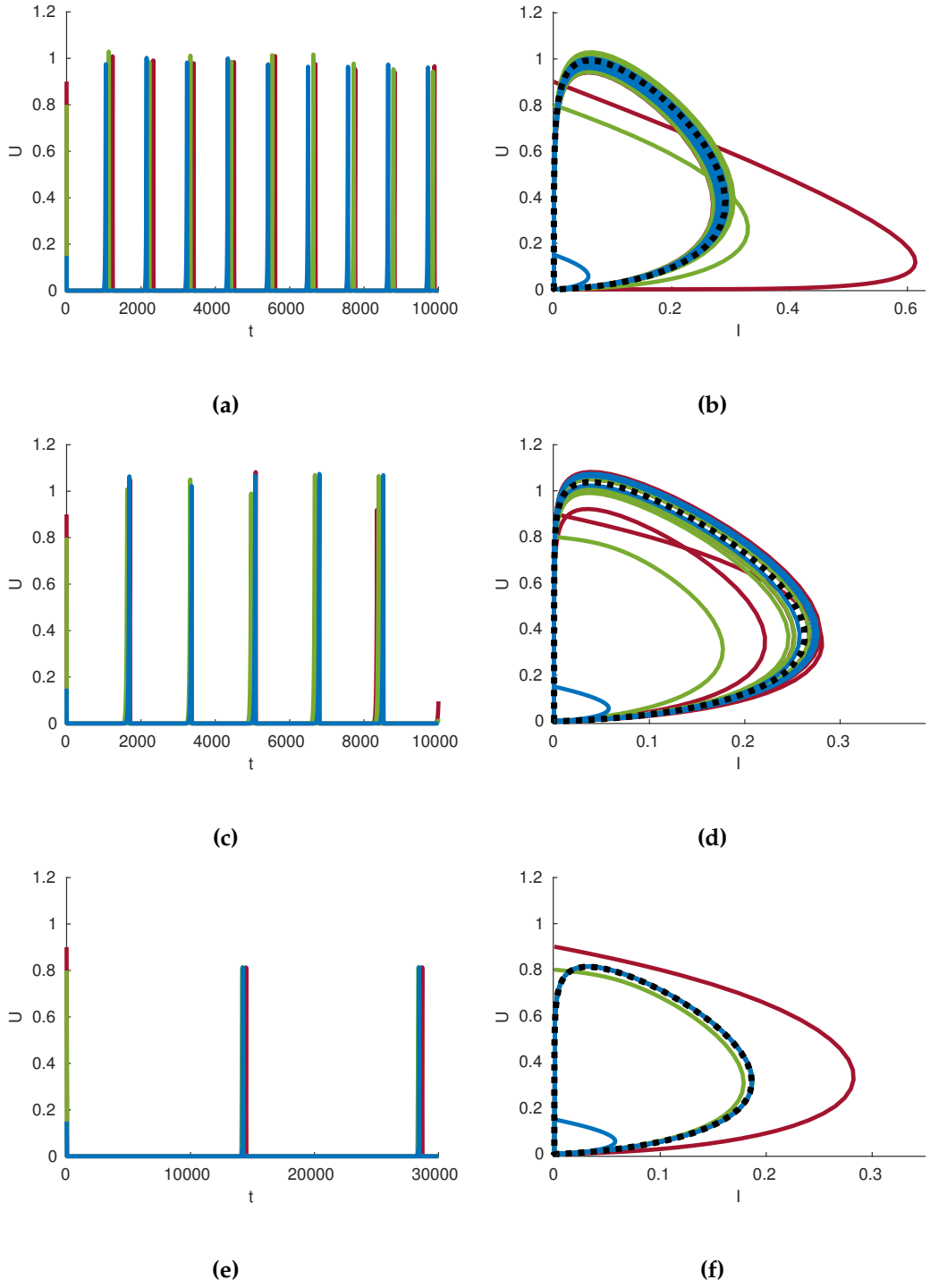

Figure 5.13: Numerical simulations of the non-dimensionalised model in Eqs. (5.4)-(5.6). For $\omega = 0.1$ and $\chi = 0.01$ (a)-(b), for $\omega = 0.06$ and $\chi = 0.01$ (c)-(d) and for $\omega = 0.06$ and $\chi = 0.001$ (e)-(f). Each coloured line represents a different initial condition: $U = 0.9, I = 0, V = 0.5$ (green), $U = 0.8, I = 0, V = 0.1$ (red) and $U = 0.15, I = 0, V = 1$ (blue). Long-period orbit attractors are black dotted curves. After a transient, all shown orbits appear to collapse onto the attractor. First published in Jenner *et al.* (2018c). Note the different scales in the plots.

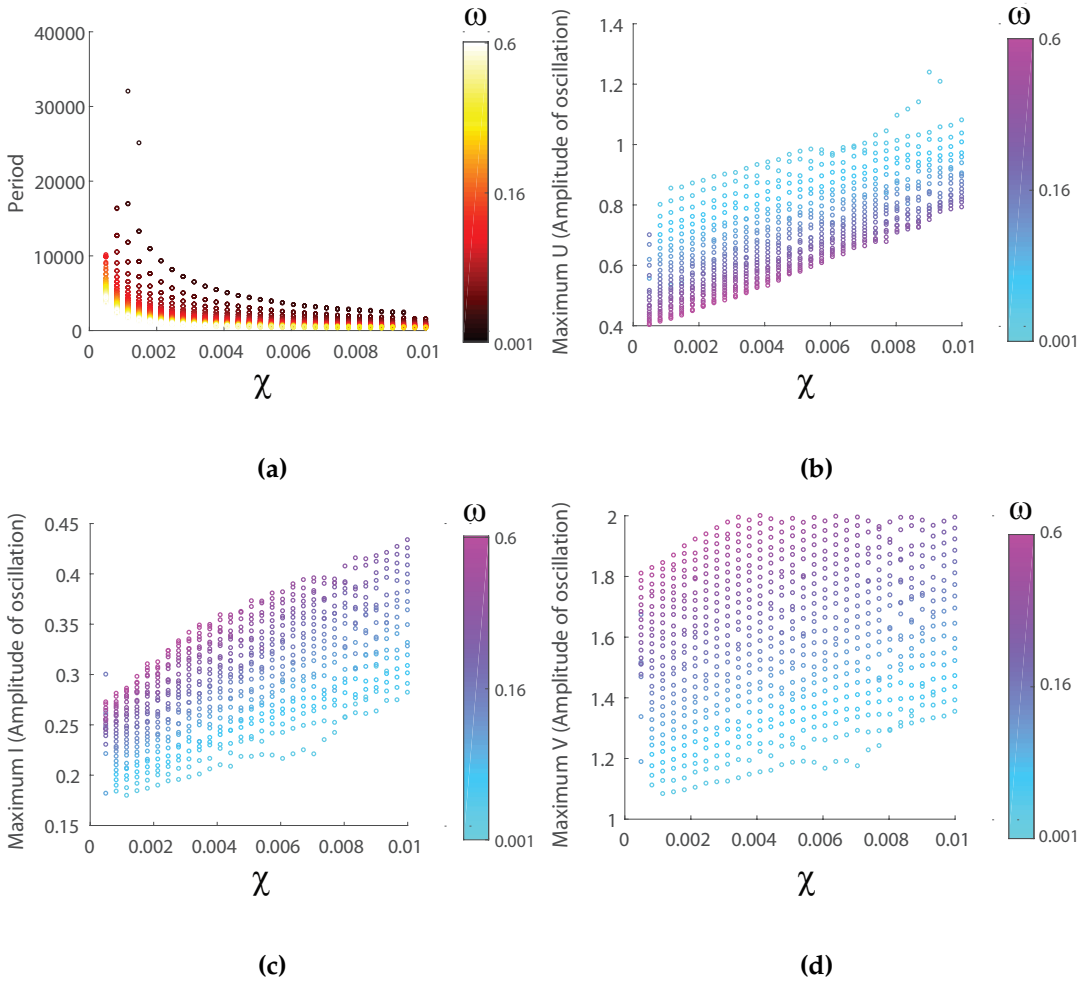

Figure 5.14: Numerical calculation of the period, (a), and amplitude, (b)-(d), for the orbits produced by the non-dimensionalised model in Eqs. (5.4)-(5.6) as a function of χ and ω. The colourbar links the colour of the circles to the corresponding value of ω used in the calculation. First published in Jenner *et al.* (2018c).

between oscillations has been calculated as a function of χ (i.e.: d_V/d_I, the ratio of viral death to cell burst rate) and ω (i.e.: r/d_I, the ratio of tumour cell replication to cell burst rate), see Fig. 5.14(a). Decreasing χ and increasing ω results in a longer period of time between the oscillations. Therefore, a slower growing tumour relative to cell burst rate would produce longer intervals of no growth between its rapid burst-like growths. Equivalently, a more rapid clearance of the viral particles relative to cell burst rate would result in longer periods between the oscillations. This can happen when the immune system has a strong response to the presence of an oncolytic virus.

The role of the immune system in oncolytic virotherapy is explained in more detail in Chapter 6 and 7.

Fig. 5.14(b)-(d) shows how the amplitude of the oscillation depends on χ and ω. There is an inverse relationship between the amplitude of the oscillation for uninfected tumour cells, U, and the amplitude of oscillation for infected tumour cells, I, and virus particles, V. Increasing ω results in a lower amplitude for U, and a larger amplitude for I and V. Improving treatment correlates to obtaining the lowest possible tumour population and therefore the lower the amplitude of the uninfected tumour cells close to the long-period orbit state, the more effective the treatment.

5.2 ANALYSIS OF AN EXTENDED MODEL FOR ONCOLYTIC VIROTHERAPY

The dimensional model in the previous Section 5.1 can be extended to consider how the outcome of oncolytic virotherapy may vary when more complex modelling terms for tumour growth and virus-infection are used. In Eqs. (5.1)-(5.3), an aggressively growing tumour was modelled; however, *in vivo* tumour growth is controlled by nutrient and spatial limitations. As such, tumour growth naturally grows towards a carrying capacity (Section 2.2.2). To account for this, the Gompertz function is now used to model tumour growth, i.e. $g(u) = r\log(L/u)u$, where L is the carrying capacity of the tumour and r is the proliferation constant, see Section 3.2.1.

The rate at which virus particles infect tumour cells depends on a number of factors. In the model outlined in Section 5.1, the rate of infection was assumed to be proportional to the number of virus particles and uninfected tumour cells. It is also common in epidemic modelling to consider that virus infection occurs at a frequency dependent rate, where the likelihood of a virus infecting a tumour cell depends on the number of tumour cells available to infect. In this case, viruses are modelled as being sufficiently close to the tumour, so that the infection rate is dominated by the number of viral particles and the occurrence of uninfected cells in the overall tumour mass. An example of this modelling term is in Kim *et al.* (2015)'s model for the effectiveness of an oncolytic virus expressing 4-1BBL and IL-12, Eqs. (3.17)-(3.21).

To model the virus infection, a frequency-dependent function, rather than a simple mass-action term, is now introduced: virus particles at the tumour site infect susceptible tumour cells according to the expression $\beta uv/(u+i)$, where β is the infectivity rate.

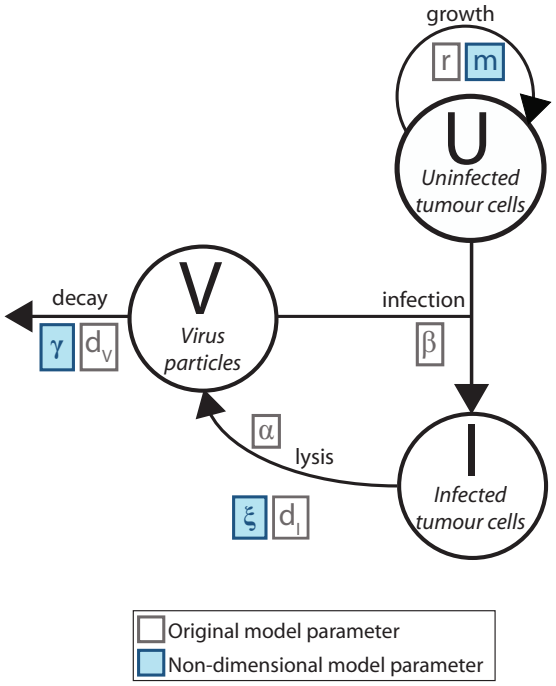

Figure 5.15: Flow diagram for the interaction between a population of uninfected tumour cells, U; virus-infected tumour cells, I; and virus particles, V. The diagram lists parameters relating to the original model Eqs. (5.10)-(5.12), in grey boxes and parameters relating to the non-dimensional form of the model, Eqs. (5.13)-(5.15), in blue boxes. First published in Jenner *et al.* (2019).

Introducing these new assumptions for the tumour growth rate and virus-infection rate into the equivalent terms in Eq. (5.1)-(5.3) gives the following system of equations:

$$\frac{du}{d\tau} = r \ln\left(\frac{L}{u}\right) u - \frac{\beta u v}{u+i}, \tag{5.10}$$

$$\frac{di}{d\tau} = \frac{\beta u v}{u+i} - d_I i, \tag{5.11}$$

$$\frac{dv}{d\tau} = -d_V v + \alpha d_I i. \tag{5.12}$$

Fig. 5.15 depicts the flow diagram of the three populations described in the Eqs. (5.10)-(5.12). To arrive at a scaled version of the system, consider the units of state variable

v and the parameter α: $[v]$ =# virions, $[\alpha]$ =#virions per cell. So, v can be re-scaled to give:

$$\hat{v} = \frac{v}{\alpha}, \quad [\hat{v}] = \frac{[v]}{[\alpha]} = \frac{\#\text{virions}}{\#\text{virions per cell}} = \#\text{cells},$$

which represents cell numbers, like u and i for the tumour. Substituting this re-scaled variable into the model gives:

$$\begin{aligned}
\frac{du}{d\tau} &= r \ln\left(\frac{L}{u}\right) u - \frac{\beta \alpha u \hat{v}}{u+i}, \\
\frac{di}{d\tau} &= \frac{\beta \alpha u \hat{v}}{u+i} - d_I i, \\
\frac{d\hat{v}}{d\tau} &= d_I i - d_V \hat{v}.
\end{aligned}$$

To eliminate time, β is used to rescale τ. The units of β are

$$[\beta] = \frac{1}{\#\text{virions}} \frac{1}{\text{per unit time}},$$

so for $\hat{\beta} = \beta\alpha$, the units of $\hat{\beta}$ would be $[\hat{\beta}] = 1/\text{time}$. Scaling time by $\hat{\beta}$ gives $[t] = [\hat{\beta}][\tau]$ and the system of equations can now be rewritten for the independent dimensionless variable t:

$$\frac{dU}{dt} = m \ln\left(\frac{L}{U}\right) U - \frac{UV}{U+I}, \tag{5.13}$$

$$\frac{dI}{dt} = \frac{UV}{U+I} - \xi I, \tag{5.14}$$

$$\frac{dV}{dt} = \xi I - \gamma V, \tag{5.15}$$

where $m = \frac{r}{\hat{\beta}}, \xi = \frac{d_I}{\hat{\beta}}, \gamma = \frac{d_V}{\hat{\beta}}$ and $\hat{\beta} = \beta\alpha$ are dimensionless parameters, and t represents a dimensionless time, with $t = \hat{\beta}\tau$. Note that the state variables are now U, I and V, which have units # cells. The three parameters m, ξ and γ that regulate the behaviour of the system represent tumour growth, tumour cell death and viral decay, respectively. As a result of the non-dimensionalisation process, where parameters are all scaled by the infectivity rate, the rate of conversion of uninfected cells U to infected cells I due to the viral load V, i.e. the term $\pm\frac{UV}{U+I}$, is not affected by any parameter.

Similar models to Eqs. (5.13)-(5.15) were discussed in Chapter 3, see Eqs.(3.1)-(3.3), Eqs.(3.13)-(3.16) and Eqs. (3.17)-(3.21). While similar, none of these models considered a growth term with a carrying capacity (logistic or Gompertz) combined with a frequency-dependent infection term as is the case in Eqs. (5.13)-(5.15).

5.2.1 *Local stability analysis*

Similar to the analysis in Section 5.1.1, a local stability analysis of Eqs. (5.13)-(5.15) shows a number of interesting results. Of particular relevance is the existence of a stable equilibrium corresponding to eradication, which is characterised by a singular Jacobian matrix. This solution can coexist with other equilibria, for example a stable focus or a stable node, which correspond to incomplete eradication of the tumour. In Section 5.2.2, this occurrence is shown to give rise to bistability for some biologically relevant parameter ranges.

5.2.1.1 *Equilibrium solutions*

Setting the right-hand-side of Eqs. (5.13)-(5.15) to zero, three equilibria are found: (a) a solution at a value for the uninfected cells equalling the carrying capacity, indicating a treatment with no effect; (b) a non-zero solution representing incomplete eradication, characterised by a quiescent tumour despite the viral load being constant and non-zero; and (c) an equilibrium at the origin corresponding to complete eradication of the tumour (in the limit as all three variables go to zero). The populations corresponding to such cases are

$$
\begin{aligned}
&(a)\quad U = L,\quad I = 0,\quad V = 0;\\
&(b)\quad U = L\exp\left(\frac{\xi}{m\gamma}(\gamma-1)\right) = U^*,\quad I = \frac{L}{\gamma}(1-\gamma)\exp\left(\frac{\xi}{m\gamma}(\gamma-1)\right) = I^*,\\
&\qquad V = \frac{L\xi}{\gamma^2}(1-\gamma)\exp\left(\frac{\xi}{m\gamma}(\gamma-1)\right) = V^*;\\
&(c)\quad U = 0,\quad I = 0,\quad V = 0.
\end{aligned}
$$

The Jacobian of the system is given by

$$J = \begin{pmatrix} m \ln\left(\frac{L}{U}\right) - m - \frac{VI}{(U+I)^2} & \frac{UV}{(U+I)^2} & -\frac{U}{(U+I)} \\ \frac{VI}{(U+I)^2} & -\xi - \frac{UV}{(U+I)^2} & \frac{U}{U+I} \\ 0 & \xi & -\gamma \end{pmatrix}, \tag{5.16}$$

and the character of the eigenvalues for the above equilibria is discussed below.

5.2.1.2 *(a) Stability of ineffective treatment equilibrium:* $U = L$, $I = 0$, $V = 0$

The first equilibrium (a) corresponds to a failed treatment where uninfected tumour cells U grow to the system's carrying capacity L and no viral particle survives. Evaluating the Jacobian at this point gives

$$J = \begin{pmatrix} -m & 0 & -1 \\ 0 & -\xi & 1 \\ 0 & \xi & -\gamma \end{pmatrix},$$

which gives rise to the characteristic equation

$$\rho(\lambda; m, \gamma, \xi) = -(\lambda + m)\left(\lambda^2 + (\xi + \gamma)\lambda + \xi(\gamma - 1)\right). \tag{5.17}$$

For a non-zero tumour growth $m > 0$, the overall stability of this equilibrium depends on the roots λ_2 and λ_3 of the quadratic factor, because the root $\lambda_1 = -m$ of the linear factor is negative. After calculating λ_2 and λ_3, the equilibrium is found to be either a stable node or stable focus when $\xi + \gamma > 0$ and $\xi(\gamma - 1) > 0$. Since the parameter values in this model are considered to be always positive, the first condition holds. The second condition implies that, if $\gamma < 1$, the equilibrium is unstable, and vice versa for $\gamma > 1$.

5.2.1.3 *(b) Stability of partial eradication solution:* $U = U^*$, $I = I^*$, $V = V^*$

The model emits a second, non-zero equilibrium where a small tumour mass coexists with virus particles. The characteristic equation for this solution, after substituting U^*, I^*, V^* in the Jacobian, is given by

$$\rho(\lambda; m, \gamma, \xi) = -\lambda^3 - \lambda^2(\gamma + m + \xi) + \lambda\left(\gamma m(\xi - 1) + \frac{\xi^2}{\gamma} - \xi(2m + \xi)\right) + \gamma m\xi(\gamma - 1). \tag{5.18}$$

For this cubic, the Routh-Hurwitz criterion, in particular the Routh array method (see Section 3.5.1), is used to deduce the parameter values that produce three roots with negative real parts. This criterion states that, given a general cubic of the form $\rho(\lambda) = a_0\lambda^3 + a_1\lambda^2 + a_2\lambda + a_3$, two conditions need to be met simultaneously for all roots to have negative real parts, i.e.

$$(i)\ \frac{a_1 a_2 - a_0 a_3}{a_1} < 0 \qquad \text{and} \qquad (ii)\ a_3 < 0$$

with, in this case, $a_0 = -1$, $a_1 = -(\gamma + m + \xi)$, $a_2 = \left(\gamma m(\xi - 1) + \frac{\xi^2}{\gamma} - \xi(2m + \xi)\right)$ and $a_3 = \gamma m\xi(\gamma - 1)$. Condition (ii) is easily satisfied for $0 < \gamma < 1$, given that all parameters are assumed to be positive. Condition (i) requires that $a_1 a_2 > a_0 a_3$, since $a_1 < 0$. The region in the ξ, m, γ parameter space that satisfies this condition can be numerically computed and is depicted in Fig. 5.16(a). Using the discriminant of Eq. (5.18) and imposing the appropriate conditions, subsections of the region corresponding to a stable node or stable focus are illustrated in Fig 5.16(b) and (c). Note that all regions are smooth and connected.

It is also interesting to consider which parameter regimes result in a low tumour burden (or threshold) U_T. To visualise how the value of the equilibrium U^* changes as a function of parameter values, the regions of parameter space satisfying the following equality for a given threshold U_T can be computed using:

$$\xi = \frac{m}{\gamma - 1} \ln\left(\frac{U_T}{L}\right). \tag{5.19}$$

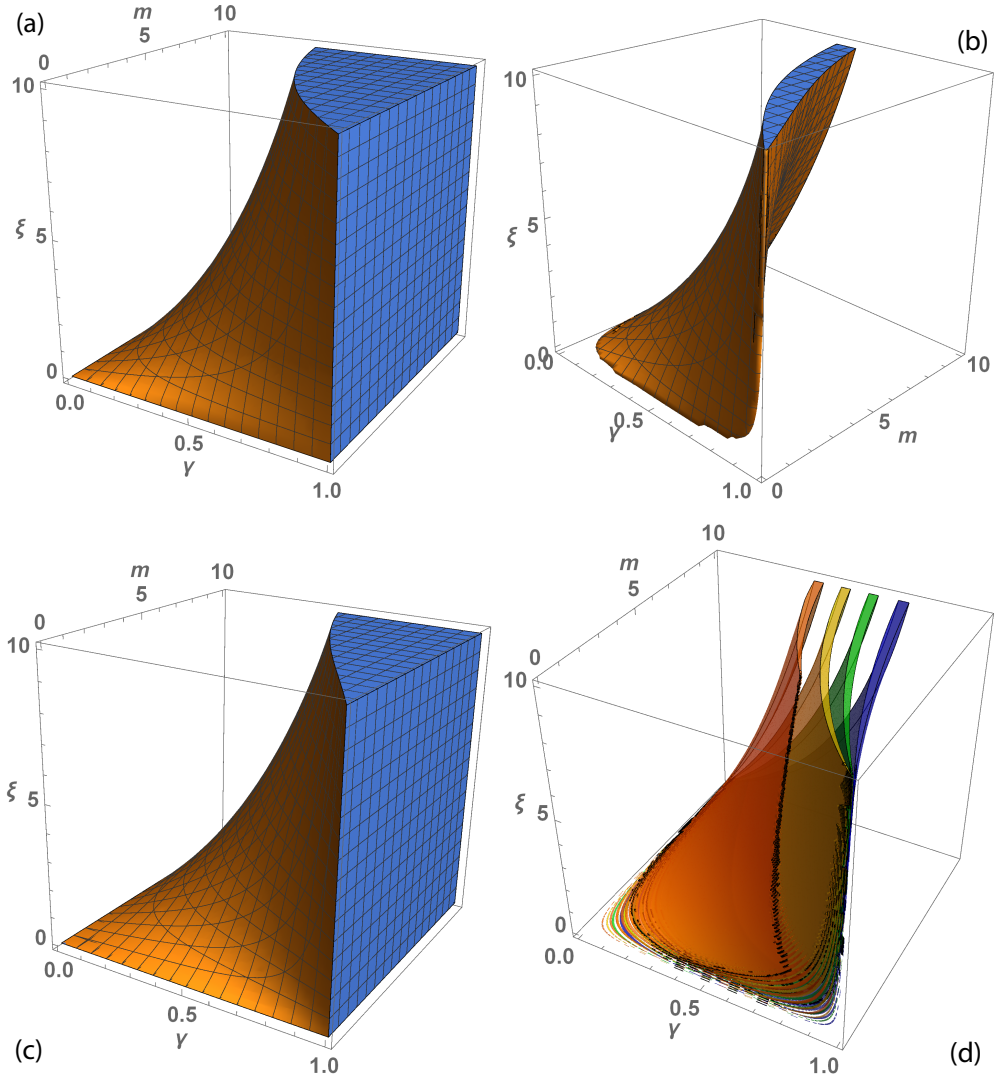

Figure 5.16: Regions representing the stability of the nonzero equilibrium, (a)-(c), and the influence of system parameters on tumour cell numbers at the equilibrium value U^*. Note that carrying capacity is chosen as $L = 100$. In (a), the section of parameter space where the non-zero equilibrium is stable is shown. Note that (b) represents the volume in (ξ, m, γ) giving rise to a stable node solution for the equilibrium (U^*, I^*, V^*), whereas (c) is the section for a stable focus. Combining the regions in (b) and (c) gives the volume in (a). Plot (d) is the stable parameter space for different values of U^*, within the following intervals: orange for $20 < U^* < 25$, yellow for $35 < U^* < 40$, green for $50 < U^* < 55$ and blue for $65 < U^* < 70$. Note that these "slices" are almost symmetrical. First published in Jenner *et al.* (2019).

Plots for four different U_T, varying within intervals, are shown in Fig. 5.16(d). For convenience, the value for L was set as $L = 100$ and fixed for all the remaining analysis. The regions are roughly symmetric, with parameter γ being the major contributor to changes in U^* values. For example, when $\gamma \lessapprox 0.5$, there is a set of ξ and m values

resulting in $20 \lessapprox U^* \lessapprox 25$. Since m represents the growth rate of tumours and U^* is mostly insensitive to its variations, the analysis indicates that a value of ξ (the lysis rate) can always be chosen to decrease the volume of the tumour, so long as the decay rate γ is low (i.e. the virus does not decay too quickly). This suggests that, irrespective of how aggressive the tumour is growing, it can be stabilised when the virus is able to induce lysis slowly and additionally avoids clearance.

5.2.1.4 *(c) Stability of full eradication solution:* $U = 0$, $I = 0$, $V = 0$

The last equilibrium of the model represents the case of complete eradication, where all variables are zero. As anticipated, the Jacobian is singular due to the presence of logarithmic and rational terms in U and $(U + I)$ respectively. An analytical treatment of the Jacobian is not possible and, in particular, the presence of logarithmic terms $m \ln(L/U)$ is not treatable with straightforward expansions for $U \to 0$. A different approach based on numerical integration and computation of eigenvalues, under specific assumptions on U, I and V, is instead used to discuss the possibility of this being a steady-state solution in the next section.

From the biological point of view, it is important to note that the Gompertz function does not represent a mechanistic model of growth and does not describe how a tumour proliferates from first principles. It is instead mostly employed as a fitting curve that describes the size of a growing tumour over time. Further, a value of uninfected tumour cells $U = 1$ equates, in this model, to a tumour volume of 1 mm^3, i.e. roughly corresponding to 10^6 cells. In the simulated time series presented and when the eigenvalues of the Jacobian have been computed, U is always treated as being zero for values $U << 10^{-6}$, which effectively represents the case when tumour cells have been thoroughly eradicated.

As far as the equilibrium's stability is concerned, the eradication solution can be stable or unstable, depending on the value of model parameters. As a general rule, it is observed that parameter sets where ξ is high, corresponding to a fast infected cell death rate, tend to yield a stable equilibrium as long as the viral decay rate γ is not excessive. This suggests that the engineered virus has to induce infected cell death quickly, whilst also being sufficiently resilient: one characteristic alone is not

sufficient. If, for example, the infected cells die at rate ξ, and the virus dies too fast, then the equilibrium turns into an unstable point and no eradication is possible. A clear picture of how eradication depends on viral characteristics will emerge with the aid of bifurcation plots, which are discussed in the next section.

5.2.2 *Characteristic dynamical regimes*

The model supports a number of dynamical regimes that represent interesting long-term possible outcomes of oncolytic virotherapy. In Fig. 5.17, four distinctive behaviours associated with the equilibria previously described are presented. Case (1) is an example of an equilibrium solution where the virus co-exists with uninfected and infected tumour cells, i.e. equilibrium (b): $U = U^*$, $V = V^*$ and $I = I^*$. The time series is for an attracting node, but similar long-term dynamics exist for the case of an attracting focus, with the only difference being an initial, oscillatory transient that then dampens to a plateau. Note how the uninfected cells U are the first to reach the equilibrium $U^* = L\exp(\frac{\xi}{m\gamma}(\gamma - 1))$, which corresponds, for the chosen parameters, to $U^* \approx 40.65$. This behaviour, under the right parameter perturbation, can transition into stable oscillatory dynamics, visible in Case (2).

Case (2) shows stable oscillations, characterised also by a quiescent phase where the system variables are close to zero and periods of growth and decay of cells and virus exist. Generally, it is observed that this refractory state tends to have a longer duration than the active phase. Also, in this case, the uninfected cells U are the first to grow, with a subsequent increase in the infected cells I and then in the virus load V. The duration of the rest and active phases of oscillations depends on the system parameters and changes continuously from Case (2) to the limiting Case (3) (illustrated with a bifurcation analysis in the following section).

Case (3) is an extreme scenario where the system oscillates between two long plateaus of quasi-complete eradication (i.e. $U = I = V \approx 0$) and quasi-ineffective treatment (i.e. $U \approx L = 100,\ I = V \approx 0$). The inset shows the "square wave" appearance of the system's trajectories on a long time scale, whereas the switch from the two states is illustrated in the main figure, showing how the growth in I and V causes the uninfec-

ted cell numbers to decrease. It is important to note that the system cannot stabilise on either equilibria, because both equilibria are unstable (illustrated with a bifurcation analysis in the following section).

In Case (3) there are long periods where the tumour is practically undetectable, followed by a rapid instantaneous increase to the tumour carrying capacity, where the tumour stabilises for a period of time, followed by a rapid reduction to an undetectable tumour. These dynamics could be explained by the presence of two or three different time scales. Biologically this is plausible as the infection and lysis of cancer cells can occur at a different time scale to the replication of cancer cells. A suitable rescaling of the mode would introduce a small parameter which in theory could reduce the model to a simpler system. Future work will investigate this; however for this thesis the full model is used as in the following chapter it will be optimised to experimental data.

Finally, a complete eradication solution is depicted in Case (4). Although, for the chosen initial conditions and parameters, the model shows a monotonic decline to zero for U, other examples have been found where U first shows a maximum, followed by an exponential decrease. Also in this final case, as for the other three scenarios just discussed, observe that U is the fastest to reach its equilibrium value, with I and V following.

To appreciate where these regimes occur and how the parameters influence their existence, two bifurcation plots with respect to system variables ξ and γ versus U are presented in Fig. 5.18. In both plots, stable branches are indicated with continuous lines, whereas unstable ones are dashed. The two black branches at $U = 0$ and $U = L = 100$ indicate the full eradication and failed treatment solutions, respectively. The red line indicates the partial eradication case, where a non-zero value for the tumour volume and the viral load is present. Numbers point to areas where the typical dynamics just discussed in Fig. 5.17 can be found.

For the case of a codimension one plot with respect to ξ, (Fig. 5.18(a)), two branch points are present: one at $U = 100$ and $\xi = 0$, where the partial eradication solution coalesces with the failed treatment case, and a second at $U = 100$ and $\xi \approx 0.098$ where the oscillatory, stable branch (green line) terminates. For this second branch, AUTO was unable to conclusively determine whether these were branch points, the software

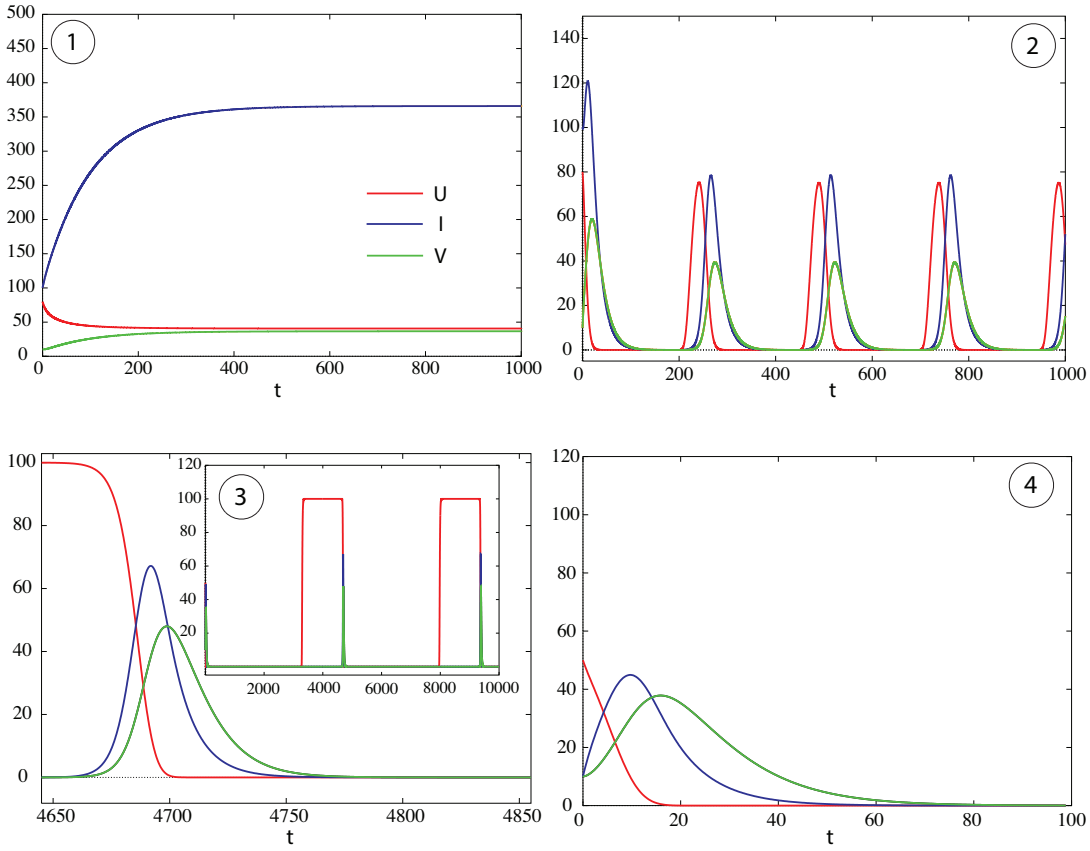

Figure 5.17: Numerical simulations of Eqs. (5.13)-(5.15) demonstrating different types of dynamics, for initial conditions $U(0) = 50, I(0) = 10, V(0) = 10$ and fixed parameters $m = 0.1, \gamma = 0.1$, with values for ξ increasing from Case (1) to Case (4). Type (1) corresponds to a stable co-existence of virus and tumour due to incomplete eradication, occurring at $\xi = 0.01$, (2) depicts a stable oscillatory solution for $\xi = 0.06$, (3) shows stable long-period oscillations of "square wave" shape for $\xi = 0.097$ and (4) is a case of complete eradication for $\xi = 0.12$. Note that the carrying capacity is chosen as $L = 100$. First published in Jenner *et al.* (2019).

indicated it was a bifurcation point and that there was a switch between the two stabilities of the branch. This branch originates from a supercritical Hopf bifurcation (HB), which causes the initial partial eradication branch to lose its stability. Note how, at this value of ξ, a change in the stability of the eradication solution $U = 0$ (black line) also occurs, with a "pseudo" saddle-node bifurcation (SN) occurring and a stable, fully eradicating regime appearing for $\xi > \xi_{SN} \approx 0.098$. The saddle-node is considered as "pseudo" because the singularity of the Jacobian implies that one eigenvalue is infinite at the origin. So, for values of the system close to zero, but not strictly zero, a change of sign in the eigenvalues occurs in the neighbourhood of SN (explained below). This

eradication solution branch regains its stability at $\xi = 0$ through a second "pseudo" saddle-node bifurcation (SN). Note also that the partial and full eradication branches (i.e. red and black lines, respectively) do not intersect. Finally, note that solution for parameter values that are negative do not bear any biological value.

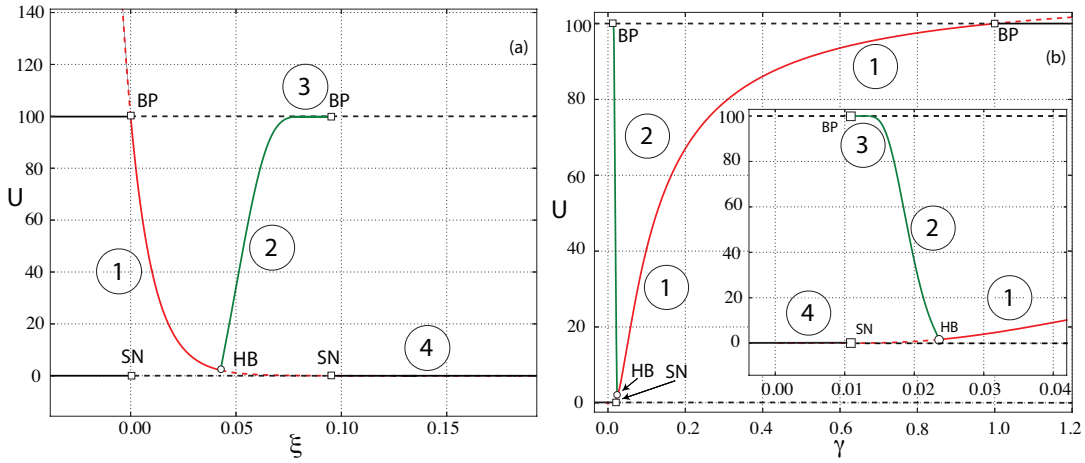

(a) **(b)**

Figure 5.18: Examples of typical bifurcation plots in one parameter for the model, for (a) ξ and (b) γ, both versus U. Circled numbers correspond to the dynamical regimes illustrated in Fig. 5.17 and, for the case of periodic orbits originating from a Hopf bifurcation, only the maximum value of U is shown. For (a), the other model parameter are $m = 0.1$, $\gamma = 0.1$. Note that the switch to Case (4) (complete eradication) occurs when the branch of periodic orbits (in green) ceases to exist, for a value $\xi \approx 0.098$. Similar results for a continuation in γ are shown in (b), with the switch to Case (4) dynamics also occurring in correspondence of a branch point for the periodic orbit, at $\gamma \approx 0.0103$. An inset with a magnification on the area that shows the richest dynamical variability is also shown. The value of the other, fixed parameters are given in this case by $m = 0.1$, $\xi = 0.01$. In both cases, solutions for negative ξ and γ have been included for reasons of consistency, but do not correspond to any biologically meaningful state. First published in Jenner *et al.* (2019).

It is worth noting that, along the red branch of coexisting solutions, U can span a large range of values, with U increasing as the infected cell death rate ξ decreases. For example, close to the HB, which occurs at $\xi_{HB} \approx 0.042$, a partial eradication solution for $\xi = 0.04$ gives a tumour burden $U \approx 2$. Note also the extension of the plateau of the periodic branch (green) close to the $U = 100$ unstable equilibrium, before the branch point. This indicates that a "square wave" type of oscillation can be present for a moderately extended parameter interval in ξ.

Although not shown in the diagram, the switch between the node and the focus equilibrium typical of the partial eradication solution takes place along the red branch. For the chosen parameters in Fig. 5.18(a), this happens at $\hat{\xi} \approx 0.01675$, with focus's existing for a value ξ such that $\hat{\xi} < \xi < \xi_{HB}$. Generally speaking and as shown in Fig. 5.16(b)-(c), the value at which the equilibrium type changes depends also on the other parameters m and γ of the model.

The system's behaviour also shows a strong, nonlinear dependence on viral death rate γ, as illustrated in Fig. 5.18(b). With respect to the case of ξ, the sensitivity of the model to γ is somewhat reversed: intuitively, a surge in infected cell death ξ should act on the model in a similar way as a reduction in virus death rate γ and vice versa. For example, the branch of oscillatory solutions (green) out of the supercritical Hopf bifurcation (HB) shows an increasing maximum in U as γ decreases, opposite to what happens for ξ (see the inset, in particular).

The stable, impartial eradication solution branch (red) shows higher tumour volumes with increasing γ, and coalesces with the unstable $U = 100$ branch (in black) at $\gamma = 1$. For $\gamma > 1$, the ineffective treatment solution is stable, as previously found from the analysis of the characteristic equation corresponding to this solution, i.e. Eq. (5.17). A virus with a decay rate $\gamma > 1$ has no effect on the tumour. It is important to note that a mechanism identical to that observed in the bifurcation plot for ξ allows the existence of Case (4) solutions, i.e. complete eradication. At a value of $\gamma \approx 0.0103$, the inset shows the termination of the oscillatory solutions (in green) and the occurrence of a "pseudo" saddle-node point in the full eradication branch, making complete destruction of the tumour possible. From the biological perspective, this indicates that the right balance between the death rate of infected cells and the viruses mortality must be achieved for an eradication to occur, depending on the growth rate m of the tumour. In particular, as γ is increased from zero, the model goes from full eradication to oscillations with an amplitude that decreases with γ, and subsequently to incomplete eradication up until $\gamma = 1$.

As previously mentioned, the full eradication solution gives rise to a singular Jacobian, making a purely numerical approach to continuation impossible. For solutions where $U \neq 0$, results have been obtained by using AUTO (Doedel, 2007) and XP-

PAUT (Ermentrout, 2002) softwares. For the case of solutions occurring for $U = 0$, a combination of numerical methods and symmetry arguments have been employed. It is assumed that $U < I < V$, as exemplified by Case (4) shown in Fig. 5.17. If $\epsilon > 0$ and small, and it is imposed that $U \to \epsilon^n$, $V \to \epsilon^m$ and $I \to \epsilon^l$ with $n > m > l$, then the eigenvalues of the Jacobian in Eq. (5.16) can be numerically computed.

For example, in determining the stability of the full eradication branch in Fig. 5.18(a), the values $U = 10^{-7}$, $V = 10^{-5}$ and $I = 10^{-4}$ were substituted into the Jacobian in Eq. (5.16) and the eigenvalues were evaluated numerically. For $\xi > \xi_{SN} \approx 0.0975$, all three eigenvalues were negative and real, whereas for $\xi < \xi_{SN}$ two were positive and one was negative. For example, choosing $\xi = 0.095$ gave eigenvalues $\lambda_1 \approx -0.15$, $\lambda_2 \approx -0.06$ and $\lambda_3 \approx 8 \cdot 10^{-5}$. For the case $\xi = 0.099$, the first two eigenvalues were basically unchanged, but the last one changed sign and is $\lambda_3 \approx -2 \cdot 10^{-3}$. Similar results hold for the "pseudo" SN on the eradication branch for continuation in γ (see Fig. 5.18(b)), and the method is consistent for all the parameters m, γ and ξ tested (not all shown here). These results were also checked by integrating the equations of motion with XPPAUT, and confirming that the solution was indeed attracting when stable or repelling when unstable, as shown in the bifurcation diagrams. Numerical integration in most cases allows for the variables U, V and I to go to values as low as 10^{-20}.

One important feature of the model is that stable oscillations exist for some biologically meaningful combinations of parameters. There is evidence of oscillations in tumour size under treatment with an oncolytic virus occuring *in vivo* (Dingli *et al.*, 2009). For some parameter choices, a different structure of bifurcation plots emerge, with significant consequences from the biological perspective. In this sense, a typical example for a continuation in ξ is illustrated in Fig. 5.19(a). An unstable periodic branch (green) originates from a subcritical Hopf bifurcation (HB) and maintains its unstable character until it collapses with the $U = L = 100$ (black) branch. For this diagram, viral decay γ is the same as in Fig. 5.18(b), but a value of $m = 0.5$ (moderately high growth rate) is chosen, whereas both previous diagrams in Fig. 5.18 have been obtained with $m = 0.1$ (moderate growth rate). A more aggressive tumour, assuming that the viral decay is the same, does not engage in oscillatory behaviour with the virus, but only partial or full eradication is possible (i.e. black and red lines).

As shown in Fig. 5.19(b), the "pseudo" saddle-node (SN) on the full eradication $U = 0$ branch (in black) occurs for a value ξ_{SN} that is less than the value ξ_{HB} at which the subcritical Hopf (HB) originates. This occurrence is due to the fact that the periodic branch shows increasing values of max U for decreasing values of ξ when it is unstable. This is the opposite of what happens for the stable periodic branch described in Fig. 5.18(a), where $\xi_{HB} < \xi_{SN}$ and the stability of the eradicated solution does not switch in this way.

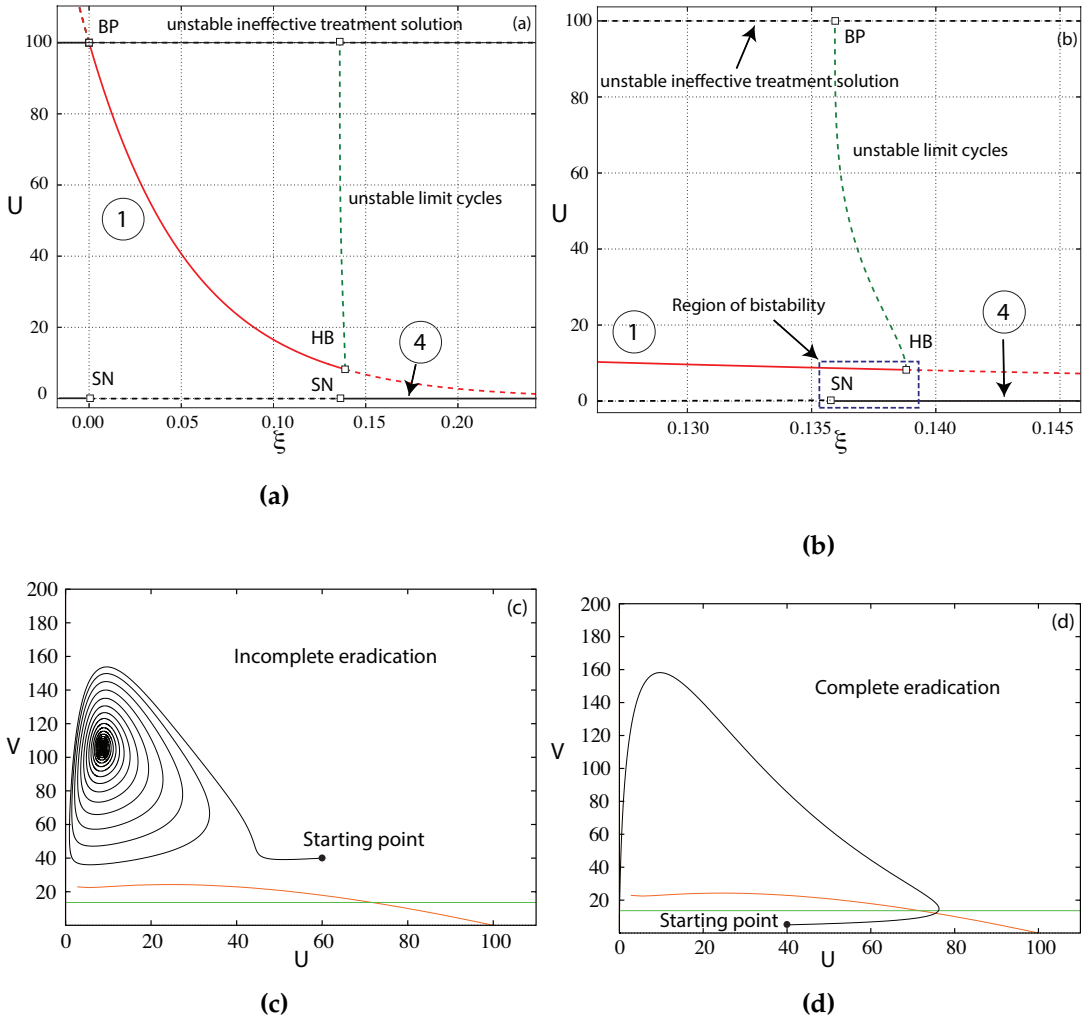

Figure 5.19: Bifurcation plots and bistable solutions for fixed parameter values $m = 0.5$, $\gamma = 0.1$. The rectangle in (b) shows the area where two solutions of different nature coexist, delimited by $\xi_{SN} \approx 0.1359$ and $\xi_{HB} \approx 0.1388$. A spiralling solution to an incomplete eradication is shown in (c) and occurs for initial conditions $U(0) = 60$, $I(0) = 10$, $V(0) = 40$, for a parameter $\xi_{SN} < \xi = 0.136 < \xi_{HB}$. A fully eradicated solution is shown in (d) and instead occurs for $U(0) = 40$, $I(0) = 10$, $V(0) = 5$, for the same value $\xi = 0.136$. Nullclines, i.e. the loci of points corresponding to $U' = 0$ and $V' = 0$, are in red and green. First published in Jenner *et al.* (2019).

The change in the order in which the SN and HB emerge as ξ is increased is responsible for the generation of a region of bistability, where two separate and distinct equilibria exist for an interval of infected cell death values. For values of ξ in this region, different initial conditions can lead to different outcomes, as shown in Fig. 5.19(c)-(d). The initial dosage of viral load and the numbers of infected and uninfected tumour cells can strongly influence the final fate of the system and, lead to somewhat unexpected results. In the first case (Fig. 5.19(c)), a spiralling solution achieves an incomplete eradication, which belongs to the red branch in Fig. 5.19(b). Conversely, the second case shows a complete eradication to a vanishing tumour, after traversing two maxima in U and V respectively, corresponding to the black branch in Fig. 5.19(b). A small variation in the initial conditions can hence result in the therapy being effective or instead giving rise to a partial eradication.

The existence of this area of bistability is associated with the presence of a subcritical Hopf bifurcation whose loci of points in ξ and m, and for different values of γ, are plotted in Fig. 5.20(a). Generalised Hopf points (GH) separate subcritical Hopf points (dashed lines) from supercritical Hopf bifurcations (continuous lines). For a revision on Generalised Hopf points see the works of Guckenheimer *et al.* (1984) and Kuznetsov (2013). Note that, if the growth m is sufficiently small, no Hopf bifurcation can be present and the system does not support oscillations, either stable or unstable. For example, as a result of the interruption of the Hopf branches shown in the inset of Fig. 5.20(a), any one-parameter bifurcation plot in ξ for a fixed $\gamma = 0.1$ and values of $m \lessapprox 0.008$, does not contain a stable or unstable oscillatory branch, since no Hopf point exists for such values. Biologically this indicates that there is a lower bound on the tumour growth rate for oscillations (stable or unstable) to exist, implying that a very slow growth in general leads to a complete eradication for sufficiently high infected cell death rates, and so long as the viruses death rate is not excessively pronounced.

A numerical analysis of the model for a range of ξ, γ and m values shows that limit cycle amplitudes for U do not follow a clear pattern, as captured by Fig. 5.20(b). Oscillations of different amplitudes can be achieved by the system and depending on the growth rate of the tumour, they can be enhanced by increases in ξ and decreases in γ (see the bifurcation diagrams in Fig. 5.18). Large and small values of γ are qualitat-

ively the primary drivers of large amplitude stable oscillations. Also, there are visible large regions of the parameter space for which small oscillations in U can be achieved. These low oscillations are primarily achieved when the decay rate of the virus is low, suggesting that low tumour sizes can be achieved when the virus is decaying slowly.

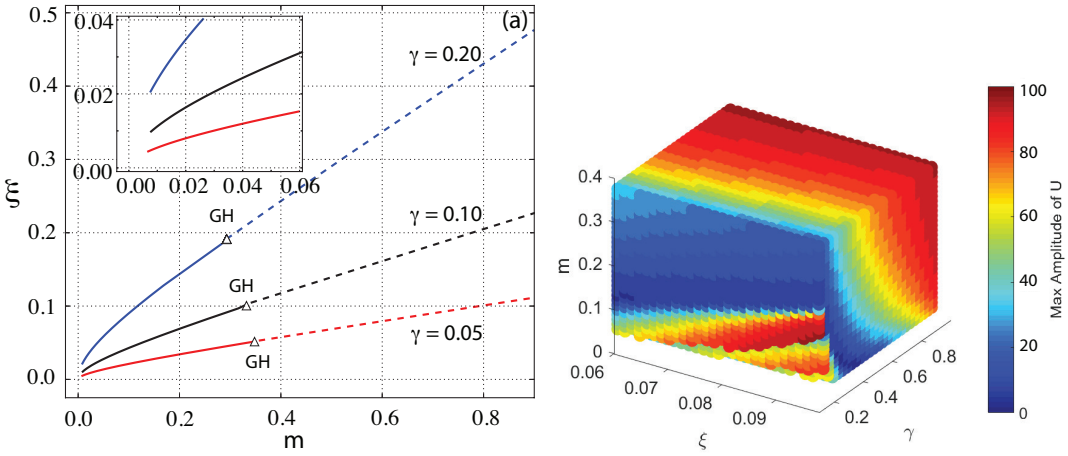

Figure 5.20: Different, two-parameters continuations in (a) for m and ξ, for branches of Hopf bifurcations at different values of γ. Branches of supercritical Hopf bifurcations are shown in continuous lines, whereas those for subcritical bifurcations are in dashed lines. Generalised Hopf points are indicated by GH. Note that the branches cease to exist for low values of (m, ξ), indicating the system cannot support either stable or unstable oscillations when parameters are sufficiently small (see the inset). Plot of the corresponding amplitude of stable limit cycles for points in the ξ, m, γ parameter space are in (b). The colour of the point corresponds to the maximal value of the amplitude of the limit cycle in U. First published in Jenner *et al.* (2019).

5.2.3 *The effect of dosage applications and their optimisation*

As shown, there are large sections of parameter space that give birth to regimes with dormant tumours or tumour-virus oscillations, which can give rise to different outcomes when coupled with clinical therapies. A typical treatment application protocol considered by experimentalists is constant dosages of virus via external intratumoural injections at given time intervals (Section 2.4.5). If the treatment is administered over

the course of n injections with ϕ number of days between injections, a virus injection protocol $u_V(t)$ can be summarised by the following generic schedule:

$$u_V(t) = \begin{cases} \dfrac{V_{T0}}{n}\delta(t-t_i) & t_i = (i-1)\phi, \quad \text{where } i = 1,\dots,n, \\ 0 & \text{otherwise.} \end{cases} \tag{5.20}$$

where V_{T0} is the total virus dosage and δ is the delta function. This injection function is added into the dV/dt equation in Eqs. (5.4)-(5.6). To numerically simulate the model in Matlab, the model was implemented as an impulsive differential equation.

Given this simple scheme in Eq. (5.20), it was possible to consider how dosage perturbations affect regions of the bifurcation diagrams and whether they result in either tumour eradication or a stable tumour size below a given threshold. The two typical scenarios considered are oscillations and bistability.

5.2.3.1 *Effects of injections on a stable, oscillatory trajectory*

After numerically exploring different areas of the parameter space that give rise to oscillations, simple therapies given by Eq. (5.20) did not alter the long term behaviour of the model. If an oscillatory, stable state were to exist between virus and tumours, increments in the viral load through injections were not predicted to achieve complete eradication. From the dynamical point of view, an increase in viral load via external perturbation cannot force the system out of the basin of attraction of a stable limit cycle. Nonetheless, transient phenomena do exist and are worth discussing.

Considering two injections, i.e. $n = 2$, for a system already in a stable oscillatory state, the number of days ϕ between injections altered the size of the tumour and virus populations as the system returned to its stable state. Assuming the first injection was a fixed initial injection, in Fig. 5.21 a single period of two different stable limit cycles of the model is shown, with arrows representing the instants at which injections that increased the viral load have been administered. The corresponding maximum and minimum tumour size, along with the maximum virus count reached, are also presented.

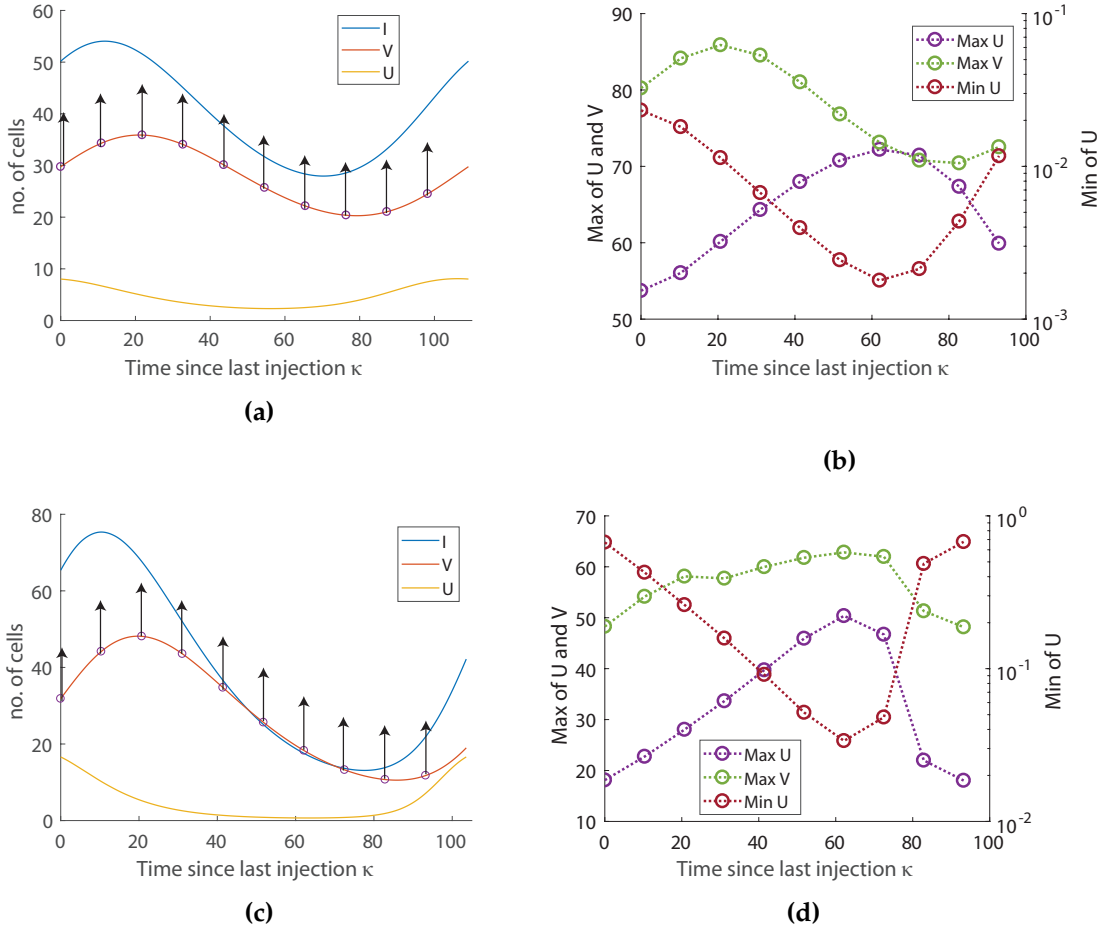

Figure 5.21: Perturbations in the days between two treatments ϕ. Two different limit cycle regimes have been plotted for $\gamma = 0.1, m = 0.2$ and (a) $\xi = 0.06915$ or (c) $\xi = 0.06993$. The maximum and minimum uninfected cell number and maximum virus count is plotted as a circle in (b) and (d) for the corresponding value of ϕ represented by an upward arrow in (a) and (c). Note the different scales used on the left and right axis, since the maximum and minimum amplitude of oscillations have different values. First published in Jenner *et al.* (2019).

Injections that occur at different phases of the cycles have different outcomes. As seen in Fig. 5.21(b)-(d) for the red and magenta curves around $\phi \approx 62$, dosing the virus close to the minimum in tumour population provides a typical outcome: the tumour initially responds to the injection by achieving a minimal size, but this is followed by a rebound that causes U to reach the highest value (max U in the plot) of all other tested injections. Note that, in some cases and for sufficiently high dosages, the minima achieved by U can be pushed to values so low that it becomes experimentally undetectable. Injections at other instants within one oscillation period yield rebounds

proportional to the original amplitude of the limit cycle, with best results occurring for the lowest amplitudes.

Perturbing the number of days between additional injections ϕ, the total injection amount V_{T0} or the number of injections n did not affect the long term dynamics (not shown here), which remains oscillatory in the long term. Reinforcing that there is no dosage protocol that can be administered for virus-tumour interactions in these parameter regimes that will result in tumour eradication.

5.2.3.2 *Effects of injections on a trajectory in the bistable region*

For a solution in a bistable region, the final outcome of any injection was highly dependent on the initial tumour size and viral load. In particular, due to the complex structure of the basin of attraction of the two competing solutions, i.e. full eradication and an incomplete quiescent state, doses that were higher than a specific threshold (highly dependent on the system parameters) could lead to a partial eradication rather than a complete one.

Consider the administration of single injections of increasing dosage as depicted in Fig. 5.22. Depending on the initial uninfected tumour population size $U(0)$, injections can lead to different outcomes or even have no effect on the final state. Considering the case of a high tumour size (Fig. 5.22(a), $U(0) = 100$), different dosages always resulted in final eradication. Some dosages lead to transient oscillations in the $U - V$ plane, but eventually eradication was achieved for all plotted trajectories.

For a smaller initial tumour size (Fig. 5.22(b), $U(0) = 50$), full eradication was only obtained if the dose was either sufficiently low or sufficiently high. There exists a considerable interval of possible doses that push the system to a stable focus corresponding to a dormant state, where eradication is not complete. Note that the first two low dosage injections, i.e. injections 1 and 2 in Fig. 5.22(b), also lead to a final eradication state after few oscillations on the $U - V$ plane.

This result is interesting, as it suggests that, for given initial tumour size and characteristics of the virus, there can be a unique interval of dosage sizes that does not result in treatment success. Boosting the amount of virus does not always guarantee a successful outcome.

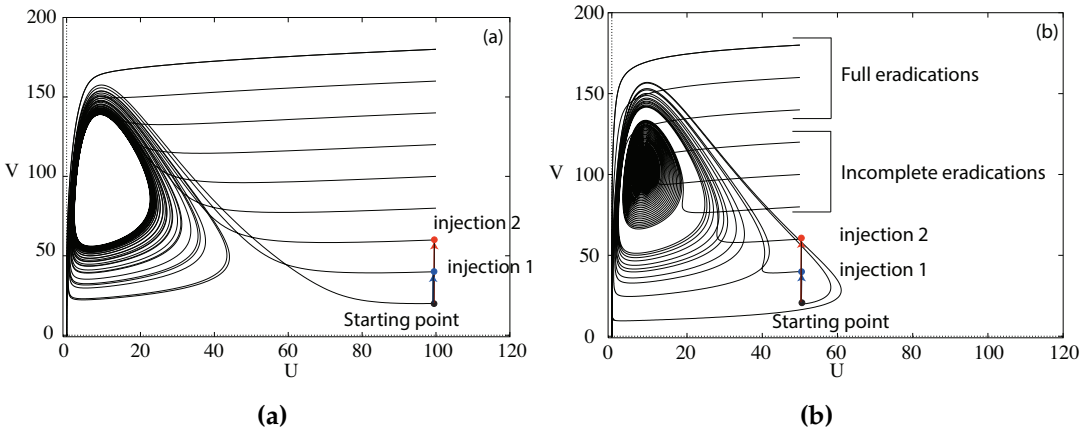

Figure 5.22: Typical cases of dependence on injected viral dosage V_{T0} for a system in a bistable scenario. Examples of two injections with increasing dosage (i.e. injections 1 and 2) are also sketched. The effect of these injections is to push the starting point to larger values of $V(0)$, depending on the dose that is administered. For the same initial tumour size, different dosages result in either tumour eradication or tumour stabilisation. Initial fixed conditions in (a) are given by $U(0) = 100$, $I(0) = 10$ and in (b) are given by $U(0) = 50$, $I(0) = 10$. In both cases, $V(0)$ varies from a minimum of 20 to a maximum of 120 in constant steps and the parameters are $m = 0.5$, $\gamma = 0.1$ and $\xi = 0.138$. First published in Jenner *et al.* (2019).

5.3 SUMMARY

Before considering the effects of specific tumour types and engineered viral derivatives, it is important to obtain an overview of what drives the efficacy of oncolytic viruses. In this chapter, two models were hierarchically developed and analysed to show a number of interesting features, both from the mathematical and the biological points of view. Firstly, a range of possible long term dynamical outcomes and stability conditions have been found for the virus-tumour interaction. From this, a number of nontrivial singular bifurcation scenarios emerged, with the presence of an important system equilibrium (i.e. full tumour eradication) in the case of the more complex model in Section 5.2. Additionally, comparing the two hierarchical models allows for a more in-depth understanding of what drives the different dynamics both mathematically and biologically. In discussing the stability of these two mathematical models, it is possible to deduce and suggest possible treatment perturbations or regimes that result in an improved outcome.

To introduce the possible long-term behaviour of virus-tumour interactions, a local stability analysis and bifurcation analysis was first conducted for the minimal model developed, Eqs. (5.4)-(5.6). The core dynamics of this interaction were captured in χ and ω representing the ratio of tumour replication and viral decay to cell burst rate respectively. Dynamics of this model can be grouped into two sub-categories: those that occur for either benign tumours or non-decaying viruses, and those that occur in the presence of tumour growth and viral decay.

The equilibrium at the origin is unstable for all biologically reasonable parameter values, except the case where $\omega = 0$ and $\chi \geqslant 0$. When $\omega = 0$, there is no tumour growth in the model: this can only occur for a specific type of tumour, i.e. a benign tumour or a tumour whose growth is extremely slow relative to the time scale of therapy. For this tumour type, the model predicts that complete tumour eradication can be obtained for a specific range of initial conditions, see Fig. 5.11. High enough initial viral dosages and initial tumour sizes result in complete tumour eradication: benign or slow growing tumours would do well under this treatment, given the right initial tumour sizes and viral dosages.

The non-zero equilibrium in Eqs. (5.4)-(5.6) is stable in the absence of viral decay, i.e. for $\chi = 0$. In Fig. 5.12 the corresponding model simulations for $\chi = 0$ and $\omega \geqslant 0$ show how the system tends to equilibrium $U = I = 0$ and $V = \mathbb{R}$. Whilst developing a virus that rigorously does not decay is impossible, experimentalists have developed ways to shield viral particles from immune detection and clearance (an example of this is the polymer polyethylene glycol (Kim *et al.*, 2011a) that is discussed in Chapter 6). However, at the moment, this is a purely hypothetical scenario, as the non-decaying virus, while harmless, will still need to be removed after it has eliminated the tumour. The model predicts that if it were possible to genetically engineer an oncolytic virus to remain within the system indefinitely, complete tumour eradication can be obtained.

Analysis of equilibria for the case of an exponentially growing tumour and viral particles undergoing decay, i.e. $\chi > 0$ and $\omega > 0$, suggested that there is no way for treatment to eradicate the tumour, as both equilibria are unstable. As shown in Fig. 5.7 and 5.8, the non-zero equilibrium is a saddle focus and the origin is a saddle, causing model solutions to spiral outwards with increasing amplitude. However, nu-

merically simulating the non-dimensionalised model for a long time period showed the appearance of long-period orbits, see Fig. 5.13. This suggests the possibility of a tumour eradication state, where long periods of tumour remission would occur.

The complexity in the behaviour of the tumour and virus populations increased with the addition of the Gompertzian tumour growth and frequency-dependent infection expression in Eqs. 5.13-5.15. As shown in Fig. 5.18, an increase in infected cell lysis ξ or a decrease in viral death rate γ drives the system through similar stages of typical dynamics, from partial eradication to tumour-virus oscillations, as those seen in the dynamics of the minimised model.

A metastable regime that appears somewhat counter-intuitive is represented by the so-called "square wave" oscillations, which are observed in a small interval of biologically relevant parameters (see Fig. 5.17(c)). Given the size of the parameter space where this dynamics takes place, it may be unlikely that such extreme tumour expansions can be directly observed in a clinical setting. Nonetheless, the switch between a quasi-eradicated to a quasi-ineffective treatment regime points to the importance of achieving a complete elimination of the tumour if a sudden resurgence is to be avoided.

There are two primary ways to interpret biologically the presence of long-period orbits in oncolytic virotherapy: complete tumour eradication or tumour remission. A long-period orbit can be considered as an example of complete tumour eradication: if the population of cells drops below certain levels, this could mean extinction. This in a more realistic setting could occur if increased likelihood of clearance or death due to nutrient deficiency is taken into account. In the long-period orbits shown in Fig. 5.13 close to zero ($<< 10^{-6}$), and in this time frame other effects are likely to eradicate the negligible number of remaining cells.

Long-period dynamics are a known feature in virotherapy models. Previously, Novozhilov *et al.* (2006) showed that for a model of oncolytic virotherapy there is a region of the parameter space where trajectories form a family of homoclinics to the origin. From the biological point of view, this occurrence implies that tumour cells can be eliminated with time, and complete recovery is possible. Similarly, Berezovskaya *et al.* (2001) showed that the origin can have its own basin of attraction in the phase space, which corresponds to deterministic extinction of both species. Berezovskaya *et al.* (2007) also

showed how certain models possess a dynamical regime of deterministic extinction, through the presence of homoclinics.

To quantify how the behaviour of long-period orbits is influenced by the parameter space, the period of oscillations as a function of both χ (the ratio of the decay of viral particles to cell burst rate) and ω (the ratio of tumour replication to cell burst rate) is computed. In Fig. 5.14(a), decreasing the ratio of viral death to cell death, i.e. χ, irrespective of the rate of tumour cell replication r and to cell burst rate d_1, i.e. ω, results in a longer period between oscillations, i.e. more time between tumour regrowth. Alternatively, decreasing the ratio of tumour cell replication to cell burst rate, i.e. ω, increases the period. Therefore, decreasing both the ratio of the decay of viral particles to cell burst rate and the ratio of tumour replication rate to cell burst rate is a very effective strategy for increasing the period of the long-period orbits.

The existence of an extended area of the parameter space where oscillations among system variables arise is also seen in the more complex model in Section 5.2. These regimes, which also tend to respond nonlinearly to external injections (see Fig. 5.22), have been known for quite some time in clinical settings (Dingli *et al.*, 2009; Wodarz, 2016). One major finding for this model is that virotherapy can prevent oscillations from occurring if the resulting infected cell death rate is sufficiently strong or, alternatively, the virus tends to survive for sufficiently long times in the infected population.

Furthermore, and this is particularly interesting, oscillations tend to have larger amplitudes and periods for increasing γ (or increasing m), before they disappear completely for sufficiently high values. This is worth reflecting on, especially from the clinical perspective. Designing a virus that results in fast infected cell death and that is still not sufficiently resilient may turn out to be a riskier strategy, since it could trigger larger fluctuations in the tumour population. These oscillations also occur at relatively distant time intervals from each other and long periods of tumour inactivity may be misinterpreted as successful eradication.

Looking at Fig. 5.18(a) and assuming that a low value of uninfected tumour cells U represents a good outcome, a slower infected cell death rate, say with a $\xi \approx 0.04$, results in a quiescent tumour of a smaller size than the amplitude of oscillations caused by a fast infected cell death rate with, for instance $\xi \approx 0.08$ (i.e. twice as fast). This is

also true from the point of view of resilience, see in particular the inset of Fig. 5.18(b): a virus that remains active for longer, say $\gamma \approx 0.015$, produces oscillations with very high values of U, whereas a virus decaying twice as fast, say with $\gamma \approx 0.03$, produces a stable tumour of a smaller size. All this shows that therapeutic strategies must be chosen carefully and thoughtfully, and that optimal design of an oncolytic virus must be targeted on the tumour characteristics, in particularly its proliferation rate.

Another key feature of the oscillations for the first model in Section 5.1, see Fig. 5.13, is their amplitude. In Fig. 5.14(b)-(d) the dependence of the amplitude of the oscillation on χ (the ratio of the decay of viral particles to cell burst rate) is examined. In all cases, the lower the value of χ the lower the amplitude of the oscillation. However, considering ω (the ratio of tumour replication to cell burst rate), increasing ω increases the amplitude of the oscillation for infected tumour cells and virus particles and decreases the amplitude for uninfected tumour cells. One of the primary objectives of a therapy is to reduce the number of uninfected tumour cells, and therefore reduce the amplitude of the oscillation for U. In that respect, a decrease in the ratio of the decay of viral particles to cell burst rate, χ, and an increase in the ratio of tumour replication to cell burst rate, ω would be ideal. This will result in the lowest possible amplitude for the uninfected tumour cells. Note that this suggestion is also associated with a long period between oscillations, so it represents overall the most effective way of improving oncolytic virotherapy.

When considering perturbations of the treatment strategy for the more complex model, therapies that couple with external injections of viral loads could have very different outcomes depending on the state of the system. They can perturb a trajectory that was meant to be of full eradication into a dormant state, see Fig. 5.22.

Comparing both models illustrates the driving mechanisms behind some of the interesting dynamics seen in the models stability. For both models, achieving complete tumour eradication is challenging and it is with the addition of the Gompertzian tumour growth and frequency-dependent virus infection that regions resulting in tumour death for growing tumours exist.

Oscillations in tumour cell population size have been seen *in vivo* in several other viral dynamic models (Bajzer *et al.*, 2008; Dingli *et al.*, 2009; Wodarz, 2016). Komarova

and Wodarz (2010) showed that using mass action to model the viral infectivity leads to strong oscillations in the population of viruses and cancer cells. Titze *et al.* (2017) suggested that the rise and fall of tumour growth, seen in oscillations, could be due to the lack of bioincubators for viral replication. This is analogous to behaviours typical of predator-prey systems, where oscillations occur due to a heavy dependence of each population on the other for survival.

One of the main limitations of both models in this chapter is the endless influx of viral load that occurs in the model: once the viral cycle is set into motion, and unless viral death rate is excessive (i.e. $\gamma > 1$ for the Gompertz model), there is no natural stopping mechanism for viral infections. This simplification is, for example, responsible for the appearance of dormant, partially eradicated tumours, which, after an initial transient, perpetually coexist with a constant viral load. These dynamics are common for models with unlimited reservoirs of populations (Wilkie, 2013) .

From the local stability and bifurcation analysis of two generic models for oncolytic virotherapy, it was possible to determine parameter regions resulting in treatment success or failure. Additionally, the effects of different treatment profiles were examined for a generic oncolytic virus. In the following Chapter, the model developed in Section 5.2 is used to optimise tumour time-series measurements for an oncolytic adenovirus conjugated with Herceptin. This allows for a specific virus and tumour parameter set to be obtained, and a subset of the full model bifurcation analysis to be discussed in detail.

6

EFFICACY OF A PEG-MODIFIED ONCOLYTIC ADENOVIRUS CONJUGATED WITH HERCEPTIN CONSIDERING ANTIVIRAL IMMUNITY AND THE ANTITUMOUR IMMUNE RESPONSE

OVERVIEW

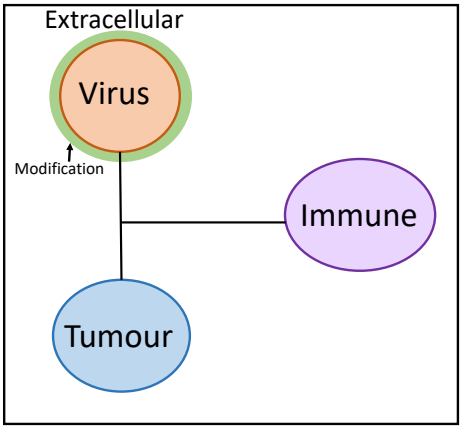

Figure 6.1: Subset of Fig.1.1, summarising the investigation of the virus-tumour interaction in this chapter

The overview of long-term dynamics for oncolytic virotherapy in Chapter 5 forms the basis of this chapter's study for a particular treatment modality: a PEG-modified oncolytic adenovirus conjugated with Herceptin. This treatment was engineered by Kim et al. *(2011a) to overcome the clearance of viral particles in the blood by the immune system. Unfortunately, PEG and Herceptin modification are unable to overcome the effect of another obstacle, interferon-mediated antiviral cell-immunity. This antiviral immunity is initiated by infected cells releasing interferon that obstructs viral replication in neighbouring cells. While this mechanism can impede the efficacy of the virus, a strong antitumour immune response (killer immune cells stimulated by virus-infected tumour cells) can be sufficient to counteract this effect and result in tumour eradication. This chapter investigates interventions that could improve the efficacy of a PEG-modified oncolytic adenovirus conjugated with Herceptin and considers how the treatment outcome may vary in the presence of interferon-mediated antiviral cell immunity and the antitumour immune response.*

Most of the work in this chapter was previously published in Jenner *et al.* (2018b) and Jenner *et al.* (2016).

A major obstacle for oncolytic virotherapy is the short retention of virus particles in the blood due to immune clearance (Kim *et al.*, 2011a). To combat this, Kim *et al.* (2011a) modified an oncolytic adenovirus (Section 2.4) with the non-immunogenic polymer polyethylene glycol (PEG). Additionally, to increase the ability of the virus to bind to and be internalised by host cells, Kim *et al.* (2011a) conjugated the PEG-modified adenovirus with a monoclonal antibody known as Herceptin (see Fig. 2.3).

PEG is an uncharged, hydrophilic, non-immunogenic polymer that is known to reduce protein-protein interactions (Kim *et al.*, 2011a). Modification of adenovirus vectors with PEG is known to increase the survival of virus particles as they travel through the bloodstream by shielding them from immune detection (Mok *et al.*, 2005). PEG-modified viruses, therefore, have a higher chance of initially reaching the tumour cells before being cleared (Mok *et al.*, 2005). The disadvantage of PEG modification is that it weakens the ability of the virus to interact with and target tumour cells, which inhibits virus infectivity (Kim *et al.*, 2011a).

For some cancer types, the decrease in efficacy of oncolytic virotherapy incurred through PEG modification can be overcome by conjugating the viruses with Herceptin. Herceptin is a Her2/neu-specific monoclonal antibody that is used regularly in breast cancer treatment as it recognises and binds to Her2, found over-expressed on the surface of certain types of breast cancer cells (Section 2.2.3.1). The conjugation of an oncolytic adenovirus with Herceptin allows the modified virus to selectively accumulate within tumours expressing Her2, leading to a higher probability of tumour cell infection and in turn tumour cell death.

6.1 VALIDATION OF A PEG-MODIFIED ADENOVIRUS CONJUGATED WITH HERCEPTIN

To quantify the effectiveness of modifying an adenovirus with PEG and Herceptin, Kim *et al.* (2011a) conducted three *in vivo* experiments. The first experiment looked at the tumour volume in six mice under treatment with different perturbations of the virus. The second experiment measured the viral decay in the blood over the first 60 minutes. The third experiment measured the spatial distribution of the viral genome on day 5.

Kim *et al.* (2011a) measured tumour volume changes under four different treatment protocols: one control treatment and three varying oncolytic adenoviruses. The control treatment was an injection of 100μL of phosphate buffered saline (PBS), and the three virus-based injections were an oncolytic adenovirus without any modification (Ad), a PEG-modified adenovirus (Ad-PEG) and a PEG-modified adenovirus conjugated with Herceptin (Ad-PEG-HER). Each treatment protocol was intravenously injected into different groups of six nude mice (mice with non-functioning immune systems) with pre-established tumours of size 100-120mm^3 that were made up of Her2/neu-expressing human breast cancer cells MDA-MB435 (Section 2.2.3.1). In each experiment 1×10^{10}, viral particles were injected intravenously on days $0, 2$ and 4. The tumour volume in each mouse was recorded every second day for 60 days from the first injection (Section 2.5.3).

Kim *et al.* (2011a) also conducted experiments to measure the viral genomes present over the first 60 minutes. The purpose of this experiment was to understand how rapidly viral particles decay after injection. Kim *et al.* injected 1×10^{10} viral particles of each Ad, Ad-PEG and Ad-PEG-HER into six BALB/c mice. The total viral genomes present in each mouse was recorded at $5, 10, 20, 30, 40$ and 60 minutes after first injection (Section 2.5.4).

Kim *et al.* also assessed the viral distribution 5 days post injection. Similar to the previous two experiments, mice with pre-established tumours of size 100-120mm^3 were injected intravenously with 1×10^{10} viral particles of Ad-PEG-HER on days $0, 2$ and 4. On day 5, the organs from each mouse were harvested and the number of viral genomes in each sample was assessed (Section 2.5.4).

6.2 OPTIMISATION OF TUMOUR GROWTH MEASUREMENTS UNDER TREATMENT WITH A PEG-MODIFIED ADENOVIRUS CONJUGATED WITH HERCEPTIN

Mathematical models have been used extensively to provide insight into oncolytic virotherapy (Section 3.2.3). In Chapter 5, a local stability analysis and bifurcation analysis was conducted for a model of the virus-tumour interaction, considering Gompertzian tumour growth and frequency-dependent virus infection (Eqs. (5.10)-(5.12)). As the tu-

mour growth measurements of Kim *et al.* (2011a) were conducted on nude mice, the model in Eqs. (5.10)-(5.12) can be used to understand the efficacy of the PEG-modified adenovirus conjugated with Herceptin in the absence of an immune response (such as the interferon-mediated antiviral immunity or antitumour immune responses). See the restated model equations below:

$$\frac{dU}{dt} = r\log\left(\frac{L}{U}\right)U - \frac{\beta UV}{U+I}, \tag{6.1}$$

$$\frac{dI}{dt} = \frac{\beta UV}{U+I} - d_I I, \tag{6.2}$$

$$\frac{dV}{dt} = u_v(t) - d_V V + \alpha d_I I, \tag{6.3}$$

$$u_V(t) = \begin{cases} V_0\delta(t-t_i), & t_i = 0,2,4, \\ 0, & \text{otherwise}, \end{cases} \tag{6.4}$$

where the uninfected tumour population is represented by U, signifying cells susceptible to infection, I is the infected cells and V is the virus particles. The injection function $u_V(t)$ has been included to account for V_0 virus particles injected intravenously on days 0, 2 and 4. Note that U and I represent numbers of cells, V represents the number of viral particles and t is time.

Any virus produced via replication within the tumour cells loses PEG modification and conjugation with Herceptin. A single average infectivity β (which also accounts for tumour cell discovery by the virus) and a single decay rate d_V are assigned for the combined populations of original and replicated viruses, noting that the population is dominated by naked (replicated) viruses over the majority of the time course of the experiments. Here the tumour volume is assumed to be proportional to the number of tumour cells, and the density is assumed to be 10^6cells/mm^3 (Wares *et al.*, 2015).

To obtain parameter estimates for the model, individual and simultaneous optimisations following the implementation detailed in Section 3.4 were performed on the tumour time-series data. Firstly, the model was optimised using the data of the tumour cell population for each individual mouse to obtain independent estimates of all parameters, see Fig. 6.2 and Table 6.1. To numerically simulate the model in Matlab, the model was implemented as an impulsive differential equation: at each injection time,

t_i, the ode solver was stopped, the virus population, V, was increased by V_0 and the simulation was iterated forward.

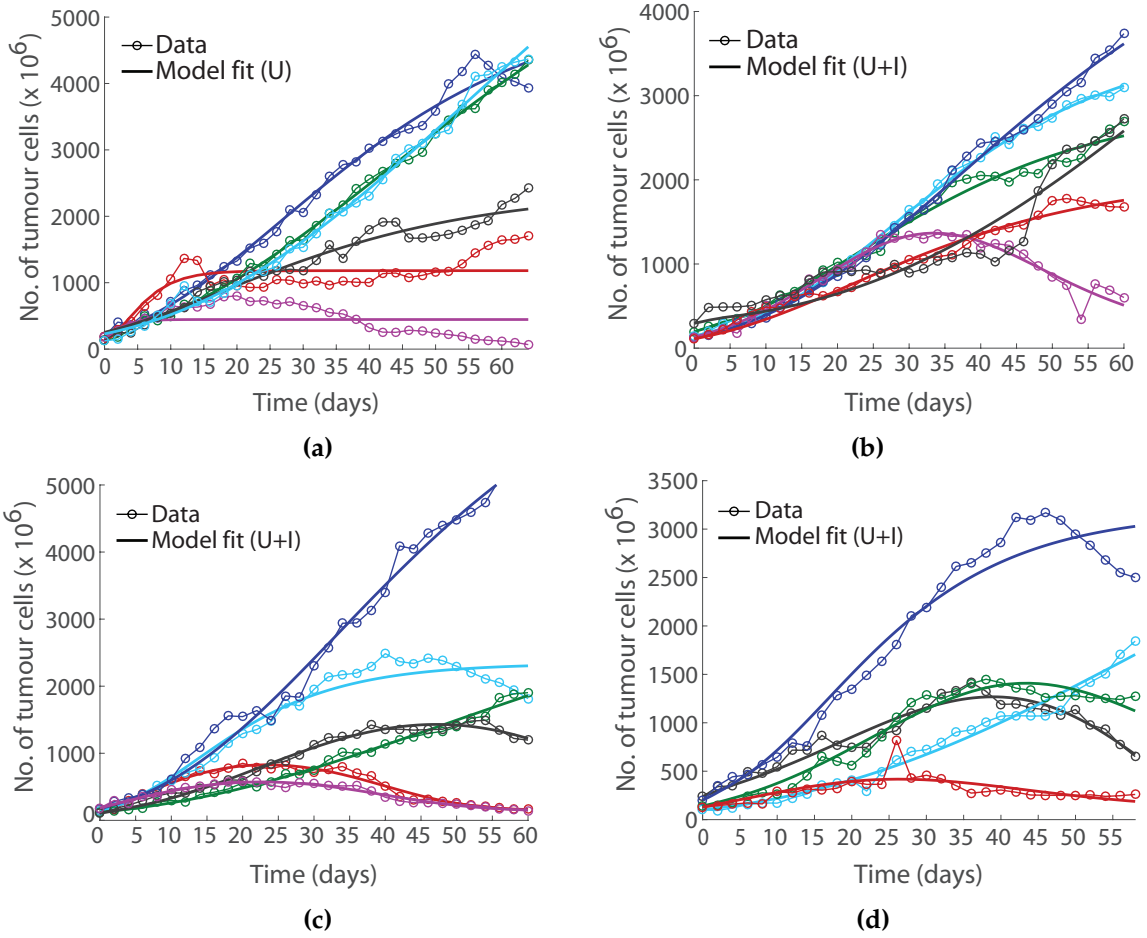

Figure 6.2: Tumour population over time for (a) PBS (Control), (b) Ad, (c) Ad-PEG and (d) Ad-PEG-HER treatments. The data for each mouse are shown with joined circles and the optimised model outputs for individual cases are shown as a thicker lines of the same colours. Note $V = I = 0$ for the control case. First published in Jenner *et al.* (2018b).

Initially, the V and I populations were zero. In the case of the PBS (control) experiment, there were no viral particles in the PBS injection and therefore no infected cells. For the viral experiments, $V_0 = 10^{10}$ particles. The number of new virus particles created through lysis (viral burst size) was fixed at 3500 as reported in Chen *et al.* (2001). When solving Eqs. (6.1)-(6.4) numerically, the denominator was replaced by $U + I + \epsilon$ for $\epsilon = 0.0001$ to avoid the singularity as $U + I \to 0$ (discussed in the previous chapter).

It is clear from Fig. 6.2 that there is quite a varied response to each treatment, reflected in the range of parameter values returned in the fit of each individual tumour

Table 6.1: Parameter values for the optimisation of the individual mouse data in Fig. 6.2. The colours used to plot the individual tumour measurements correspond to the parameter values given in the table below. Values have been rounded to two significant figures.

PBS								
Param.	Units	Description	Dark blue	Light blue	Green	Black	Red	Pink
L	cells$\times 10^6$	carrying capacity	5300	10000	7300	2400	1200	450
r	day^{-1}	growth rate	0.043	0.024	0.03	0.05	0.26	0.24
U_0	cells$\times 10^6$	initial tumour size	220	230	230	250	95	150

Ad								
Param.	Units	Description	Dark blue	Light blue	Green	Black	Red	Pink
α	virus$\times 10^9$	viral burst size	2	2	2.5	2	4	4
L	cells$\times 10^6$	carrying capacity	5600	3700	3000	10000	2100	10000
r	day^{-1}	growth rate	0.036	0.057	0.05	0.022	0.049	0.039
d_I	day^{-1}	burst rate	0.1	2	2	2	0.1	0.1
d_V	day^{-1}	viral decay rate	3.5	3.05	2.5	2.4	3.5	2
β	day^{-1}	infection rate	0.2	1.5	0.85	1.2	0.2	1.4

Ad-PEG								
Param.	Units	Description	Dark blue	Light blue	Green	Black	Red	Pink
α	virus$\times 10^9$	viral burst size	4	2	4	3.3	4	4
L	cells$\times 10^6$	carrying capacity	7500	2300	3900	3500	1200	830
r	day^{-1}	growth rate	0.042	0.09	0.28	0.055	0.12	0.1
d_I	day^{-1}	burst rate	0.24	2	0.15	2	0.86	0.48
d_V	day^{-1}	viral decay rate	2.1	1.8	2.1	1.9	1.4	1.4
β	day^{-1}	infection rate	0.58	0.8	0.6	0.63	0.43	0.47

Ad-PEG-HER							
Param.	Units	Description	Dark blue	Light blue	Green	Black	Red
α	virus$\times 10^9$	viral burst size	2.03	2	3.8	2	3.8
L	cells$\times 10^6$	carrying capacity	3200	5000	7900	8500	940
r	day^{-1}	growth rate	0.073	0.022	0.032	0.038	0.6
d_I	day^{-1}	burst rate	2	2	0.1	2	0.1
d_V	day^{-1}	viral decay rate	3.3	3.5	1.9	2.09	1.8
β	day^{-1}	infection rate	1.5	0.2	1.2	1.1	1.4

time-series measurement to the model, see Table 6.1. As such, it is not possible to use the optimised parameter values to the individual tumour time-series measurement to predict the characteristics of treatment, instead the averaged response needs to be used.

Table 6.2: Common and experiment-specific parameters for the simultaneous optimisation in Fig. 6.3.

	Experiment			
Parameter	PBS	Ad	Ad-PEG	Ad-PEG-HER
Tumour growth rate	r			
Tumour carrying capacity	L			
Tumour cell burst rate	-	d_I		
Viral decay rate	-	d_V		
Initial tumour size	$U_{0\ PBS}$	$U_{0\ Ad}$	$U_{0\ Ad-PEG}$	$U_{0\ Ad-PEG-HER}$
Infection rate	-	$\beta_{\ Ad}$	$\beta_{\ Ad-PEG}$	$\beta_{\ Ad-PEG-HER}$

In future work, it may be worth investigating the variability in individual response using a random effects model, where parameters are random variables.

To quantify the average response to the treatment protocol, the model parameters were then optimised using all the experimental data simultaneously for both common parameters and those specific to that experiment, see Table 6.2. The tumour growth dynamics, governed by parameters r and L, were considered to be common across all experiments. Similarly the parameters relating to cell lysis rate, d_I, and viral decay, d_V, were considered to be common to all viral experiments. The infectivities and initial tumour sizes were taken to be protocol specific. The different levels of modification in the virus were hypothesised to result in different infectivity rates; therefore, this value must be free to vary between experiments. Overall, 11 parameters were optimised using 750 data points across four protocols of five or six data sets each. The fit equally weighted each of the experimental data sets, accounting for any differences in the number of data time points between sets (for example, the PBS experiment had 198 data points and the Ad experiment had 186 data points, but each set was taken to have equal weight in the optimisation, see Section 3.4).

The four data sets (PBS, Ad, Ad-PEG and Ad-PEG-HER) were used simultaneously to optimise the model parameters. The model output is shown overlaid with the experimental data in Fig. 6.3. The parameter values and fit characteristics of the simultaneous optimisation are shown in Table 6.4. The parameter values obtained from both the individual and the simultaneous optimisations are shown in Fig. 6.4. Some of the simultaneous fit parameters lie within the distribution of the estimates obtained in the individual optimisations.

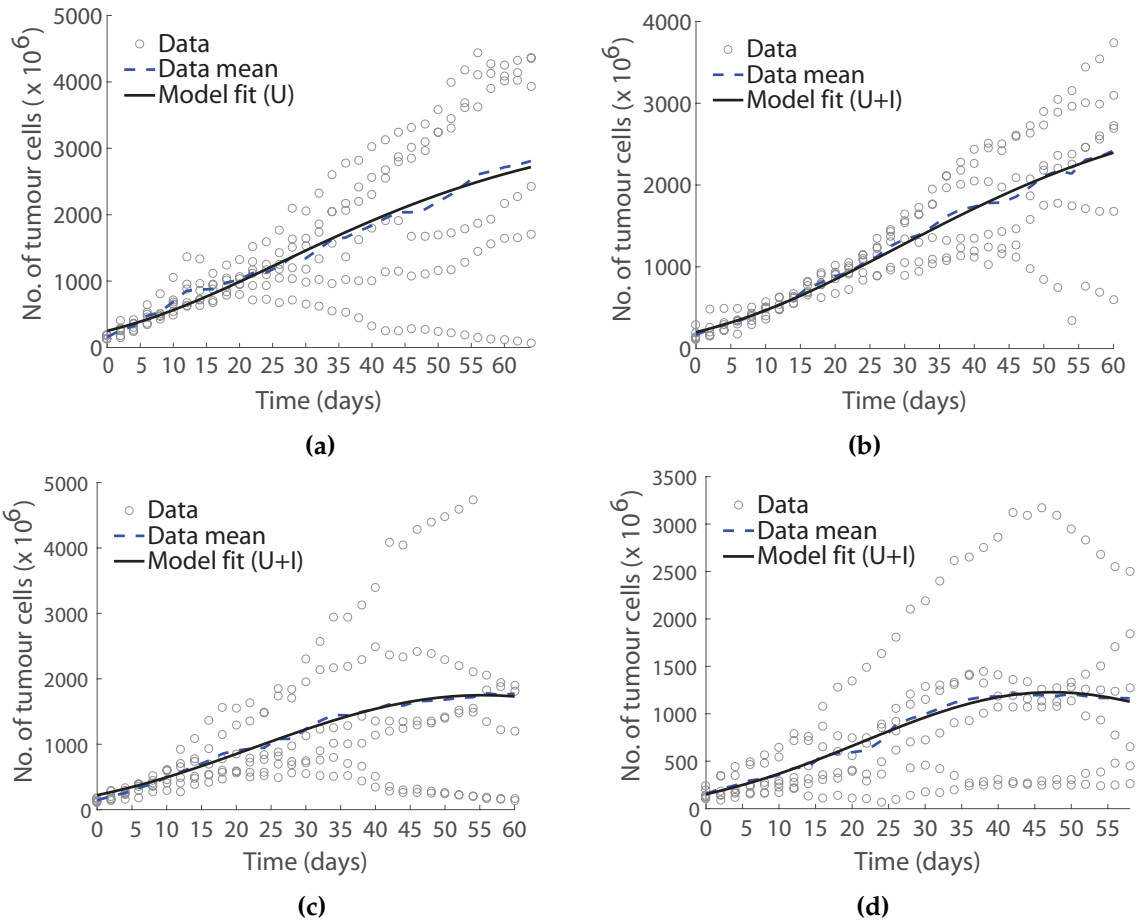

Figure 6.3: Tumour populations over time for (a) Control, (b) Ad, (c) Ad-PEG and (d) Ad-PEG-HER. The experimental data are plotted as circles (grey), and the trajectories for the simultaneous optimisation to all data points are shown as solid lines. The means of the data are shown as dashed lines. Note $I = 0$ for the control case. First published in Jenner *et al.* (2018b).

As evident in Fig. 6.2 and 6.3, the simple mathematical model in Eqs. (6.1)-(6.4), describes the interaction between an oncolytic virus and tumour cells. The model is able to identify the primary processes and capture observed experimental results. When fit to the data for individual cases it can be seen that the model easily replicates a wide range of treatment responses. The ability of the model to reproduce the data closely is measured by the R-squared and Pearson's r Correlation coefficient Table 6.4. From this, the model is a reliable representation for the interaction between an oncolytic virus and tumour cells.

For parameters held in common across experiments, all data points constrained the values. However, in the case of experiment-specific parameters such as the infectivity rate, β, which took different values for different experiments, fewer data points

constrained the values. Thus for some experiment-specific parameters the simultaneous estimates were dissimilar to those from the individual optimisations (Fig. 6.4). Although each data set was weighted equally, the constraints on the common parameters resulted in different optimal values.

6.2.1 *Simulating perturbations in tumour and virus characteristics*

To determine if the outcome of Ad-PEG-HER treatment was dependent on the tumour characteristics, the tumour population over time was simulated with separate perturbations to the growth rate r and initial tumour size U_0, keeping the other parameters constant, see Fig. 6.5. Perturbations in viral characteristics are also thought to alter the treatment outcome. To examine the effect of changes in the viral infectivity on the tumour population, perturbations in β are shown in Fig. 6.5(c).

It is clear that there is a relationship between a successful treatment outcome and the aggressive nature of the tumour. Treatment efficacy is highly dependent upon the initial tumour size and proliferation rate. The simulations suggest that the slower the tumour cells are proliferating, the higher the likelihood of the viral treatment reducing the tumour to a manageable size. For aggressive tumours, there is an initial plateauing of the tumour cell population, showing the treatment taking effect; however, this is followed by an increase in tumour size. Increasing virulence of the virus by increasing viral infectivity is also shown to reduce the tumour size significantly.

6.2.2 *Simulating the effects of different treatment dosage protocols*

In Section 5.2.3, a general investigation into the effect of changes to the dosage protocols for the model was undertaken. Perturbations in dosage amounts were shown to result in significantly different long-term outcomes in the region of bistability, see Fig. 5.22, and also influence the maximum and minimum tumour sizes in regimes of stable limit cycles, see Fig. 5.21. The equivalent non-dimensional form of the variables

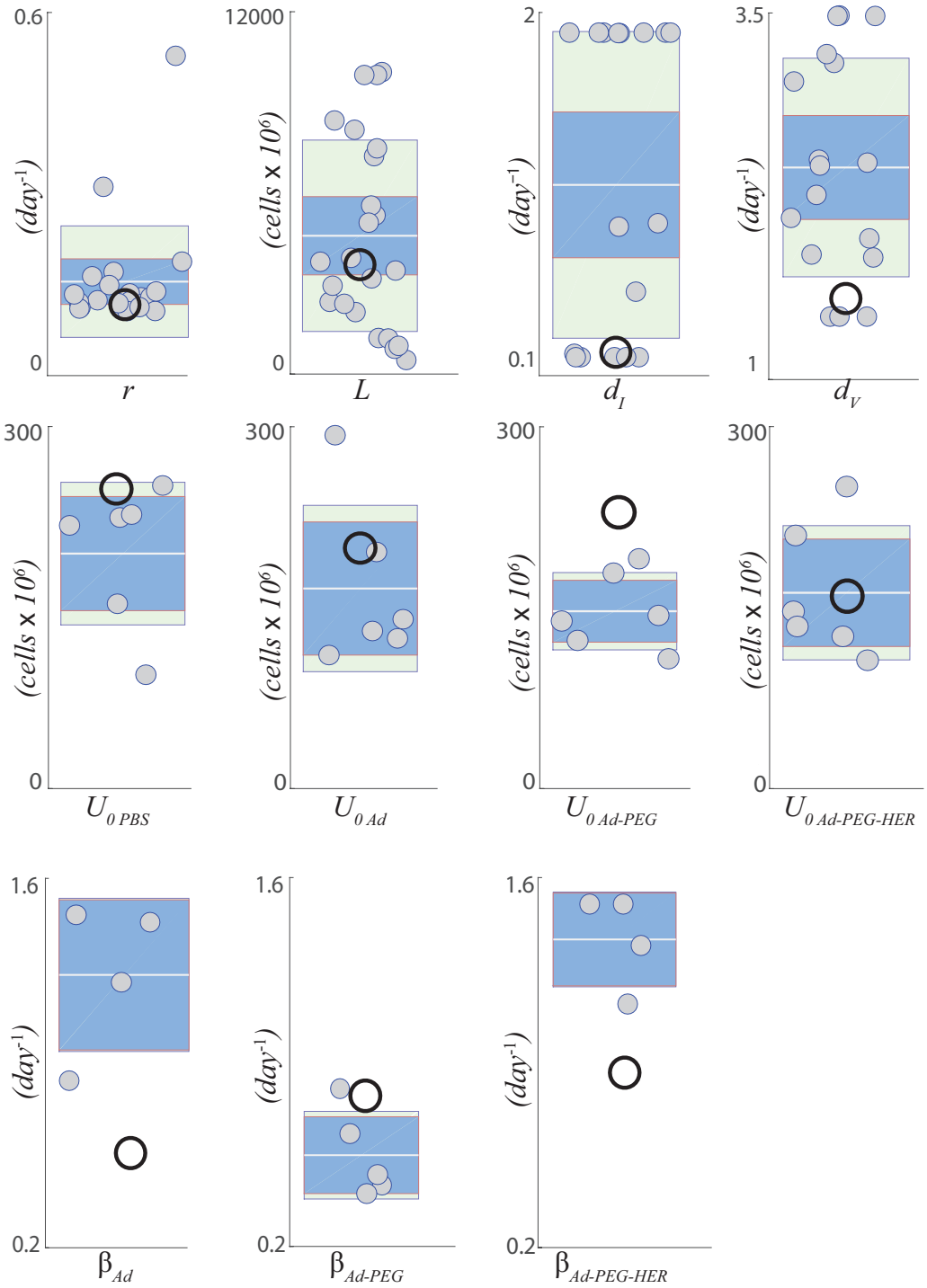

Figure 6.4: Parameter estimates from the individual and simultaneous optimisations to the data. The small (grey) circles correspond to the estimates of the parameters for each mouse. The large open circles correspond to parameter estimates from the simultaneous optimisation. The infectivity of the virus, β, and the initial tumour size, U_0, were experiment specific. The central white lines are the means of the data, the blue boxes indicate the 95% confidence intervals and the green boxes indicate one standard deviation from the means. Note that there were fewer data points constraining the experiment-specific parameters. First published in Jenner *et al.* (2018b).

Table 6.3: Parameter values for the simultaneous optimisation of the model with all data, shown in Fig. 6.3.

Parameter	Units	Description	PBS	Ad	Ad-PEG	Ad-PEG-HER	95% Confidence Interval
α	virus$\times 10^9$	viral burst size	-	3500	3500	3500	-
L	cells$\times 10^6$	carrying capacity	3490	3490	3490	3490	(2230, 4750)
r	day^{-1}	growth rate	0.037	0.037	0.037	0.037	(0.018, 0.056)
d_I	day^{-1}	burst rate	-	0.1	0.1	0.1	(-2, 2)
d_V	day^{-1}	viral decay rate	-	1.38	1.38	1.38	(-52, 55)
U_{0PBS}	cells$\times 10^6$	initial tumour size	251	-	-	-	(139, 453)
U_{0Ad}	cells$\times 10^6$	initial tumour size	-	200	-	-	(63, 337)
$U_{0Ad-PEG}$	cells$\times 10^6$	initial tumour size	-	-	223	-	(69, 378)
$U_{0Ad-PEG-HER}$	cells$\times 10^6$	initial tumour size	-	-	-	153	(37, 269)
β_{Ad}	day^{-1}	infection rate	-	0.562	-	-	(-16, 17)
β_{Ad-PEG}	day^{-1}	infection rate	-	-	0.771	-	(-19, 21)
$\beta_{Ad-PEG-HER}$	day^{-1}	infection rate	-	-	-	0.862	(-20, 22)

Table 6.4: Fit statistics for the simultaneous optimisation of the model with all data, shown in Fig. 6.3.

Goodness of fit statistics	Value
R-squared	0.4286
Pearson's r correlation coefficient	0.6547

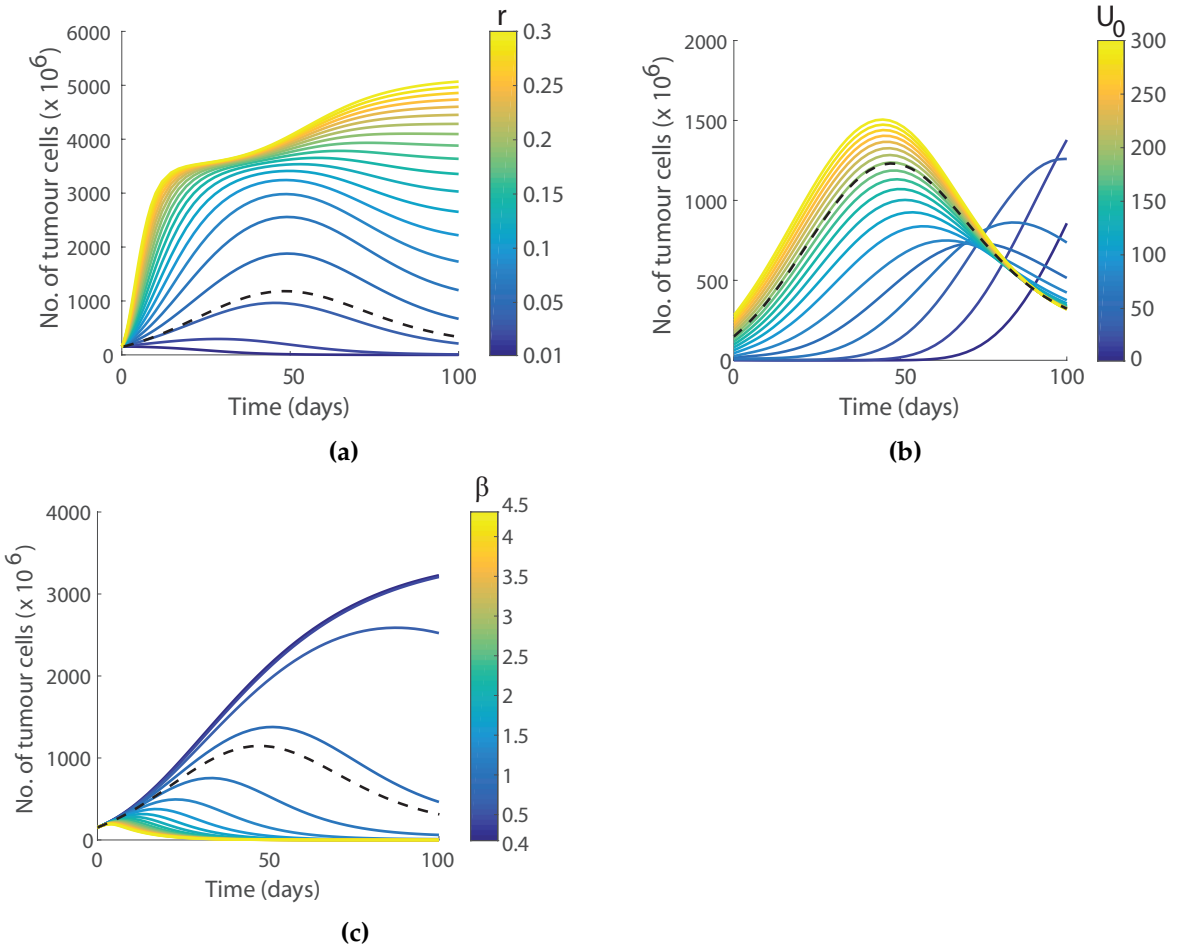

Figure 6.5: Tumour population over time predicted by the simultaneously optimised model for various (a) growth rates r between 0.001 and 0.3 (day^{-1}), (b) initial tumour populations U_0 between 1 and 300 (cells $\times 10^6$) and (c) infectivity rates β between 0.4 and 4.5 (day^{-1}). The colourmap bar matches the corresponding parameter value. All other parameters for each set were given by Table 6.4 for common and Ad-PEG-HER experiment-specific values. The dashed line represents the model solutions for unperturbed Ad-PEG-HER parameters in Table 6.4. Note the plots have different vertical scales. First published in Jenner *et al.* (2018b).

for the Ad-PEG-HER virus are $m = 0.0429$, $\gamma = 1.6009$ and $\xi = 0.1160$, (see Eqs. (5.13)-(5.15)), which according to the two-parameter bifurcation plot in Fig. 5.20, is not in a region close to a Hopf bifurcation. As such, for the Ad-PEG-HER parameter set, limit cycles or bistability will not emerge.

While the interesting dynamics in Section 5.2.3 will not be seen for the Ad-PEG-HER virus, it is still worth investigating the sensitivity of the model to alterations in the application profile $u_V(t)$ for this virus. Using the generic dosage schedule previously defined in Eq. (5.20) the effect on the tumour cell population was simulated from day

0 to 100 under different total dosages and application profiles $u_V(t)$. The model was simulated using the parameters simultaneously optimised for the Ad-PEG-HER virus, Table 6.4, with the dose, V_{T0}, between 0 and 1500, the number of injections, n, between 0 and 6 and the period between injections, ϕ, between 0 and 10 days.

One major concern in viral treatments is the toxicity caused through the accumulation of the virus in the system. To examine this, the maximum virus level reached at any time between day 0 to 60 for each application profile was determined, Fig. 6.6(a). To quantify the effects of differing application profiles on treatment outcome, the changes in eradication half-time were measured. The eradication half-time is defined as the time taken for the tumour to decrease to and remain smaller than half its initial size. The minimum viral dose required for a finite eradication half-time was determined for each application profile, Fig. 6.6(b). From Fig. 6.6(b), it would seem that the best strategy for fast tumour eradication is a single high dose injection.

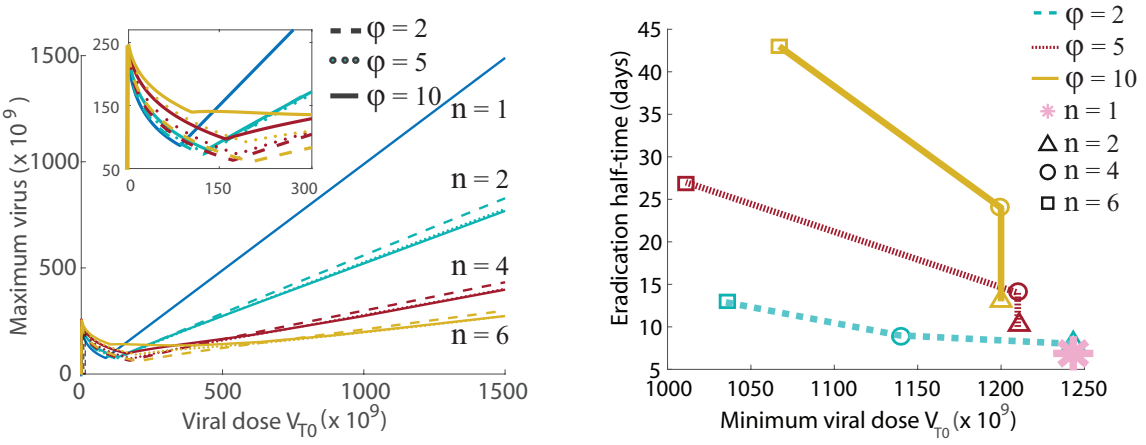

(a) (b)

Figure 6.6: Effect of treatment profile. (a) Maximum viral population as a function of the total viral dose, V_{T0}, for each application profile with inset detail at low doses. (b) Eradication half-time as a function of the minimum total viral dose, V_{T0}, required. Seven different application protocols were simulated for the simultaneous optimised model for Ad-PEG-HER, Table 6.4 for the indicated number of injections, n, and days between injections, ϕ. First published in Jenner *et al.* (2018b).

6.3 COMPARTMENTALISATION OF THE VIRAL POPULATION TO OPTIMISE VIRAL GENOME CLEARANCE AND SPATIAL DISTRIBUTION MEASUREMENTS

To use the viral genome clearance measurements and spatial distribution data from Kim *et al.* (2011a) described in Section 6.1, the virus population V is now compartmentalised to virus in the blood, organs and tumour site. In the previous model, Eqs. (6.1)-(6.4), the viral decay was modelled using the approximation $dV/dt = -d_V V$. To capture data for the clearance of the virus from the blood, the interaction and transfer of virus between the blood, organs and tumour must be modelled explicitly. The timescales of the two viral genome experiments are significantly different and this is considered when extending the model to compartmentalise the virus populations.

6.3.1 *Viral genome clearance from the blood*

The viral genome clearance data measured the viral number in the blood over 60 minutes post injection. In this time, the liver quickly removes the bulk of the virus particles circulating in the blood (Ganesan *et al.*, 2011). Liver sinusoidal endothelial cells (LSECs) are the most efficient endocytotic cell population of the body; they scavenge molecules from the bloodstream and possess potent immune functions (Knolle and Wohlleber, 2016). Ganesan *et al.* (2011) showed in their experiments with an adenovirus, that nearly all virus was cleared by LSECs. Ganesan *et al.* (2011) suggested that LSECs take up and destroy the majority of an injected virus, doing so quickly (minutes) and extensively (>90%), leaving only a small fraction of circulating virus to infect the body. Ganesan *et al.* (2011) notes that virus in the bloodstream undergoes rapid biexponential clearance.

A minimal model for the clearance of viral particles in the blood V_B by LSECs L_C is given by

$$\frac{dV_B}{dt} = -d_L L_C - d_B V_B - \tau_O V_B, \tag{6.5}$$

$$\frac{dL_C}{dt} = \alpha_L V_B, \tag{6.6}$$

where t is time. Viral particles are cleared by LSECs at a rate d_L proportional to the number of LSECs. Virus is also cleared from the blood by other factors (e.g. complement immune system) at a rate d_B. Additionally, viral particles leave the blood and travel to the organs at a rate τ_O. Initially there is a population L_0 of LSECs, and more LSECs are stimulated and recruited by the presence of virus in the blood at a rate a_L. See the schematic in Fig. 6.8.

Since d_B and τ_O can be combined, these viral decay terms can represented by a single parameter $d_B + \tau_O = \omega$. Solving the system in Eqs. (6.5)-(6.6) gives a biexponential expression for $V_B(t)$:

$$V_B(t) = Ae^{k_1 t} + (V_0 - A)e^{k_2 t}, \quad \text{for} \quad k_{1,2} = \frac{-\omega \pm \sqrt{\omega^2 - 4d_L a_L}}{2}, \tag{6.7}$$

where the initial condition $V_B(0) = V_0$ has been used to eliminate one constant of integration. Fitting Eq. (6.7) to the viral genome measurements in the blood by Kim *et al.* (2011a) gives the resulting curve in Fig. 6.7 and values in Table 6.5. It is clear from Fig. 6.7, that the dynamics of the Ad-PEG virus are significantly different to those of

Table 6.5: Parameter values for the simultaneous optimisation of the model with all data.

Parameter	Units	Ad	Ad-PEG	Ad-PEG-HER
A	virus	2.013×10^8	7.775×10^6	3.155×10^7
k_1	day^{-1}	-0.8563	-0.02412	-0.2923
k_2	day^{-1}	-0.0001	-4.149	-0.003715
V_0	virus	11×10^2	10^{22}	10^{12}

the Ad and Ad-PEG-HER viruses. As such, it is not possible to assume that this model is able to capture the dynamics of the Ad-PEG data. The underlying mechanisms of viral clearance for the Ad-PEG virus are unexpected and future work will investigate this in further detail.

To use these results in the second viral genome experiment by Kim *et al.* (2011a), the quasi-steady-state dynamics for Eq. (6.7) needs to be considered as the time scale of the second experiment was on the order of days. As t increases, one term will dominate the

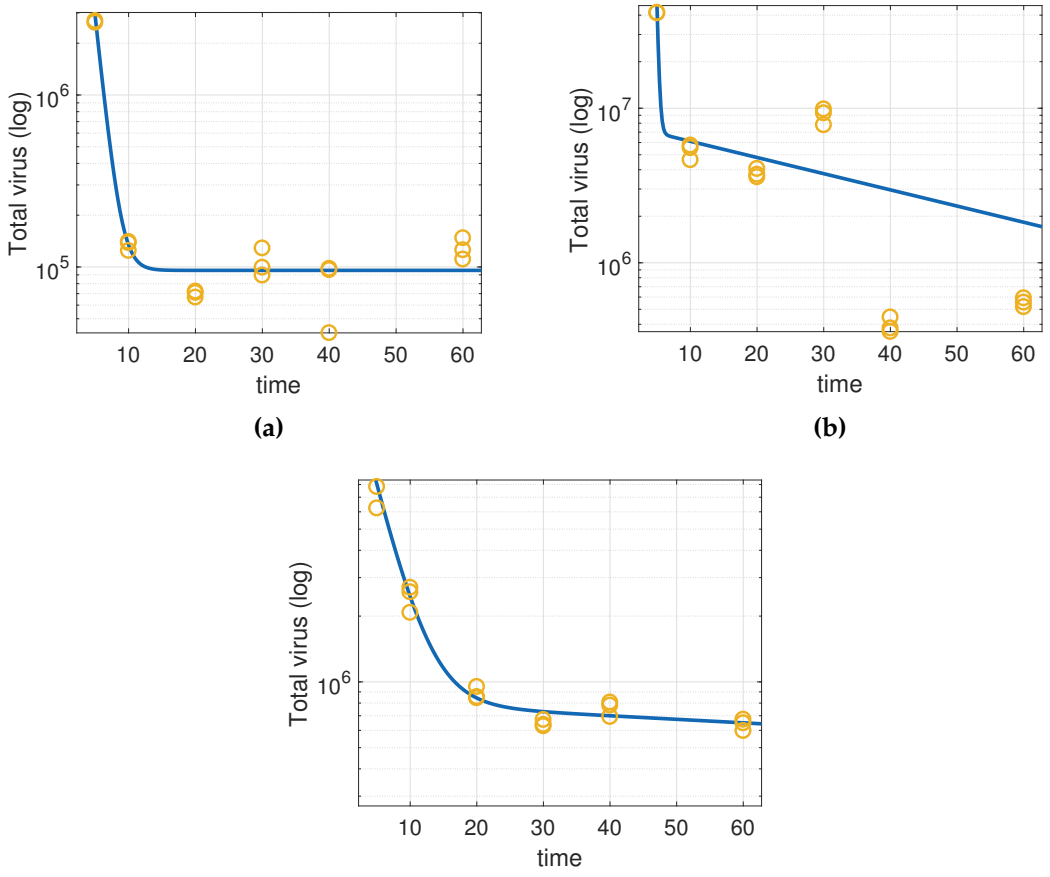

Figure 6.7: The results of fitting biexponential decay to the viral time-series data from Kim *et al.* (2011a). Fig.6.7a is for the fit to the Ad data, Fig.6.7b is for the fit to the PEG data and Fig.6.7c is for the fit to the HER data. The solid line (blue) represents the fit, and the data is plotted as circle (yellow).

expression for $V_B(t)$. For $k_1 >> k_2$, this means that $Ae^{k_1 t} \to 0$ faster than $(V_0 - A)e^{k_2 t}$, and therefore the quasi-steady-state form of this equation is

$$V_B(t) = A_2 e^{k_2 t} = (V_0 - A)e^{-k_2 t}$$

with the rate of change for $V_B(t)$ approximated by

$$\frac{dV_B}{dt} = k_2(V_0 - A)e^{k_2 t} = k_2 V_B \tag{6.8}$$

with initial condition now $V_B(0) = V_0 - A$. Since the units of the decay rate is minutes, this is re-scaled into days to obtain the parameter for the decay from the blood for the second viral genome experiment, i.e. $d_B + \tau_O = k_2 \times 60 \times 24$. Note that variations on

the model in Eqs. (6.5)-(6.6) were examined; however, since the viral genome in the blood was measured on a much faster time scale then the other experiments, further complexity was not needed.

6.3.2 *Spatial distribution of virus*

In the second set of virus-based experiments, Kim *et al.* (2011a) measured the viral genome number in the organs and tumour site. In this experiment, the viral genome distribution was measured on day 5. The model in the previous section considered the viral clearance in the first 60 minutes in the absence of both the immune response and tumour cells. To model the spatial distribution of viral genome on day 5, the quasi-steady-state approximation in Eq. (6.8) is combined with the model used to optimise the tumour time-series measurements, Eqs. (6.1)-(6.4). See the below system of equations:

$$\frac{dV_B}{dt} = u_V(t) - d_B V_B - \tau_O V_B - \tau_T V_B T, \tag{6.9}$$

$$\frac{dV_O}{dt} = \tau_O V_B - d_V V_O, \tag{6.10}$$

$$\frac{dV_T}{dt} = \tau_T V_B (S + I) - d_V V_T + \alpha d_I I \tag{6.11}$$

$$\frac{dU}{dt} = r \log\left(\frac{L}{U}\right) U - \frac{\beta U V_T}{U + I}, \tag{6.12}$$

$$\frac{dI}{dt} = \frac{\beta U V_T}{U + I} - d_I I, \tag{6.13}$$

$$u_V(t) = (V_0 - A)(\delta(t) + \delta(t-2) + \delta(t-4)), \tag{6.14}$$

where V_O is the virus population in the organs and V_T is the virus population at the tumour site. The virus in the blood is cleared by the immune system at a rate $d_B V_B$ proportional to the amount circulating. Virus in the blood travels to other organs at a rate $\tau_O V_B$ proportional to the amount of virus in the blood. The population of the virus in the regions other than the blood or tumour arrives at a rate $\tau_O V_B$ proportional to the amount in the blood, and decays at a rate $d_V V_O$ proportional to the amount in the other location. The virus from the blood then arrives at the tumour site at a

rate $d_T V_B(U+I)$ proportional to the amount in the blood and the total population of tumour cells, accounting the effects of Herceptin. See the schematic in Fig. 6.8.

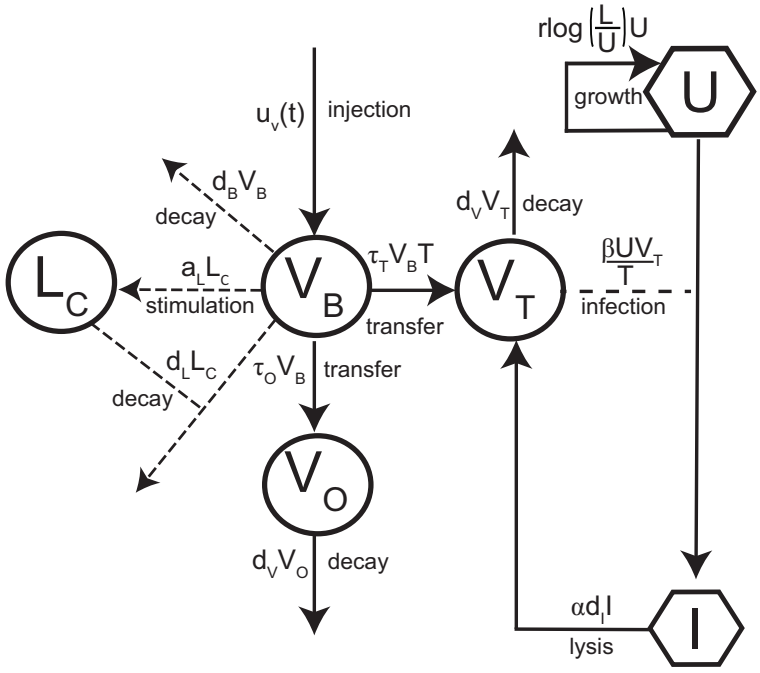

Figure 6.8: Diagram of the interaction between a population of uninfected tumour cells U, infected tumour cells I and an intravenously injected oncolytic virus in the blood V_B, organs V_O and tumour site V_T, see Eqs. (6.9)-(6.14). The variable T represents the total tumour population $U+I$. The dashed lines represent the fast dynamics of the system which is due to clearance from LSECs L. These are approximated by simple exponential decay.

To optimise the measurement of viral genome in the organs and tumour on day 5, the parameter values of r, K, α, d_I, U_0 and d_V were fixed to those obtained from fitting to the tumour time-series data, see Table 6.4. Since the virus used in these experiments is the Ad-PEG-HER virus, the value of β was fixed to be the value for the Ad-PEG-HER virus. Using the results of the previous fit to the viral time-series data (Section 6.3.1), τ_O was fixed to be: $\tau_O = k_2 - d_B$, where k_2 has been re-scaled to units of day^{-1} as opposed to min^{-1}. Fitting the viral genome in the organs and tumour on day 5 to the model, while allowing d_B and τ_T to vary, gives the fit in Fig. 6.9 and parameter values in Table 6.6. The optimisation algorithm followed the numerical implementation in Section 3.4.

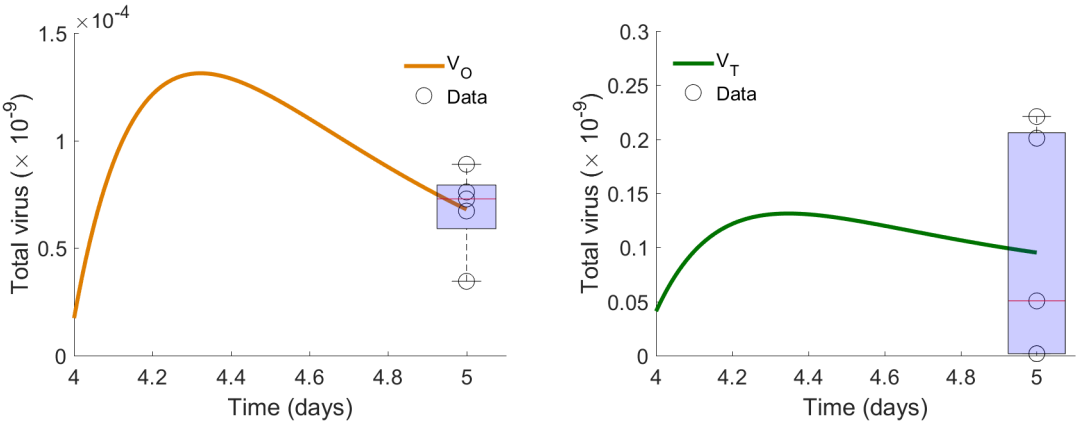

Figure 6.9: Optimisation of the model in Eqs. (6.9)-(6.14) to the virus genome accumulation data for the organs and tumour from Kim *et al.* (2011a). The total model's predicted virus count (a) in the organs, V_O, is plotted as a solid line (orange) and (b) at the tumour, V_T, is plotted as a solid line (dark green). The experimental data from Kim *et al.* is plotted in the form of a box plot (purple) with the data represented as circles (black).

Table 6.6: Parameter values for the optimisation of the viral genome in the organs and tumour on day 5, see Fig. 6.9.

Parameter	Units	Description	Value	95% Conf. Inf
d_B	day^{-1}	Decay rate from the blood	5.3495	(5.3483, 5.3507)
τ_T	day^{-1}	Transfer to the tumour site	3.3×10^{-4}	(0.0001,0.0006)

As the confidence intervals were tight on these parameters and visual inspection of the fit shows the model's predicted viral counts sit well within the range of experimental results, it is possible to conclude that these parameter values provide a good model approximation to the data.

6.4 THE EFFECTS OF THE ANTIVIRAL AND ANTITUMOUR IMMUNE RESPONSES

To establish infections *in vivo* viruses must compete against powerful immune defence mechanisms. The immune system is developed to respond to the presence of viral particles in the body and clear any virus-infected cells (see Section 2.3). The previous experiments by Kim *et al.* (2011a) considered only nude mice (mice without a functioning immune system) and the immune response was neglected. It is worth considered

how the system would behave in the presence of interferon-mediated antiviral cell immunity and the antitumour immune response.

6.4.1 *Interferon-mediated cell antiviral immunity*

Infection of a cell by a virus triggers the production of antiviral factors that induce an antiviral state in neighbouring cells (Hertzog, 2012; Shiroki and Toth, 1988). The main antiviral factor is the cytokine interferon (IFN), which is a known preventer of intracellular viral replication (Barber, 2001; Goodbourn *et al.*, 2000). IFN stimulates an antiviral state in target cells, whereby, once these cells are infected, the replication of the virus is blocked due to synthesis of a number of enzymes that interfere with the replication processes (Goodbourn *et al.*, 2000). Infection of cells in an antiviral state causes the induction and secretion of more interferons that alert nearby cells and activate the immune system, (Levy *et al.*, 2001). It has been hypothesised that antiviral factors play a crucial role in the outcome of treatment of tumour cells with an oncolytic virus (Wodarz *et al.*, 2012), and the work in this section looks to investigate this further.

6.4.2 *Antitumour immune response*

In recent years the interplay of the immune system with cancer therapies has become a topic of increasing interest. As an oncolytic virus replicates only within tumour cells, the localised viral infection recruits the immune response to the tumour site. Once there, the immune cells kill virus-infected cells through inducing apoptosis (Section 2.3). Immune cells also have the ability to kill tumour cells, even if they aren't infected by a virus. Studies have shown that the release of tumour antigen into the microenvironment, through lysis of tumour cells, stimulates the immune cells and instigates killing of uninfected tumour cells (Section 2.3). In this thesis, the ability of immune cells to kill uninfected tumour cells is referred to as the antitumour immune response.

6.4.3 *Model extension*

There are currently many virus-tumour-immune mathematical models in the literature (Section 3.2.4). However, none have accounted for the combined effects of interferon-mediated antiviral immunity, the antitumour immune response and the intravenous injection of an oncolytic virus. Kim *et al.* (2011a)'s tumour time-series experiment (Section 6.2) and two viral genome experiments (Section 6.3) considered the response to an oncolytic adenovirus in nude mice. Therefore, in these experiments the function of the antiviral immunity and the antitumour immune response were negligible. In reality, the antitumour and antiviral immune responses can play a major role in the outcome of therapy.

The model in the previous section is now extended to include the effects of the antiviral cell immunity and antitumour immune response, giving the below system of equations:

$$\frac{dV_B}{dt} = u_V(t) - d_B V_B - \tau_O V_B - \tau_T V_B T, \tag{6.15}$$

$$\frac{dV_O}{dt} = \tau_O V_B - d_V V_O, \tag{6.16}$$

$$\frac{dV_T}{dt} = \tau_T T V_B - d_V V_T + \alpha d_I I, \tag{6.17}$$

$$\frac{dU}{dt} = r \log\left(\frac{L}{U}\right) U - \frac{\beta U V_T}{T} - \frac{\gamma U (I + R_I)}{T} + \tau_R R_S - \frac{\kappa U K}{T}, \tag{6.18}$$

$$\frac{dI}{dt} = \frac{\beta U V_T}{T} - d_I I - \frac{\kappa I K}{T}, \tag{6.19}$$

$$\frac{dR_S}{dt} = \frac{\gamma U (I + R_I)}{T} - \frac{\beta_R R_S V_T}{T} - \tau_R R_S, \tag{6.20}$$

$$\frac{dR_I}{dt} = \frac{\beta_R R_S V_T}{T} - d_{RI} R_I, \tag{6.21}$$

$$\frac{dK}{dt} = s_K (I + R_I) - d_K K, \tag{6.22}$$

$$T = U + I + R_S + R_I, \tag{6.23}$$

where R_S is the uninfected cells in an interferon-mediated antiviral state, R_I is the infected tumour cells in an interferon-mediated antiviral state and K is the killer immune cell population. Cells in an antiviral (or refractory) state are those that have been temporarily removed from the uninfected population due to signalling by antiviral factors.

A single state variable has been chosen to account for the complex antitumour immune response. In Chapter 7, the antitumour immune response is considered in more detail, but for the analysis to follow this assumption is sufficient.

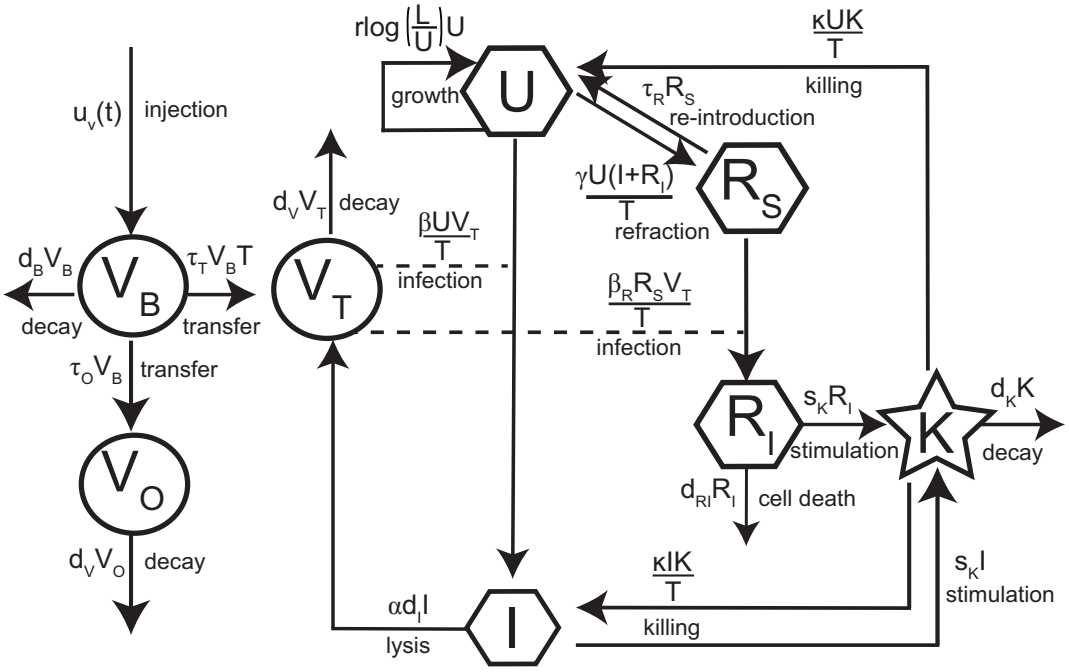

Figure 6.10: Compartmental diagram of the interaction between a population of uninfected tumour cells U, infected tumour cells I, and an intravenously injected oncolytic virus in the blood V_B, organs V_O and the tumour site V_T. Tumour cells may join the uninfected refractory population R_S or the infected refractory population R_I through interferon-mediation. Killer immune cells K are able to remove tumour cells through the antitumour immune response. See Eqs. (6.15)-(6.23) for the full model. First published in Jenner *et al.* (2016).

The new interactions in the model are detailed as follows. Uninfected cells join the refractory population due to antiviral factors released by the infected tumour cells at a rate γ proportional to the frequency of the interferon-producing populations, I and R_I. Cells in the refractory state can be infected by the virus to become infected refractory cells, R_I, at a rate β_R. Cells leave the refractory population to re-join the uninfected population at a slow rate τ_R, where $\tau_R << \gamma$. Apoptosis, or programmed cell death occurs due to infection at rate d_{RI}. It is assumed the immune cells are stimulated proportionally by the infected tumour populations, I and R_I, at rate s_K. This stimulation is due to antigen presentation and the secretion of antiviral factors. Immune cells die at a rate d_K. The uninfected and infected cells are killed by the immune system at a frequency-dependent rate κ. See Fig. 6.10 for a summary of model interactions.

For the most part, the parameters in the model can be approximated based on literature and the previous optimisations in Sections 6.2 and 6.3. The decay rate of the killer cell population was approximated by the decay rate of T cells which have a half-life of 48 hours giving $d_K = 0.35(\text{day}^{-1})$ (De Boer *et al.*, 2001). Killer immune cells are stimulated by the infected tumour cells, I and R_I, through antigen presentation and the secretion of antiviral factors. This stimulation takes 1 day, so $s_K = 1(\text{day}^{-1})$ (van Stipdonk *et al.*, 2001; Veiga-Fernandes *et al.*, 2000). For the killing rate parameter κ, de Pillis *et al.* (2005) estimated a maximum fractional kill rate of 1.43 (day^{-1}), which we approximate with $\kappa = 2(\text{day}^{-1})$. All of these parameter values can be found in Table 6.7.

Table 6.7: Parameter values for Eqs. (6.15)-(6.23). Note the reference to other parameters that may be found in Table 6.4

Parameter	Units	Description	Value
d_B	day^{-1}	decay rate of virus in the blood	5.3495
τ_O	day^{-1}	transfer rate of virus from blood to organs	0.0001
τ_T	day^{-1}	transfer rate of virus from blood to tumour	3.3×10^{-4}
γ	day^{-1}	antiviral stimulation rate of tumour cells	$\beta/50$
τ_R	day^{-1}	re-introduction rate	10^{-4}
κ	day^{-1}	killing rate	2
β_R	day^{-1}	infection rate of antiviral tumour cells	β
d_{RI}	day^{-1}	infected antiviral cell burst rate	d_I
s_K	day^{-1}	stimulation rate of immune cells	1
d_K	day^{-1}	decay rate of immune cells	0.35

Unfortunately, it is difficult to find approximations for the rate γ of removal of uninfected cells into the refractory state and the rate τ_R these cells re-join the uninfected population. For now, it is assumed that γ is $1/50$th the rate of the viral infection, i.e. $\gamma = \beta/50$. In addition, the rate at which the refractory cells rejoin the uninfected population is assumed to be slow, so we set $\tau_R = 10^{-4}$.

Whilst refractory cells have increased viral defences, it is assumed that the infection rate of refractory cells is equivalent to the infection rate of uninfected cells, i.e., $\beta_R = \beta$. Similarly, the rate of programmed cell death due to viral infection is equivalent to the rate of lysis, i.e., $d_{RI} = d_I$.

6.4.4 *Influence of the antiviral and antitumour immune responses*

To quantify the importance of the antiviral and antitumour immune responses, a parameter sensitivity analysis was conducted for Eqs. (6.15)-(6.23), see Fig. 6.11. To gain a thorough understanding of what underlying interactions were most affected by small perturbations, two sensitivity measures were chosen. The first metric was a measurement of how the total number of tumour cells from day 0 to 100 changed with perturbations in each parameter value in Table 6.7. The second measure monitored whether or not the tumour volume had decreased below 10^{-1}, which was deemed as tumour death. The parameter sensitivity analysis can be used to discuss the sensitivity of the unknown parameters β_R and γ. The sensitivity of the parameter τ_R has not been plotted as the relative tumour volume only changed 10^{-1} fold, which can be considered negligible. Instead, the viral-infectivity rate β has been included.

Parameters relating to the antiviral immune response are apparently insensitive in comparison to parameters relating to the antitumour immune response. This could be due to the approximation for these parameters being in a regime where the antiviral response is insignificant. Overall, the sensitivity analysis shows that heterogeneity in the antiviral immune response has a lesser effect on overall treatment outcome in comparison to heterogeneity in the antitumour immune response.

Fig. 6.11(f) shows that perturbations in d_B lead to the lowest total tumour population compared to all other parameter perturbations. This suggests that a reduction in the rate of decay of viral particles in the blood would lower the tumour growth substantially. However, whilst producing a low total tumour population over time, the tumour is not eradicated within the time interval.

6.4.5 *Perturbations in the initial tumour size* U_0.

To investigate the effect of the initial tumour size U_0 on overall treatment efficacy, numerical solutions to Eqs. (6.15)-(6.23) are plotted for initial tumour sizes ($\times 10^6$) ranging from 1 to 400, see Fig. 6.12(a). Parameter values were fixed to those in Table 6.2 and

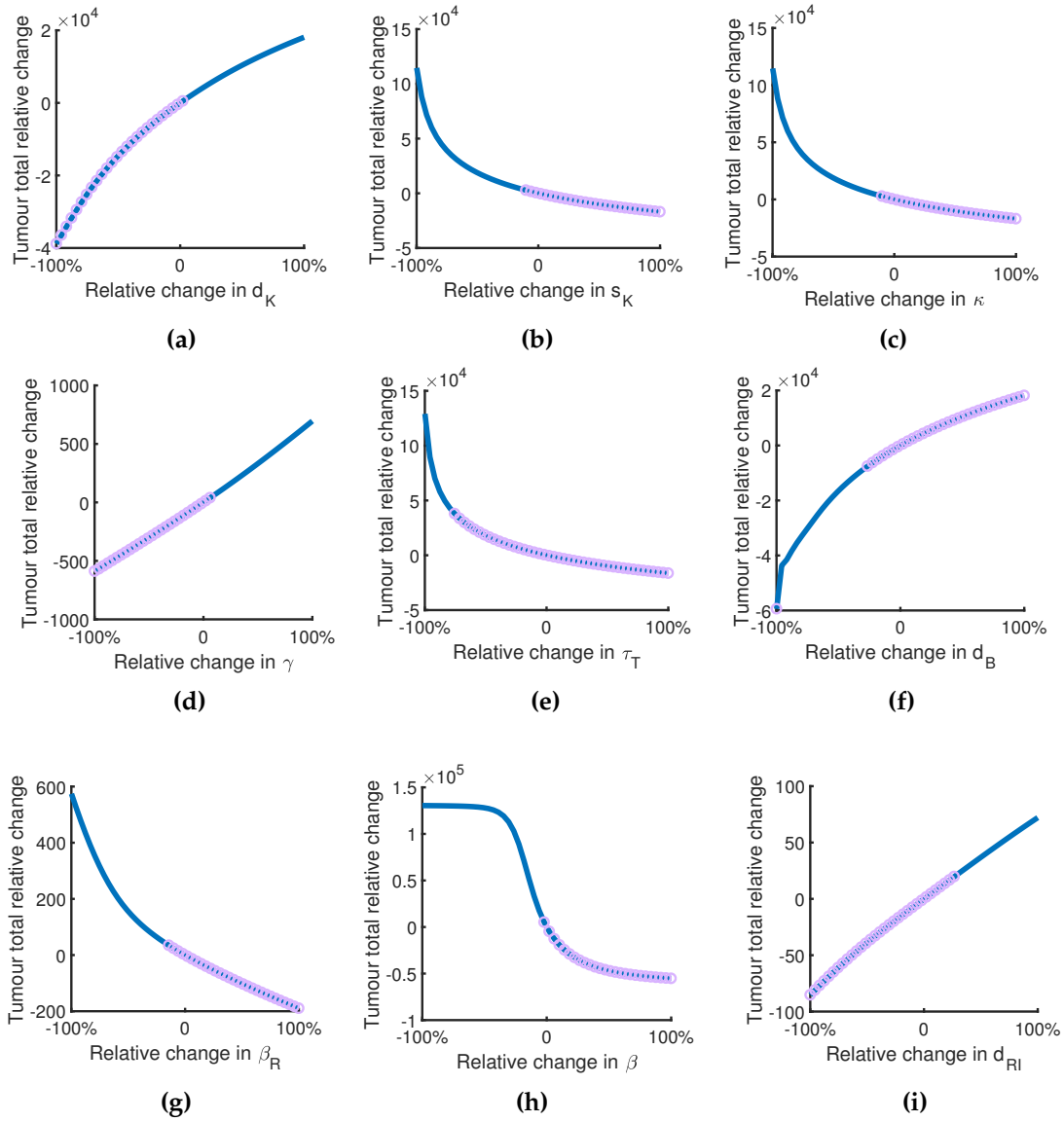

Figure 6.11: Sensitivity analysis of parameters in the Eqs. (6.15)-(6.23) using values from Table 6.2 and 6.7 as base parameters. The change in the total number of tumour cells from day 0 to 100 dependent on the relative change in each parameter value is plotted as a solid (blue) line. The (purple) circles plotted over the blue line represent the death of the tumour within 100 days.

Table 6.7. Perturbations in U_0 suggest that the larger the initial tumour size, the quicker the tumour will die out. Fig. 6.12(a) also suggests that starting treatment on a tumour of size < 40 will both delay the maximum turning point and increase the maximum tumour size reached.

To evaluate what role the antitumour immune response plays in the sensitivity of U_0, the killer immune population was set equal to zero and the same numerical simulation

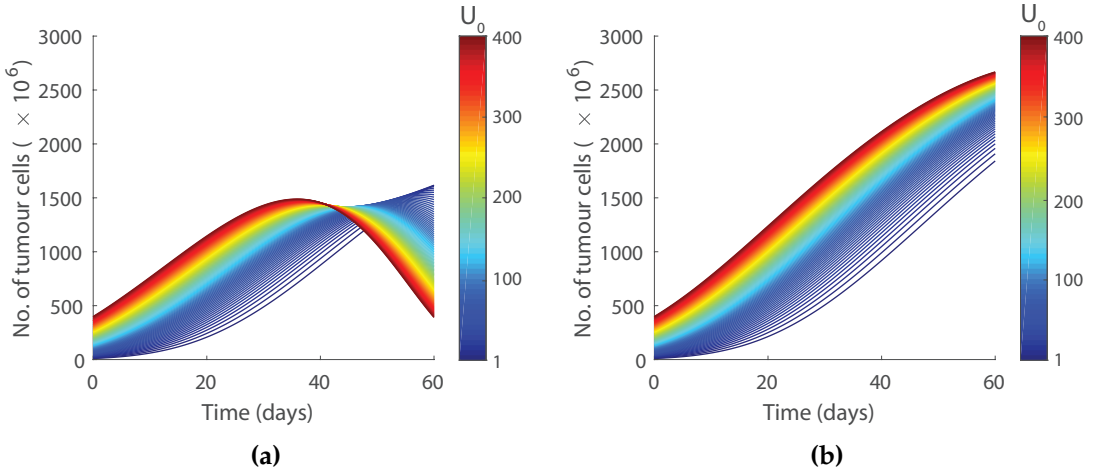

Figure 6.12: Numerical solution to Eqs. (6.15)-(6.23) using a range of initial tumour populations U_0 for (a) $K \neq 0$ and (b) $K = 0$. The colourmap bar on the right hand side matches the corresponding U_0 value with the model's predicted tumour volume over time. First published in Jenner *et al.* (2016).

as for Fig. 6.12(a) was conducted, see Fig. 6.12(b). In the absence of the antitumour response, the change in initial tumour size has a monotonic effect on the total number of tumour cells. In comparing Fig. 6.12(a) and Fig. 6.12(b), the effect of initial tumour size is evidently extremely different, reinforcing that the addition of an antitumour immune response causes the dynamics of the system to change dramatically. The larger the initial tumour size the better the treatment outcome, and the smaller the initial tumour size the larger the tumour will grow over time. Without the antitumour immune response, the initial tumour size has no substantial effect on treatment outcome, leading to the conclusion that with the addition of the antitumour immune response, a dramatic shift in the dynamics of the model occurs, largely dependent on the initial tumour size.

6.5 SUMMARY

By extending the model derived in Chapter 5, it is possible to closely reproduce the experimental results from Kim *et al.* (2011a) for a PEG-modified adenovirus conjugated with Herceptin. The tumour time-series measurements for the PEG-modified adenovirus conjugated with Herceptin were obtained using the model in Eqs. (6.1)-(6.4). To determine the decay rate of virus in the blood over 60 minutes using the viral gen-

ome measurements, a compartmentalisation of the virus population was developed, see Eqs. (6.5)-(6.6). Then, by combining the two models, a model was developed to embody the spatial distribution of the virus genome collected by Kim *et al.* (2011a), see Eqs. (6.9)-(6.14). The parameter values obtained in all optimisations in this chapter were then combined to develop a model for the efficacy of the virus in the presence of the interferon-mediated antiviral immunity and antitumour immune response.

An individual and simultaneous optimisation approach was used for the tumour-time series measurements in this chapter. When fit to the data for individual cases, it can be seen visually that the model easily captures a wide range of treatment responses, see Fig. 6.2 and Table 6.1. The ability of the model to reproduce the data closely in the simultaneous optimisation is reaffirmed by the R-squared and Pearson's r Correlation coefficient Table 6.4 and the results in Fig. 6.3. This illustrates that the model is a reliable and adaptable representation for the interaction between a PEG-modified adenovirus conjugated with Herceptin and tumour cells. Examining specifically the parameter values in Table 6.4 obtained through the simultaneous fitting of the model to the tumour time-series data, it is evident that increasing viral modification, Ad to Ad-PEG to Ad-PEG-HER, increased the infectivity of the treatments with Ad-PEG-HER having the highest infectivity rate.

It is widely known that humans are incredibly heterogeneous and as such, individual responses to treatment will vary. The treatment efficacy is highly dependent upon the initial tumour size and proliferation rate, Fig. 6.5(a) and 6.5(b). Simulations of the treatment protocol on tumours of differing characteristics shows that the treatment is capable of slowing and possibly reversing tumour growth. The results of Fig. 6.5(a) suggest that the slower the tumour cells are proliferating the more likely the viral treatment can reduce the tumour to a manageable size. However, for aggressive tumours with high growth rates r, there is an initial plateauing of the tumour cell population showing the viral treatment taking effect; however, this is followed by an increase in tumour size. This suggests that the overall tumour proliferation is eventually too high for the viral lysis to overcome and an increase in tumour cell population with time occurs. If the infectivity of the virus were higher then the outcome would most likely be similar to that of less aggressively growing tumours.

Interestingly, it would appear that the treatments are more effective in halting tumour progression when the initial tumour size, U_0, is mid-range, around 50×10^6 cells (or 50 mm^3), see Fig. 6.5(b). It may be that smaller tumours are initially hidden from the treatment, delaying the treatment effect. This may be caused by the infectivity rate being highly depending on the frequency of uninfected cells to total cells, which would be variable for an initially small tumour. The maximum tumour population was reduced as U_0 reduced and the peak was delayed. However, for extremely small U_0, the tumour appears to escape the treatment with the peak tumour population again increasing as U_0 decreases. Considering this dependence on initial tumour size, in the presence of interferon-mediated antiviral immunity and the antitumour immune response, there is quite a different outcome, see Fig. 6.12. For larger initial tumours, the treatment is more effective on day 60, when compared to smaller initial tumours in the presence of the antiviral and antitumour immune responses. Then, in the absence of the antitumour immune response, this dynamic is absent and tumour growth for all initial tumour sizes is seen.

One major concern in viral treatments is toxicity. Tracking the maximum viral level during the first 100 days of treatment shows an initial decrease as the application dose increases, independent of the application profile, Fig. 6.6(a). This likely corresponds to the increasing effectiveness of the dose in decreasing the tumour population, and thus also limiting the maximum viral population. For small values of the total injection, V_{T0}, one injection achieves a smaller maximum virus level compared to spreading the dose over increasing numbers of injections. The maximum viral population then goes on to climb linearly as V_{T0} is further increased irrespective of the application profile. This can be interpreted as the virus being too effective in killing off the tumour cells before they proliferate, thus also slowing viral replication.

By spreading the total viral dose into multiple injections, the peak viral load is constrained, despite having an initial higher dose as seen in the lesser gradients of the multiple-injection profiles, see Fig. 6.6(a) and 6.6(b). From this, it could be possible that viral replication is not the driving force behind tumour cell eradication in these scenarios, but rather the intravenous virus is the major player in the eradication. Naturally many application profiles can be considered. Given a particular viral treatment,

and the biological constraints such as maximum viral load tolerance, the model can be used to optimise the proposed application profile.

In Section 6.3, a simple model for the clearance of virus by Liver Sinusoidal Endothelial Cells (LSECs), see Eqs. (6.5)-(6.6), was used to reproduce the dynamics of viral genome measurements in the blood over 60 minutes, see Fig. 6.7. Comparing the parameter values obtained for this optimisation, Table 6.5, it is clear that the PEG-modification and conjugation with Herceptin decreases the rapid initial decay of the virus, but increases the slow rate of decay.

Taking the quasi-steady-state approximation to the model for LSEC clearance of the viral genome in the blood and the model for the overall virus-tumour interaction, a model for the spatial distribution of the virus on day 5 is presented in Eqs. (6.9)-(6.14). Parameter values are then obtained for an optimisation of the model to the viral genome measurements on day 5, see Fig. 6.9 and parameter values in Table 6.6. Since the confidence intervals were tight, the parameter values were then fixed for the decay rate from the blood and transfer rate to the tumour site and used to build a model that considered the antiviral cell immunity and antitumour immune responses.

To understand the significance of the antiviral and antitumour immune responses, a sensitivity analysis of the model developed in Eqs. (6.15)-(6.23) was conducted, see Fig. 6.11. Overall, the antitumour immune response appears more sensitive than the antiviral immune response. Perturbations in the killing rate κ, the stimulation rate of killer immune cells s_K and the death rate of killer cells d_K are all able to achieve significant changes in the tumour size with tumour eradication possible for subsets of the parameter perturbations. It is worth noting that decreasing the stimulation rate of killer immune cells or the killing rate has an adverse effect on the tumour size and renders the treatment unsuccessful.

In this chapter, the outcome of treatment with a PEG-modified adenovirus conjugated with Herceptin was shown to depend on the initial tumour size and the presence of the antitumour immune response. The field of immunotherapy looks to harness the power of the antitumour immune response and increase the stimulation of specific immune cells. In Chapter 7, an investigation into a perturbation of the oncolytic aden-

ovirus in this chapter is examined and the antitumour immune response is investigated in more detail.

7

IMPROVING THE ANTITUMOUR IMMUNE RESPONSE FROM AN ADENOVIRUS MODIFIED WITH IL-12 AND GM-CSF

OVERVIEW

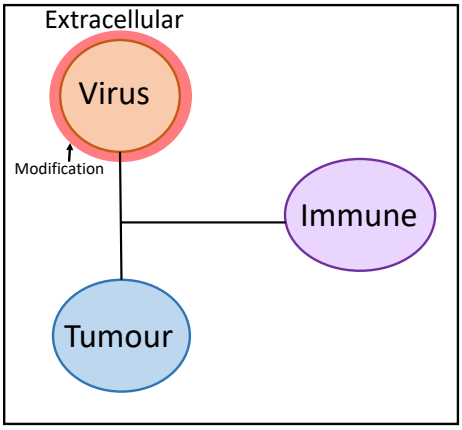

Figure 7.1: Subset of Fig.1.1, summarising the investigation of the virus-tumour interaction in this chapter

Combined virotherapy and immunotherapy has been emerging as a promising and effective cancer treatment for some time. As discussed in Chapter 6, the strength of the antitumour immune response can be crucial to the outcome of oncolytic virotherapy. In this chapter, this response is investigated in more detail by considering an oncolytic adenovirus expressing immunostimulatory cytokines interleukin 12 (IL-12) and granulocyte-monocyte colony-stimulating factor (GM-CSF). These cytokines are known to heighten the antitumour immune response by stimulating the activation of killer T cells and helper T cells. Extending the framework in Chapter 6, a system of ordinary differential equations (ODEs) is developed to model the immune response to an oncolytic adenovirus modified with IL-12 and GM-CSF. To quantify the impact of clearance on this treatment, two delivery mechanisms are considered: single intratumoural injection and degradable virus-loaded hydrogels. Gel-release mechanisms allow for a sustained release of the therapy so that their efficacy may be extended. A major challenge facing gel-release therapies is determining the optimal release profile. Using the mathematical model developed, perturbations to the application protocol that achieve optimal treatment effectiveness can be determined.

Some of the work in this chapter was previously published in Jenner *et al.* (2018a).

The focus of immunotherapy is to overcome the suppression of the immune system by cancer, through stimulating an antitumour immune response (Section 2.4.7). As discussed in Chapter 6, oncolytic viruses represent a promising novel immunotherapy, as they elicit an immune response that can lead to the death of tumour cells.

Interleukin 12 (IL-12) and granulocyte-monocyte colony-stimulating factor (GM-CSF) have been used regularly as immunotherapeutic agents in cancer gene therapy, see Sections 2.3.2.1 and 2.3.2.2. To strengthen the therapeutic efficacy of these cytokines, Choi *et al.* (2012a) modified an oncolytic adenovirus to express IL-12 and GM-CSF. They investigated how intratumoural injections of viruses expressing different combinations of the cytokines prevented tumour growth. IL-12 is known to have potent anti-tumour effects through promotion of the immunity of helper T cells and activation of killer T cells, see Section 2.3.2.1. Choi *et al.* (2012a) found that intratumoural doses of adenovirus expressing IL-12 strongly induced the activation and recruitment of T cells, including helper T cells and killer T cells. The cytokine GM-CSF is known to enhance the processing and presentation of antigen on antigen presenting cells (APCs), see Section 2.3.2.2. Choi *et al.* (2012a) found that intratumoural injections of adenovirus expressing GM-CSF strongly recruited APCs to the tumour site.

One major challenge for the oncolytic adenovirus expressing IL-12 and GM-CSF is sustaining the antitumour immune response. Oh *et al.* (2017) developed a gelatin-based hydrogel for sustained virus release. They also examined the impact of co-delivery of the virus and dendritic cells (DCs) from within the gel. DCs are highly efficient and specialized APCs that can induce a T cell response to antigen, see Section 2.3. By presenting tumour-associated antigens to killer T cells, DCs can induce tumour-specific immunity. These closely related therapies of Choi *et al.* (2012a) and Oh *et al.* (2017) have the potential to be an effective therapeutic tool if their delivery can be optimised.

7.1 THERAPEUTIC EFFICACY OF AN ONCOLYTIC ADENOVIRUS EXPRESSING IL-12 AND GM-CSF, AND DENDRITIC CELLS

To determine whether modification of an oncolytic adenovirus with either IL-12 or GM-CSF could improve oncolytic virotherapy, Choi *et al.* (2012a) investigated the antitu-

mour effect of an oncolytic adenovirus (Ad) co-expressing IL-12 and GM-CSF (Ad/IL12/GMCSF) compared to an oncolytic adenovirus expressing IL-12 (Ad/IL12) or GM-CSF (Ad/GMCSF). B16-F10 murine melanoma (Section 2.2.3.2) tumours in six to eight C57BL/6 mice were injected intratumourally with either phosphate-buffered saline (PBS), Ad, Ad/IL12, Ad/GMCSF or Ad/IL12/GMCSF on days $0, 2$ and 4. Beginning when the average size of the tumour was 80-100mm^3, tumour size was measured from initial treatment injection (Section 2.5.3).

Building on the experiments of Choi *et al.* (2012a), Oh *et al.* (2017) considered the effectiveness of a gelatin-based hydrogel as a co-delivery system for Ad/IL12/GMCSF and DCs. The gel matrix enables sustained release of both the virus and DCs while preserving their biological activity over a considerable time period, leading to efficient retention of both therapeutics in tumour tissue. Oh *et al.* (2017) conducted an *in vitro* study to determine the release profiles for the dendritic cells (DCs) loaded onto the hydrogel, see Section 2.5.5.

Oh *et al.* (2017) then examined how tumour size changed under treatment in an *in vivo* setting. Once Lewis lung carcinoma (LLC) cell based tumours reached an average size of $100 - 150$mm^3 in C57BL/6, they were administered with a single treatment of PBS, gel, Ad/IL12/GMCSF (2×10^{10} VP), DC (2.5×10^6 cells), Ad/IL12/GMCSF (2×10^{10} VP) in combination with DCs (2.5×10^{10} cells) (Ad/IL12/GMCSF+DC) or combination of Ad/IL12/GMCSF and DCs encapsulated in GHPA gel (Ad/IL12/GMCSF+DC +gel). See Section 2.2.3.3 for more information on lung cancer and LLCs or Section 2.5.3 for the tumour growth measurement protocol.

7.2 ANTITUMOUR IMMUNE RESPONSE TO ADENOVIRUS EXPRESSING IL-12 AND GM-CSF

To create a model for the antitumour effect of an oncolytic adenovirus expressing IL-12 and GM-CSF, the previous model in Eqs. (6.1)-(6.4) for an oncolytic virus and a

population of tumour cells is extended to consider individual immune cell types. There are six state variables considered in the system of equations below:

$$\frac{dU}{dt} = r\log\left(\frac{L}{U}\right)U - \beta\frac{UV}{T} - \kappa\frac{KU}{T}, \tag{7.1}$$

$$\frac{dI}{dt} = \beta\frac{UV}{N} - d_I I - \kappa\frac{KI}{T}, \tag{7.2}$$

$$\frac{dV}{dt} = u_V(t) - d_V V + \alpha d_I I, \tag{7.3}$$

$$\frac{dA}{dt} = s_A I - d_A A, \tag{7.4}$$

$$\frac{dH}{dt} = s_H A - d_H H, \tag{7.5}$$

$$\frac{dK}{dt} = s_{KH} H + s_{KA} A - d_K K, \tag{7.6}$$

$$u_V(t) = \begin{cases} V_0\delta(t-t_i), & t_i = 0,2,4, \\ 0, & \text{otherwise}, \end{cases} \tag{7.7}$$

$$U(0) = U_0, \quad V(0) = 0, \quad H(0) = 0,$$

$$I(0) = 0, \quad A(0) = 0, \quad K(0) = 0,$$

where t is time (days), U is the uninfected tumour population, I is the infected tumour population and V is the number of virus particles. As the model was developed for an adenovirus expressing IL-12 and GM-CSF the populations of immune cells considered here are those most affected by these cytokines: antigen-presenting cells (APCs), A; helper T cells, H; and killer T cells, K. The total cell population at the tumour site at any time t is given by $T = U + I + A + H + K$. In Fig. 7.2 there is a schematic for the interactions modelled. As the virus was administered intratumourally, there is no need to model the virus in the organs and blood (as was discussed in Chapter 6). Additionally, the influence of the interferon-mediated antiviral immunity is not considered crucial in this chapter. Note that this is the same killer T cell population that was considered in Eqs. (6.15)-(6.23), but this time the activation mechanism is modelled in more detail. Note that the above model is similar to the model used by Kim *et al.* (2015) detailed in Eqs. (3.17)-(3.21).

APCs include dendritic cells and macrophages. These cells are stimulated by infected cells at rate s_A and decay at a rate d_A. Helper T cells are then stimulated by APCs at

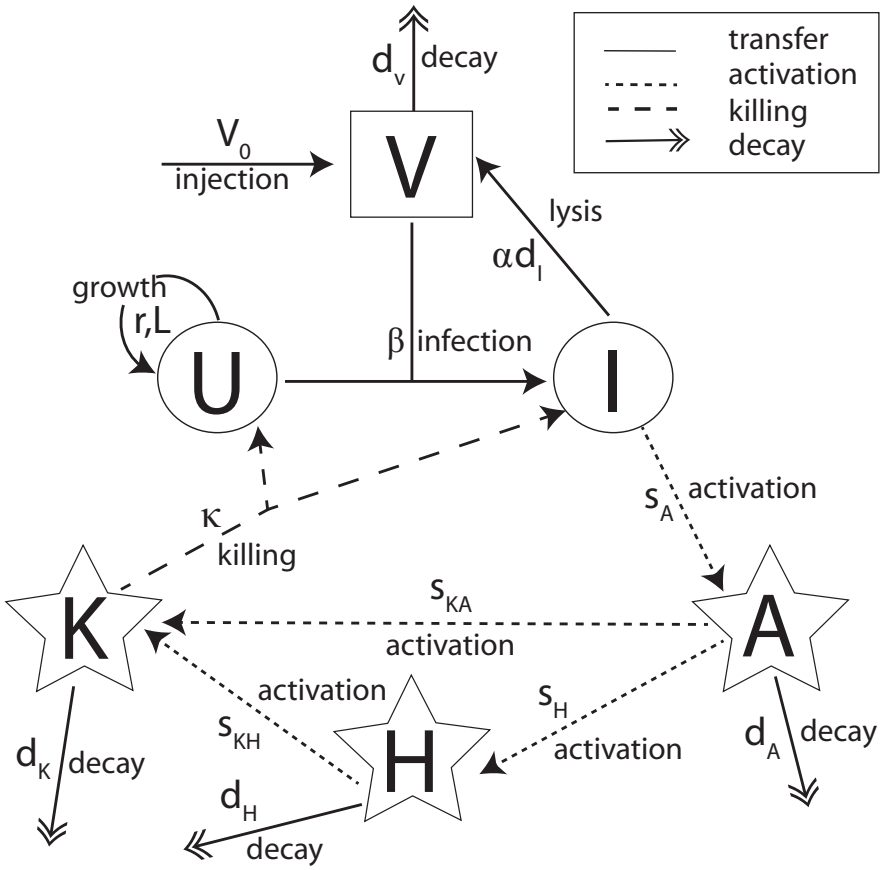

Figure 7.2: Compartmental diagram for the tumour-virus interaction of an oncolytic adenovirus expressing IL-12 and GM-CSF. U and I are the uninfected and infected tumour cell populations respectively. V is the virus population, A is the APC population, H is the helper T cells population and K is the killer T cells population. Transition between states (e.g. uninfected to infected) is represented by a solid line, stimulation or activation is represented by a dotted line, death or decay is represented by a double arrow and programmed killing of tumour cells is represented by a dashed line. First published in Jenner *et al.* (2018a).

rate s_H and decay at rate d_H. Both APCs and helper T cells then activate killer T cells at rate s_{KA} and s_{KH} respectively. Killer T cells induce apoptosis in uninfected and infected tumour cells at a frequency-dependent rate with constant κ. Killer T cells decay at rate d_K. Initially, it is assumed there are no stimulated immune cells as these are only generated through the presence of virus-infected tumour cells, I. For more biological detail about the immune interactions, see Section 2.3.

The interaction between tumour cells and immune cells are modelled using mass action as an approximation of the geometric and spatial effects. Frequency-dependent rates have been incorporated to model cell-cell and cell-virus interactions at the tumour

site as it is assumed these occur at a rate proportional to the frequency of the interacting cells. In other words, virus infection or killer T cell killing of tumour cells just depends on the number of viruses or killer T cells and the frequency of the population they are infecting or killing.

To fit the model to the data from Choi *et al.* (2012a), certain parameters were fixed to those found in the literature. The average time taken for an infected tumour cell to undergo lysis is one day, so $d_1 = 1(\text{day}^{-1})$ (Ganly *et al.*, 2000). The estimation for the rate that the virus leaves the tumour site d_V is based on laboratory observations of Li *et al.* (2008) and Wang *et al.* (2006), which observe 90% of the virus population decays in one day. Using the half-life decay formulas assuming expoential decay gives $d_V = -\log(0.1) = 2.3/\text{day}$. Helper T cells are known to have a half-life of 3 days (Kim *et al.*, 2011c), which gives $d_H = -\log(2)/3 = 0.23/\text{days}$. For the immune cell death rates, it was assumed that APCs and helper T cells die or exit the system at a similar rate, therefore $d_A = d_H = 0.23/\text{day}$ (Kim *et al.*, 2011c). The number of viral particles created through lysis α and the decay rate of killer T cells d_K was set to the values in Table 6.1 and 6.7.

All of the parameter estimates are summarised in Table 7.2. The remaining parameters in the model were obtained by sequentially fitting parameters for submodels of Eqs. (7.1)-(7.7) to the data, and fixing their values for higher level models in accordance with gradual modifications of the base adenovirus, see Table 7.1 for the summary. Sequential or hierarchical fitting is different to the simultaneous fitting method employed in Chapter 6, where all parameters were fit to their corresponding data sets simultaneously. The numerical implementation of the optimisation is detailed in Section 3.4.

To assess the antitumour effectiveness of the immunostimulatory adenovirus, Choi *et al.* (2012a) first conducted a control (PBS) experiment that monitored tumour growth in the absence of treatment. Since there were no viral particles present in the control experiment, the model was reduced to the uninfected tumour population, U, by fixing $V = I = A = H = K = 0$ in Eqs. (7.1)-(7.7). The tumour volume is assumed proportional to the number of tumour cells, and the density to be $10^6 \text{cells}/\text{mm}^3$. The parameter values, describing the tumour replication constant, r, and carrying capacity, L, were fit to the data and fixed for all subsequent simulations.

Table 7.1: Experiment-specific optimisation conditions Choi *et al.* (2012a). Equations used to optimise each experiment are listed along with the state variables considered and parameters fitted or fixed.

	Experiment				
	PBS	Ad	Ad/GMCSF	Ad/IL12	Ad/IL12/GMCSF
Relevant equations	Eq. (7.1)	Eq. (7.1) Eq. (7.2) Eq. (7.3)	Eq. (7.1) Eq. (7.2) Eq. (7.3) Eq. (7.5) Eq. (7.6)	Eq. (7.1) Eq. (7.2) Eq. (7.3) Eq. (7.4) Eq. (7.6)	Eq. (7.1) Eq. (7.2) Eq. (7.3) Eq. (7.4) Eq. (7.5) Eq. (7.6)
Variables	U	U, I, V	U, I, V, H, K	U, I, V, A, K	U, I, V, A, H, K
Params fit	r, L, U_0	β	s_H, s_{KH}, κ	s_A, s_{KA}, κ	s_{KA}, s_{KH}, κ
Params fixed (Table 7.2)	-	r, L, U_0, α, d_V	$r, L, U_0, \beta, d_I, \alpha, d_V, d_H, d_K$	$r, L, U_0, \beta, d_I, \alpha, d_V, d_A, d_K$	$r, L, U_0, \beta, d_I, \alpha, d_V, d_A, s_A, s_H, d_H, d_K$

The first virus-based experiment was the oncolytic adenovirus (Ad) with no immunostimulatory cytokines. It is assumed that the immune reponse to Ad alone would be significantly less than the response to oncolytic adenovirus modified with either IL-12 or GM-CSF. As such, the presence of the populations of immune cells were assumed negligible, i.e. $A = H = K = 0$ in Eqs. (7.1)-(7.7). This resulted in the PEG and Herceptin-modified adenovirus model in Eqs. (6.1)-(6.4). The remaining parameters of the model describing the infection rate of the virus β and initial tumour size U_0 were fit and their values were fixed for all subsequent simulations.

The last three viruses tested were modifications of the adenovirus with the different cytokines Ad/GMCSF, Ad/IL12 and Ad/IL12/GMCSF. Choi *et al.* (2012a) found that intratumoural doses of adenovirus expressing IL-12 strongly induced the activation and recruitment of T cells, including helper T cells and killer T cells. Hence, to fit the tumour time-series measurements under treatment with Ad/IL12, the population of APCs was considered negligible, $A = 0$ in Eqs. (7.1)-(7.7). Similarly for the adenovirus expressing GM-CSF, it was assumed the effect on the helper T cell population was negligible as GM-CSF primarily stimulates the antigen presenting cells (Choi *et al.*, 2012a). Therefore, for this experiment the model was adjusted to exclude the helper T cells by setting $H = 0$, and the remaining model was fit to the data. For the Ad/IL12/GMCSF

virus the full model, Eqs. (7.1)-(7.7), was used to fit the model parameters as both cytokines were present.

Due to the overlap in the cytokines expressed by the three viruses, the stimulation rates of the APCs, s_A, and helper T cells, s_H, could be determined specifically from optimisation to the Ad/GMCSF and Ad/IL12 data respectively. Once the values were obtained, they were fixed in the fit of the model to the Ad/IL12/GMCSF experiment. The remaining parameters s_{KA}, s_{KH} and κ were then allowed to vary between the three experiments and were used to quantify the major differences in the outcome of treatment from the cytokine expression of the three viruses. A full summary of the experiment-specific sequential optimisation for the five data sets can be found in Table 7.1.

The model was fit to the mean of the data with normalisation using the standard error. When solving Eqs. (7.1)-(7.7) numerically, T was replaced by $T + \epsilon$ for $\epsilon = 0.001$, to avoid the singularity occurring as $T \to 0$. As a second and third injection of treatment was given on days 2 and 4, the model was solved piecewise to account for the addition of V_0 virus particles at each injection time.

7.2.1 *Tumour growth under treatment with an oncolytic adenovirus co-expressing IL-12 and GM-CSF.*

The model parameters r, the replication rate of tumour cells, and L, the carrying capacity of the tumour, were first optimised using the PBS tumour time-series measurements, see Fig. 7.3. The trajectory of tumour growth arising from the optimised model is close to the tumour growth data from the experiment. The estimates obtained for the parameters are presented in Table 7.2 with the corresponding goodness of fit estimates in Table 7.3. These values were then used when optimising the model parameters using the other, virus-based, experiments.

To create a baseline for the effectiveness of oncolytic adenoviruses without IL-12 or GM-CSF, Choi *et al.* (2012a) monitored the growth of pre-established tumours in 8 mice after treatment with an adenovirus, previously discussed in Section 7.1. The tumour time-series measurements exhibited high variability and illustrate the heterogeneity

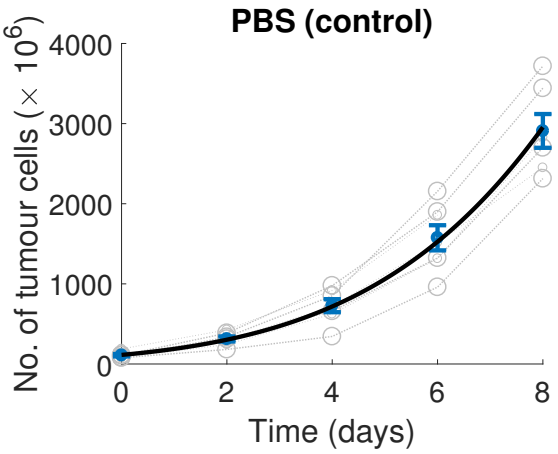

Figure 7.3: Output of the optimised tumour growth model, Table 7.1, for the PBS (control) case. The individual mouse data are plotted as grey circles with the mean and standard error bar at each time point in blue. The model output is plotted as a solid black line. First published in Jenner *et al.* (2018a).

in response to treatment, see Fig. 7.4. Multiple mice did not survive the experiments duration. Within this data, however, there were three clear subgroups of treatment responses: those that died early, Fig. 7.4(a); low responders, those whose tumours grew slowly until about day 10, after which point the tumours grew exponentially, Fig. 7.4(b); and high responders, those with small tumours over the whole duration of the experiment, Fig. 7.4(c).

To determine whether the model could adequately represent the observed behaviour, model and parameter values were optimised using each subgroup of data, Fig. 7.4. The optimised values for the infection rate, β, and initial tumour size, U_0, differed for the different subgroups. For the subset that died early $\beta = 1.3$ and $U_0 = 220$. For the low responder subgroup $\beta = 0.92$ and $U_0 = 27$, and for the high responder subset $\beta = 1.1$ and $U_0 = 18$.

The dynamics of the model optimised to each subgroup was qualitatively similar: each of the solutions rises to a maximum and then decays. Perturbations in β and U_0 alter the location and value of the turning point, not the existence. The large range of initial tumour sizes, U_0, obtained is an accurate reflection of the initial tumour sizes observed in the experiment. The difference in the infection rates, β, between the three treatment response subgroups was less variable, and the model output was less sensitive to changes in β than U_0.

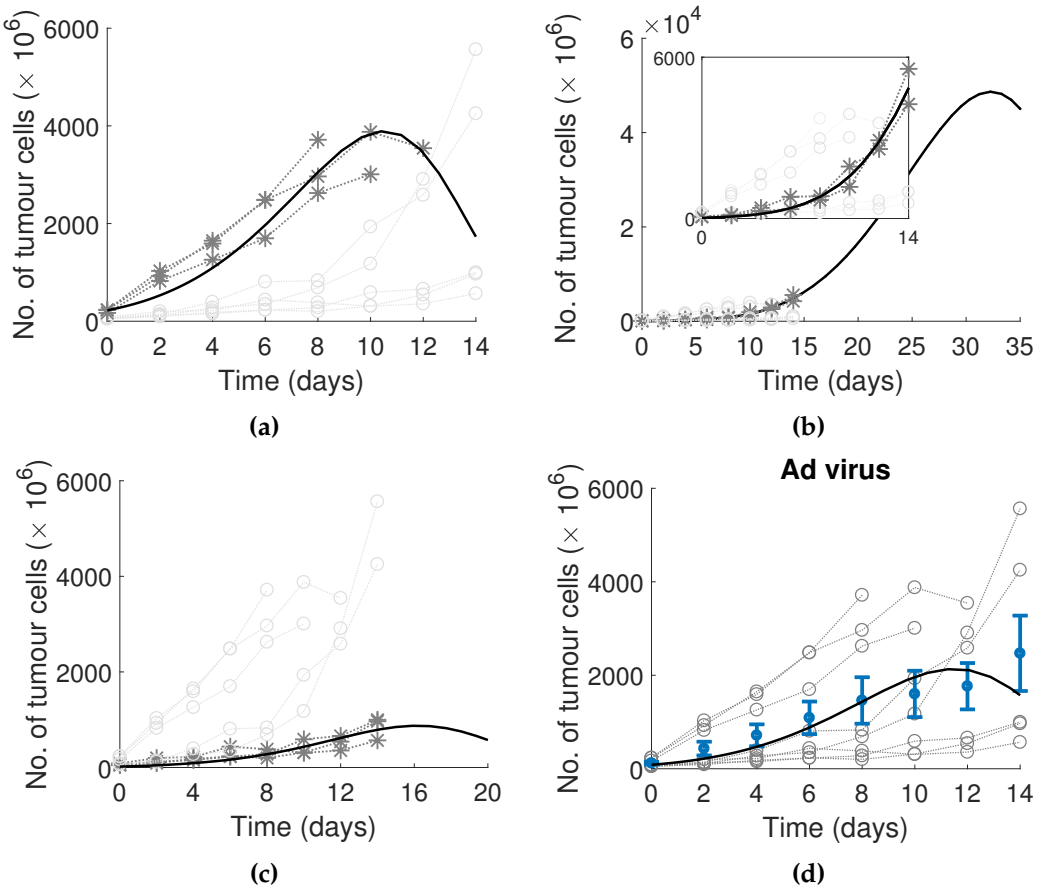

Figure 7.4: Output of the optimised tumour growth models for the adenovirus (Ad) with no immune-stimulatory cytokines. The model parameters were optimised using (a) the early-death subgroup, (b) the low-responder subgroup, (c) the high-responder subgroup and (d) all data. The individual mouse data are plotted as grey circles with the mean and standard error bar at each time point shown in (d) in blue. The model outputs are plotted as solid black lines. Note the time axis has been extended in (b) and (c) to reveal the longer-term behaviour of the dynamics. First published in Jenner *et al.* (2018a).

Optimising the parameters to all data simultaneously, Fig 7.4(d), resulted in $\beta = 1.2$ and $U_0 = 85$, inside the range obtained for the 3 subgroups. Due to the different trajectories, the mean trend of the data and the individual points diverge around day 11 and do not represent any given mouse in the observations. For mice undergoing different treatment protocols it is not possible to predict whether they would have been high or low responders if treated with adenovirus with no immunostimulatory cytokines. The estimates $\beta = 1.2$ and $U_0 = 85$ obtained using all the data simultaneously lie within the range of the other subgroup estimates, and all the model outputs exhibit the same

features. Thus, these values are used when optimising the other model parameters using the data from the more highly modified treatments.

The model parameters were optimised to each immunostimulatory adenovirus-based experiment of Choi *et al.* (2012a) (i.e. Ad/IL12, Ad/GMCSF, Ad/IL12 GMCSF) as detailed in Table 7.1. Fig. 7.5 shows the tumour cell population over time for each experiment overlaid with the optimised model. The parameter values obtained are presented in Table. 7.2 and the goodness of fit measures in Table 7.3.

It can be seen that the model is a good representation of the features of the tumour growth trajectories. As with the Ad experiments, some of the experiments show different response levels to the treatments. In these cases, the model presented reflects the mean behaviour of the data rather than that of any particular subgroup (for instance in Fig. 7.5(c) the mean value straddles two subgroups of responders).

7.2.2 *Simulating heterogeneity in immune efficacy*

To determine ways of improving the efficacy of Ad/IL12/GMCSF, it helps to consider how the outcome of treatment depends on heterogeneity in immune characteristics. Using model parameters from the optimisation to the Ad/IL12/GMCSF data (Table 7.2), the effects of perturbations in the rates of immune stimulation and apoptosis induction were investigated. The effect of increasing the immunostimulatory capability of infected cells on APCs or APCs on helper T cells was considered. To investigate stronger immune stimulation, the APC stimulation rate, s_A, and the helper T cells stimulation rate, s_H, were perturbed individually by approximately 20-30%, keeping the other parameters constant, see Fig. 7.6(a) and 7.6(b) respectively. To further investigate how changes in the rate of killer-T-cell-induced apoptosis alters treatment outcome, the killing rate of killer T cells, κ, was also perturbed, Fig. 7.6(c). As the experiments of Choi *et al.* (2012a) showed significant tumour growth over the space of 33 days, it is assumed that this is the therapeutic window over which this treatment needs to be effective.

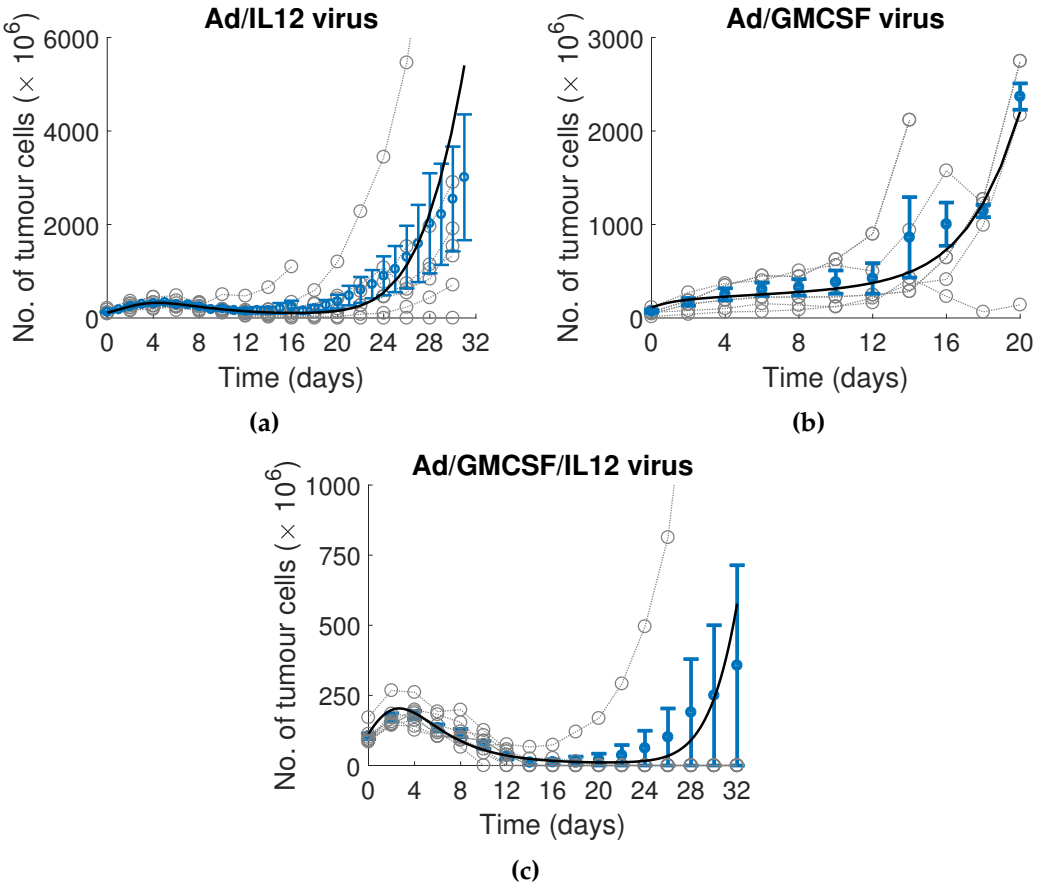

Figure 7.5: Output of the optimised virus-tumour-immune models for the (a) Ad/IL12, (b) Ad/GMCSF and (c) Ad/GMCSF/IL12 treatment cases, see Table 7.1. The individual mouse data are plotted as grey circles with the mean and standard error bar at each time point shown in blue. The model outputs are plotted as solid black lines. First published in Jenner *et al.* (2018a).

In Fig. 7.6(a), it is evident, as expected, that the higher the stimulation rate of APCs by infected tumour cells, the larger the number of tumour cells. Decreasing the stimulation rate of APCs, results in a much smaller tumour burden, smaller than even the initial tumour size. These findings suggest that increasing APC stimulation has a negative effect on the ability of the treatment to reduce tumour size, and this rate should actually be decreased for an optimal treatment to be obtained. Comparing this to the perturbation in the immunostimulatory rate of helper T cells, Fig. 7.6(b), the opposite occurs with the larger stimulation rates resulting in the smallest tumour size.

Table 7.2: Parameter estimates fixed from the literature and obtained from the sequential fit shown in Figs. 7.3, 7.4 and 7.5 to the measurements of Choi *et al.* (2012a)

	Parameter	Units	Description	PBS	Ad	Ad/IL12	Ad/GMCSF	Ad/IL12/GMCSF
Fixed	α	virus$\times 10^{10}$	viral burst size	-	3500	3500	3500	3500
	d_I	day^{-1}	burst rate	-	1	1	1	1
	d_V	day^{-1}	viral decay rate	-	2.3	2.3	2.3	2.3
	d_A	day^{-1}	decay of APCs	-	-	0.23	-	0.23
	d_H	day^{-1}	decay of helper T cells	-	-	-	0.23	0.23
	d_K	day^{-1}	decay of killer T cells	-	-	0.35	0.35	0.35
Fit	r	day^{-1}	tumour growth rate	0.066	0.066	0.066	0.066	0.066
	L	cells$\times 10^6$	carrying capacity	3.2×10^5	3.2×10^5	3.2×10^5	3.2×10^5	3.2×10^5
	β	day^{-1}	infection rate	-	1.2	1.2	1.2	1.2
	U_0	cells$\times 10^6$	initial tumour size	85	85	85	85	85
	s_A	day^{-1}	APC activation rate	-	-	1.2	-	1.2
	s_{KA}	day^{-1}	APC activate killer T cell	-	-	5.4	-	7.1
	s_H	day^{-1}	helper T cell activation	-	-	-	0.78	0.78
	s_{KH}	day^{-1}	helper T cell activate killer T cell	-	-	-	5.0	1.6
	κ	day^{-1}	killing rate	-	-	0.84	1.1	1.4

Table 7.3: Goodness of fit measures for each parameter optimisation

	Residual norm	Coefficient of determination	Pearson's correlation coefficient
PBS	0.33	0.99	0.99
Ad	7.4	0.99	0.87
Ad/GMCSF	90	0.99	0.96
Ad/IL12	6.6	0.99	0.97
Ad/GMCSF/IL12	26	0.99	0.91

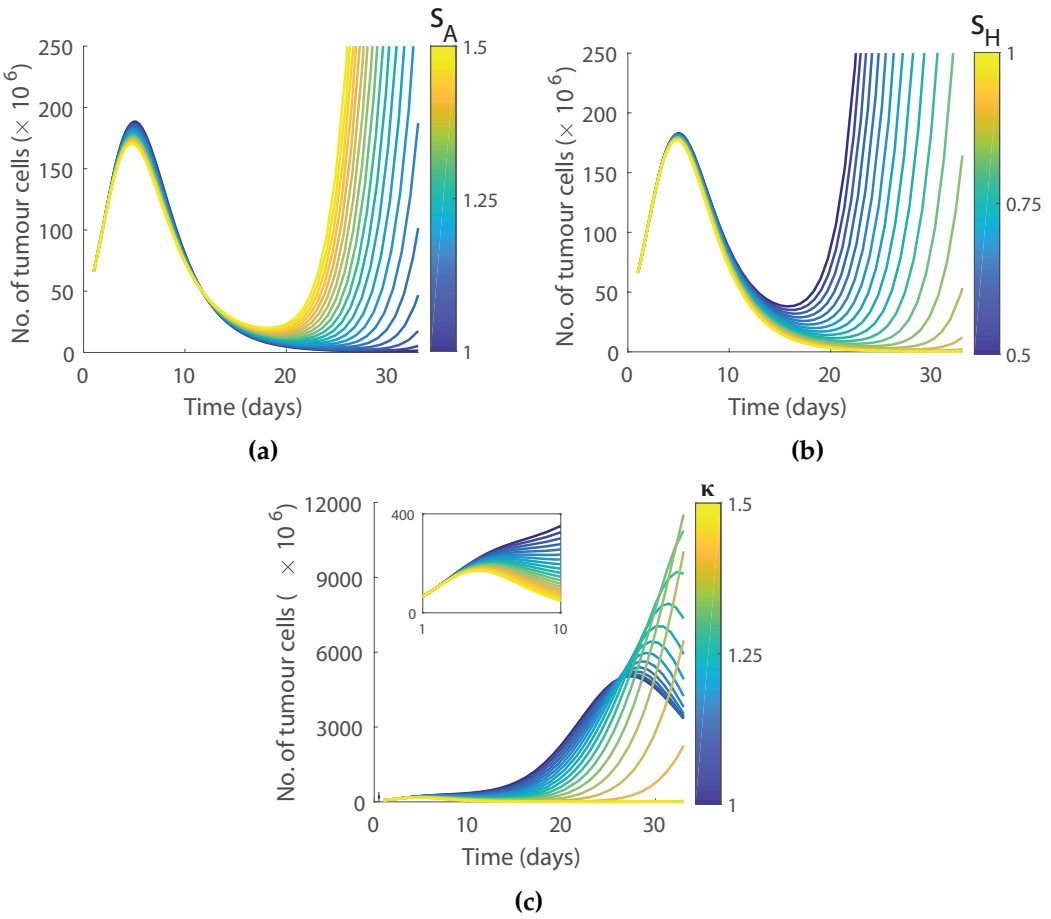

Figure 7.6: Tumour cell population over time predicted by the optimised model for Ad/IL12/GMCSF for various values of (a) APC stimulation rates $s_A \in (1,1.5)$, (b) helper T cell stimulation rates $s_H \in (0.5,1)$and (c) killer T cell killing rate $\kappa \in (1,1.5)$, indicated by the colour. The remaining parameters were fixed to the values presented in Table 7.2 column Ad/IL12/GMCSF, a detailed view for short times is shown inset for (c). First published in Jenner *et al.* (2018a).

In Fig. 7.6(c), larger κ values resulted in effective early containment of tumour growth. For very large values of κ, close to $\kappa = 1.5$, the tumour is completely eradicated (for this model, we consider complete tumour eradication to occur if the total tumour population drops below 10^{-3}) in this window of time. However, for mid-range values of the apoptosis rate, e.g. $\kappa = 1.25$, the treatment results in a large growth of the tumour around day 25. These two treatment responses (complete eradication or unbounded growth) mimic the results seen in Fig. 7.5(c).

Interestingly, when κ is much smaller, e.g. $\kappa = 1$, a lower maximum tumour count is achieved within this time frame. These findings suggest the existence of a mid-range interval of κ values for which the treatment is significantly less effective in the time frame of 33 days (the therapeutic window discussed earlier) than may have been anticipated outside of this interval. Also, for large values of κ complete tumour eradication can be obtained. This indicates that tumour cell apoptosis is a critical feature in the efficacy of treatment.

7.3 RESPONSE TO TREATMENT WITH DENDRITIC CELLS AND ADENOVIRUS EXPRESSING IL-12 AND GM-CSF RELEASED FROM AN INJECTABLE GEL

In the previous section, the model developed assumed that the primary driver of the immune response was virus-infected tumour cells. The virus-infected tumour cells stimulated APCs which in turn activated killer T cells and helper T cells. Using the Ad/IL12/GMCSF virus created by Choi *et al.* (2012a), Oh *et al.* (2017) considered injections of both the virus and immature dendritic cells (DCs). As such, the stimulation of the immune system by uninfected tumour cells needs to be modelled explicitly. Below is a modified version of Eqs. (7.1)-(7.7) from Section 7.2:

$$\frac{dU}{dt} = r \log\left(\frac{L}{U}\right) U - \beta \frac{UV}{T} - \kappa \frac{KU}{T}, \tag{7.8}$$

$$\frac{dI}{dt} = \beta \frac{UV}{T} - d_I I - \kappa \frac{KI}{T}, \tag{7.9}$$

$$\frac{dV}{dt} = u_V(t) - d_V V + \alpha d_I I, \tag{7.10}$$

$$\frac{dA_I}{dt} = u_{DC}(t) - s_{AU} A_I U + r_{AI} I - s_{AI} A_I I - d_{AI} A, \tag{7.11}$$

$$\frac{dA_A}{dt} = s_{AU} A_I U + s_{AI} A_I I - d_A A, \tag{7.12}$$

$$\frac{dH}{dt} = s_H A - d_H H, \tag{7.13}$$

$$\frac{dK}{dt} = s_{KH} H + s_{KA} A - d_K K, \tag{7.14}$$

where t is time. A schematic for the model is given in Fig. 7.7.

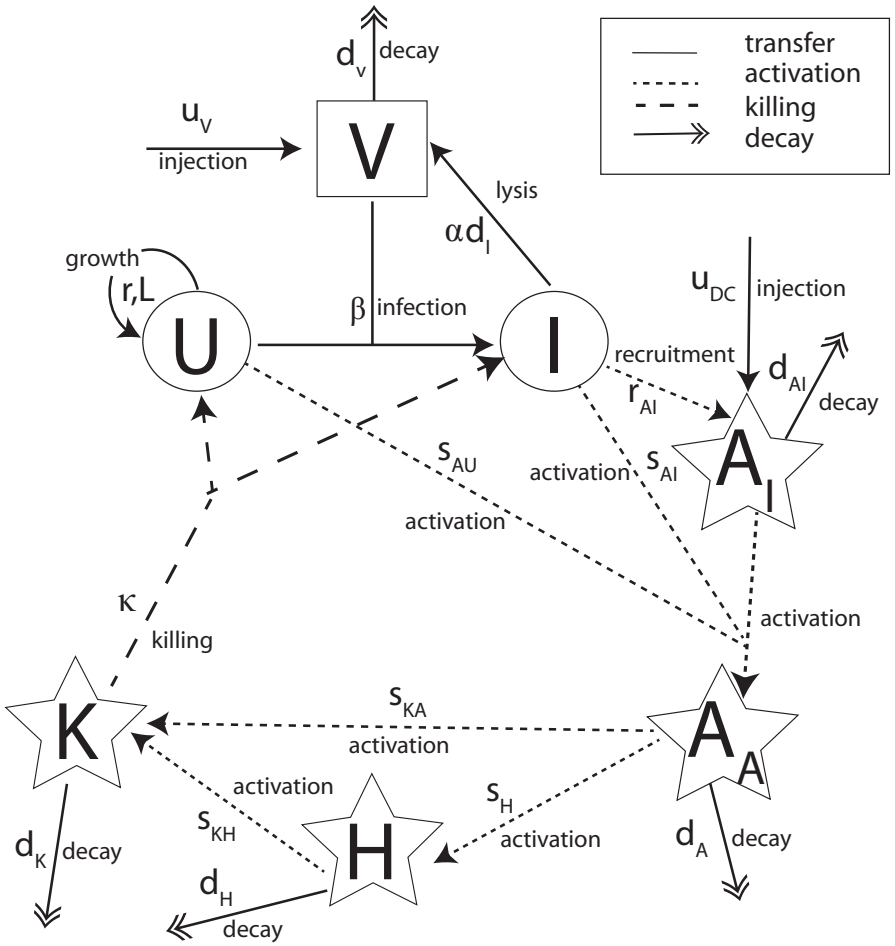

Figure 7.7: Compartmental diagram for the tumour-virus interaction of co-delivered DCs and oncolytic adenovirus expressing IL-12 and GM-CSF. Variables U and I are the uninfected and infected tumour cell populations, V is the virus population, A_I is the immature APC population, A_A is the mature APC population, H is the helper T cell population and K is the killer T cell population. Transition between states (e.g. uninfected to infected) is represented by a solid line, stimulation or activation is represented by a dotted line, death or decay is represented by a double arrow and programmed killing of tumour cells is represented by a dashed line. This schematic builds on the one presented in Fig. 7.2.

The function $u_V(t)$ is now the rate at which virus is introduced into the system, either from an intratumoural injection or released from a hydrogel. Immature DCs are introduced into the system either through direct intratumoural injection or release from the gel at a rate described by the function $u_{DC}(t)$. The immature DCs are activated by interacting with uninfected or infected tumour cells at rate s_{AU} and s_{AI} respectively. Infected cells recruit immature DCs to the tumour site at rate r_{AI} and immature DCs die at rate d_{AI}.

Using the *in vitro* study on the gel-release profile by Oh *et al.* (2017) (see Section 7.1), the function describing the release of DCs, $u_{DC}(t)$, can be determined. This function will then be used to optimise the *in vivo* tumour time-series measurements.

7.3.1 *In vitro DC release profile*

To obtain the function $u_{DC}(t)$ that describes the rate at which DCs leave the gel, first consider the simple model for DCs:

$$\frac{dD}{dt} = u_{DC}(t) - d_{DC}D, \tag{7.15}$$

where D is the number of DCs outside the gel, and DCs in the gel leave at a rate $u_{DC}(t)$ and decay at a rate d_{DC}. Let D_0 be the initial number of DCs. The function for the rate that dendritic cells flow out from the gel, u_{DC}, is a function of time as it depends on the rate at which the gel is degrading, which can either occur slowly or quickly depending on the stiffness of the gel (soft or hard). It also depends on the number of DCs left inside the gel. The schematic in 7.8 summarises the model.

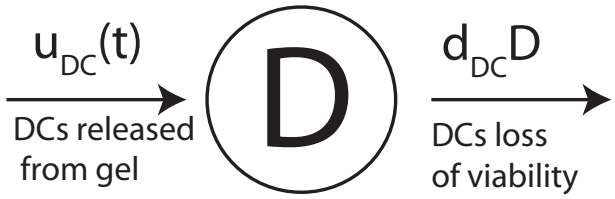

Figure 7.8: Schematic for the simplified model for the release of DCs from the gel. It relates to Eq. (7.15).

The viable DC count (in the absence of the gel medium) can be used to obtain the decay rate d_{DC}. Since there is no gel in this experiment, only the decay rate of the DCs is present in the model, see Fig. 7.9 and Table 7.9 for the resulting fit.

The results for the number of DCs released from the soft and hard gel are plotted in Fig. 7.10(b) and 7.10(d) respectively. These relate to the function $D(t)$ in Eq. (7.15). Since the function for $D(t)$ and $u_{DC}(t)$ are both left undetermined, the most that can be obtained from the data is an approximation to $u_{DC}(t)$ at each time-point of $D(t)$. Using a finite difference approximation, Eq. (7.15) can be written as

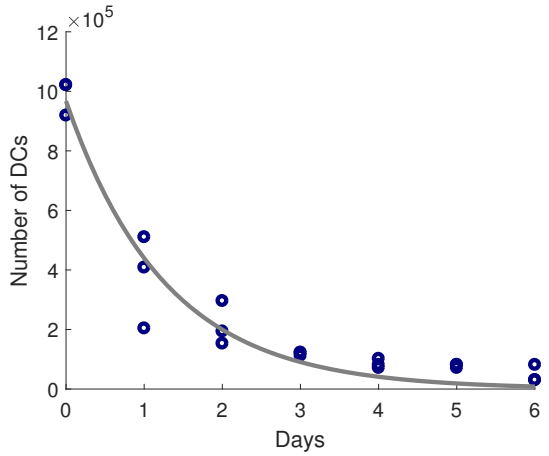

Figure 7.9: Viability profile of dendritic cells (DCs) not loaded into a gel system. Circles represent the number of released viable DCs as counted by trypan blue staining from three experiments. Fit of viable DC number data to exponential decay is given by the grey curve.

Table 7.4: Parameter estimates relating to Fig 7.9

Parameter	Units	Description	Value	95% confidence interval
d_{DC}	day^{-1}	decay rate of DCs	0.7889	(-0.9972, 0.5805)
D_0	No. of DCs	Initial number of DCs	967100	(840500, 1094000)

$$\frac{D(t+h)-D(t)}{h} \approx u_{DC}(t) - d_{DC}D(t). \tag{7.16}$$

Rearranging gives an expression for $u_{DC}(t)$:

$$u_{DC}(t) \approx D(t+1) + (d_{DC}-1)D(t). \tag{7.17}$$

Assuming that DCs outside the gel lose viability at a rate d_{DC}, equivalent to that obtained in Table 7.4 for Fig. 7.9, the expression for the rate of change of DCs outside the gel can be used to calculate $u_{DC}(t)$. Taking the forward finite difference in Eq. 7.17 for all time points up until day 6, where the backward finite difference equivalent is used, $u_{DC}(t)$ can be calculated. The results of this approximation to the soft gel data are plotted in Fig. 7.10(a) as stars.

To extract a function describing the release rate of DCs from the gel, it is sufficient to approximate $u_{DC}(t)$ as closely as possible. Fitting a 6^{th} order polynomial to Eq. (7.17), gives the curve for $u_{DC}(t)$ in Fig. 7.10(a). Using this expression for $u_{DC}(t)$ and simulating Eq. (7.15) gives the curve overlayed on the DC measurements for soft gels, see

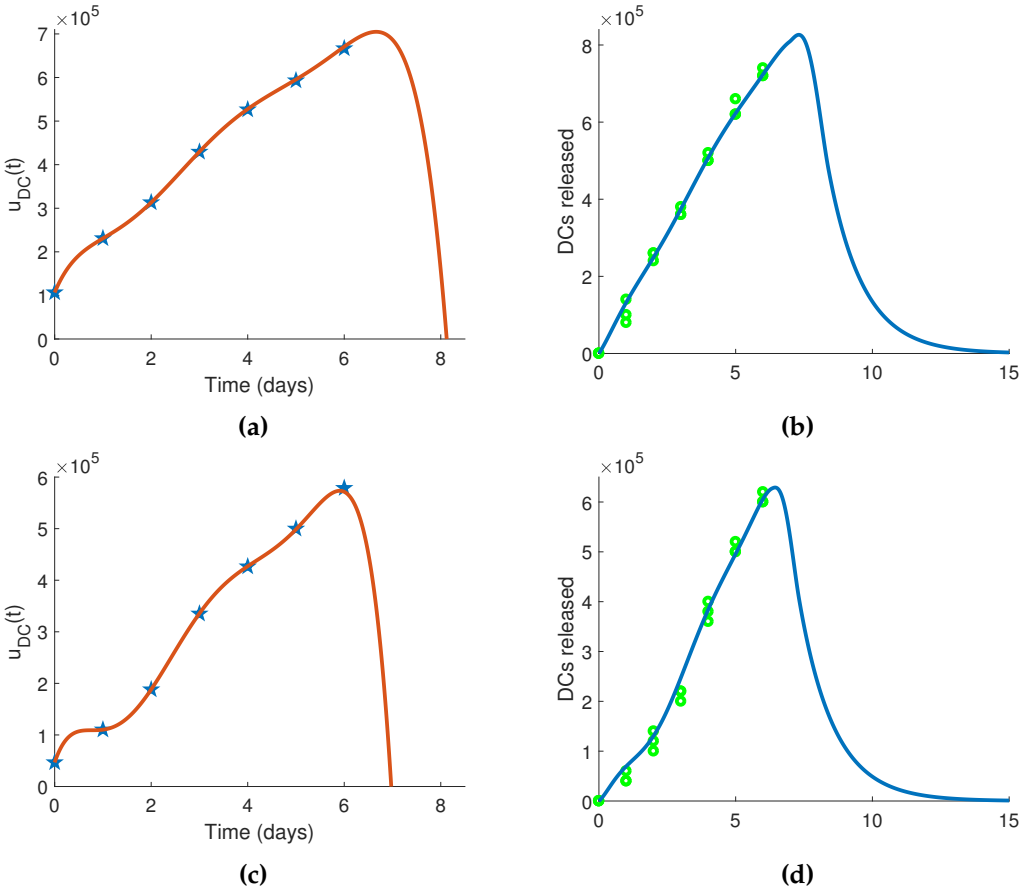

Figure 7.10: Sustained release profile of dendritic cells (DCs) from soft (a)-(b) and hard (c)-(d) gelatin gel system. The stars in (a) & (c) represent the finite difference approximation to the release rate $u_{DC}(t)$ of DCs from the gel, Eq. (7.17), along with the 6th order polynomial fit to the approximations. The circles in (b) & (d) represent the number of released viable DCs from GHPA gels as counted by trypan blue staining from three experiments. The curve is the approximation to the number of DCs using Eq. (7.15)

Fig. 7.10(a)-(b). Repeating this for the DC measurements for hard gel, gives Fig. 7.10 (c)-(d), assuming that the expression for $u_{DC}(t)$ is a 6th order polynomial. As $u_{DC}(t) \geqslant 0$, for values of the 6th order polynomial approximation that are negative, $u_{DC}(t) = 0$.

To determine whether there was a simpler biologically reasonable way to model the DCs released from the gel, two other models were tested. Assuming the rate at which DCs leave the gel is a constant rate k gives

$$\frac{dD}{dt} = k - d_{DC}D. \tag{7.18}$$

Optimising this model for the value of k to the data gives the approximation in Fig. 7.11(a). It is clear from this fit, that a constant release rate from the gel is unable to capture the dynamics of the data. This can be seen mathematically, since the rate of change of $D(t)$ with this formulation will be exponential as opposed to linear.

Considering instead that the rate of release of DCs from the gel is proportional to the number of DCs in the gel at any point in time, D_I, gives

$$\frac{dD_I}{dt} = -kD_I, \tag{7.19}$$

$$\frac{dD}{dt} = kD_I - d_{DC}D. \tag{7.20}$$

Optimising k from this model gives model solution in Fig. 7.11(b). Again, this simple assumption is unable to produce a model that can approximate the data. This highlights that, while a 6th order polynomial is not a biological representation of the release rate of DCs from the gel, it is able to approximate the data more accurately than models that were based on biological reason. Note that the expression for $u_{DC}(t)$ is only an approximation of the true release profile, motivated by the need to model the gel-release profile in the *in vivo* experiments in the following section.

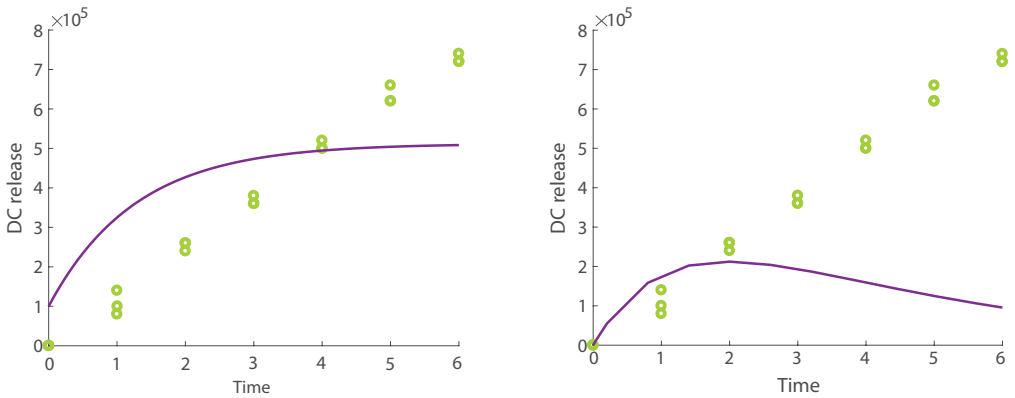

(a)

Figure 7.11: Fit of constant release and DC proportional release rates to the dendritic cells (DCs) released from soft gelatin gel systems. In (a) the constant release rate model in Eq. (7.18) is fit to the viable DCs released from. In (b) the DC proportional release rate model in Eqs. (7.19)-(7.20) is fit to the viable DCs released. The fitted model solution is the purple curve and the green circles are the data.

Table 7.5: Experiment-specific optimisation conditions Oh *et al.* (2017). Equations used to optimise each experiment are listed along with the state variables considered and parameters fitted or fixed. Note that Ad/IL12/GMCSF has been shortened to Ad/I/G

	Experiment				
	PBS & Gel	Ad/I/G	DC	DC+Ad/I/G	DC+Ad/I/G+Gel
Relevant equations	Eq. (7.8)	Eq. (7.1) Eq. (7.2) Eq. (7.3) Eq. (7.4) Eq. (7.5) Eq. (7.6)	Eq. (7.8) Eq. (7.11) Eq. (7.12) Eq. (7.13) Eq. (7.14)	Eq. (7.8) Eq. (7.9) Eq. (7.10) Eq. (7.11) Eq. (7.12) Eq. (7.13) Eq. (7.14)	Eq. (7.8) Eq. (7.9) Eq. (7.10) Eq. (7.11) Eq. (7.12) Eq. (7.13) Eq. (7.14)
Variables	U	U, I, V A, H K	U $A_I, A_A H$ K	U, I, V $A_I, A_A H$ K	U, I, V A_I, A_A, H K
Params fit	r, L, U_0	β, U_0 κ	$s_{AU}, U_0,$ κ	$r_{AI}, s_{AI}, U_0,$	$a, b, U_0,$
Params fixed (Table 7.6)	-	r, L	$r, L,$ d_{AI}	$r, L, \beta,$ d_{AI}, κ	$r, L, \beta,$ $d_{AI}, r_{AI}, s_{AI}, \kappa$
Params fixed (Table 7.2)		d_V, α, s_H, d_H d_I, s_A, d_A s_{KH}, s_{KA}, d_K	$s_H, d_H,$ d_A s_{KH}, s_{KA}, d_K	$d_V, \alpha, s_H, d_H,$ $d_I, s_{AU}, d_A,$ s_{KH}, s_{KA}, d_K	$d_V, \alpha, s_H, d_H,$ d_I, s_{AU}, d_A s_{KH}, s_{KA}, d_K

7.3.2 *Tumour growth under treatment with DCs and oncolytic adenovirus co-expressing IL-12 and GM-CSF*

In a similar manner to the sequential fit to the data from Choi *et al.* (2012a) in Section 7.2, the model in Eqs. (7.8)-(7.14) was fit sequentially to the tumour time-series measurements of Oh *et al.* (2017) for PBS, gel, Ad/IL12/GMCSF, DC+Ad/IL12/GMCSF and DC+Ad/IL12/GMCSF+gel. Table 7.5 gives a summary of the fitting algorithm.

Oh *et al.* (2017) conducted two control experiments: one where the tumour growth was measured over time with a PBS injection and the other where the tumour growth was measured over time with an injected empty gel, see Fig. 7.12. In both of these experiments the underlying tumour growth should be identical; however, it is clear that they are different. Fitting r, L and U_0 with the model from Eqs. (7.8)-(7.13) in the absence of treatment and immune cells, i.e. $I = V = A_I = A_A = H = K = 0$ gave the fits in Fig. 7.12 and the value for the tumour growth rate and carrying capacity $r = 0.082$ and $L = 1800$ for the PBS injection, and $r = 0.127$ and $L = 12000$ for the gel. It was not

possible to deduce whether the gel influences the growth of the tumour or whether the difference was inherent heterogeneity. As such, the PBS control and gel control were fit together to given Fig. 7.12 and parameter values in Table 7.6. To fit the remaining *in vivo* treatment data sets, the underlying growth rate of the tumour was fixed to the parameter values obtained from the simultaneous fit of the PBS and gel data.

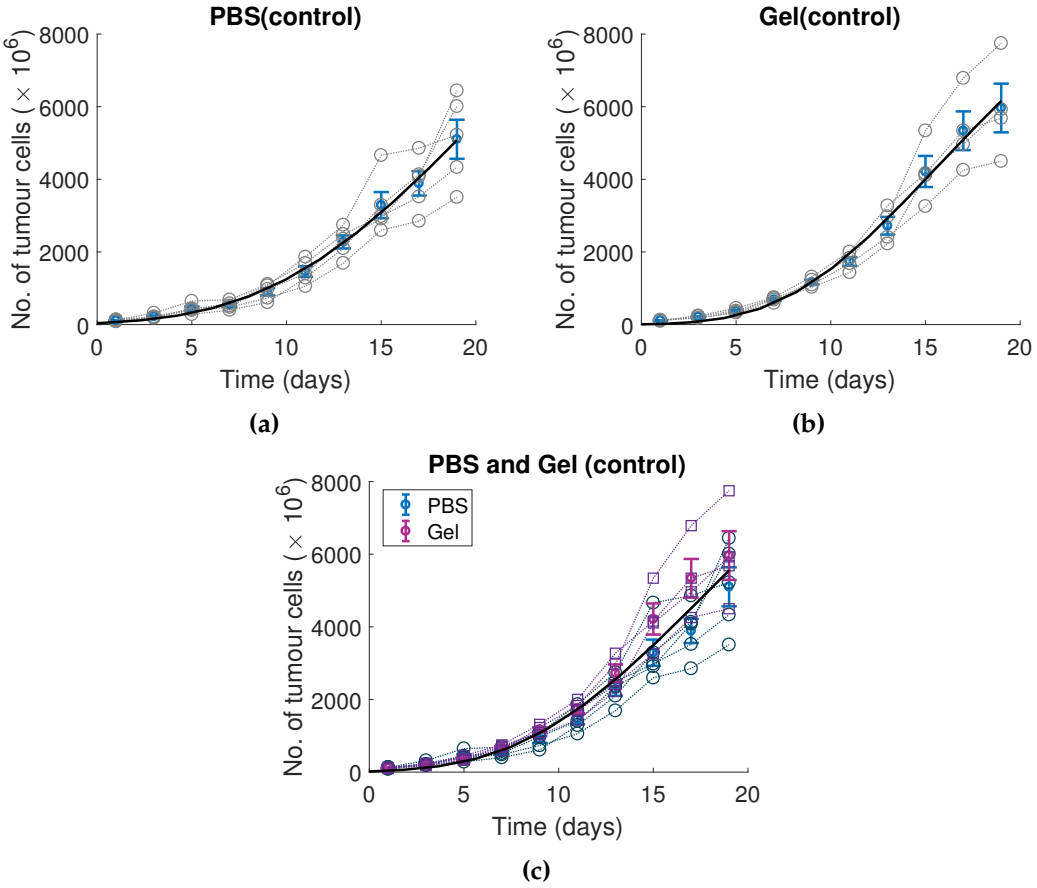

Figure 7.12: Output of the optimised control data, Table 7.5 for the (a) PBS (control) case and (b) gel (control) case. The individual mouse data are plotted as grey circles with the mean and standard error bar at each time point in blue. The model output is plotted as a solid black line. In (c), both data sets were fit together. The individual mouse data are plotted as purple squares for gel data and blue circles for PBS data with the mean and standard error bar at each time point in blue for PBS data and purple for gel data.

.

In the previous Section 7.2, the model parameters in Eqs. (7.1)-(7.6) were optimised to Choi *et al.* (2012a)'s B16-F10 cell tumour measurements in C57BL/6 mice under treatment with an adenovirus expressing IL-12 and GM-CSF. Oh *et al.* (2017) used the same adenovirus expressing IL-12 and GM-CSF and measured the size of Lewis Lung

Carcinoma (LLC) cell generated tumours under treatment with this virus in C57BL/6 mice. The treatment protocols were also different; Choi *et al.* (2012a) injected 1×10^{10} VP on days $0, 2$ and 4, whereas Oh *et al.* (2017) injected 2×10^{10} on day 0.

As there was no injection of DCs initially, it was assumed that immune stimulation is driven solely by the injected virus with the effects of endogenous DCs assumed negligible. As the modifications to the model were made for the addition of a DC injection, the original Eqs. (7.1)-(7.6) were used to fit the injection of Ad/IL12/GMCSF into LLC tumours. Additionally, since the underlying virus and mice are the same, the parameter values obtained in Section 7.2 for the Ad/IL12/GMCSF virus were used for the optimisation of the Ad/IL12/GMCSF virus in Oh *et al.* (2017)'s experiment. Note to obtain the original model in Section 7.2 from Eqs. (7.8)-(7.14), $A_I = 0$ in Eq. 7.11 and A_A are directly stimulated by infected cells I, i.e., $s_A I$.

As different tumour cell lines were used for the experiments of Choi *et al.* (2012a) and Oh *et al.* (2017), this was hypothesised to affect both the viruses infectivity β, along with the killing rate of the immune cells κ. Fixing all other parameter values to those in Table 7.2 for the Ad/IL12/GMCSF results and Table 7.6 for the underlying tumour growth and allowing the initial size S_0, the infectivity rate β and the killing rate κ to vary gave the fit in Fig. 7.13(a) and parameter values in Table 7.6.

To determine the true effectiveness of combined DC and Ad/IL12/GMCSF injections, Oh *et al.* (2017) also tested tumour growth under a single injection of 2.5×10^6 immature DCs. The likelihood of a DC recognising and becoming activated by a tumour cell is much lower than that of a DC recognising and becoming activated by an infected tumour cell. Since there was no virus present, the model in Eqs. (7.8)-(7.13) simplified by fixing $I = V = 0$

The *in vitro* experiment in Section 7.3.1 fitted the decay rate d_{DC} of a group of immature DCs and this value was used to approximate the decay rate d_{AI} of immature DCs. Assuming that the rate at which APCs stimulate helper cells and helper cells stimulate killer cells was independent of the type of antigen, the parameter values were taken from those used in Section 7.2, Table 7.2. The parameters left to fit were then the stimulation rate of the immature DCs, s_{AU}, and the killing rate of killing cells, κ. The killing rate κ was allowed to vary as previously it was fit considering a virus

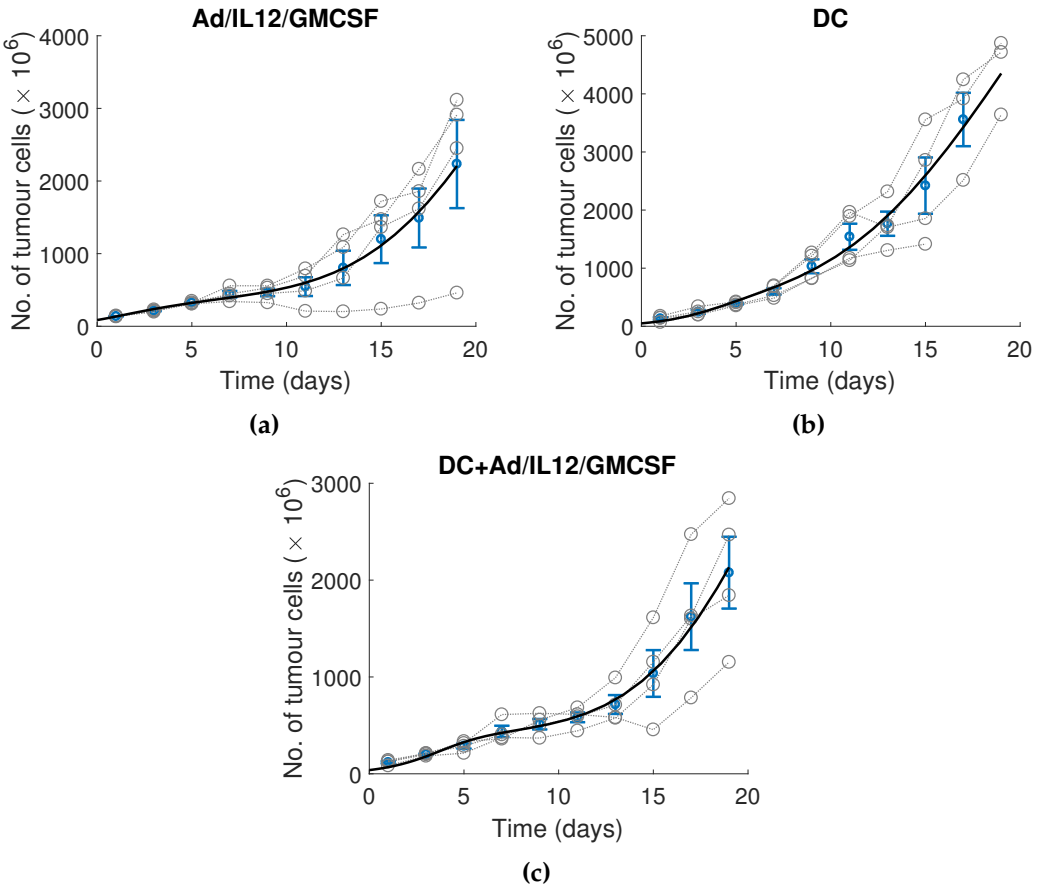

Figure 7.13: Output for the fit of the virus-tumour-immune models for (a) Ad/IL12/GMCSF injection, (b) single DC injection and (c) DC+Ad/IL12/ GMCSF single injection. The individual mouse data are plotted as grey circles with the mean and standard error bar at each time point in blue. The model output is plotted as a solid black line. All parameters fitted are in Table 7.6

treatment, see Fig. 7.5(b) and Table 7.6, providing optimised parameter values for β, U_0 and κ.

As expected the stimulation rate of immature DCs by tumour cells is very low, and the killing rate is on par to the one obtained in the previous section. This leads to the hypothesis that the killing rate κ is not affected by the antigen that has been used to stimulate the killer T cells.

In Section 7.2, and for the Ad/IL12/GMCSF fit in Fig. 7.13(a), the immature and mature DCs were considered to be one population of APCs. It was assumed that, since the experiment looked at only a virus treatment, APCs would only be stimulated by infected tumour cells. This term in the previous sections model incorporated the rate of recruitment of new immature DCs to the tumour site as well as the rate at which

they were stimulated to be activated DCs. For the injection of immature DCs and Ad/IL12/GMCSF, the immature and mature populations and the rate at which they are recruited and stimulated was considered separately as in Eqs. (7.8)-(7.13).

Assuming the rate s_{AU} that uninfected tumour cells stimulate immature DCs can be taken from the previous optimisation in Fig. 7.13(b), the rates r_{AI} and s_{AI} at which infected cells recruit inactivated APCs and also stimulate inactivated APCs were obtained. Fixing κ to be what was also obtained in the Ad/IL12/GMCSF optimisation, gave the optimised parameter values for r_{AI}, s_{AI} and U_0 with the simulated tumour cell number in Fig. 7.13(c) and parameter values in Table 7.6.

The final experiment of Oh *et al.* (2017) combined all the previous *in vitro* and *in vivo* experiments to examine the effects of virus and DC release from a hydrogel material. Oh *et al.* (2017) injected DC+Ad/IL12/GMCSF loaded gel into C57BL/6 mice with LLC tumours. The release profile of the DCs was fixed to be $u_{DC}(t)$ from the *in vitro* soft gel release profile optimised in Section 7.3.1. Once outside the gel, the dynamics of the tumour, DC and virus interaction were assumed to be the same as the model optimised to the DC+Ad/IL12/GMCSF tumour time-series measurement, Fig. 7.13(c).

Oh *et al.* (2017) added 2×10^{10} virus particles and 2.5×10^6 DCs to the gel which was more initial DCs than in the *in vitro* experiment. As there were no time-series data for the viral release profile from the gel, the function $u_V(t)$ was obtained from the data for the DC+Ad/IL12/GMCSF+gel experiments. All other parameter values were fixed to those obtained in the previous section. Assuming the release rate was linear with time, similar to the dynamics evident in the $u_{DC}(t)$ finite difference approximation, gave the formula

$$u_V(t) = \begin{cases} at + b, & \text{for } t \leqslant 6 \\ 0 & \text{otherwise} \end{cases}$$

where $a > 0$ and $b \geqslant 0$. Fixing all parameters to that obtained in Table 7.6, it was then possible to fit for a and b and U_0 to give Fig. 7.14 and the parameter values in Table 7.6. A full summary of the experiment-specific sequential optimisation followed above for the five data sets can be found in Table 7.5.

As evident in Fig. 7.14(a), the model is able to approximate the data. The optimisation returns a release profile for the virus, plotted in Fig. 7.14(b), that is similar to that

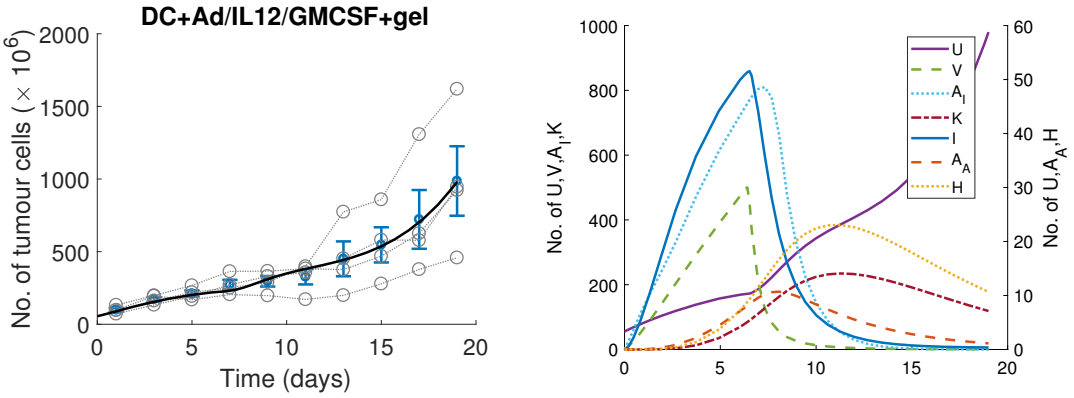

(a) (b)

Figure 7.14: Output of the optimised virus-tumour-immune models for the gel DC+Ad/IL12/GMCSF, see Table 7.5. In (a) the individual mouse data are plotted as grey circles with the mean and standard error bar at each time point shown in blue. The model outputs are plotted as solid black lines. In (b) the model simulations for $U, I, V, A_I, A_A H$ and K are plotted as numbers of cells

of that of the DCs, by definition. From the plot of all the populations in Fig. 7.14(b), it is clear that the initial immune response is driven by a large increase in helper T cells consecutively with mature APCs. This then prolongs the killer immune cell population's survival. From the model, it does appear though, that it is the initial viral infection that drives the tumour population down significantly. From this, it is possible to investigate how the release profile of the gel could be altered to optimise and reduce the tumour burden further.

7.4 OPTIMAL RELEASE PROFILE FOR DC+AD/IL12/GMCSF-LOADED GEL

As seen in the previous section, the gel-based medium effectively delivered a sustained therapeutic efficacy for the Ad/IL12/GMCSF treatment combined with a population of immature DCs. Unfortunately, due to high costs and large multitude of possible engineered derivatives, Oh *et al.* (2017) were not able to determine whether they had created a gel with an optimal treatment release profile. Using the model parameters for the DC+Ad/IL12/GMCSF+gel experiment of Oh *et al.* (2017), it was possible to investigate whether the gel's release profile could be altered to result in a more effective therapy using an exhaustive numerical approach.

Table 7.6: Parameter estimates from the sequential optimisation of the model following the algorithm in Table 7.5 to the experimental measurements of Oh *et al.* (2017). Note that Ad/IL12/GMCSF has been shortened to Ad/I/G.

	Param	Units	Description	PBS& Gel	Ad/I/G	DC	DC+Ad/I/G	DC+Ad/I/G+gel
Fit	d_{AI}	day^{-1}	Immature DCs decay rate			0.7889	0.7889	0.7889
	L	cells$\times 10^6$	carrying capacity	14000	14000	14000	14000	14000
	r	day^{-1}	growth rate	0.10	0.10	0.10	0.10	0.10
	U_0	cells$\times 10^6$	initial tumour size	20	86	50	41	55
	β	day^{-1}	infection rate	-	0.7286	-	0.7286	0.7286
	κ	day^{-1}	killing rate	-	0.8231	0.5633	0.8231	0.8231
	s_{AU}	day^{-1}	APC activation rate by U	-	-	5.5×10^{-6}	5.5×10^{-6}	5.5×10^{-6}
	r_{AI}	day^{-1}	recruitment rate of A_I	-	-	-	0.0006	0.0006
	s_{AI}	day^{-1}	APC activation rate by I	-	-	-	0.0001	0.0001
	a		linear release slope	-	-	-	-	157
	b		initial linear release	-	-	-	-	43
Fixed (Table 7.2)	α	virus $\times 10^{10}$	viral burst size	-	3500	-	3500	3500
	d_I	day^{-1}	burst rate	-	1	-	1	1
	d_V	day^{-1}	viral decay rate	-	2.3	-	2.3	2.3
	d_A	day^{-1}	decay of APCs	-	0.23	0.23	0.23	0.23
	d_H	day^{-1}	decay of helper T cells	-	0.23	0.23	0.23	0.23
	d_K	day^{-1}	decay of killer T cells	-	0.35	0.35	0.35	0.35
	s_A	day^{-1}	APC activation rate	-	1.2	-	-	-
	s_{KA}	day^{-1}	APC activatet killer T cell	-	7.1	7.1	7.1	7.1
	s_H	day^{-1}	helper T cell activation	-	0.78	0.78	0.78	0.78
	s_{KH}	day^{-1}	helper T cell activate K	-	1.6	1.6	1.6	1.6

To investigate possible optimal release profiles from the gel, three general release rate functions were chosen: constant, linear and sigmoidal, given by

$$f(x) = \frac{A_0}{tr}, \qquad f(x) = ax + b \qquad f(x) = \frac{A}{1 + e^{-k(x-x_0)}}, \tag{7.21}$$

where A_0 is the initial amount of either DCs or virus, tr is the length of time the treatment is released from the gel, a and b are the gradient and initial release rate, and A, k and x_0 are the maximum release rate, steepness of the curve and the midpoint of the curve. Fixing the total virus and DCs released over tr days to the V_0 and D_0 amounts determined in the previous section gives the constraint

$$V_0 = \int_0^{tr} u_V(s)ds, \quad D_0 = \int_0^{tr} u_{DC}(s)ds, \tag{7.22}$$

where $u_V(t > tr) = u_{DC}(t > tr) = 0$, and restricts the parameter search space. Fixing all parameter values not related to the release curves to those in the DC+Ad/IL12/GMC SF+gel column in Table 7.6, the tumour size on day 20 under different gel release profiles was simulated using Eqs. (7.8)-(7.13).

Starting with the constant release function described above in Eq. (7.21), the release period, tr, was allowed to be independent for DCs and virus. Varying this constant release rate gave the tumour size on day 20 in Fig. 7.15. To illustrate how the tumour growth changes under different constant release profiles, two simulated release profiles corresponding to the red points in Fig. 7.15 are plotted in Fig. 7.16. It is clear there is a major shift in the dynamics of the tumour growth, depending on the length of time that the DCs and virus are released from the gel, and a global minimum of approximately $10mm^3$ is achieved.

The original gels developed by Oh *et al.* (2017) had an increasing linear release, see Fig. 7.10. Considering variations on this linear release rate could improve the efficacy of the therapy. Assuming that the gradient of the release rate from the gel is increasing, i.e., $a > 0$, then using Eq. (7.22) to conserve the total amount of virus and DCs released from the gel, leaves two free variables to describe the linear release rate from the gel: the length of time the gel is releasing, tr, and the initial release rate, b. By fixing the release time tr to be equal for the virus and DCs, the values of b and tr were simulated to give

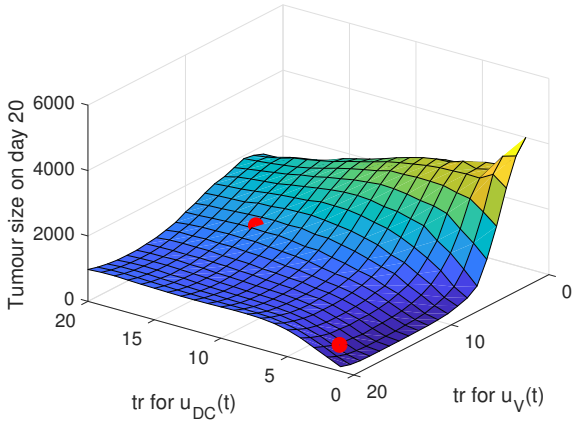

Figure 7.15: Tumour size at day 20 as a function of the constant gel-release period, tr, which varies for the virus ($u_V(t)$) and DCs ($u_{DC}(t)$), see Eq. 7.21. The red points correspond to the simulated release profiles in Fig. 7.16.

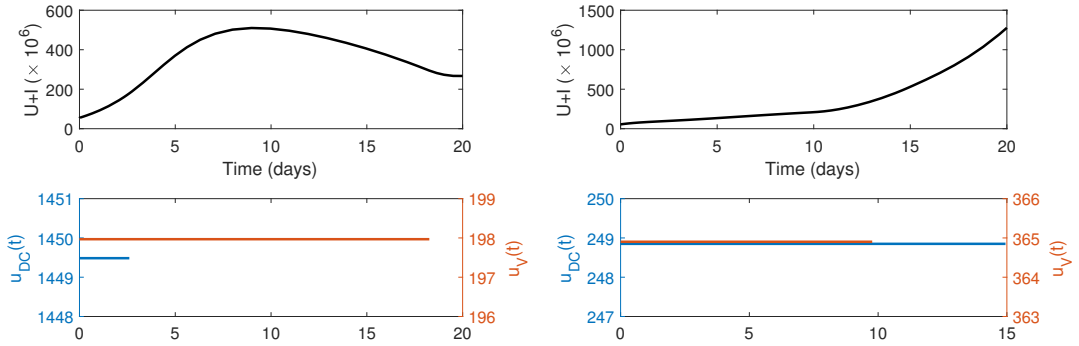

Figure 7.16: Constant gel-release profiles for the DCs ($u_{DC}(t)$) and virus ($u_V(t)$) where the release period, tr, corresponds to the red points in Fig. 7.15 where (a) $tr = 3$ for DCs, $tr = 18$ for virus, and (b) $tr = 15$ for DCs, $tr = 10$ for virus. The top row of figures corresponds to the total number of tumour cells $U + I$ and the bottom row of figures is the corresponding release profile.

different tumour sizes at day 20, see Fig. 7.17. To illustrate how the tumour growth changes under different release profiles, two linear release profiles corresponding to the red points in Fig. 7.17 are simulated in Fig. 7.18. The global minimum achieved under an increasing linear release in Fig. 7.17 is 500mm^3.

The tumour size under treatment with a gel releasing at a increasing linear rate is clearly influenced by how long the gel releases the virus and DCs, i.e. tr, see Fig. 7.17. To investigate how different values of tr for the virus and DC might influence this tumour size minimum, b was fixed to 41.2 for the virus and DCs and tr was allowed

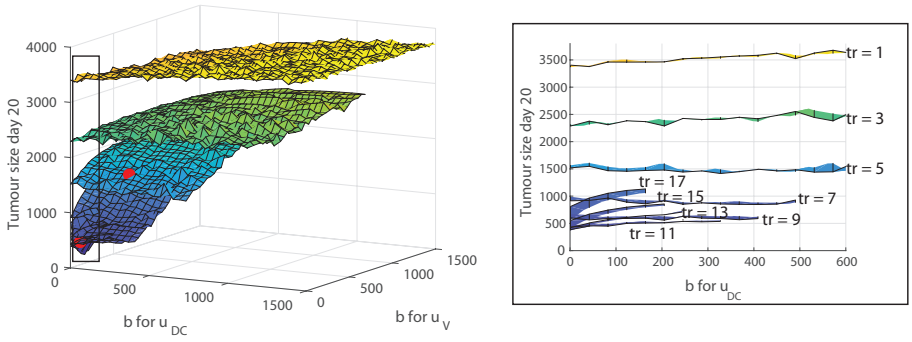

Figure 7.17: Tumour size at day 20 as a function of the gel-release period, tr, and the initial release rate, b, for the virus ($u_V(t)$) and DCs ($u_{DC}(t)$). Each plane corresponds to the labelled value of tr in the inset and the red points correspond to the simulated release profiles in Fig. 7.18.

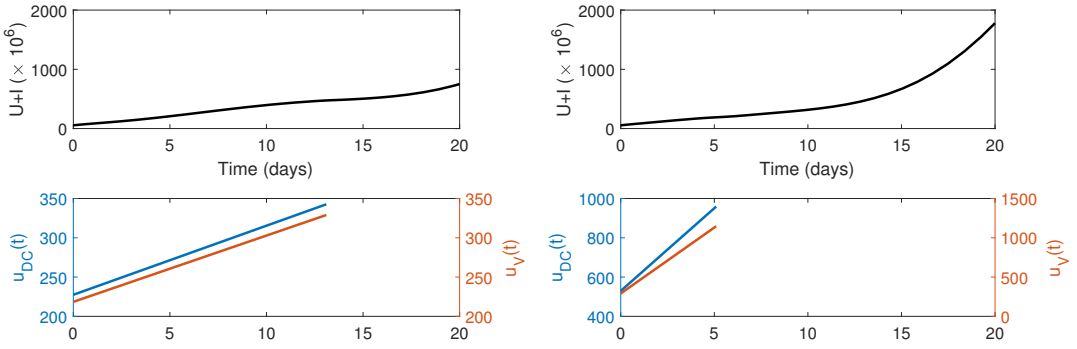

Figure 7.18: Increasing linear gel-release profiles for the DCs ($u_{DC}(t)$) and virus ($u_V(t)$) where the initial release rate and release period for each vector corresponds to the red points in Fig. 7.17 where (a) $b = 154$ for DCs, $b = 13$ for virus and $tr = 13$, and (b) $b = 358$ for DCs, $b = 18$ for virus and $tr = 5$. The top row of figures correspond to the total number of tumour cells $U + I$ and the bottom row of figures is the corresponding release profile.

to vary, see Fig. 7.19. Interestingly, this simulation resulted in a qualitatively similar optimisation surface to that in Fig. 7.15, suggesting that a very short release period for the DCs and a release period of 10 to 15 days for the virus may be able to achieve a global minimum of 60mm^3.

While the gel release mechanisms measured by Oh *et al.* (2017) had an increasing gradient, it is worth considering how effective a treatment would be when released at a decreasing linear rate. In contrast to the previous linear-release investigations,

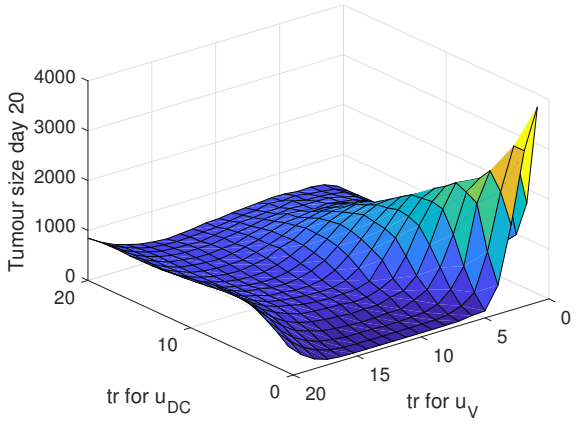

Figure 7.19: Tumour size at day 20 for increasing linear release rates as a function of the release period, tr, for the virus ($u_V(t)$) and DCs ($u_{DC}(t)$) fixing the initial release rate at $b = 41.2$.

a negative linear release function meant that under the constraint in Eq. 7.22, if the function crossed the horizontal axis before tr, i.e. $-b/a < tr$, then the release function would be zero at $t \geqslant -b/a$. Alternatively, if $-b/a > tr$ then the function would always be positive. This meant that modifying the constraint in Eq. 7.22 to be

$$D_0 = \int_0^{-b/a} (as + b)ds, \quad V_0 = \int_0^{-b/a} (as + b)ds,$$

would mean that the value of the dosage from the gel could be less than or equal to D_0 and V_0 and that initial release rate b would be the only free variable. In Fig. 7.20, the tumour size on day 20 after treatment with a gel with a decreasing release gradient has been plotted. It is clear that there are values for which the tumour size is minimised. Time evolutions of the release profiles corresponding to the red points in Fig. 7.20 are plotted in Fig. 7.21. A quite interesting result from Fig. 7.21 is the global minimum of 20mm^3 is obtained when both the initial rate of DCs released and the total amount of DCs released is low, see the $u_{DC}(t)$ profile in Fig. 7.21(b).

Using the constraint in Eq. 7.22, there are two possible formulations of A for either an increasing or decreasing sigmoidal release rate:

$$A = \frac{D_0 k}{\ln\left(\frac{1+e^{k(tr-x_0)}}{1+e^{-kx_0}}\right)}, \qquad A = \frac{-D_0 k}{\ln\left(\frac{1+e^{-k(tr-x_0)}}{1+e^{kx_0}}\right)},$$

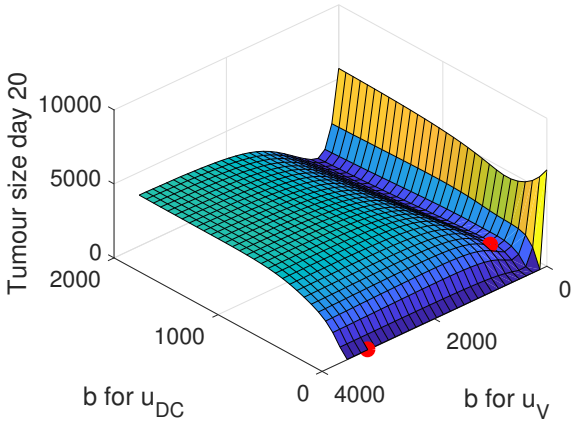

Figure 7.20: Tumour size at day 20 for a gel releasing virus, $u_V(t)$, and DCs, $u_{DC}(t)$, at a linear rate with a decreasing gradient. The initial release rate b has been varied for both the virus and the DCs. The red points correspond to the simulated release profiles in Fig. 7.21.

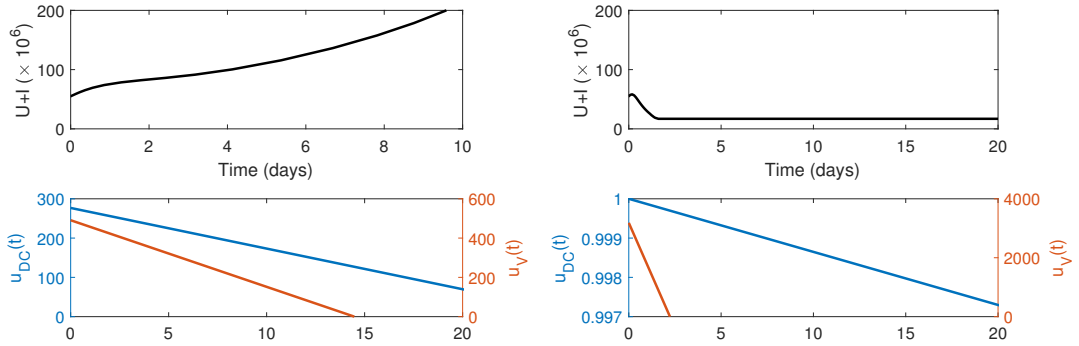

Figure 7.21: Decreasing linear gel-release profiles for the DCs ($u_{DC}(t)$) and virus ($u_V(t)$) where the initial release rate b corresponds to the red points in Fig. 7.20 where (a) $b = 277$ for DCs, $b = 490$ for virus, and (b) $b = 1$ for DCs, $b = 3186$ for virus. The top row of figures correspond to the total number of tumour cells $U + I$ and the bottom row of figures is the corresponding release profile.

where the sign of k depicts either an increasing or decreasing sigmoid function. If the profiles for the virus and the DCs are considered equivalent, the increasing sigmoidal release results in the range of tumour sizes plotted in Fig. 7.22(a) for $tr = 18$. Reducing tr reduces the surfaces overall tumour size until $tr = 10$, after which point the surface's minimum begins to increase again, see Fig. 7.22(b) for $tr = 10$. In Fig. 7.23 are simulations of the release profiles corresponding to the red points in Fig. 7.22. For a decreasing sigmoidal release curve, variations in the curve steepness k and curve

midpoint x_0 gives Fig. 7.24(a). It is clear this dosage profile performs the worst out of possible gel profiles, with an example simulation in Fig. 7.24(b).

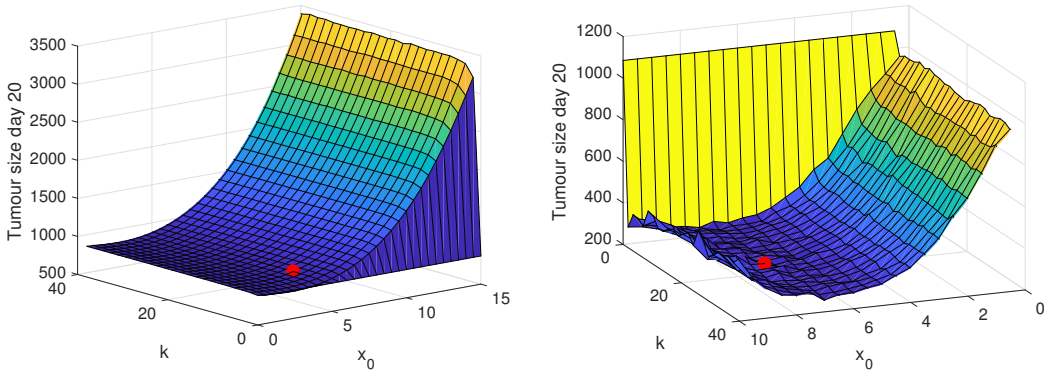

(a) **(b)**

Figure 7.22: Simulations of increasing sigmoidal release profiles for the DCs ($u_{DC}(t)$) and virus ($u_V(t)$) where k and x_0 are varied for the fixed value of (a) $tr = 18$ and (b) $tr = 10$. The red points correspond to the release profiles simulated in Fig. 7.23.

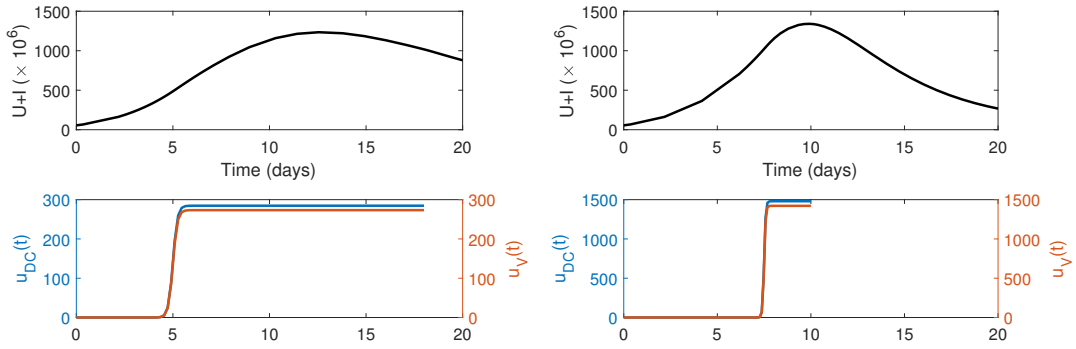

(a) **(b)**

Figure 7.23: Simulations of increasing sigmoidal release profiles for the DCs ($u_{DC}(t)$) and virus ($u_V(t)$) corresponding to the red points in Fig. 7.22 where (a) $k = 8.6$, $x_0 = 5$, $tr = 18$ and (b) $k = 24$, $x_0 = 7.5$, $tr = 10$. The top figure corresponds to the total number of tumour cells $U + I$ and the bottom figure is the corresponding release profile.

7.5 SUMMARY

The two mathematical models presented in this chapter were used to identify the primary processes in the interaction between a population of tumour cells and an

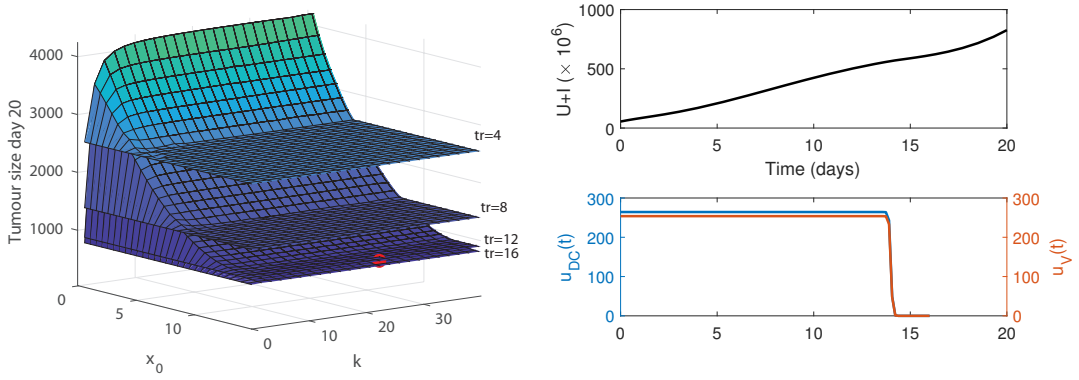

(a) **(b)**

Figure 7.24: Simulations of increasing sigmoidal release profiles for the DCs ($u_{DC}(t)$) and virus ($u_V(t)$) where (a) k and x_0 are varied for the fixed value of $tr = 18$. The red point in (a) corresponds to the release profile simulated in (b) where $k = 24$, $x_0 = 14$. The top figure corresponds to the total number of tumour cells $U + I$ and the bottom figure is the corresponding release profile.

oncolytic adenovirus co-expressing IL-12 and GM-CSF with and without a DC injection. The results of Choi *et al.* (2012a) and Oh *et al.* (2017) related to this therapy, were successfully replicated by parameter optimisation, see Fig. 7.3-7.5, 7.9 and 7.12-7.14. It is evident through visual inspection of these figures, that the model, along with the hierarchical fitting algorithm in Table 7.1 and 7.5, provides a reliable representation of the data. Goodness of fit measurements in Table 7.3 for the optimisation to variants of an Ad/IL12/GMCSF virus (Section 7.2), confirm that the model closely approximated the true system with R^2 values greater than 0.98 and Pearson's correlation coefficient greater than 0.87.

Heterogeneity within individual mice tumour responses is visible under all treatment's investigated in this chapter. Most significant is the tumour response to an unmodified oncolytic adenovirus (Ad), Fig. 7.4. There are three noticeable subgroups of treatment responses: those that died early; low responders, those whose tumours grew slowly until about day 10, after which point the tumours grew exponentially; and high responders, those with small tumours over the whole duration of the experiment. To examine the differences behind the heterogeneity between the subgroups, and to see whether the model was sufficiently flexible to embody all the observed behaviour, the model was optimised to each subgroup. All were well explained by the model. The sub-

groups had slightly different rates of infectivity of the treatment, but more importantly started with different initial tumour sizes. Examining the models for the subgroups and that for all the data, Fig. 7.4, it is evident that the long-term dynamics of these underlying subgroups are qualitatively similar.

Quantifying the effects of IL-12 and GM-CSF combinations on treatment efficacy is possible through optimising parameters in the model to the experiments of Choi *et al.* (2012a). The nature of the hierarchical experiments allows for the primary differences between the immunostimulatory oncolytic adenoviruses to be examined. Comparing killer-T-cell-induced apoptosis rates, κ, for the Ad/IL12 and Ad/GMCSF viruses, Table 7.2, it is clear that expression of cytokine IL-12 results in a higher immune cell killing rate. Therefore, the addition of IL-12 has a greater effect on improving immune-cell killing rate κ, and consequently tumour-cell death. This is also evident when comparing the tumour time-series measurements obtained in Fig. 7.5(a) and 7.5(b) where it is clear that Ad/IL12 has a greater antitumour potency then Ad/GMCSF. The largest immune-cell killing rate was obtained for co-expression of both cytokines -Ad/IL12/GMCSF. This suggests that it is only with both cytokines that the treatment reaches its maximal effectiveness in stimulating the immune system to attack the tumour cells.

While the results of the Ad/IL12/GMCSF experiments reduce the tumour population most significantly out of the virus-only five experiments, the finding that helper T cell activation is decreased requires further investigation. How exactly this might be hindering the immune interaction and the obtaining of optimal treatment efficacy will be the subject of future work. In Fig. 7.5, it can be seen that only one mouse in the Ad/IL12/GMCSF experiment had tumour growth after day 20. The optimisation results propose that tumour cells in this case may have escaped immune removal by down-regulation of helper T cell activation.

Since Oh *et al.* (2017) used the same Ad/IL12/GMCSF virus developed by Choi *et al.* (2012a) to treat LLC tumour cells, it is possible to quantify further the impact of this combined cytokine combination on the killer T cell killing rate. Since the only difference between the Ad/IL12/GMCSF tumour time-series experiments was the underlying tumour cell type, it was assumed this would only influence the infectivity

rate, β, and the killing rate, κ. Both the infectivity rate of virus particles and the killing rate of the killer T cells was decreased when treating LLC tumours. This shows that it is quite possible that immune activity may be driven by the underlying tumour cell type.

To investigate the possible effects of immune heterogeneity, individual responses to changes in immune efficacy were simulated. The analysis in Fig. 7.6 suggests there is a counter-intuitive relationship between treatment efficacy and immune stimulation rates. The dependence of treatment efficacy on APC simulation, s_A, and helper T cell stimulation, s_H, differs significantly (Fig. 7.6(a) and 7.6(b)) when using the model optimised for Ad/IL12/GMCSF on B16F10 tumour cells (Table 7.2). Simulations show that increasing the stimulation rate of APCs has a negative effect on the treatment efficacy, allowing for the tumour cell population to escape the control of treatment and grow unbounded. However, increasing helper T cell stimulation rates has a positive effect on treatment efficacy, allowing for the tumour cell population to be controlled for longer and, for certain parameters, to be completely eliminated. These results suggest that there is a sensitive threshold of APC stimulation, above which a negative effect on the immune response occurs. Biologically, this could signify an over-stimulation of immune cells results in the original virus treatment becoming ineffective as the immune cells kill off the virus. On the other hand, increased stimulation of helper T cells consistently promoted tumour cell death. The results presented are purely hypothetical and suggest that further investigations of this cancer treatment could examine how increasing the expression of IL-12 cytokine and decreasing GM-CSF expression has a downstream effect of the probable increase in helper T cell stimulation and decrease in APC stimulation.

Heterogeneity in immune-cell-induced apoptosis is a key determinant of treatment outcome. Perturbations in the rate of killer-T-cell-induced apoptosis, κ, for the Ad/IL12/GMCSF model, see Fig. 7.6(c), demonstrate a very interesting phenomenon: the existence of a parameter window for which the treatment is relatively ineffective compared to parameter values outside this interval. An extremely sensitive non-linear relationship exists between treatment outcome and κ. In Fig. 7.6(c), at lower values of κ, the tumour population is initially controlled with slow growth over time, reaching a turn-

ing point after which tumour volume decreases. It may be that the immune system is able to control the tumour growth even with this smaller killing rate.

Interestingly, if the killer T cell killing rate is increased, the tumour volume at the turning point increases and, for a range of κ values, the tumour population is able to grow unbounded. Increasing κ further, the tumour population can be completely eradicated (in this model, we assume complete eradication is obtained when the total tumour population drops below 10^{-3}). From this result, the different responses in the mice in Fig. 7.6 (i.e. tumour eradication or unbounded growth) could possibly be explained by a difference in the immune cell killing rate of tumour cells. These results also suggest that there may be a window of killer-T-cell-induced apoptosis rates for which the treatment is ineffective, but outside of which either controlled tumour growth within the time period of 33 days is achieved or complete eradication.

In Fig. 7.6(c), it is also evident that there is an exchange in the dominant processes acting as a function of the cell-induced apoptosis rate, κ . For high values of κ, it is clear that tumour cells are predominantly removed by the immune system, which is why the tumour is eventually completely eradicated. However, reducing the value of κ results in the initial decrease in tumour cell numbers due to viral interactions rather than the immune system. This result reinforces the importance of stimulating the correct mechanisms at the right stage of tumour growth when investigating improvements for combined oncolytic virotherapy and immunotherapy. This sensitivity of the killer T cell response was also seen in the analysis of de Pillis *et al.* (2005), detailed in Section 3.2.4

While it is helpful to understand how the immune characteristics can be manipulated to improve the outcome of treatment, realistically this may be challenging. Oh *et al.* (2017) decided to further extend the work of Choi *et al.* (2012a) to consider an additional injection of immature DCs. By extending the model in Eqs. (7.1)-(7.6) to consider the activation of APCs from immature to mature APCs, Eqs. (7.8)-(7.14), it was possible to reproduce their tumour time-series measurements, see Fig. 7.13. Following this, Oh *et al.* (2017) investigated a gel-release mechanism for delivery of their DC+Ad/IL12/GMCSF therapy. They found that tumour size under the gel-release mechanism decreased by 50% on day 20; however, tumour eradication was not obtained, see Fig. 7.14(a). To help understand ways of improving this therapy, it was

necessary to obtain the release profile of the virus from the gel, something not measured by Oh *et al.* (2017). By fixing the parameter values in the model to all previous optimisations, it was possible to obtain the curve describing the rate at which the virus was released from the gel, see Fig. 7.14(b). Using this model as a platform, it was then possible to investigate alternative gel-release profiles and determine if an optimal exists.

One of the simplest gel-release profiles is a constant. This is qualitatively similar to what could be thought of as a prolonged transfusion of a drug or treatment. Fixing the underlying model parameter values to those in Table 7.2 and 7.6 and simulating unique lengths of time for the virus and DCs to be released from the gel gives the tumour size on day 20 in Fig. 7.15. There is a global minimum tumour size of 10mm^3 achieved for a very short release period of the DCs and a prolonged release period of the virus. This implies that an initial burst of a large number of DCs stimulates an immune response that under a prolonged constant release of virus from the gel is able to result in approximate tumour eradication.

The original gel-release profile was approximately linear, and a natural extension was to examine the tumour volume under different linear releases. If the release period tr is equivalent for both the DCs and the virus, as is the case with the original gel, an increasing linear release is unable to achieve a tumour volume much lower than what was already achieved with the current gel, see Fig. 7.17. A gel with a release period of approximately $tr = 11$ and initial release rate of $b = 50$ is able to reduce the tumour volume by 50% of what was obtained in the original gel.

Allowing for the gel to have different increasing linear release periods for the virus and DCs results in a minimum tumour size at day 20 of 60mm^3, see Fig. 7.19. Interestingly, to achieve this minimum, similar constraints are needed on the release period for the DCs and virus as that of the constant gel-release simulations in Fig. 7.15. This reinforces that tumour treatment is significantly improved when the DCs are given very rapidly and the virus is given over an extended period of time. The converse to this is seen when considering a gel with a decreasing linear release rate, see Fig. 7.20. A minimum tumour size of 20mm^3 is achieved by releasing a very small amount of DCs for a long time, with a rapid release of the initial virus dose, see Fig. 7.21(b). This

infers that if the immune response is not too heavily stimulated initially, the virus is able to reduce the tumour volume considerably.

A sigmoidal gel-release profile was unable to achieve a tumour volume as low as that of the constant and linear release profiles. Simulations of increasing sigmoidal release profiles in Fig. 7.22 show that as t_r is decreased from 18 to 10 days, it is possible to obtain a low tumour volume of 225mm^3, which is still an improvement on the original gel's efficacy. Unfortunately, changing the release profile to be a decreasing sigmoidal curve increases the tumour size overall, see Fig. 7.24. For low enough release periods, e.g. $t_r = 16$, there is still a reduction in tumour volume when compared to the original gel. However, this is still much larger than if an optimal constant or linear release profile is used.

One major assumption in the models developed in this chapter is that the rate at which immune cells are stimulated is independent of the antigen type. The immune response modelled in this chapter allows for killer T cells to kill both uninfected and infected tumour cells; however, in reality immune cells are antigen specific (Janeway *et al.*, 2005). In response to an oncolytic virus there will be two types of antigen: tumour-specific and virus-specific. This results in immune cells becoming activated as either tumour-antigen or virus-antigen specific. In Eq. 7.11, this was considered by allowing for immature APCs to be stimulated by both uninfected tumour cells (tumour-antigen) and infected tumour cells (virus-antigen). Unfortunately, there is insufficient data to determine the individual activation and stimulation rates of the antigen specific immune cells for the APCs, helper cells and killer T cells. As such, they were modelled as one activated immune population, similar to the works of Wares *et al.* (2015) and Kim *et al.* (2015) (Section 3.2.4).

From the results in this chapter, it is clear that systems of ODEs can be used to replicate data and determine possible treatment improvements. The limitation in this style of modelling is the inability to consider the possible spatial dependency of tumour growth or viral movement. It is possible that the position of the intratumoural injection or the gel could significantly influence the outcome of treatment. Additionally, while the effects of heterogeneity were discussed through a parameter sensitivity analysis, it is not possible to model a heterogeneous population of cells through an ODE or

PDE system. In the following chapter, an agent-based model is developed that aims to capture these missing aspects and investigate them in relation to oncolytic virotherapy.

8

ENHANCING ONCOLYTIC VIROTHERAPY: INSIGHTS FROM A VORONOI CELL-BASED MODEL

OVERVIEW

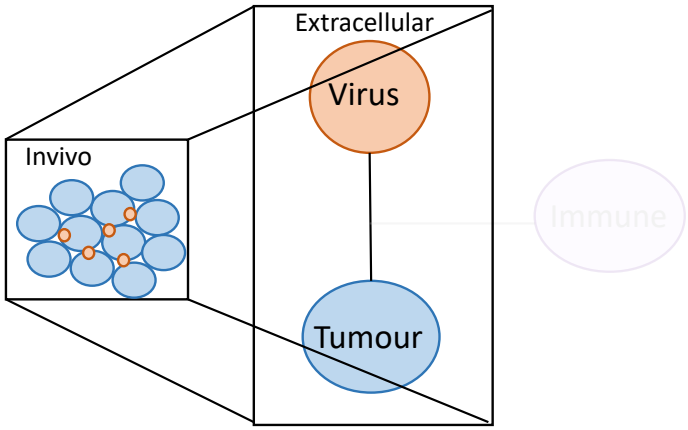

Figure 8.1: Subset of Fig.1.1, summarising the investigation of the virus-tumour interaction in this chapter

The previous Chapters 5-7 presented investigations of oncolytic virotherapy using predominantly mean-field mathematical approaches. It is well known that spatial interactions can influence the behaviour and outcome of cancer therapy. In this chapter, a spatially driven Voronoi cell-based model (VCBM) is developed to investigate the hindrance of oncolytic virotherapy previously mentioned in Chapter 6: the rapid decay of virus particles within the body. The VCBM derived captures the interaction between oncolytic virus particles and cancer cells in a 2-dimensional setting by using an underlying agent-based model framework, where the agents are cells defined by edges of a Voronoi tessellation. The sensitivity of treatment efficacy is investigated in response to the configuration of the initial treatment injections for different tumour shapes: circular, rectangular and irregular. Additionally, the effect of delaying the infection of cancer cells by modifying viral particles with alginate (a hydrogel polymer used in a range of cancer treatments) is investigated.

The work in this chapter has been submitted to the Journal of Theoretical Biology (Nov. 20 2018) entitled "Enhancing Oncolytic Virotherapy: Observations from a Voronoi cell-based Model ".

The rapid decay in the concentration of viral particles due to clearance and dispersion at the tumour site shortens the window of effectiveness for oncolytic virotherapy. The treatment needs to act quickly and effectively to compete with the division of the cancer cells. Additionally, the inability to efficiently distribute the viruses within solid tumours represents a significant barrier limiting the success of clinical trials (Liu *et al.*, 2007; Parato *et al.*, 2005). The relatively static viral distribution within a tumour is caused primarily by two factors: the non-uniformity of the tumour structure and the increase in viral clearance as a function of the number of infected tumour cells.

Regardless of whether the therapeutic viral vector has been administered through intravenous injection (discussed in Chapter 6) or intratumoural delivery (discussed in Chapter 7), inhomogeneous infection and diffusion of the viral particles will occur. Some studies have tried to improve the efficacy of oncolytic virotherapy by combining it with treatments to disrupt the tumour structure and reduce viral clearance, including degradation of the extracellular matrix (ECM) with relaxin (Ganesh *et al.*, 2007; Kim *et al.*, 2011b) and Anti-VEGF therapies (Kottke *et al.*, 2010). This chapter investigates *in silico* how coating the virus particles in alginate (a hydrogel polymer used in a range of cancer treatments) to delay viral infection could help overcome the effects of viral clearance and inhomogeneous infection and diffusion.

Mean-field mathematical models of an oncolytic virus interacting with cancer cells have been shown to effectively provide insight into a range of treatment perturbations (Chapters 5-7). For aggressive tumours, however, stochasticity in tumour cell characteristics and behaviours can be the dominant driver of cancer progression, and mean-field models are unable to fully capture this process.

In this investigation an agent-based approach (Section 3.3.2) is developed to model tumour formation and treatment with an oncolytic virus. A Voronoi tessellation is used in an off-lattice framework to mimic tumour formation. Researchers have demonstrated that Voronoi tessellations successfully replicate tumour histopathological images (Haroske *et al.*, 1996). Voronoi tessellations allow for tumour cells to be modelled as heterogeneous convex polygons which reflects the abnormal morphology of tumour cells. Therefore, the use of this Voronoi cell-based model (VCBM) allows for a more spa-

tially realistic representation of the interaction between cancer cells and virus particles compared to other off-lattice model formulations, see Section 3.3.1.

8.1 MODEL DEVELOPMENT

Agent-based models can be used effectively to simulate mechanical and physiological phenomena in cells and tissues, see Section 3.3. In off-lattice agent-based models, interactions between cells are usually described by forces or potentials, and position changes in cells can be obtained by solving an equation of motion (Metzcar *et al.*, 2019; Van Liedekerke *et al.*, 2015). The Voronoi cell-based model (VCBM) designed in this chapter is an off-lattice agent-based model that mimics tumour formation and treatment with an oncolytic virus. In the model, cells are generated from a set of points with boundaries obtained from a Voronoi tessellation. Viruses are modelled as a separate agent-based population that diffuses across the Voronoi tessellation of cells. The model evolution is driven by the virus and cell characteristics.

8.1.1 *Virus characteristics*

The success of oncolytic virotherapy relies on the inherent ability of viruses to replicate and lyse cells. Oncolytic viral particles are genetically engineered to replicate preferentially within tumour cells (Kim *et al.*, 2006b; Russell *et al.*, 2012). A summary of the infection process of an oncolytic virus and corresponding death of a tumour cell is shown in Fig. 8.2. Viruses are unable to distinguish between tumour cells and healthy cells and can infect both; however, it is assumed that the effects of viral infection of healthy cells are negligible as a result of the viral genetic modifications. More than one virus can infect a single cell (Phan and Wodarz, 2015; Syverton and Berry, 1947) but it is assumed here that the multiplicity of infection does not affect the replication rate.

The immune system is stimulated by the presence of virus-infected cells 2.3.3, initiating the clearance of extracellular virus particles. Virus-infected cells activate a cascade of killer T cells, and these cells clear viral particles from the tumour. In this model,

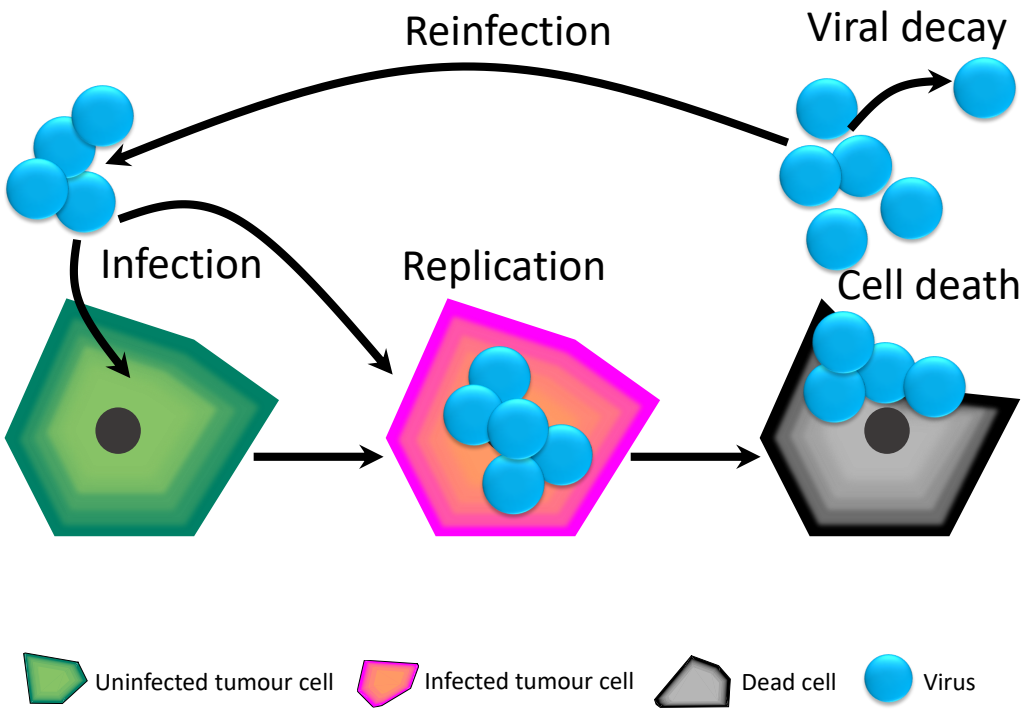

Figure 8.2: Oncolytic virus life cycle. Virus particles infect either uninfected or infected tumour cells. Once inside a cell, virus particles undergo replication for a period of time. Eventually they lyse the cell, causing it to burst, and release new viral progeny that will infect other tumour cells.

immune clearance and viral decay are proportional to the number of infected cells in a neighbourhood of a given virus particle, as defined by the quadrant within which the virus lies.

The movement of individual viral vectors in tumour tissues is governed by the structure of the tumour, see Section 2.4.4. Current continuous spatial models for oncolytic virotherapy either do not explicitly model viral movement (Wein *et al.*, 2003; Wodarz *et al.*, 2012) or model viral movement by classical diffusion (Friedman *et al.*, 2006; Mok *et al.*, 2009). Agent-based models that consider individual viral movement have similarly used lattice random walks to model individual viral movement through a tumour (Paiva *et al.*, 2011). However, since virus particles can struggle to diffuse due to the dense extracellular matrix and disorganised structure of the tumour cells, particles commonly can get stuck for long periods of time at their initial entry site (Kim *et al.*, 2006b). This is analogous to a population of particles diffusing anomalously. This difference in diffusive motion of the virus can be crucial to the outcome of oncolytic

virotherapy, as particles cannot disseminate and infect cells within the tumour if they get stuck at the periphery.

Anomalous diffusion, as opposed to classical diffusion or lattice random walks, has been chosen to model the possible crowding or trapping of viruses at the initial injection site. Anomalous diffusion is a diffusion process whose variance scales non-linearly with time. The analogy between anomalous diffusion and diffusive motion of macromolecules due to overcrowding has previously been discussed in Höfling and Franosch (2013). The movement of viral vectors through the tumour microenvironment is thus achieved using subdiffusion, a type of anomalous diffusion. In this way, the movement of viral particles can be modelled using a continuous-time random walk (CTRW), where a stable distribution is used to determine the waiting times between individual particles consecutive movement. In this model, anomalous diffusion of a population of virus particles is approximated on discrete-time intervals.

8.1.2 *Cell characteristics*

To model the interaction between an oncolytic virus and a growing tumour, consider five different types of cell agents: uninfected tumour cells, virus-infected tumour cells, dead tumour cells, empty space and normal healthy cells. The position of each cell in 2-D space is defined by a singular point and when all points are connected they form a lattice. The Voronoi tessellation of the lattice is used to define the edges of a particular cell in the VCBM and determine the neighbourhood of interaction for a particular point in the lattice, see Fig. 8.3(a).

The Voronoi tessellation is generated by determining the region of space where the Euclidean distance to a point is less than the distance to any other point in the lattice. The boundary of a particular cell is the line equidistant from that cell's point and another point in the lattice, such that the set of cells generated by all the points of the lattice forms the tessellation. Voronoi cells on the boundary of the tessellation will have infinite area, by definition. To avoid any interference from these boundary Voronoi cells, the generated grid of points is always made to be sufficiently larger than the simulation area so that the boundary cells do not influence the dynamics of the

model. The advantage of the chosen lattice topology is that cells are not fixed in space, and are not inherently confined to a particular arrangement.

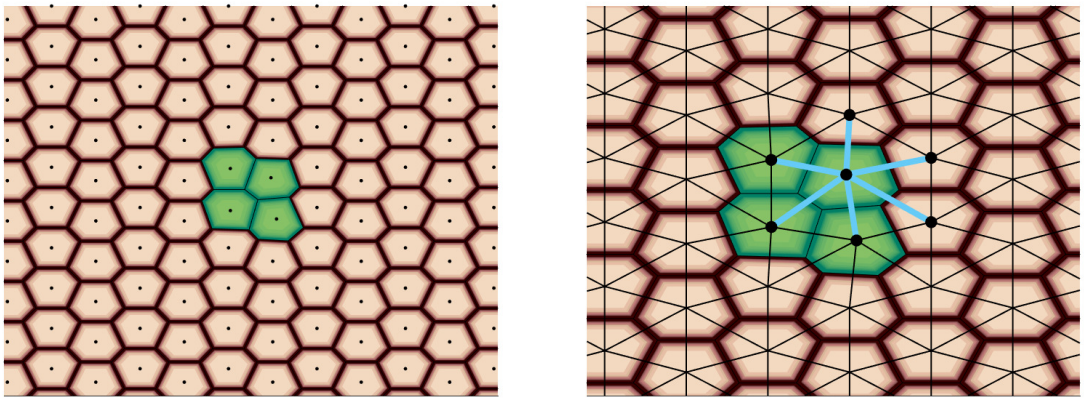

(a) (b)

Figure 8.3: Initial Voronoi tessellation. Healthy cells are coloured pale pink and tumour cells are bright green. The boundaries for each cell are represented by a solid line and the lattice points are small dots in the centres of the cells in (a). (b) shows the tessellation overlaid with the network of connected lattice points obtained using a Delaunay triangulation. The neighbourhood of interaction is indicated in blue for one point in the lattice.

A finite domain of tumour cells and the surrounding environment is considered and Dirichlet boundary conditions are employed (i.e. cell states are fixed beyond the boundary). The complete grid of points is larger than the necessary domain for the dynamics seen in all simulations in this study. Initially, the points in the lattice are arranged so that the corresponding Voronoi cells form a hexagonal tessellation (see Fig. 8.3(a)) analogous to other work in the literature (Buijs *et al.*, 2004; Lobo, 2014).

There are many mechanisms governing cell movement within a tumour, such as pressure-driven motility. The primary movement of tumour cells in the VCBM is driven by cell proliferation. The spatial relationship between points in the lattice is defined by a network of springs and modelled using Hooke's Law. The lattice employed uses the Hooke's Law formalism to maintain a fixed separation between mature cells by setting the spring rest lengths between the points of mature cells to be identical.

The neighbourhood of interaction for a particular Voronoi cell is defined as the neighbouring cells that share a connecting edge with it, i.e. the nearest neighbour set of points in the lattice that are joined to that point by a single spring, see Fig. 8.3(b).

These points are determined by taking a Delaunay triangulation of the lattice and finding the set of cells that are conntcted in the triangulation. Cells in the neighbourhood of interaction for a particular Voronoi cell are the cells that can influence the movement of that cell at each time step.

A known hallmark of cancer is rapid cell proliferation. For tumour cells to divide, there must be sufficient surrounding space and nutrients. Pressure from closely packed neighbouring cancer cells restricts the access of oxygen and nutrients, hence cells towards the centre of an enlarging tumour receive a smaller level of nutrients than those near the edge and tend to form a quiescent tumour cell population, see Section 2.2.2.

Neither virus-infected tumour cells nor healthy cells proliferate in the model. Typically, viruses replicate their genomes and generate new progeny by deregulating cell-cycle checkpoint controls and modulating cell proliferation pathways (Bagga and Bouchard, 2014). Hence, the likelihood of a virus-infected cell proliferating is low and the effects are taken to be negligible in the model. Additionally, to facilitate the rapid formation of a tumour in a static tissue environment, it is assumed that healthy cells divide at a much slower rate than tumour cells, so for the timescale and extent of the model, the effects of healthy cell proliferation are also neglected. It is also assumed that healthy cells do not die as viral particles do not replicate within them.

Once a cancer cell has died from viral-induced cell lysis, the remnants disintegrate over a period of time. Once a dead cell has disintegrated, it turns into empty space. In the model, there are cells designated as empty space. These cells are removed from the lattice and do not contribute to the force calculation for any individual cell. These empty cells are only part of the model to keep the size of each living cell bounded in the visualisation.

8.2 MODEL IMPLEMENTATION

At any given time, there exists a set of virus and cell agents, each obeying the rules defined below. Each cell is endowed with one of five possible states: uninfected tumour cell, virus-infected tumour cell, dead tumour cell, empty space or normal healthy cell. Uninfected tumour cells can either proliferate, move or become infected cells. Virus-

infected tumour cells can either move or die. Dead cells can disintegrate into empty space. Healthy cells can only move over the time-scale of the investigation.

Since it is assumed that healthy cells can only move and do not proliferate, healthy cells are unable to regenerate and proliferate back into the empty space left by any dead tumour cells in the time frame of the simulations. This is biologically plausible, for example in the case with breast cancer. Once the tumour has been resected, patients are often left with soft tissue defects and disfigurations due to the inability of the nearby tissue to regenerate (Stosich and Mao, 2005).

8.2.1 *Viral movement*

In the VCBM, it is assumed that the movement of virus particles through a tumour can be captured realistically with random waiting times between consecutive movements drawn from a heavy-tailed distribution of the form $\mathbb{P}(W > w) \sim w^{-1-\alpha}$ where $\alpha \in (0, 1)$. Trajectories of particles with waiting times W from this probability measure may be simulated exactly on a discrete-time grid by drawing a waiting time W for each particle after a single step from the stable distribution with stability parameter α using

$$W = \frac{\sin(\alpha(V + \pi/2))}{\cos(V)^{1/\alpha}} \left(\frac{\cos(V - \alpha(V + \pi/2))}{E} \right)^{\frac{1-\alpha}{\alpha}}, \tag{8.1}$$

where V is uniformly distributed on the interval $(-\pi/2, \pi/2)$ and E is exponentially distributed with unit rate parameter, see Carnaffan and Kawai (2017); Janicki and Weron (1993).

To simulate the viral motion, the following algorithm is used. Initially, each virus particle is assigned a waiting time W, drawn from the distribution in Eq. (8.1). Once the virus has waited the appropriate number of time intervals, the step length of the displacement of the virus particle is drawn from a gamma distribution with mean r_μ and variance r_σ. The angle the virus rotates relative to its previous position is a random variable drawn from the uniform distribution $[0, 2\pi)$. Whilst other distributions could have been used, the choice of the gamma distribution was motivated by its strictly positive bell-shape, definite average and 'tunable' characteristics, (Frank, 2009). This

was similar to the reasoning in Section 4.3 for the virus titer model. After each step in the virus particle's motion, a new waiting time W is then drawn from the above distribution in Eq. (8.1).

In Fig. 8.4, the density of viral particles after 200 hours is compared with and without waiting times W (Fig. 8.4(a)-(b) and Fig. 8.4(c) respectively). The variance of the distribution of the anomalously diffusing population scales as a power-law, proportionally to t^{α} (Carnaffan and Kawai, 2017). Smaller values of α (corresponding to heavier tails in the waiting time distribution) result in slower spreading of viruses, while as $\alpha \to 1$, linear scaling of variance with time is recovered as the regularity of long trapping events decreases (Carnaffan and Kawai, 2017; Janicki and Weron, 1993). As a result, as the value of α is increased in Fig. 8.4(a)-8.4(b), the spread in the histograms is noticeably increased.

To provide more insight into how subdiffusive viral motion differs from a continuous random walk, in Fig. 8.4(d) the mean-squared displacement (MSD) is plotted, corresponding to the density of viral particles after 200 hours in Fig. 8.4(a), (b) and (c). It is evident from Fig. 8.4(d) that viral movement without waiting times results in a linear MSD as a function of time. This is in contrast to viral particles with waiting times between consecutive movement generated from Eq. (8.1) with stability parameter of $\alpha = 0.6$ and $\alpha = 0.8$ which resulted in a nonlinear MSD over time. Initially the displacement of viral particles from the initial seeding location increases quickly, and then as time goes on, there is a decrease in how rapidly the mean displacement increases. For a review of the time averaging of CTRW with a broad distribution of waiting times, see Neusius *et al.* (2009).

8.2.2 *Viral clearance*

To simulate rapid clearance of virus due to immune stimulation, individual viral particles are assumed to die based on the proportion of the total number of infected cells I_T in that quadrant i that the virus is in, i.e. I_i/I_T.

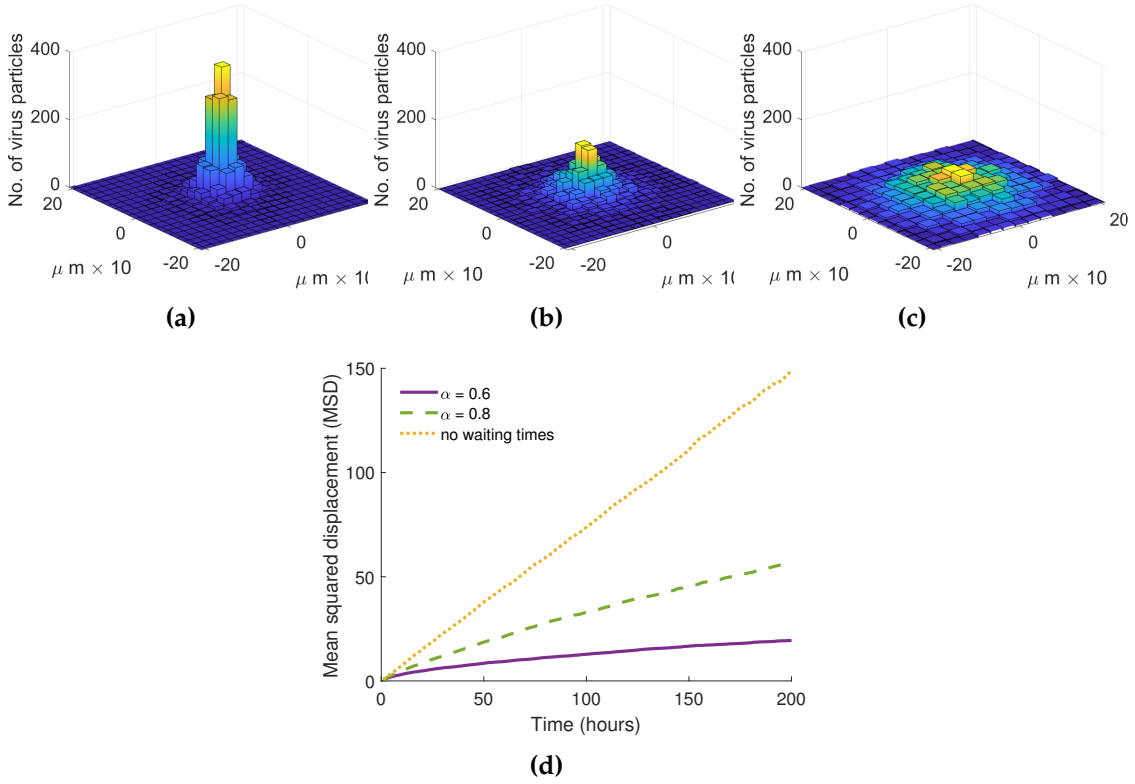

Figure 8.4: Spatial histograms of the distribution of 3000 virus particles initially located at the origin after 200 hours, where particles are diffusing with stable distributed waiting times with (a) $\alpha = 0.6$, (b) $\alpha = 0.8$ and (c) no waiting times. The corresponding mean-squared displacement (MSD) of the virus particles in (a), (b) and (c) are plotted in (d).

8.2.3 *Cell movement*

The position of each cell (except for dead and empty cells) is updated by calculating the effective displacement of the cell's lattice point using Hooke's Law. Force is modelled as a network of damped springs connecting the kth point to its neighbouring points. The spring connecting the kth and jth point has a rest length $s_{k,j}(t)$, which can vary over time t. All points in the lattice are connected in this way and the spring rest lengths between points can be unique. Fig. 8.5 shows an example of the set-up between three points k, j and i. In this example the spring connecting $s_{k,j}$ is shorter than the spring connecting $s_{k,i}$, allowing for cell growth and decay.

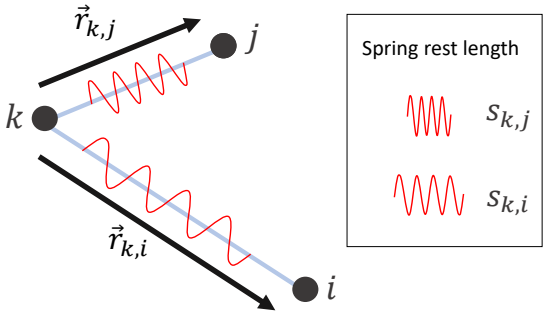

Figure 8.5: Schematic illustrating the connection between points k, j and i in the lattice at a fixed time t. Springs connect points in the lattice and the movement of each point depends on the force derived from Hooke's Law, assuming that motion is overdamped due to strong friction. The spring rest length between point k and j is $s_{k,j}$, and point k and i is $s_{k,j}$.

Following the implementation in Meineke *et al.* (2001); Murray *et al.* (2009); Osborne *et al.* (2017), the displacement of the kth point (cell) on the lattice is given by

$$m_k \frac{d^2 \mathbf{r}_k}{dt^2} = \sum_{j \in \tilde{N}(k)} \mathbf{F}^I_{k,j} + \mathbf{F}^V_k, \tag{8.2}$$

where m_k is the mass of the kth point, $\mathbf{r}_k$ is its spatial position, $\mathbf{F}^I_{k,j}$ is the interaction force between a pair of neighbouring points, $\mathbf{F}^V_k$ is the viscous force acting on the kth point, and the sum is taken over neighbouring points to k in the lattice, i.e. $\tilde{N}(k)$, determined by the Delaunay triangulation. The total interaction force $\mathbf{F}^I_k(t)$ acting on the kth point at time t is equal to the sum of all forces from the springs of all points i connected to k:

$$\mathbf{F}^I_k(t) = \sum_{j \in \tilde{N}(k)} \mathbf{F}^I_{k,j} = \mu \sum_{\forall i} \frac{\mathbf{r}_{k,i}(t)}{\|\mathbf{r}_{k,i}(t)\|} \left(s_{k,i}(t) - \|\mathbf{r}_{k,i}(t)\| \right), \tag{8.3}$$

where μ is the spring constant, $\mathbf{r}_{k,i}(t)$ is the vector from the kth to the ith point at time t, $s_{k,i}$ is the spring rest length from the kth to the ith point at time t and $\|\mathbf{r}_{k,i}(t)\|$ is the L2-norm of the vector $\mathbf{r}_{k,i}(t)$, see Fig. 8.5.

Eq. (8.2) can then be simplified using two key assumptions. The first is that the viscous force $\mathbf{F}^V_{k,j}$, i.e. point-point, point-medium and point-matrix interactions, can be

modelled by assuming that the drag on the kth point is independent of the springs and is proportional to its velocity, with constant of proportionality η. Secondly, the points are assumed to be in a relatively dissipative environment, so point motion can be approximated as being overdamped due to strong friction. Hence

$$m_k \frac{d^2\mathbf{r}_k}{dt^2} \sim 0.$$

Prior cell-centered models have used this same inertialess assumption ($m_k \frac{d^2\mathbf{r}_k}{dt^2} \approx 0$) (Drasdo *et al.*, 1995; Galle *et al.*, 2005; Macklin *et al.*, 2012). Thus

$$\mathbf{F}_k^I = -\mathbf{F}_K^V = \eta \boldsymbol{\nu}_k,$$

where $\boldsymbol{\nu}_k$ is the velocity of the kth point. Approximating this velocity over a small time interval Δt, gives

$$\mathbf{F}_k^I \approx \eta \frac{\mathbf{r}(t+\Delta t) - \mathbf{r}(t)}{\Delta t}.$$

Thus the effective displacement of the kth point within a small time interval Δt in the overdamped limit is

$$\mathbf{r}_k(t+\Delta t) = \mathbf{r}_k(t) + \frac{1}{\eta}\mathbf{F}_k(t)\Delta t = \mathbf{r}_k(t) + \lambda \sum_{\forall i} \frac{\mathbf{r}_{k,i}(t)}{\|\mathbf{r}_{k,i}(t)\|} \left(s_{k,i}(t) - \|\mathbf{r}_{k,i}(t)\|\right), \qquad (8.4)$$

where $\mathbf{r}_k(t)$ is the position of the kth point in the lattice at time t and η is the damping constant. Cell mobility is described by the ratio $\lambda = \mu/\eta$, which is known to influence the velocity of the relaxation process (Meineke *et al.*, 2001).

Adhesion effects between neighbouring cells are modelled using a linear force and cut-off distance a_l. When the Euclidean distance between points on the lattice of neighbouring cells is longer than $s_{k,l} + a_l$, no interaction takes place, see Fig. 8.6.

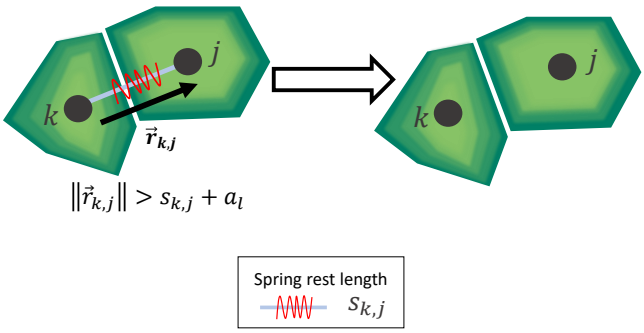

Figure 8.6: Schematic illustrating how cell-to-cell adhesion is assumed to be negligible after the cells have reached a distance apart greater than $s + a_l$.

8.2.4 *Cell proliferation*

To model cell proliferation, a cell's distance to the nutrient source and local spatial limitations are considered. The distance from a cell to the nutrient source d is assumed to be the Euclidean distance between the cell and its closest peripheral tumour cell, which are assumed to be adjacent to nutrient sources. The effect of mechanical confinement pressure is accounted for by d_{max}, the maximum radial distance that still allows a cell to obtain nutrients from its surroundings. If $d > d_{max}$, then the cell does not proliferate, essentially becoming a quiescent cell. The probability of a cell dividing based on the nutrients it receives is

$$p_d = p_0 \left(1 - \frac{d}{d_{max}}\right), \tag{8.5}$$

where p_0 is a proliferation constant. Note that p_0 is dimensionless as p_d is the dimensionless probability of a cell proliferating in a given time step $t + \Delta t$.

Fig. 8.7 illustrates how d_{max} segregates the tumour into a rim of proliferating and non-proliferating cells. Additionally, to account for the spatial limitation on proliferation, tumour cells only divide if there is least r_{min} space between a tumour cell and any cell in its neighbourhood of interaction. This formulation is based on similar probability calculations in cellular automata and agent-based models (Jiao and Torquato, 2011; Kansal *et al.*, 2000b).

If a cell proliferates, the framework also allows the encoding of the addition and movements of lattice points (and the associated VCBM) as a cell divides into two

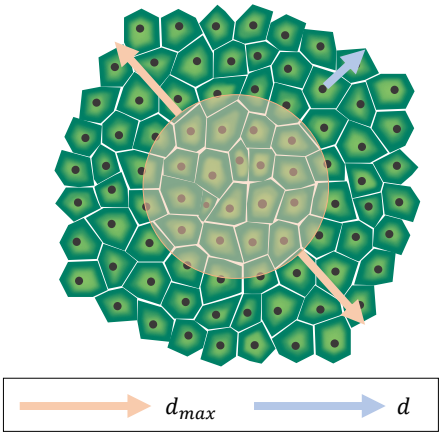

Figure 8.7: Schematic for the probability of a particular cell proliferating given a particular distance d from the edge of the tumour, see Eq. (8.5). The maximum radial distance for which proliferation occurs, d_{max}, separates the tumour into proliferating and non-proliferating sections, with the cells inside the shaded circle having a distance greater than d_{max} from the edge, and hence being unable to proliferate.

daughter cells. When a cell at position k divides, a new lattice point l is created, so that k and l are now the points associated with the two daughter cells, see Fig. 8.8.

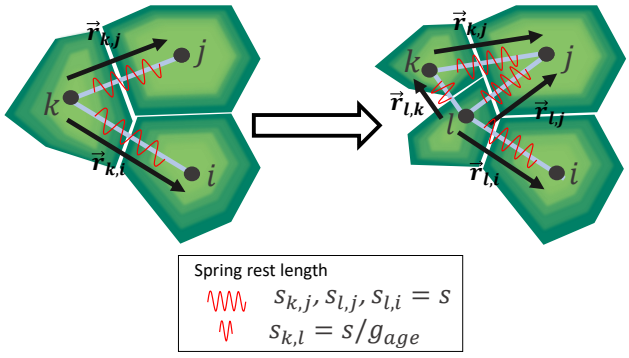

Figure 8.8: Schematic for cell motility, illlustrating the proliferation of cell k into two new cells k and l. The resulting spring rest length $s_{k,l}$ between daughter cells is then s/g_{age}, which increases over time to s, the mature cell separation.

To simulate the enlargement and repositioning of the daughter cells, allowing for gradual cell volume changes (Ghaffarizadeh *et al.*, 2018; Mumenthaler *et al.*, 2013), the resting spring length of the connection between k and l is taken to be a linear ramp from a value s/g_{age} up to the mature resting spring length, s, over a time g_{age} as indicated in Fig. 8.9. Note the two daughter cells are placed at a random angle of orientation from the original position of the mother cell at a random distance less than

or equal to s/g_{age} apart. Once a cell has proliferated, it takes p_{age} time steps before the daughter cells will proliferate again, including the g_{age} time steps for the daughter cells to mature and re-position.

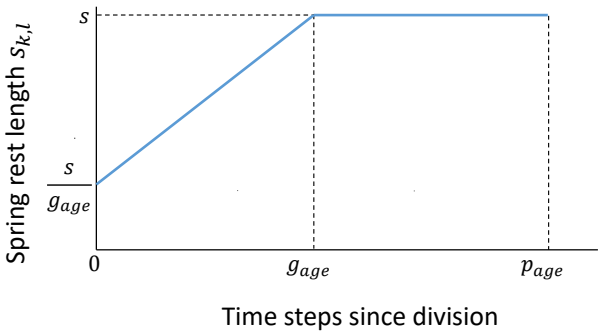

Figure 8.9: Schematic for cell adhesion. Fig. 8.9 illustrates how the spring rest length $s_{k,l}$ increases as a function of the time since division.

8.2.5 *Cell infection*

In each time step, all uninfected and infected tumour cells are checked to see whether they will be infected. If there is at least one virus agent within the perimeter of a cell, then the cell becomes infected with probability p_i. If there are ζ_T virus particles within the perimeter of a cell, then a random number of virus particles ζ, drawn from a uniform distribution of the number of viruses able to infect that cell, i.e. $\zeta = U(0, \zeta_T)$, infects the cell. These virus agents are then removed from the extracellular virus population and the tumour cell becomes an infected cell.

8.2.6 *Cell death*

Once inside a tumour cell, viral particles undergo replication for i_{age} time steps, after which the cell will burst and release ν new virus particles. These new particles are placed randomly within the perimeter of the cell that burst. If the cell bursts, it becomes a dead cell. Once a cell has died from a virus infection, it is assumed that it takes d_{age} time steps to disintegrate: at each time increment, the spring rest lengths of the dead cell to all its neighbours reduces by d_{frac} to simulate cell disintegration.

8.3 PARAMETER OPTIMISATION AND SENSITIVITY

All parameters in the model are collated in Table 8.1. The parameters relating to cell state characteristics were optimised using time-series measurements for the growth of cervical cancer SK-OV3 cells (Section 2.2.3.4) *in vivo* (Kim *et al.*, 2011b). The model was assumed to be updated on a time step of 4 hours for the parameter optimisation and all future numerical simulations.

Table 8.1: Parameters in the model and their meanings.

Cell parameters	
g_{age}	Time steps taken for a daughter cell to grow to adult size
p_0	Probability constant for proliferation
d	Distance from a tumour cell to the nearest cell on the tumour edge
d_{max}	Radial distance that nutrient reached by diffusing from the tumour edge
r_{min}	Minimum distance between neighbouring cells for proliferation to occur
p_{age}	Age a cell needs to reach before it can proliferate again
d_{frac}	Distance spring length of a dead cell decreases at each time step
d_{age}	Time taken for dead cell to disintegrate
Cell motility parameters	
s	Spring rest length
μ	Spring constant
η	Damping constant
a_l	Adhesion distance between two cell positions
Virus parameters	
i_{age}	Time steps taken from infection to when the infected cell bursts
p_i	Probability of infection occuring
r_μ	Mean distance of viral movement per time step
r_σ	Standard deviation for virus displacement
ν	Number of new virus agents created through lysis

8.3.1 *Optimising cell state characteristics*

To verify the robustness and predictive capability of the model, the growth of cervical cancer in mice was investigated. The volume of cervical cancer SK-OV3 cells has been measured in three mice over time by Kim *et al.* (2011b). SK-OV3 cells have an average diameter of 14.1μm (Chen *et al.*, 2011) and, interpolating the calculation of Del Monte (2009), this equates to approximately 4.8×10^8 cells per mm^3. Due to computational and geometric constraints in the model, rather than representing a single cell in the

2D setting, each Voronoi cell was taken to represent the average characteristics of 10^{10} SK-OV3 cells, and the data scaled accordingly by a factor of 10^{10}. The VCBM was then used to determine the growth of SK-OV3 cells, with the trend showing good correspondence with the data, see Fig. 8.10 and Table 8.2.

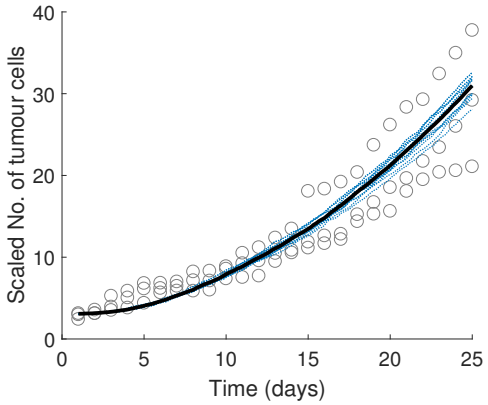

Figure 8.10: Model calibration for *in vivo* cervical cancer SK-OV3 cell growth. Individual mouse tumour cell numbers recorded by Kim *et al.* (2011b) are plotted as grey circles. Overlayed in light blue dotted lines are 15 model simulations of tumour growth with the mean of these simulations in black.

Table 8.2: Cell parameter values. The calibrated parameters are obtained by optimising the model to the measurements of SK-OV3 cell growth seen in Fig. 8.10. The fixed parameters r_{min} and s are taken from the original lattice set up, parameters μ, η and λ are taken from Meineke *et al.* (2001), but scaled to the time step of 4 hours, and a_l is arbitrary.

Calibrated parameters	SK-OV3 data
g_{age}(hour)	12
p_0	0.7
d_{MAX} (μm)	45
p_{age} (hour)	28
Fixed parameters	
r_{min} (μm)	17.28
s (μm)	18.50
$\mu(\mu g/hour^2)$	0.01
η ($\mu g/hour^{-1}$)	0.133
a_l (μm)	0.15

Note that the volume of cervical cancer SK-OV3 cells was measured over 25 days, and the parameters returned were therefore a function of days. The number of Voronoi cells is plotted as a function of hours, see Fig. 8.10 as are the parameter values in

Table 8.2. The simulation implementation was additionally tested to ensure that there were no artefacts in the results due to the choice of time step.

8.3.2 *Viral characteristic parameters*

Table 8.3: Virus characteristic parameter values

Parameter	Value	Source
p_i	0.9	Chapter 6
i_{age} (hour^{-1})	24	Chapter 6
ν (no. of virus particles)	5	Chapter 6
r_μ (μm)	0.05	Mok *et al.* (2009)
r_σ (μm)	0.1	Mok *et al.* (2009)

The remaining parameter values in the model were approximated from the literature. The probability p_i of infection occurring was approximated by the rate of infection determined in Chapter 6, assuming that the infection rate can be modelled by an exponential probability distribution. The decay rate was approximated using the average duration of cell lysis of 24 hours. The number of new viruses created, ν, was approximated from the value of α in Chapter 6, increased slightly, because this chapter considers individual virus agents rather than a mean-field approximation to the viral dynamics (closer to some of the individual mice values returned in Table 6.1). The mean and variance for viral step length were scaled from the diffusion coefficient of HSV particles reported at 5×10^{-10}cm^{2}s^{-1} by (Mok *et al.*, 2009). See Table 8.3 for a summary.

8.3.3 *Model simulation*

Cancer cell proliferation, spatial limitations and obstructions influence the shape of a tumour, see Section 2.2.2 and Fig. 2.2. To understand the sensitivity of the treatment to tumour shape, the outcome of virotherapy is investigated on three generic tumour shapes: circular (Fig. 8.11(a)), rectangular (Fig. 8.11(c)), and irregular (Fig. 8.11(e)). To generate each shape, the same basic underlying VCBM rules have been used, with some additions in the case of rectangular and irregular tumour growth.

Circular tumours can be generated directly using the model described in the previous section If there are no spatial limitations for proliferating cancer cells *in vivo*, a roughly circular tumour will form, similar to the cross-section of a hanging drop tumour spheroid (Weiswald *et al.*, 2015), see Fig. 2.2. Note the apparent difference between the exponential growth seen in Fig. 8.10 and the more linear growth seen in Fig. 8.11(b). The difference is due to the slower growth of the tumour on the time scale of hours as opposed to days, and also due to the smaller number of cells.

When there is an obstruction above and below an initial seeding of tumour cells in vivo, a rectangular tumour shape will form. This obstruction can be considered as stiffer stromal tissue, similar to that seen in breast ductal carcinomas in situ (DCIS), see Fig. 2.2, which have approximately rectangular cross sections. These tumours form in a rectangular shape due to spatial limitations above and below the tumour. To encourage rectangular tumour formation in the VCBM, a horizontal impenetrable boundary is positioned above and below the initial grouping of tumour cells. This was simulated by placing a dense horizontal line of points into the lattice (not plotted) at the position of the impenetrable boundary, and then requiring that all healthy cells above and below this horizontal boundary are unable to move.

In certain cancers, cells on the periphery of a tumour can become invasive cells, allowing them to degrade the ECM and remove nearby cells, forming irregular branches, see Fig. 2.2. To generate an irregular tumour, a collection of tumour cells on the tumour periphery are designated that are able to invade the space of healthy cells and occupy their position. These cells move in a direction that maximises their nutrient and oxygen supply (Jiao and Torquato, 2011). In the model, nutrients are assumed to flow in from the boundary of the domain, so these invasive cells move in a direction away from the tumour.

Typical evolutions of the model for three tumour shapes: circular, rectangular and irregular are presented in the Appendix B Fig. B.1, B.2 and B.3 respectively. While the shapes generated have not been directly matched to experimental tumour images, they represent shapes occurring in tumour formation as discussed above and in Section 2.2.2.

Using the aforementioned automaton rules for oncolytic viruses and corresponding parameter values in Table 8.1 and 8.3, a representative model evolution is shown for a circular tumour with viral treatment in Fig. 8.12. Over time, healthy cells are surrounded by the tumour cell population and this is reminiscent of the true biological scenario, since healthy cells are regularly found within tumours (Park *et al.*, 2000).

All simulations presented in the following results section use the same VCBM virus rules, unless specified otherwise. Since the size of the adenovirus is approximately 90-100 nm (Appert *et al.*, 2012), this means that based on the size of an SK-OV3 cell, an adenovirus is 0.65%-0.7% of the cell's size. Therefore virus transport mechanisms are assumed to not be influenced by whether they are in a cell filled area or an area with no cells.

8.4 RESULTS: SIMULATING ALTERNATIVE TREATMENT PROTOCOLS

In this chapter, oncolytic virotherapy effectiveness is only considered on small tumours, aiming to improve the diffusive viral properties of this therapy for early-stage cancers. Two major therapy perturbations are examined in the following subsections: the configuration of the viral injections entry sites and the effects of delaying the infection of cancer cells by viral particles. These modifications to the current therapy are examined in detail on the three tumour shapes generated.

8.4.1 *Dependence of treatment outcome on entry site configuration*

Traditional viral therapy is administered by either intravenous or intratumoral injection (Wang and Yuan, 2006). However, the possible dependence of therapy outcome on the position of initial treatment injection has not been investigated systematically. Using the VCBM, it is investigated whether there is an optimal injection configuration for the three tumour shapes: circular (Fig. 8.13), rectangular (Fig. 8.14) and irregular (Fig. 8.15). The varying initial injection configurations considered are represented pictorially by

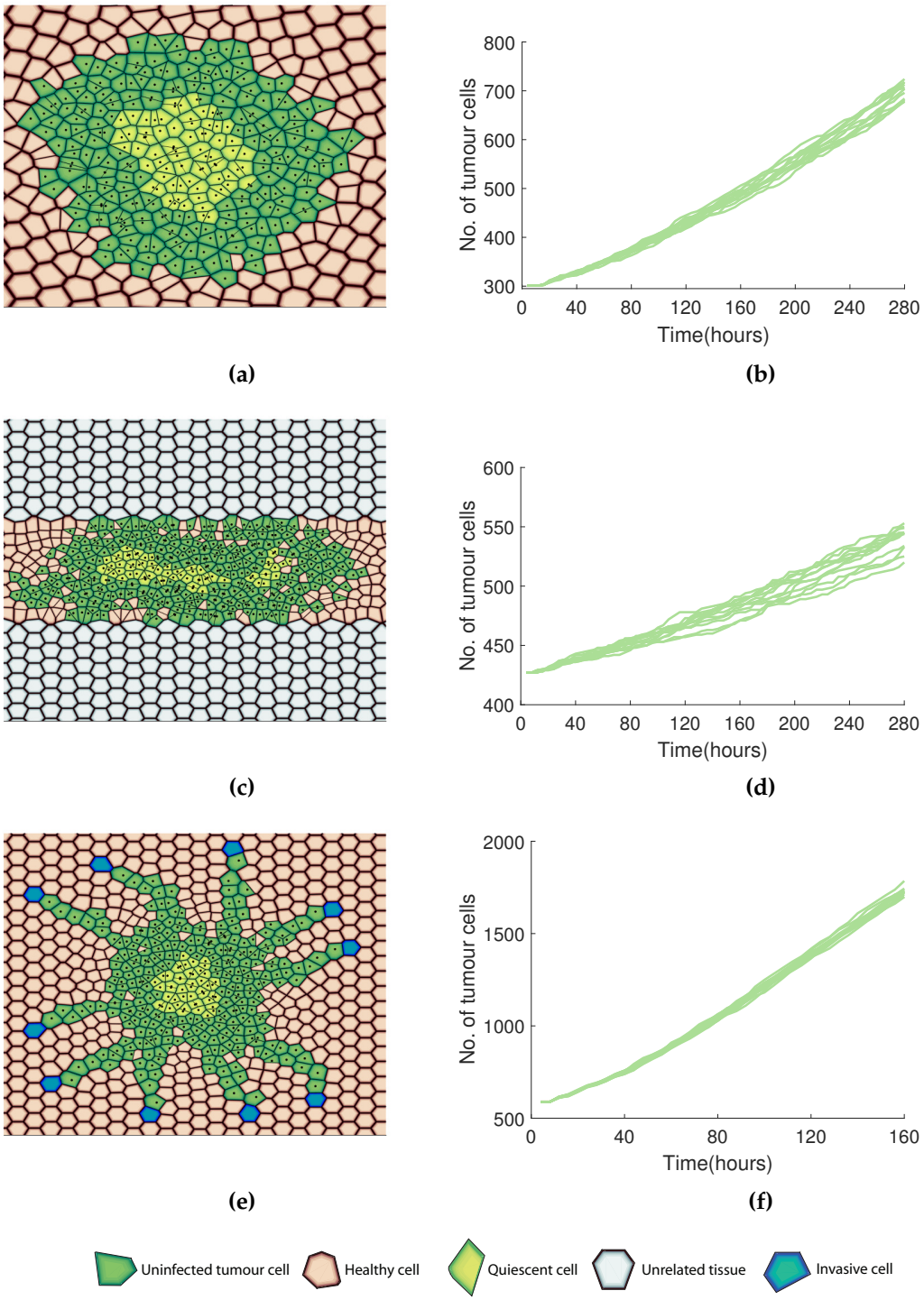

Figure 8.11: Representative tumour shapes considered for treatment with an oncolytic virus (a)-(b) circular, (c)-(d) rectangular, and (e)-(f) irregular. The corresponding number of tumour cells as a function of time from 12 simulations has been plotted for each shape. Typical evolution plots for each of these shapes can be found in the Supplementary material, Fig. B.1, Fig. B.2 and Fig. B.3 respectively. Note the different scale for (f) due to the extremely fast growth of the irregular tumours.

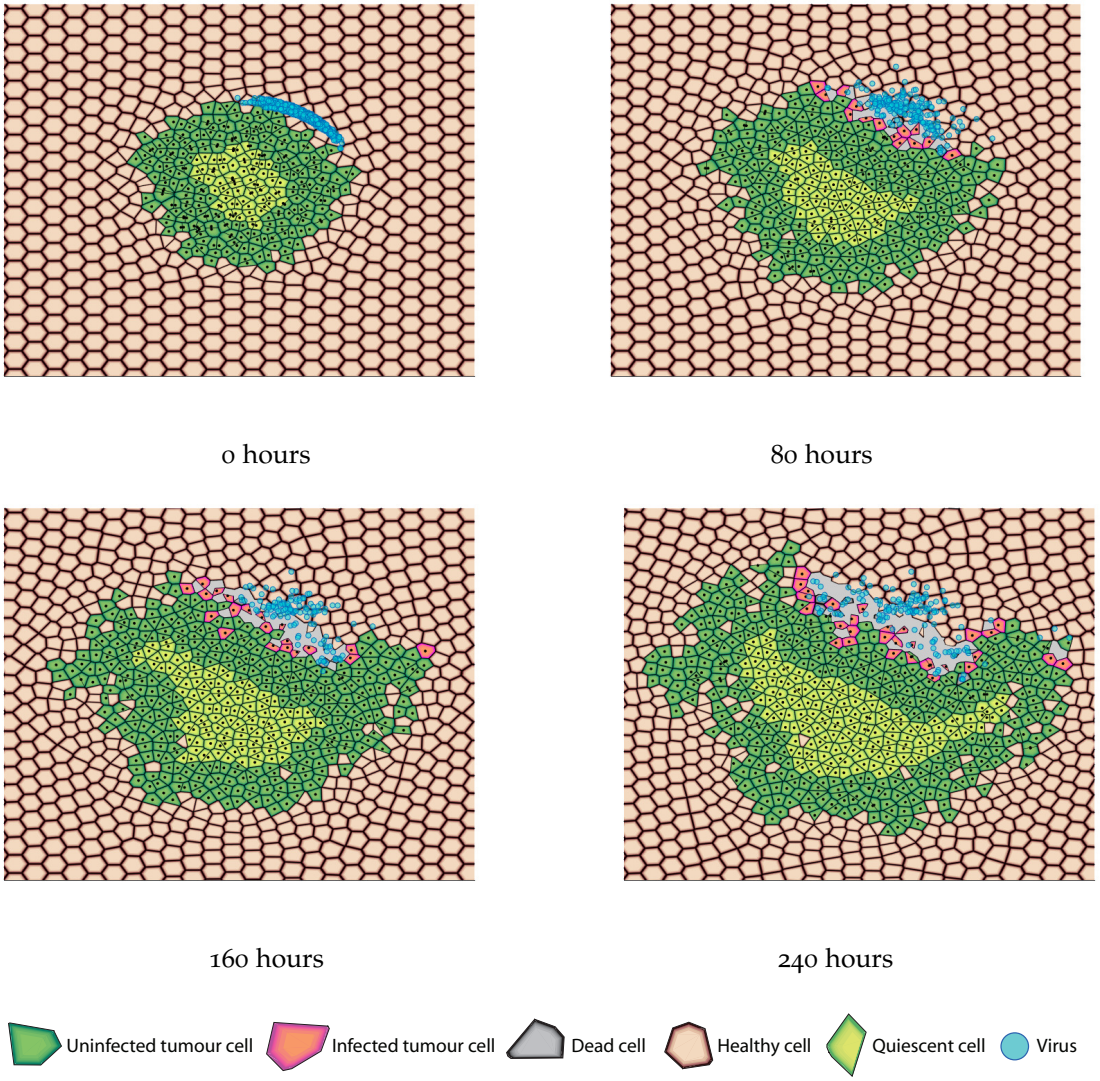

Figure 8.12: Representative evolution of the VCBM model in a circular configuration. The four snapshots above represent equal intervals of model dynamics. Pale pink cells represent healthy cells, dark green cells represent tumour cells, light green cells represent quiescent cells, bright pink cells represent infected tumour cells and grey cells represent dead cells with empty space shaded in light grey.

enumerated and coloured virus shapes with the resulting number of tumour cells as a function of time also shown. Across all injection configurations considered, the total dosage was the same. In the case where more than one injection was considered, the dosage was split evenly amongst the injections.

Increasing the multiplicity of the treatment injection sites improved the overall treatment efficacy for circular tumours, see Fig. 8.13. On average, the tumour cell count at 280 hours and the overall rate of tumour growth was highest when the total viral dose

was given in a single injection, profiles A, B and C in Fig 8.13(b), irrespective of the injection location. In comparison, the average tumour size at 280 hours was smaller for three radially symmetric treatment injections, profiles D, E and F Fig 8.13(d). Furthermore, the tumour size was dramatically reduced in the first 160 hours when three radially symmetric injections were administered mid tumour, see injection profile E. While a greater initial reduction in tumour size occurred with injection profile E than profile F, the average tumour size achieved at 280 hours was smaller when radially symmetric injections were applied at the periphery of the tumour, profile F. The reason for injections on the periphery performing better than intratumoural injections, is due to peripheral injections controlling the outward growth of the tumour more than intratumoural injections. These dynamics are similar to three non-symmetric injections at the same radial position from the tumour centre, as in profiles G, H and I in Fig. 8.13(f). However, overall injections need to be given radially symmetrically to see an optimal effect in the treatment efficacy.

In rectangular tumours, the size after treatment was slightly more variable than in circular tumours, see Fig. 8.14. On average, single injections resulted in smaller tumour reductions, see injection profiles A, B and C in Fig. 8.14(b) respectively, along the major (long) axis of the rectangle, and G in Fig 8.14(f), which was off both the major and minor (short) axes of the rectangle at the periphery of the long edge of the tumour. There were examples of individual tumour growths after a single injection that stabilise; however, these occurred rarely. This shows that despite the tumour's vertical growth being restricted, a single injection along a major or minor axis was unable to control the tumour growth to the same extent as two injections. Apart from two injections off the short-axis of the rectangular tumour on the periphery of the long side (injection profile F), all other two injection profiles lowered the tumour growth see profiles D and E and profile H in Fig 8.14(d).

The lowest tumour size was obtained with two intratumoural injections in the direction of the long edge, i.e. profile D, and on the periphery of the long edge of the minor axis, and off the major axis, i.e. profile H in Fig. 8.14(f). Additionally, the rate of growth on average was significantly reduced when two injections are given intratumourally or

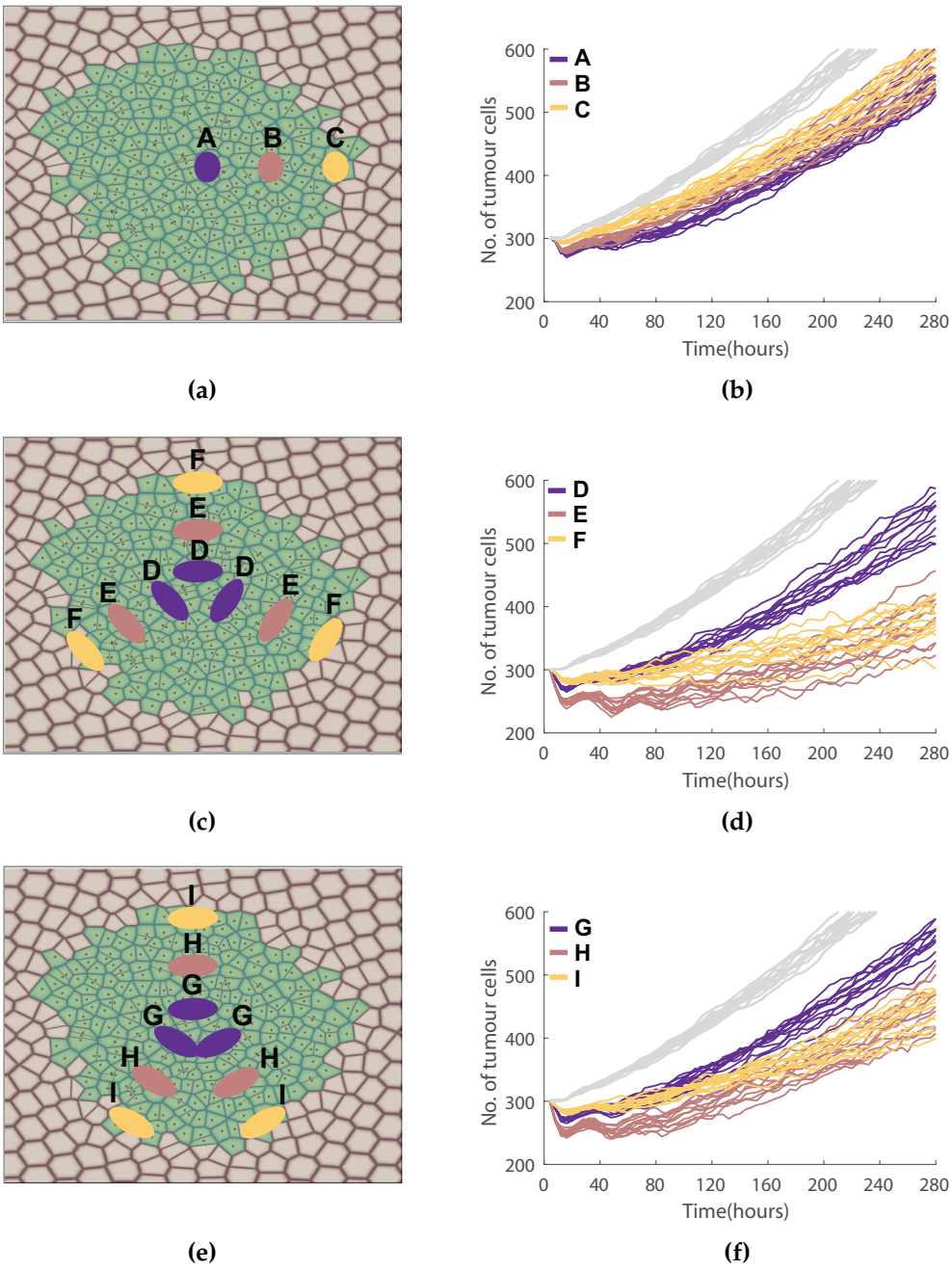

Figure 8.13: The effects of the multiplicity and configuration of the injection site on a circular tumour. The initial injection configurations considered are represented in Fig. 8.13(a), 8.13(c) and 8.13(e) by the coloured regions, depicting viral particles. The corresponding total number of tumour cells over time for each injection type is plotted in Figs. 8.13(b), 8.13(d) and 8.13(f), respectively for 12 simulations. For reference, untreated tumour growth is plotted for 12 simulations in grey. Note quiescent cells are not plotted.

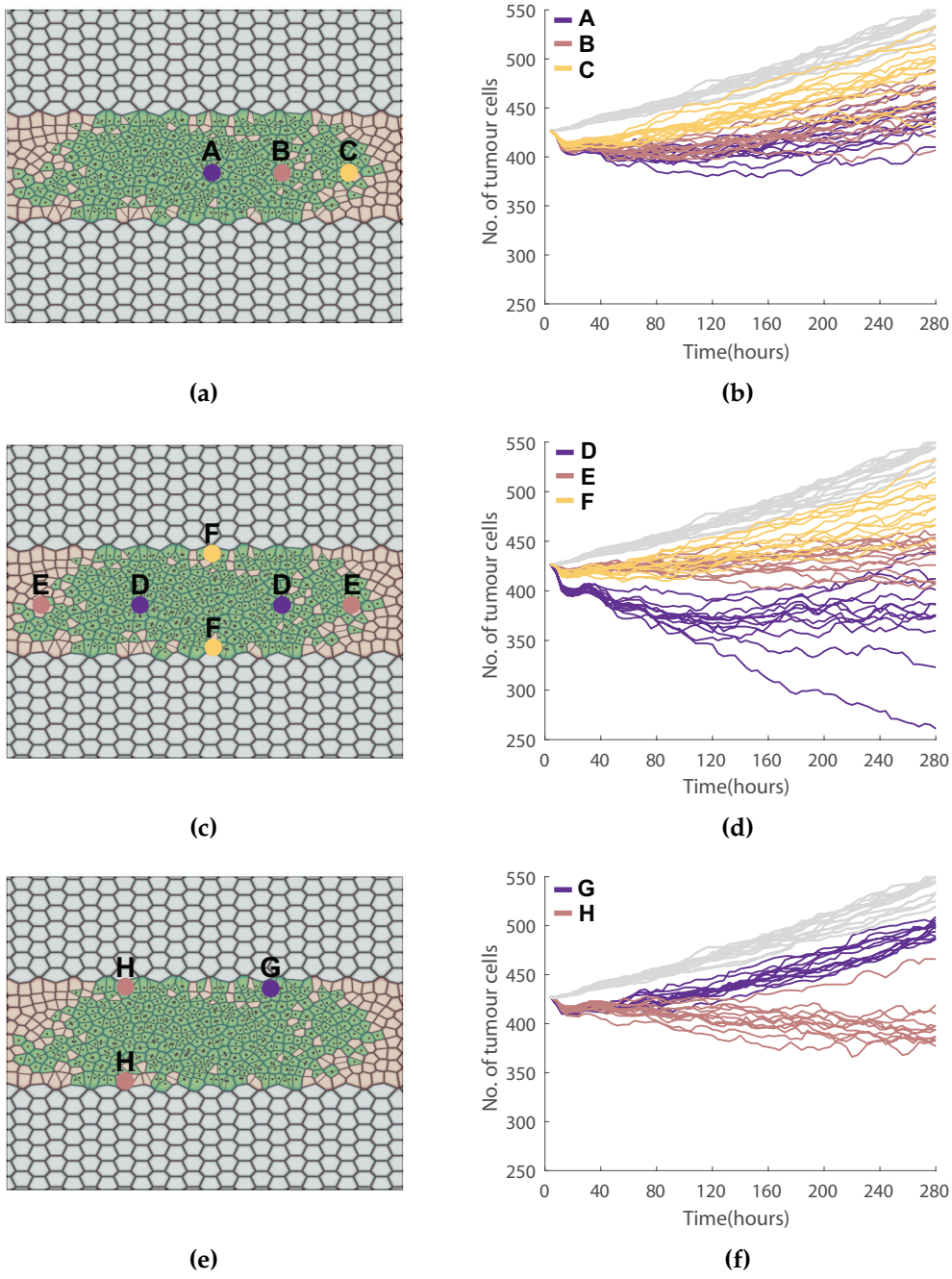

Figure 8.14: The effects of the multiplicity and configuration of the injection site on a rectangular tumour. The initial injection configurations considered are represented in Fig. 8.14(a), 8.14(c) and 8.14(e) by the coloured regions, depicting viral particles. The corresponding total number of tumour cells over time for each injection type is plotted in Figs. 8.14(b), 8.14(d) and 8.14(f), respectively for 12 simulations. For reference, untreated tumour growth is plotted for 12 simulations in grey. Note quiescent cells are not plotted.

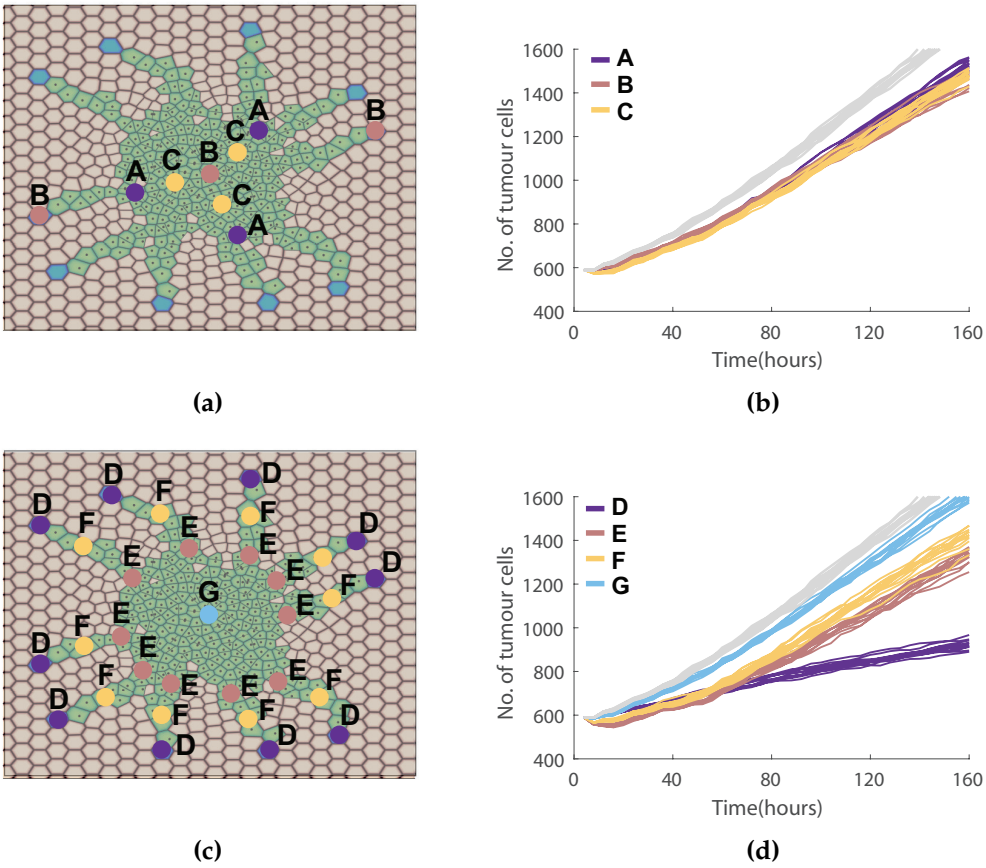

Figure 8.15: The effects of the multiplicity and configuration of the injection site on an irregular tumour. The initial injection configurations considered are represented in Fig. 8.15(a) and 8.15(c) by the coloured regions, depicting viral particles. The corresponding total number of tumour cells over time for each injection type is plotted in Figs. 8.15(b) and 8.15(d), respectively for 12 simulations. Note the shorter timescale, and greater growth compared to Fig. 8.13 and 8.14. For reference, untreated tumour growth is plotted for 12 simulations in grey. Note quiescent cells are not plotted.

on the periphery and off-centre. Profile D intuitively results in a low tumour burden as these injections have access to more tumour cells than any other injection; however, this is not the case for profile H. In this case, the efficacy of this injection comes from the virus controlling one of the proliferating directions of the tumour.

For the irregular tumours, spreading the dose across multiple injection sites lowered the tumour size. A single intratumoural injection, profile G Fig. 8.15(d), produced the largest average tumour at 160 hours. This is not surprising, since the irregular tumour has invasive cells that generate rapid tumour growth away from the centre of the tumour, where only quiescent cells would be present. If the injection multiplicity

is increased to three, then intratumoural radially symmetric injections profiles A and C in Fig. 8.15(b) resulted in a marginally better treatment in the first 80 hours than three diagonal injections (profile B in Fig. 8.15(b). Long-term, the best injection profile for three injections was along the diagonal of the tumour bulk, i.e. profile B. However, overall, three injections were unable to inhibit the tumour growth significantly, possibly due to the irregular arms of the tumour providing a higher surface area of tumour growth.

When ten injections were administered for an irregular tumour, the velocity of tumour growth was significantly reduced compared to the untreated system, see Fig. 8.15(c)-(d). In early stages, the lowest tumour growth was obtained when multiple injections were given on the tumour periphery, i.e. profile E in Fig. 8.15(c)-(d). However, later on, injections that wiped out the invasive cells, profile D in Fig. 8.15(c)-(d), ultimately reduced the tumour burden the most. Comparing the difference at 60hours for injection profiles D and E in Fig. 8.15(d) to 160 hours, it is evident that the tumour evolution was significantly different. While initially profile D seemed to be not as effective, over time it was the most successful administration protocol.

8.4.2 *Treatment with delayed initial viral-infection*

To improve virotherapy, a more advanced delivery system that provides sustained infection of tumour cells is needed (Choi *et al.*, 2013b). While optimising the injection configuration shown in the previous section can help, more needs to be done to improve the treatment. One idea is to modify viral vectors with a substance, such as an alginate gel, to delay the initial infection time, allowing for further diffusion through the tumour bulk prior to the initial infection and activation of clearance.

Alginate, a naturally occurring biopolymer, has several unique properties that have enabled it to be used for delivery of a variety of biological agents, including viruses (Choi *et al.*, 2013b; Sharma *et al.*, 2003). The ability to encapsulate viral particles in alginate microbeads has been tested as a vaccine delivery system, (Kwok *et al.*, 1989; Wee *et al.*, 1995). Choi *et al.* (2013b) show that the biological activity of viral particles loaded in alginate gel is prolonged compared with naked virus (Choi *et al.*, 2013b). The

microenvironment around the gel-encapsulated virus also provides protection from clearance by the immune system over an extended time period (Choi *et al.*, 2013b; Muruve *et al.*, 1999; Ruzek *et al.*, 2002). This idea is theoretical and has not yet been shown to be biologically plausible. Additionally, as the size of an adenovirus is 0.6%-0.7% the size of an SK-OV3 cell, it is assumed that alginate coating will not influence the size as significantly as to warrant a change in the transport properties and rates.

The effects of delayed viral treatment on circular, Fig. 8.17, rectangular, Fig. 8.18, and invasive tumours, Fig. 8.19, was investigated. In each of these figures, the predicted number of tumour cells under treatment with the original oncolytic virus is overlaid with that of the delayed-initial infection virus for the various values of the delay time. The pore size, degradation rate and release kinetics of alginate can also be controlled (Gombotz and Wee, 1998), so four different initial infection delays of 40, 52, 60 and 80 hours were simulated.

Delaying the infection of viral particles allows the treatment to disseminate further into the tumour before the first infection, see Fig. 8.16 for a visual representation of the dynamic, and Figs. 8.17(f) and 8.18(f) for the distribution of viral particles at different times. In Fig. 8.17(f) and 8.18(f), it is clear that the variance of the position of the viral particles initially is smaller than that of the delayed viral particles before their initial infection, after their corresponding wait periods. Typical evolutions of the model for circular tumours under treatment with a non-delayed and delayed virus is plotted in the Appendix B, see Fig. B.4 and B.5 respectively.

The treatment was administered in three injections on the periphery for circular tumours (profile F, Fig. 8.13(c)), two injections on the short ends for rectangular tumours (profile E, Fig. 8.14(c)) and three injections on the tumour bulk periphery for irregular tumours (profile A, Fig. 8.15(a)). For circular and rectangular tumours, Fig. 8.17 and Fig. 8.18, the modified delayed virus resulted in lower tumour cell numbers than that of the non-delayed virus. Each injection had the same amount of virus particles, irrespective of the tumour shape or delay length.

In the circular tumours, the delay of the onset of viral infection initially allowed the tumour cell numbers to increase rapidly compared to the tumours undergoing non-delayed viral treatment, Fig. 8.17. At the onset of the infection, however, a dramatic

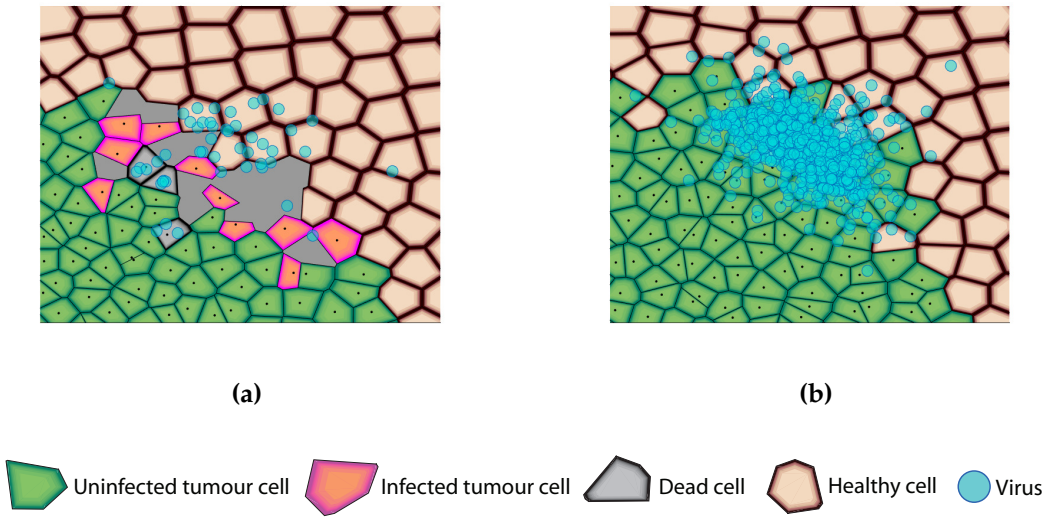

Figure 8.16: Virus diffusion for (a) non-modified and (b) modified virus particles at 52 hours. A comparison of the two cases shows that the region within which the virus particles have diffused is similar in both cases; however, there are less virus particles in the non-modified case due to immune clearance.

.

drop in tumour cell numbers was observed. For shorter delay times, Fig. 8.17(a) and (b), the tumour numbers were similar under the delayed and non-delayed treatments following the onset time. For treatments with longer delays, Fig. 8.17(c) and (d), the tumour numbers under the delayed treatment dropped below that of the non-delayed treatment at the onset time, and the trend of the subsequent increase was on average below that of the non-delayed treatment. This illustrates that while the addition of a delay in the viral infection allows the tumour to grow to a size larger than the initial one, the viral treatment's effectiveness is increased due to its ability to disseminate further into the tumour, see Fig. 8.17(f).

For non-circular tumours, delaying the onset of viral infection results in tumour growths with equivalent slopes. In the case of rectangular tumours, Fig. 8.18, delaying the viral infection means that once the virus particles infect, the size of the tumour is lower at that point than the size of the tumour under treatment with non-delayed virus. So while the tumour growths have the same rate, the size of the tumour is smaller for the delayed viral treatment. In the case of irregularly shaped tumours, Fig. 8.19, whilst the dramatic drop in tumour cell numbers was observed upon the onset time in the

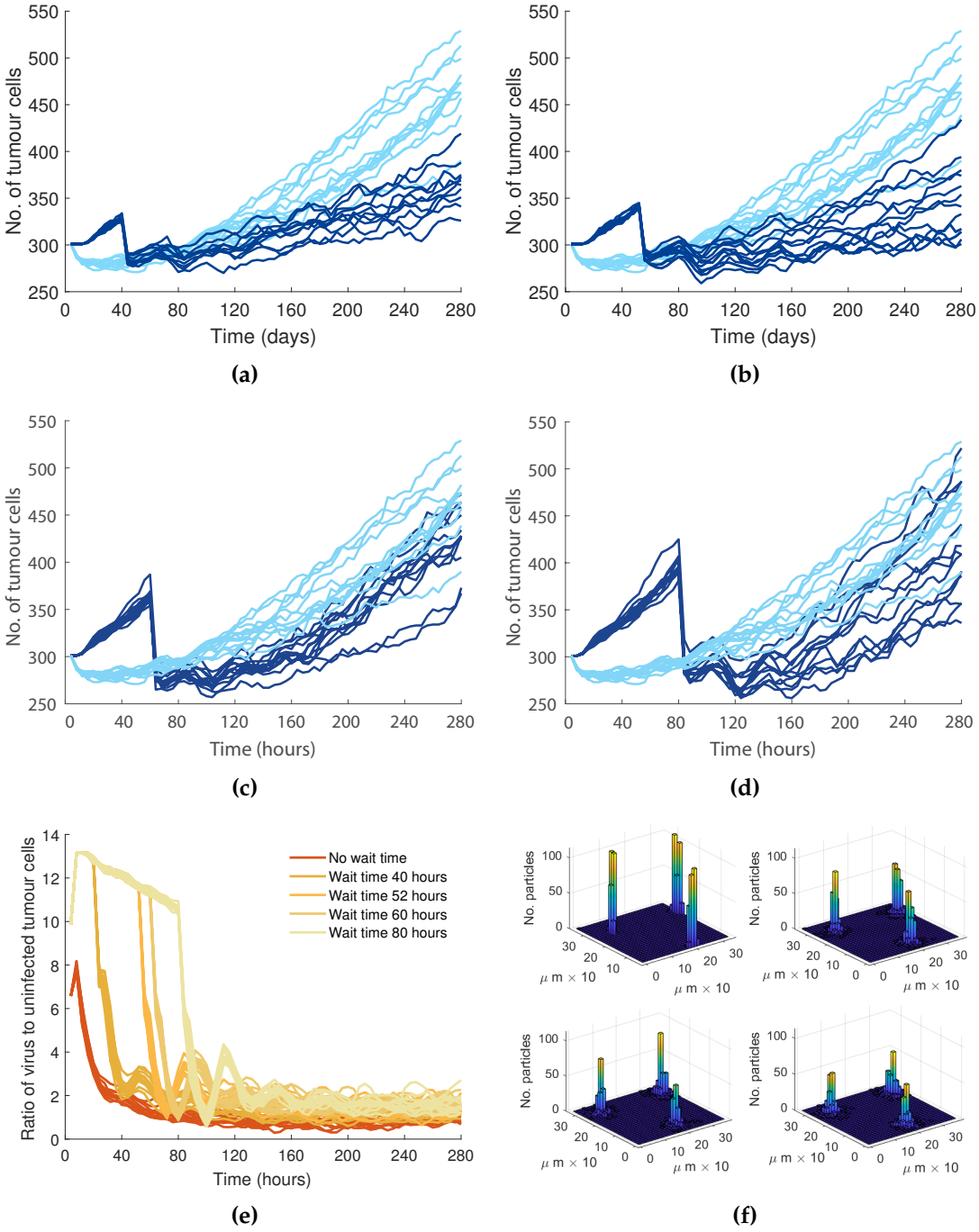

Figure 8.17: Circular tumour size under treatment with a delayed infecting oncolytic virus. The number of tumour cells predicted by the model over time is plotted under treatment with the original oncolytic virus (light blue) and with the delayed virus (dark blue) applied using profile F, Fig. 8.13. Twelve model simulations were considered for each case. The wait times for the delayed virus cases were (a) 40, (b) 52, (c) 60 and (d) 80 hours. Note the dramatic drop in tumour cell numbers upon initial viral infection in each case. In (e), the ratio of the number of extracellular virus particles to uninfected tumour cells is plotted for each treatment as a function of time. The corresponding distribution of viral particles before they can initially infect for the case of no wait time, 40 hours wait time, 60 hours wait time and 80 hours wait time is plotted in (f).

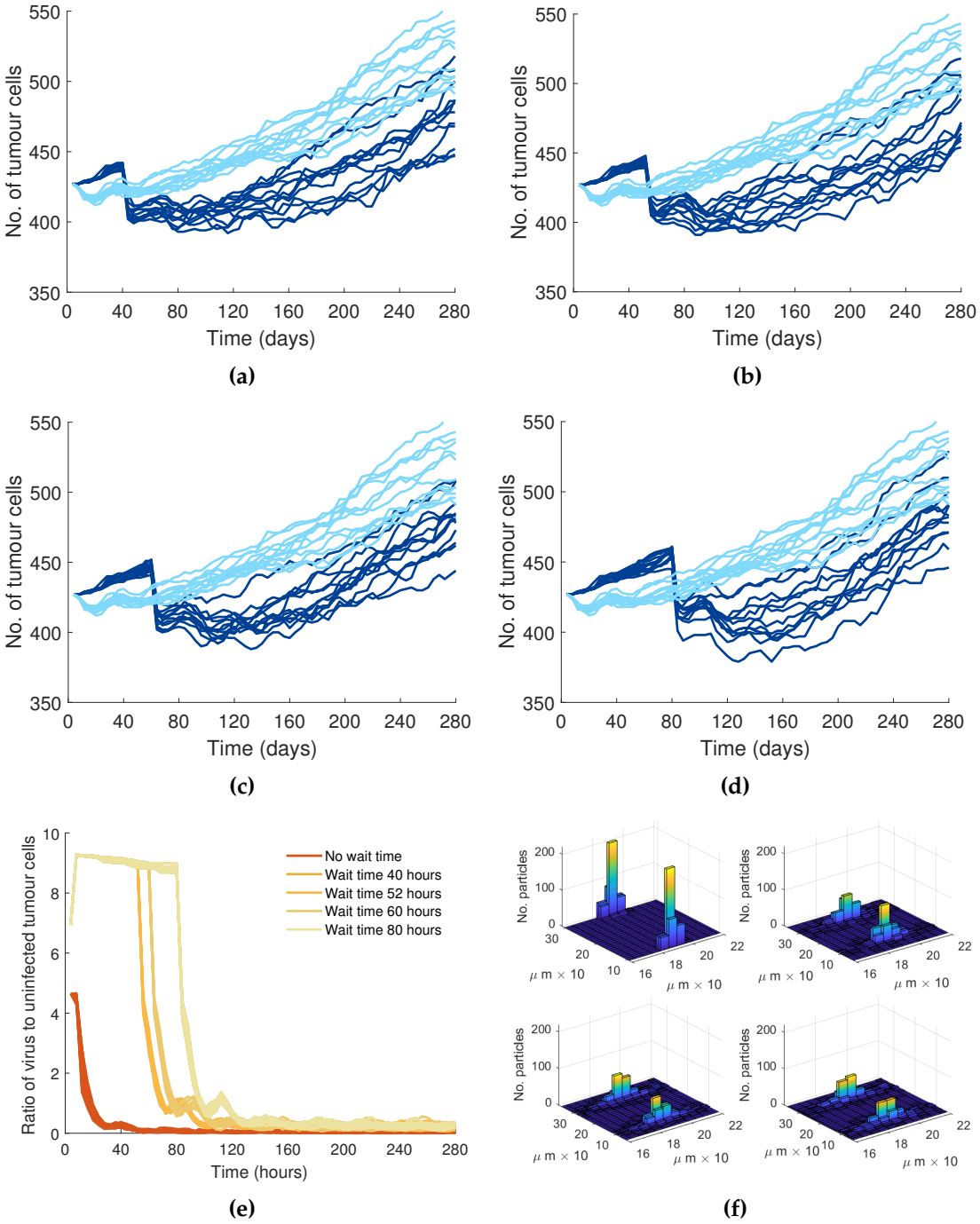

Figure 8.18: Rectangular tumour size under treatment with a delayed infecting oncolytic virus. The number of tumour cells predicted by the model over time is plotted under treatment with the original oncolytic virus (light blue) and with the delayed virus (dark blue) applied using profile E, Fig. 8.14. Twelve model simulations were considered for each case. The wait times for the delayed virus cases were (a) 40, (b) 52, (c) 60, and (d) 80 hours. Note the dramatic drop in tumour cell numbers upon initial viral infection. In (e), the ratio of the number of extracellular virus particles to uninfected tumour cells is plotted for each treatment as a function of time. The corresponding distribution of viral particles before they can initially infect for the case of no wait time, 40 hours wait time, 60 hours wait time and 80 hours wait time is plotted in (f).

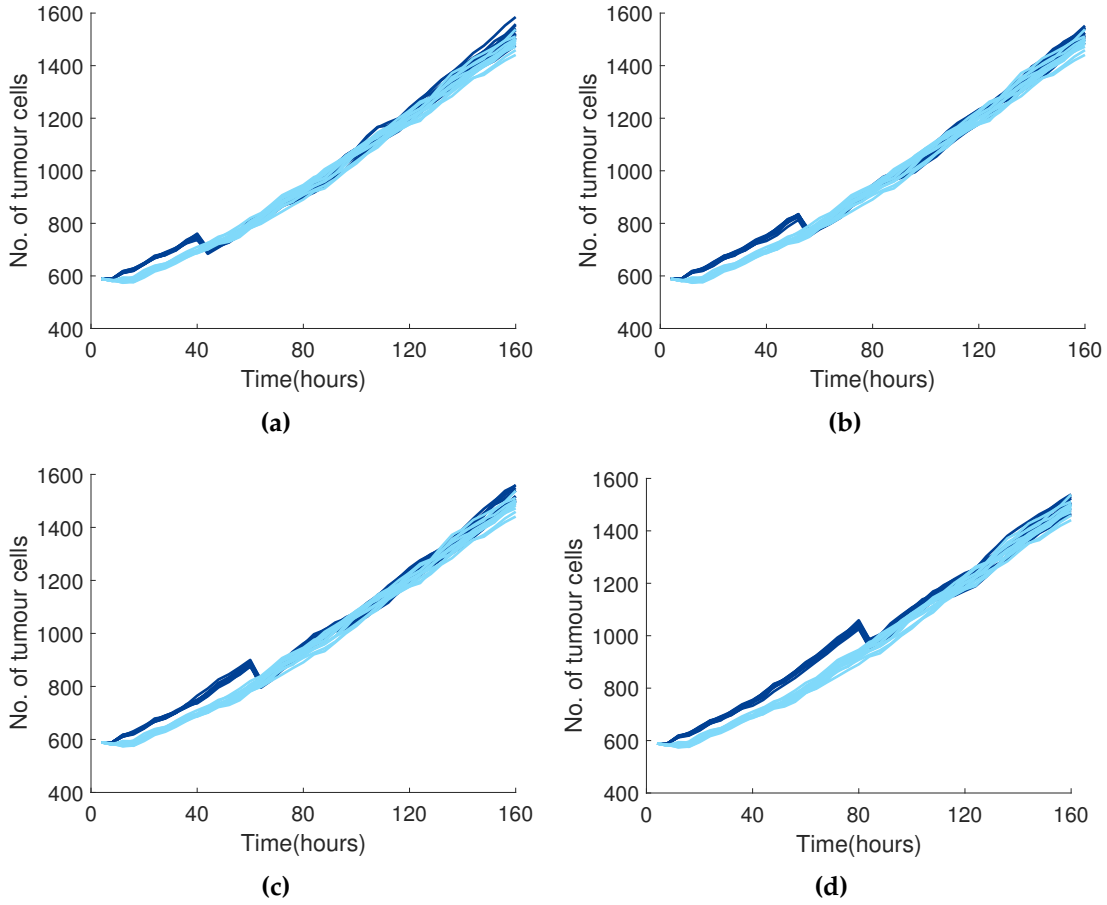

Figure 8.19: Invasive tumour under treatment with a delayed infecting oncolytic virus. The number of tumour cells predicted by the model over time is plotted under treatment with the original oncolytic virus (light blue) and with the delayed virus (dark blue) for profile A, Fig. 8.14. Twelve model simulations were considered for each case. The wait time for the delayed virus cases was (a) 40, (b) 52, (c) 60, and (d) 80 hours.

delayed treatments, this did not decrease the numbers below that of the non-delayed treatments, and the long term trends were the same, possible caused by the rapid growth of the irregular tumours. Therefore, while modifying viral particles to delay their infection could significantly improve therapy, the model simulations showed that it depends heavily on tumour shape.

In Fig. 8.20, a comparison of the treatment effectiveness at discrete time points is presented. The number of tumour cells as a function of the virus delay, at 100, 140 and 200 hours have been summarised for circular and rectangular tumours. In every case it is clear that the delayed virus was more effective on average than the non-delayed treatment, or the control case when no treatment was administered, irrespective of the

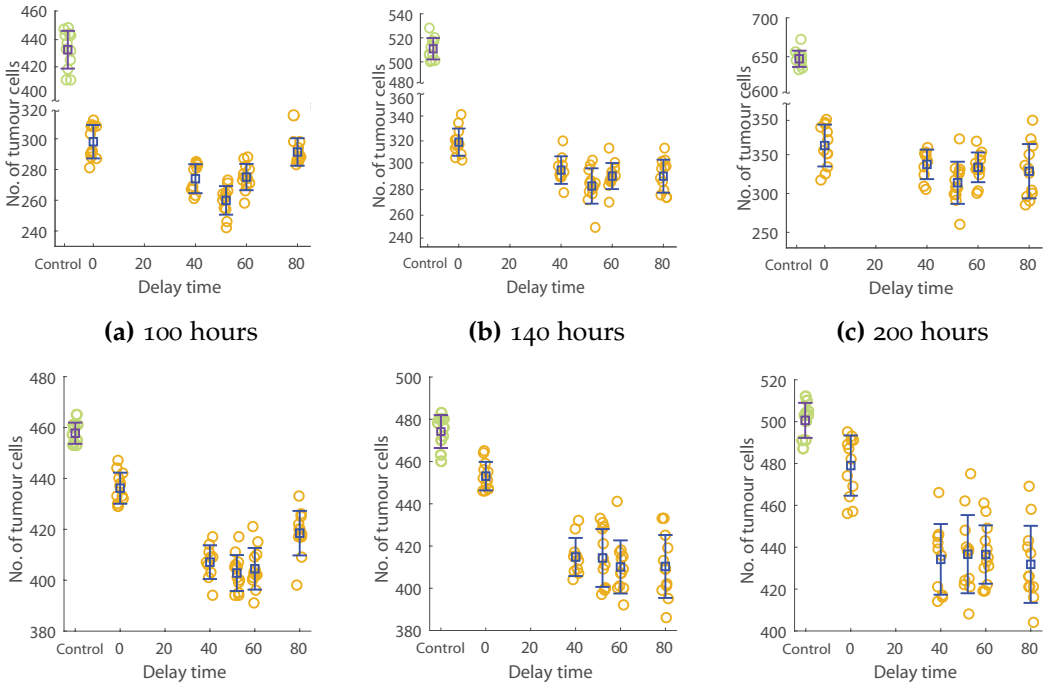

(a) 100 hours **(b)** 140 hours **(c)** 200 hours

(d) 100 hours **(e)** 140 hours **(f)** 200 hours

Figure 8.20: Comparison of treatment effectiveness at discrete time points. Individual, mean and standard deviation measurements corresponding to the number of tumour cells from the simulations Fig. 8.17 and 8.18 after (a) & (d) 100 hours, (b) & (e) 140 hours and (c) & (f) 200 hours is plotted for circular tumours (a)-(c) and rectangular tumours (d)-(e). The number of tumour cells without treatment, Fig. 8.11(b) and (d) has also been plotted on each figure as a control. Note the vertical axis break in the top row and the different vertical scales.

length of the delay. It was clear however that at 100 hours, the choice of delay had an effect on the number of tumour cells, with a delay of 52 hours resulting in the smallest average tumour cell number for both circular and rectangular tumours. However, at 200 hours, there was less sensitivity to the initial delay. This illustrates that in the short term, the length of the delay before the initial viral infection can play a significant role in the size of the tumour. To determine whether this result solely relied on the fact that the tumour size at the start of a delayed virus' infection is larger, the two types of treatment were simulated on the same size tumour at the start of their infection time (image not included). Since the delayed virus had disseminated further, the treatment performed much better than the non-delayed virus, given its inability to disseminate as far.

8.5 SUMMARY

The rapid clearance of viral particles is a major obstacle in the effectiveness of oncolytic virotherapy. Viral particles are cleared by the immune system, reducing both the numbers of particles acting and the window of time within which the treatment persists. In this chapter, a Voronoi cell-based model (VCBM) is developed for the interaction between a growing tumour and an oncolytic virus treatment and ways to optimise the treatment protocol are investigated. By optimising the injection site configuration and modifying the viruses to delay their infection, it is possible to improve the efficacy of this therapy with a particular focus on small early stage tumours.

There are two primary protocols for administering an oncolytic virus, either intratumourally or intravenously. When treatment is administered intravenously, it is challenging to predict where the treatment will enter a tumour and it is usually at multiple sites on the tumour periphery. Alternatively, when treatment is administered intratumourally, it is possible to designate the entry site location to some extent. In Fig. 8.13, 8.14 and 8.15, the application location is shown to be a crucial determinant of treatment efficacy for circular, rectangular and irregular tumours. The position and multiplicity of the intratumoural injections can significantly affect the outcome of the therapy.

To determine which injection profile results in the most effective treatment, the number of tumour cells over time for 12 model simulations has been plotted in Fig. 8.13-8.15. From visually inspecting the plots, it is not clear in every case which treatment is the most effective, and so the mean and standard deviation for each injection profile was also calculated. Using these measurements it was established that the best treatment outcome across the different shapes was achieved with 3 or more injections, where the same total dosage was divided evenly among the number of injections. In the short-term, injections that were within a tumour produced the most effective treatment. However, long term, the optimal injection configuration depends significantly on the tumour shape.

For a circular tumour, Fig. 8.13, single injections of oncolytic virus particles gave rise to the highest average tumour size over time of any of the injection configurations considered. The location of the single injection had no significant effect on the tumour

size. The lack of response to the single injection protocol is due to single injections promoting an increased multiplicity of infection with a subsequent enhancement of viral trapping that limits the breadth of spread irrespective of the location on the tumour.

In contrast, the mean and standard deviation of a circular tumour size at 280 hours was noticeably lower for three injections along the radius of the tumour or at the periphery. Increasing the injections allows for an improved diffusivity and virus to cell contact rate. The best performing injection protocol on circular tumours for a window of 50 hours was three radial and rotationally symmetric injections. After 50 hours, the efficacy of central tumour injections was overtaken by injections on the tumour periphery. This effect is due to injections on the periphery of circular tumours restricting cell growth on the boundaries, where the growth rate is usually the fastest.

The optimal treatment injection configuration for rectangular tumours, Fig. 8.14, was not dissimilar to that of circular tumours: on average, increasing the injection multiplicity improved the treatment efficacy. However, there were some cases where a single injection close to the edge of a tumour caused a reduction of tumour growth similar to that of multiple injections, see Fig. 8.14(b) and (d). This stochasticity of tumour response is explained by the fact that the tumour's primary growth occurs in a horizontal direction. Since Ductal Carcinoma In Situ (DCIS) have approximately rectangular cross sections, this could suggest that treating these cancers with virotherapy would result in a wide variety of unpredictable responses, depending on the location and multiplicity of injection.

From the injection configuration model simulations, the optimal injection profile for rectangular tumours can also be determined. Two intratumoural injections positioned halfway from the centre along the horizontal semi-axes (profile D, Fig. 8.14) reduced the tumour volume the most out of all injection configurations considered. However, administering treatment in this way could be difficult. An alternative is to administer two injections above and below the tumour (profile H, Fig. 8.14), a third of the way along the horizontal. In real tumours, this could be a simpler way of administering treatment as the tumour itself does not need to be penetrated.

It is also interesting to note that there is a pronounced oscillation in tumour cell numbers soon after injection for both the circular and rectangular tumours, see Fig. 8.13,

8.14, 8.17 and 8.18. There are two reasons why oscillations occur in the model. Firstly, the oscillations are caused by the increase in free-space within the tumour allowing cells to proliferate that were previously too confined. The second reason is, in the case of the delayed virus, a significant amount of cells are infected once the virus delay has passed, and these cells lyse simultaneously, allowing nutrients to access cells, that previously had a low probability of proliferating.

For an irregular tumour shape, it is shown in Fig. 8.15 that the most successful treatment outcome in the first 60 hours was obtained when the treatment was administered at the periphery of the tumour bulk as opposed to the invasive spines. The multitude of injections significantly affects this outcome: when ten injections are given at the periphery of the tumour, the treatment did considerably better than when three injections were administered at the periphery. Additionally, comparing this option to one single intratumoural injection, it fared the worst out of all the possible profiles. After 60 hours, the optimal injection configuration was the one that eliminated all invasive cells on the tumour spines. By eradicating the invasive cells the tumour growth is reduced significantly so that, while treatment takes longer to be effective, the overall tumour growth rate gets reduced.

While optimising the treatment injection configuration can help to improve the standard of the current treatment, there is more that can be done to increase the efficacy. To tackle the diffusivity obstacle presented by the tumour microenvironment, oncolytic viral particles can be modified to delay their infection for a specific period of time. Delaying the onset of viral infection within a tumour allows for further infiltration of the tumour prior to the onset of immune clearance.

For circular tumours it was shown that the delayed virus caused an average reduction of tumour volume at 200 hours of between 5% and 11% (depending on the length of the delay), Fig. 8.17. While the delay of 100 hours resulted in the largest initial infected cell population of 105 cells, the long-term average size of a tumour was lowest for the treatment with a 52-hour delay, the latter is the treatment recommended for further investigation. Future investigations will look at whether additional doses of the treatment can further improve this result.

The success of delayed virus infection on circular tumours can be attributed to the diffusive properties of the virus. Since the infection of the tumour cells is initially delayed, the virus is able to disseminate further into the tumour before it initially infects the cells. Additionally, due to the coating of the virus, the immune system is unable to clear the virus during the period of time before its initial infection. Therefore, since the mean squared displacement of the virus is larger for a virus that has had a delayed infection, then more virus undergoes the first round of infection. From this, more secondary virus is created from the first round of infection than the non-delayed virus' first round of infection.

In Fig. 8.17, it is clear there is an optimal timing for the delay of initial viral infection with a 52-hour delay resulting in the lowest tumour size. This has to do with the tumour growth relative to the length of infection delay. If the virus is delayed from infecting the tumour cells for too long, then the tumour will have grown to a size that is too large for the current diffusion rate of the virus to have an effect. Future work will investigate optimising the relationship between the delay of infection onset, the size of the initial tumour and the diffusivity of the virus.

For rectangular tumors, the modified virus, irrespective of the delay, had a considerable effect on reducing the tumour burden Fig. 8.18. By 200 hours (Fig. 8.20), each delayed virus reduced the tumour numbers to approximately the same level: the only major difference in the delay was how many cells were initially removed by the virus, but even this was not significant. There appeared to be no optimal delay in this case as all worked just as well as each other. This is due to rectangular tumours having a maximum tumour growth rate, since they are bounded above and below by an impenetrable boundary. The overall growth rate of rectangular tumours was less affected by the delayed viral infection treatment compared to that of the circular tumours. Since the virus diffuses radially from the initial injection and rectangular tumours grow primarily horizontally, the effectiveness of the delayed virus, due to its ability to disseminate further into the tumour, could be reduced accordingly. It is clear, however, that the use of a delayed onset virus overall improved the treatment outcome for rectangular tumours.

In the case of irregular tumour formation, the modified delayed virus was no more effective than the original non-delayed form. In a few cases, the non-delayed form resulted in lower tumour sizes than the delayed form. This is due to the aggressive nature of the tumour shape. Invasive tumours are able to grow away from the treatment sites in a multitude of ways, evading the viruses swiftly and efficiently.

The sensitivity of the number of tumour cells as a function of the treatment delay is summarised in Fig. 8.20. By comparing the different tumour cell numbers, at 100 hours a delay of 80 hours led to a higher tumour cell count, compared to the other delays, whereas at 200 hours, a delay of 80 hours had a lower average that most of the other delayed viruses. This illustrates how the delayed virus takes time to catch up with a growing tumour.

In general, after around 140 hours, the chosen delay doesn't contribute significantly, with all delays resulting in smaller tumour cell numbers on average than the treatments with no delay or for a tumour growing without treatment. As such, the effectiveness of the delay is a function of time. If this treatment was to be tested experimentally, this suggests that only early measurements would reveal any difference between the effectiveness of the different delay treatments. Overall, this result suggests that there could be a significant dependence of tumour size on the timing of the measurement.

In conclusion, for circular and rectangular tumours, modifying viral particles to delay their infection can produce a notable advantage to therapy; however, for irregular tumours the benefit remains unclear. This model is presented in 2-dimensions and with the addition of a third dimension, the drop in tumour cell numbers could be significantly larger. Future work will investigate the delayed virus efficacy on 3-dimensional tumour shapes.

It is worth noting here that the results are dependent on the underlying dynamics of the model. To investigate the possible validity of these results on a more heterogeneous sampling of tumour types and viral treatment modalities, it would be worth considering different viral dissemination profiles, tumour growth dynamics and viral clearance rates. In the next stage of this work, it also would be worth investigating how the immune system dynamics may influence the viral clearance and whether the delayed virus is truly more effective in the presence of an antiviral immune response.

The spatial investigation in this chapter has allowed for a visual in-depth appreciation of the general virus-tumour cell dynamics in oncolytic virotherapy. Using a Voronoi tessellation to form the shapes of cells, combined with force balance equations, allows for a good approximation of the real life spatial effects of pressure and cell-to-cell interactions.

9

DISCUSSION

In this thesis, mathematical models have provided valuable insight into oncolytic virotherapy and immunotherapy. Deterministic, probabilistic and agent-based modelling were used to model the intricate and complex interactions between viruses, immune cells and tumour cells at the intracellular and extracellular scale. Often the data used to optimise parameter values was sparse and creative techniques were developed to draw insight from this data.

SUMMARY OF THESIS RESULTS

A challenge facing oncolytic virotherapy is determining how to maximise both viral spread and anticancer cytotoxicity. Many experimentalists are investigating genetic attenuation for this purpose. To assist in the understanding of variations in characteristics and effect of these gene-attenuated viruses, a novel integro-differential system with distributed parameters was developed (Eq. (4.1)). Intracellular viral and tumour heterogeneity was modelled using distributed parameters for viral replication start times and cellular burst times. This is an important and significant inclusion as the intracellular replication process is known to be extremely stochastic (see Section 2.4.2).

Miyashita *et al.* (2015) showed that stochastic processes govern the number of viral genomes that establish infection and the accumulation of their progenies in an infected cell. Additionally, as reviewed in Section 3.2.5, time delays are intrinsic to the infection and replication processes of viruses and have been considered in numerous models for human immunodeficiency virus (HIV). As the generation of new viral progeny drives the success of oncolytic virotherapy, it is crucial to model the intracellular dynamics using distributed delays. At the smallest biophysical scale considered in this thesis, an integro-differential model was used to understand the effects of E1B gene-attenuation of the adenovirus (Chapter 4). This mathematical framework can be used to understand the genetic characteristics of many oncolytic viruses and is a useful step in the direction of creating a safer and more effective viral treatment platform.

Scaling up, an extracellular mean-field approach for the viral-tumour interaction was developed (Chapter 5), consisting of two systems of ordinary differential equations (ODEs). Comparison to, and tuning with, experimental data showed that these

deterministic models can be successfully used to represent the extracellular dynamics of the virus-tumour interaction. Initially, a minimal coupled system of ODEs was introduced to capture the infection and lysis of tumour cells, see Eqs. (5.1)-(5.3). Whilst a number of biological limitations existed in this model (such as unimpeded tumour growth) the simplicity allowed for a thorough local stability and bifurcation analysis to be conducted. Interestingly, this model did not possess any regimes that could result in complete tumour eradication, demonstrating that models similar to this would also predict treatment failure.

Changing the biological assumptions of the minimal extracellular model to consider Gompertzian tumour growth and frequency-dependent viral infectivity rates, resulted in the extended model in Eqs. (5.10)-(5.12). This model showed a singular equilibrium and a number of highly nonlinear behaviours that had interesting biological consequences, see Fig. 5.17. For example, the model predicts long-period "square wave" oscillations, something not seen regularly in mean-field models of oncolytic virotherapy. This suggests that long-periods of remission can be followed by rapid regrowth of the tumour to the environmental carrying capacity. At this point, the virus population builds back up and the brings the tumour back to remission (see Fig. 5.17 case (4)). Additionally, the model illustrates regions of bistability, i.e. where two different outcomes can occur depending on the initial conditions, see Fig. 5.22.

These interesting dynamics were the result of a number of non-trivial bifurcation scenarios in the presence of an important system equilibrium (i.e full tumour eradication) that is characterised by a singular Jacobian. This occurrence required the use of a hybrid combination of numerical continuation, symmetry considerations and integration of the model to map out the dynamics as a function of relevant model parameters. The methodology could hopefully be used in future studies of singular equilibria systems.

The analysis of the minimal system of ODEs with Gompertzian tumour growth was then applied to an experimental oncolytic adenovirus modified with polyethylene glycol (PEG) and conjugated with Herceptin (Chapter 6), and an oncolytic adenovirus expressing IL-12 and GM-CSF (Chapter 7). Mean-field formulations were chosen for these studies as the inclusion of spatial dependencies or stochasticity into these

models would have added too many degrees of freedom to enable conclusions to be drawn regarding optimisation of the therapies. The models allowed insight into the efficacy of the viral infectivity and immune stimulation in improving oncolytic virotherapy and immunotherapy. For example, increasing the viral infectivity rate for a PEG and Herceptin-modified adenovirus resulted in a dramatic drop in the tumour size (see Fig. 6.5(c)). A similar effect was seen for the IL-12 and GM-CSF expressing virus, where reducing the virus-infected cell stimulation of APCs was shown to increase the effectiveness of the therapy (see Fig. 7.6).

Moving from consideration of well-mixed mean-field systems, geometric effects on the virus-cell interactions were encoded using a Voronoi cell-based model (VCBM) (Chapter 8). While deterministic models can provide invaluable insight, agent-based models (ABMs) allow for more realistic simulations of the actions and interactions of tumour cells and individual virus particles at the smaller scale. The two dimensional investigations explored indicated the utility of the approach, justifying the extension to model realistic three-dimensional geometries in future studies, and tuning to other growth rates and formation characteristics. The VCBM could also be applied beyond the particular cancer and viral interactions of the PEG and Herceptin-modified virus and the IL-12 and GM-CSF expressing virus analysed in this thesis.

Additionally, the studies indicate that the VCBM can act as an excellent visualisation tool for biologists and clinicians, for example to pinpoint the depth of the treatment spread and its effectiveness, as shown in Fig. 8.12. One difference of this model to previous spatial models for oncolytic virotherapy (Section 3.3.1) is that viruses are assumed to follow a continuous-time random walk, with waiting times between successive movements drawn from a stable distribution. This particular modelling was chosen specifically to capture the trapping phenomena and the inability of viruses to diffuse through the tumour microenvironment (Kim *et al.*, 2006b), something that is not captured through the use of classical diffusion (Friedman *et al.*, 2006; Mok *et al.*, 2009) or simple lattice random walks (Paiva *et al.*, 2011).

OPTIMISATION APPROACHES AND APPLICATIONS

A large portion of this thesis centered around the development of fitting algorithms that could optimise model parameters to a range of different experimental measurements. To improve oncolytic virotherapy and immunotherapy, mathematical models were optimised to data. Different approaches were used for time-series measurements (e.g. Fig. 6.3) versus single time-point values (e.g. Fig. 6.9). Additionally, sparse data sets (e.g. Fig. 4.7) required a different interpretation focusing on the identification of the primary determinants of the system behaviour.

A simultaneous optimisation approach was taken for the PEG and Herceptin- modified adenovirus. The model for this virus was optimised both to individual data sets and also simultaneously to the combined data for tumour growth (Fig. 6.2 and Fig. 6.3 respectively). Whilst the tumour growth rate and the initial number of tumour cells were relatively tightly distributed (due to the constraint of multiple data points) amongst the individual parameter fits (Table 6.1), the lysis rate and the viral decay had more variance (being constrained by fewer data points). More specifically, for the lysis rate of the infected tumour cells there is evidence of a bimodal distribution from the individual data set optimisations. This bimodal behaviour is not experiment specific, but instead appears to be an underlying bimodal response in the mice. Restricting this parameter to be common across all data sets in the simultaneous optimisation (Table 6.2) constrained the search space and determined which mode best represents the mean response under all experimental protocols.

Hierarchical fitting algorithms are useful when the processes differing between successive data sets are clear. An extensive hierarchical fitting approach was taken to tune the mean-field model for an oncolytic adenovirus expressing IL-12 and GM-CSF (without immature dendritic cell (DC) injections, Eqs. (7.1)-(7.7), and with immature DC injections, Eqs. (7.8)-(7.14)). Eleven time-series measurements from *in vitro* and *in vivo* experiments were combined for the optimisation process. The results suggest some underlying competition between the IL-12 and GM-CSF's effectiveness on immune cell stimulation. Examining the parameter values in Table 7.2 shows a decrease in the rate of helper T cell activation, s_H and an increase in the rate of antigen-presenting cell

(APC) activation, s_A, when both cytokines are being expressed. Mechanistically, this suggests that combining both cytokines reduces the number of T cells produced and increases the presence of APCs at the tumour site, indicating the existence of negative feedback.

To improve treatment with the adenovirus expressing IL-12 and GM-CSF, the virus was combined with a population of immature DCs. Hierarchically combining the previous virus-based experiments with the *in vitro* DC decay measurements, parameters for the stimulation of immature DCs by infected and uninfected tumour cells were estimated, see Table 7.6. From this work, the unknown release profile of the virus from the gel could then be obtained, see Fig. 7.14, demonstrating the effectiveness of this method in combining multiple data sets.

A two-tier hierarchical and simultaneous optimisation allowed the identification of the key differences in the actions of the gene-attenuated adenoviruses: Ad-wt, Ad-ΔE1B19, Ad-ΔE1B55 and Ad-ΔE1B1955. This method was employed to combat the sparse nature of the virus titer measurements, see Fig. 4.7. Firstly, the parameters affected by the cell type were separated. The viruses were then grouped based on the differences in their virus titer measurements with the replication rate as the main difference between subgroups. Simultaneous optimisations were used to obtain the overall parameters for the subgroups of the viruses, see Table 4.1. Parameter perturbations for each subgroup were then used to determine the defining process of each virus, see Figs. 4.8 and 4.9. This two-tier hierarchical optimisation approach enabled differences in related gene manipulations to be identified (summarised below).

DETERMINSTIC AND PROBABILISTIC MODELLING

There were limitations to each of the different modelling frameworks developed in this thesis. In the ODE systems, only well-mixed populations were considered and the ability of the virus to infect already infected tumour cells was ignored. This restriction was relaxed in the VCBM investigation and had a noticeably significant effect. For example, in the case of the delayed-infection virus, Fig. 8.16, it is clear that with multiple viral infections there is a reduction in the total number of extracellular viruses available to

infect uninfected cells. This finding could be fed back into future mean-field modelling. By comparing the models and results from the different scales and modelling bases, it is possible to make deductions about the sensitivity of biological extracellular interactions.

LOWER SCALE MODELLING AND ITS BIOLOGICAL IMPACT

Modelling the intracellular dynamics of viral infection, replication and cell lysis has led to ways of improving viruses by attenuating their genetic material. The dominant processes for induced genetic mutations of an oncolytic adenoviruses were identified by a two-tier hierarchical optimisation of the integro-differential equation with distributed parameters to virus titer measurements. The *E1B 55* gene primarily influences the replication rate of the virus with the deletion of this gene resulting in a significant reduction in the rate (Fig. 4.7(b)). On top of this, the deletion of both the *E1B 55* and *E1B 19* genes resulted in a long delay in the average replication start time of the virus. The differences in the Ad-wt and Ad-ΔE1B19 virus populations (Fig. 4.9) indicated that deleting only the *E1B 19* gene has an effect on the replication rate, a characteristic not previously hypothesised to be connected with this gene.

WHAT CAN BE INFERRED FROM PARAMETER PERTURBATIONS AND MODELLING CHOICES

It is widely known that humans are incredibly heterogeneous and everyone's response to treatment is slightly different. The extracellular virus-cell interactions (such as virus infectivity) and the way they influence treatment outcome has been a major theme of this thesis. The parameter sensitivity analyses provided insight into which dynamics are the key drivers of interactions and how parameters, and therefore interactions, may be tuned to better improve treatment.

The juxtaposition of the two minimal models for the extracellular dynamics of viruses and tumour cells (Chapter 5), allows for a comparison of how the outcomes of

therapy change with different biological modelling assumptions. Assuming an exponential tumour growth rate and mass-action viral infectivity, a bifurcation analysis showed that oncolytic virotherapy is unable to eradicate the tumour, see Fig. 5.9. However, oscillations that appear like homoclinics emerge for certain regions in the parameter space, indicating a quasi-eradication or remission state is possible, see Fig. 5.13.

Extending this model to consider Gompertzian tumour growth and frequency - dependent virus infection, it was shown through a bifurcation analysis that tumour eradication can be achieved for viral characteristics that fit well with the growth rate of the tumour, see Fig. 5.17 (4) and 5.18. Interestingly, the model shows that therapies involving oncolytic viruses endowed with high potency do not universally constitute successful strategies for eradication. The model points to a number of interesting findings regarding the role of oscillations between a tumour and an oncolytic virus, specifically in the region of bistability, see Fig. 5.22. This shows that including either the Gompertzian tumour growth or frequency-dependent virus dynamics was able to introduce stability of the equilibrium at the origin.

Parameter regimes that result in tumour eradication were then investigated for the PEG and Herceptin-modified adenovirus (Chapter 6). A constrained parameter perturbation was used to explore the effects of the alteration of different characteristics of the treatment, see Fig. 6.5. The tumour characteristics were shown to have a profound effect on the efficacy of treatment, along with viral infectivity. Increasing the viral infectivity or decreasing the tumour replication rate reduce the tumour size most significantly. These results suggest that there may be ways of manipulating viral infectivity to achieve clinically realistic tumour eradication.

Interestingly, the efficacy of this PEG and Herceptin-modified treatment in the presence of the inteferon-mediated antiviral cell-immunity and antitumour immune response is still driven by the viral infectivity rate (Fig. 6.11). This aligns with the intuition that increasing the infectivity increases initial cell death and subsequent antitumour immune response. Initial tumour size also influences the eventual tumour size only in the presence of the antitumour immune response. In the absence of this response, if the antiviral-immunity is present, this sensitivity is not present (comparing Figs. 6.5(b) and 6.12).

Further investigations into the immune sensitivity were made for an oncolytic adenovirus modified with IL-12 and GMCSF (Chapter 7). The results showed the existence of certain killer-T-cell-induced apoptosis rates for which this treatment is ineffective, see Fig 7.6(c). For fast and slow killer T cell induced apoptosis rates, the tumour size was dramatically reduced around day 30. This demonstrates that this interaction and the time frame of the treatment can result in vastly different outcomes. Controlling the killer-T-cell-induced apoptosis rates could be achieved through the introduction of an experimental cancer treatment known as CTLA-4 blockades (Henson *et al.*, 2008; Parry *et al.*, 2005). Using the CTLA-4 blockade, researchers have shown that this treatment can enhance T cell cytotoxic responses and induce the differentiation of CD_4 T cells (or helper T cells) (Leach *et al.*, 1996).

The model for the adenovirus modified with IL-12 and GM-CSF also suggested that reducing APC stimulation and increasing helper T cell stimulation could possibly improve treatment, see Fig 7.6(a) and (b). Researchers have suggested the possibility that chemical inhibition of the MAPK ERK pathway in DCs reduces the maturation of these APCs and therefore the stimulation rate (Liechtenstein *et al.*, 2012; Puig-Kröger *et al.*, 2001). This is one possible avenue of investigation that could be undertaken to test the results in Fig. 7.6(a). To increase the helper T cell activation, both cytokines IL-1 and IL-12 are known to heavily stimulate the differentiation of naive T cells (Macatonia *et al.*, 1995; Liechtenstein *et al.*, 2012). So to test the results seen in Fig. 7.6(b), an additional intravenous injection of IL-12 or IL-1 could be a possible way of increasing the stimulation rate of helper T cells.

Whilst the immune system can be an asset to oncolytic virotherapy, it can also be a hindrance. The rapid decay in the concentration of viral particles due to clearance by the immune system shortens the window of effectiveness for oncolytic virotherapy. To avoid this clearance, oncolytic viral particles can be modified to delay their infection for a specific period of time as investigated by the VCBM in Chapter 8.

Delaying the onset of viral infection within a tumour allows for further infiltration of the tumour bed, see Fig. 8.16. This modified treatment results in a reduced tumour population over time for circular and rectangular tumour shapes, see Fig. 8.17 and 8.18. This addition to therapy could prove to be a simple yet effective way to improve the

efficacy of oncolytic virotherapy for some tumour types. The suggested viral modification is worth investigating further and verifying experimentally as it could prove to be a better treatment protocol. These simulations illustrate both the usefulness of mathematical modelling and the importance of the extracellular dynamics, specifically viral clearance.

THE IMPACT OF THE TREATMENT DELIVERY SYSTEM

The development of an effective delivery system would further advance virotherapy and immunotherapy by maximising safety, efficacy and duration of transgene expression. In Chapters 5-8, alternative application protocols were investigated with two main categories: administration protocol (intravenous vs intratumoural) and dosage protocol (discrete versus continuous). The two possible administration protocols are investigated generally (Chapter 5 and 8) and for specific therapies (Chapters 6 and 7). Whilst these investigations above considered discrete dosing strategies, continuous delivery through the use of a gel-release mechanism was also considered (Chapter 7). From all these investigations, conclusions can be drawn about the influence of dosage protocol on the interactions. Overall, this thesis has used mathematics to illustrate ways that oncolytic virotherapy and immunotherapy may be improved through better viral application protocols.

Using the VCBM developed in Chapter 8 it was possible to find optimal intratumoural injection locations as a function of tumour shape. The injection site configuration was shown to play a significant role in the overall treatment outcome, see Figs. 8.13 - 8.15. The distance between intratumoural injections and their corresponding distances to the centre of the tumour had a significant effect on the overall treatment outcome for circular tumours, see Fig. 8.13. When the three injections reside at the same location, the resulting tumour burden was quite high, irrespective of the distances from the injections to the centre of the tumour. Whereas, if the injections were given at a reasonable distance apart, the treatment reduced the tumour size significantly. Furthermore, in this scenario, the further the injections were from the tumour centre, the more

effective the treatment. This suggests that intratumoural injections should be given far from the tumour centre and distant from each other.

The sensitivity of the injection protocol was also considered for a rectangular tumour shape and an invasive tumour shape, see Fig. 8.13 and 8.14. In the case of a rectangular tumour, the model predicated that injections at either end of the tumour would be considerably more effective that injections in the centre or above and below the tumour. For an invasive tumour shape, it was shown in Fig. 8.15 that the most successful treatment outcome is obtained when the treatment is administered at the periphery as opposed to the invasive spines. Also the multitude of injections significantly affected the outcome. When ten injections were given at the periphery of the tumour, the treatment did considerably better than when three injections were given at the periphery. Additionally, comparing this to one single intratumoural injection, in every case this fared the worst out of all the possible injection combinations.

Discrete injections of oncolytic virus can result in vastly different outcomes depending on the state of the virus-tumour interaction. The existence of a bistable region in the extracellular virus-tumour interaction resulted in different initial viral loads causing vastly different outcomes, often in a counter-intuitive way (see Fig. 5.22). If the initial tumour size is small, full eradication can only be achieved if the dose is either sufficiently low or sufficiently high. Small viral loads are effective because they first allow the tumour to growth to larger sizes, thus eliciting stronger viral responses. In addition, this result indicates that if subsequent injections are given too quickly, the system can be pushed into a dormant tumour regime, whereas if only a single initial dose was administered the tumour could have been eradicated. The modelling could then be used to design experiments to investigate this positive effect of low viral doses. The initial results of this model also indicate the need to extend the system to include the dynamics of virus penetration and diffusion which certainly play a fundamental role in the success of virotherapy.

Not only can additional injections perturb a trajectory that may have resulted in full eradication into a dormant state, but as shown for oscillations in Fig. 5.21, they can have a transient, often negative effect on the whole system. If additional dosages are administered when the system resides on a stable oscillating state, these injections, de-

pending on when in the cycle are provided, tend to increase the amplitude a of few cycles of oscillations before the system goes back to its original fluctuations with no ability to drive the model out of this phase, see Fig. 5.21. Strategies that instead optimise the quality of the oncolytic virus or reduce the tumour growth rate are preferable as oscillations can be reduced or damped to zero either by increasing the speed of infected cell death or the life span of virus at the right amount or suppressing tumour growth, see Fig. 5.18. In this sense, rather than complex injection schedules or larger amounts of externally provided virus, the model suggests that pharmacological interventions that aim at blocking or reducing the growth of the tumour would be most effective.

Experimental studies can only explore a finite number of strategies, and using the parameters optimised for the PEG and Herceptin-modified virus, the effects of increasing the viral dose and dosage protocol were demonstrated (Fig. 6.6). In the absence of negative effects of viral overload, it would seem from Fig. 6.6(b) that the best strategy for fast-tumour eradication would be a single, very high dose injection. Realistically, however, the choice of treatment strategy will depend on interplay between dosage size and eradication half-time.

Comparing the high dose single injection to application protocols with ten days between injections, it is clear that much lower viral doses are required to reach finite eradication half-times. Increasing the days between injections can lessen the dose required to reach eradication, and this trend appears insensitive to the number of injections. Overall, application protocols with two injections appear to provide good combinations of lower doses and reasonably short eradication half-times. The analysis shows that limiting and reducing tumour size and growth is a possibility under the current or slightly modified treatment regime. Shrinkage and then surgical removal may be a possible treatment design utilising oncolytic viruses and may be less detrimental than chemotherapy.

Moving from discrete to continuous treatment administrations, hydrogels are an effective way of providing a long-term continuous local treatment. A full numerical simulation of the possible dosage protocols for a gel loaded with DCs and adenovirus expressing IL-12 and GM-CSf was investigated in Chapter 7. Through an exhaustive

numerical search using the optimised model for the IL-12 and GM-CSF-expressing adenovirus combined with DC injections, it was possible to determine constant, linear and sigmoidal gel-release profiles that would significantly reduce the tumour population. In essence, the optimal constant gel-release (Fig. 7.15) and increasing linear gel-release (Fig. 7.19) profiles occur when DCs are released for a shorter period of time than viruses. The idea of manufacturing a gel that released its contents at type-specific rates such as this, does not appear to have been considered previously. The analysis in Chapter 7 indicated this would make a significant impact on the efficacy of treatment.

Overall, the results around the treatment administration protocol provided insight into the significance of the extracellular dynamics. Vastly different outcomes are seen when mean-field modelling compared to agent-based modelling are used to simulate discrete dosage protocols (Fig. 5.22, 6.6 and 8.13). For certain parameter regimes of the mean-field models, it is possible to achieve tumour eradication either in the regions of bistability (Fig. 5.22) or for a high enough initial dosage (Fig. 6.6). However, eradication appears not to be possible in the VCBM (Fig. 8.13). This shows that modelling the extracellular processes and the manner in which they are simulated can be crucial to predicting the outcome of tumour eradication.

SIGNIFICANCE OF THE RESEARCH

To significantly improve the prognosis of cancer treatments, there is a need for more multidisciplinary collaborations. The range of stochastic and deterministic mathematical models and analysis techniques developed in this thesis are applicable in future oncolytic virotherapy and immunotherapy studies. A large majority of the work is also translatable to other novel cancer therapies that need further analysis with regards to intracellular or extracellular dynamics. Through the treatment studies presented, a range of data-fitting techniques have been applied and the relative advantages and applicability explored. This thesis has suggested a range of treatment improvements that would significantly change the face of oncolytic virotherapy. With future collaborations and mathematical analysis, it may be possible to advance these results and determine a range of effective anti-cancer treatments.

10

CONCLUSION AND FUTURE WORK

Cancer and cancer treatment presents a highly complex, multidisciplinary problem and with the help of mathematical modelling, new effective ways of treating this disease can be devised. This thesis aimed to improve the efficacy of oncolytic virotherapy and immunotherapy using a range of mathematical techniques. The mathematical models were created to embody the processes underlying the dynamic interactions between cancer cells, normal tissue, the different treatment vectors and immune system. They were tuned to accurately reflect the biological system using multiple *in vitro* and *in vivo* experimental measurements from a range of different oncolytic virotherapies and immunotherapies. These models then provided both quantitative and qualitative insight into the virus-tumour interplay, the application protocols and the efficacy of the treatments. The results indicate that the key features of viral infectivity and therapy administration protocol are the primary determinants of the outcome of the therapy.

Drawing on both deterministic and stochastic modelling, it has been possible to develop a useful representation of the biological interaction between an oncolytic virus, the immune system and cancer. The mathematics has provided insight into the fundamental questions about the effects of gene-attenuation on an oncolytic adenovirus, and identified the specific processes that particular mutations alter in the virus-cancer dynamics. In turn, through modelling the antiviral-mediated cell-immunity, it has been possible to deduce the role refractory sub-populations of tumour cells play in therapy outcome.

A core theme through the studies in this thesis is that both viral infectivity and therapy administration protocols are key to improving the tumour eradication ability of oncolytic viral vectors. The bifurcation analyses showed that regions of bistability result in a highly sensitive outcome to the application protocol. These results were seen most significantly in the case of gel-release therapy, where it was clear that altering the gel-release rate could improve the therapy to the point of complete tumour eradication. The inclusion of spatial heterogeneity also indicated the effect of the treatment administration geometry on the optimal treatment results.

This thesis has identified key tunable features of both the virus and application protocols that improve treatment outcomes for a range of different virotherapies. In this work, it was shown how different mechanistic ways of modelling extracellular

and intracellular interactions may influence the outcome of therapy. The scale of the effects of the extracellular interactions were then clear. The studies have identified that extracellular interactions are a major determinant of the success or failure of cancer therapy.

Mathematical modelling has been showen to be a highly effective tool for improving oncolytic virotherapy and providing insight into the mysteries surrounding the cancer-virus interaction. The modelling work in this thesis has provided a range of useful and malleable models that can be used both for the specific engineered viruses modelled and also as a methodology for other therapies. Future extensions of the work in this thesis, and applications of it to other therapies, will help to further cancer research and hopefully bring us one step closer to a cure.

The mathematical and biological techniques and insight in this thesis provide a platform for further work. In this section, an overview of some possible future directions is provided. This is then followed by a preliminary investigation that complements the work in the previous chapters of this thesis.

10.1 OVERVIEW OF FUTURE DIRECTIONS

The heterogeneous intracellular viral replication process was investigated in this thesis using a minimal integro-differential model (Eq. (4.1)). The model developed is not specific to oncolytic virotherapy, and could be used to understand the heterogeneity in the intracellular processes of a wide range of viruses, such as HIV. The ability of the model to capture the virus titer dynamics suggests that future modelling of oncolytic viruses should consider the stochasticity induced by cellular heterogeneity. A logical extension of the model is to include the extracellular dynamics examined in the other chapters.

A simplifying assumption of the model in Eq. (4.1) was that the multiplicity of infection (MOI) (i.e. the number of viruses entering a single cell) can be approximated by an average replication rate. D'Halluin and Milleville (1984) demonstrated that the MOI does actually influence the rate of synthesis of viral DNA during production. It

is, therefore, worth adding this assumption for the multiplicity of infection into the model, to determine its effect on the virus titer.

Surface modification of an oncolytic virus, for example PEG-modification and Herceptin conjugation (Chapter 6), poses a problem in treatment optimisation: any virus produced via replication within a tumour cell will lose surface modification after one replication. This transformation was not explicitly modelled in Eqs. (6.1)-(6.4). A future extension could investigate how different decay rates for the coated and non-coated viruses influences the model dynamics. Additionally, it would be worth re-investigating the dosage protocol to determine whether the loss of surface modification influences the results of Fig. 6.6, i.e. a large single dosage preforms best.

The viral time-series measurements for the PEG-modified adenovirus were noticeably different compared to the measurements for the unmodified adenovirus, and the PEG and Herceptin modified adenovirus, see Fig. 6.7. The standard model assumption of biexponential decay was unable to capture the behaviour of the PEG-modified adenovirus as there appears to be two clear phases to this viruses decay. An interesting extension would be to determine what mechanism governs this virus's clearance and how it might effect the treatment's efficacy.

A natural extension of the gel-release profile investigations (Section 7.4) is to analyse this system using techniques from optimal control theory. Optimal gel-release profiles to reduce the size of the tumour could then be determined computationally. Also of note is the difference in the tumour growth under a single PBS or empty gel injection (Fig. 7.12). Future work should examine the possibility of the gel having an effect on the underlying tumour growth. Subsequently, the gel-release profile should be optimised taking this effect into account.

The Voronoi cell-based model (VCBM) (Chapter 8) could be used to investigate other oncolytic viruses. For example, oncolytic viruses expressing relaxin (a hormone which breaks down the extracellular matrix) are becoming more popular as a treatment for solid tumours (Kim *et al.*, 2006b). Using the VCBM, the effects of relaxin on virus spread and infectivity could be investigated by changing the cell-cell spring dynamics, or changing the stability parameter of the stable distribution of viral movement waiting times (see Fig. 8.4). The VCBM could also be broadened to a three-dimensional

framework, allowing for other tumour characteristics to be included, such as vascularisation and necrosis. This extension would, however, increase the computational cost, as both the number of cells and time period over which they require simulation would be much larger than the current investigation.

Above, are just a few of the possible future directions and extensions from the research in this thesis. The following section details a preliminary investigation that was inspired by the work in this thesis. An agent-based modelling platform known as PhysiCell (Ghaffarizadeh *et al.*, 2018), was used to model an oncolytic adenovirus expressing secretable tumour necrosis factor (TNF)-related apoptosis-inducing ligand (TRAIL). Drawing on the work in the preceding chapters, models for the intracellular and extracellular dynamics of this oncolytic virus were developed. The model was then used to investigate the influence of intravenous injections and TRAIL production, providing insight into an unexplored biological mechanism. A succient overview of the model is provided below with specific details of the PhysiCell setup and model implementation given in Appendix C and D respectively.

10.2 A PRELIMINARY INVESTIGATION INTO THE INFLUENCE OF VIRAL-INDUCED TRAIL RELEASE KINETICS: A PHYSICELL REALISATION

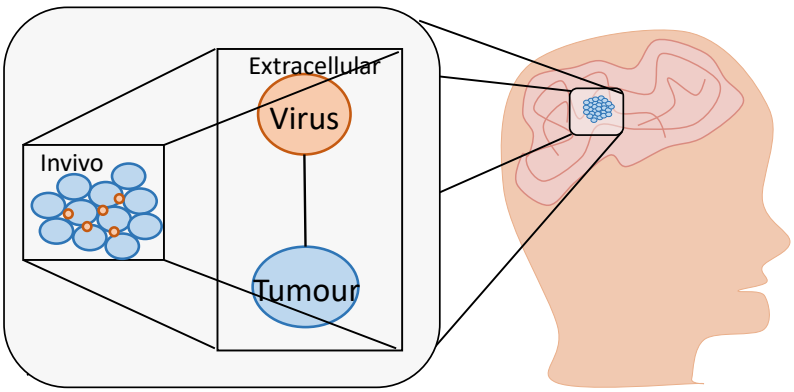

Figure 10.1: Subset of Fig.1.1, summarising the investigation of the virus-tumour interaction in this section

Glioblastoma is an aggressive and malignant form of brain cancer. Most glioblastomas develop from normal glial cells (such as astrocytes which support nerve cells) by multistep tumourigenesis (Urbańska *et al.*, 2014). The tumours are characterised by infiltrating growth, making them difficult to distinguish from normal tissue (Urbańska *et al.*, 2014). Glioblastomas are is difficult to cure with conventional cancer therapies (Oh *et al.*, 2018). Some of this difficulty can be attributed to tumour cells failing to undergo apoptosis. Research has thus begun to focus on triggering apoptosis in glioblastoma cells via alternative routes (Hawkins, 2004). A wide variety of apoptosis-inducing molecules have been identified as possible alternative apoptosis triggers (Kim *et al.*, 2006a). The best characterised are the ligand-type cytokine molecules of the tumour necrosis facor (TNF) family. Binding of TRAIL to the receptors of glioblastoma cancer cells has been shown to effectively trigger the apoptosis pathway (Kim *et al.*, 2006a; Hawkins, 2004). In addition, TRAIL has negligible effects on normal cells making it an excellent addition to glioblastoma therapy (Hawkins, 2004).

While TRAIL has shown potent and cancer-selective killing activity, concerns over delivery and toxicity have limited clinical progress (Jeong *et al.*, 2009). As such, researchers have been investigating using an oncolytic adenovirus as a delivery vector (Kim *et al.*, 2006a; Jeong *et al.*, 2009; Oh *et al.*, 2018). To evaluate the therapeutic potential of TRAIL-based virotherapy in brain tumours, Kim *et al.* (2006a) engineered a replication-incompetent adenovirus ri-Ad-stTRAIL to deliver the gene that encodes secretable trimeric TRAIL. The ri-Ad-stTRAIL virus was designed to induce the secretion of TRAIL in virus-infected cells, leading to apoptosis in uninfected neighbouring tumour cells. Kim *et al.* (2006a) showed that the ri-Ad-stTRAIL effectively decreased cell viability (Section 2.5.2) to 42% by day 3. They also showed that ri-Ad-stTRAIL treatment of U-87MG glioblastoma murine tumours suppressed and controlled tumour growth for the first 20 days, after which the tumour grew back.

To improve the effectiveness of the adenovirus-TRAIL therapy, Oh *et al.* (2018) developed a replication-competent oncolytic adenovirus expressing secretable TRAIL (Ad-stTRAIL). They investigated the efficacy of this virus on U-87MG glioblastoma tumours *in vivo* and showed that the cancer cell-killing effects were markedly higher

with the expression of secretable TRAIL. Unfortunately, the treatment was unable to completely eradicate the tumour, similar to the results of Kim *et al.* (2006a).

Oh *et al.* (2018) found that Ad-stTRAIL yielded a more extensive viral distribution within tumour tissue than just the replication-competent adenovirus alone. They suggested that this phenomenon could be mediated by neighbouring cell spread using apoptotic bodies or cell death causing voids that influence treatment spread. Oh *et al.* (2018) noted that the complex nature of the tumour microenvironment, such as the network of blood vessels, is also a critical limiting factor of the spread of virus within the tissue. In this section, a preliminary and introductory investigation is conducted into the possible causes of treatment failure. Additionally, the dependence of the treatment efficacy on the TRAIL-release mechanisms is explored.

10.2.1 *Model development*

While the Voronoi call-based model (VCBM) developed in Chapter 8 was helpful in determining the dependence of treatment outcome on tumour shape, to understand the effects of TRAIL secretion and intravenous injections, a smaller scale tissue off-lattice agent-based model (ABM) is needed. To create this ABM, the open source multicellular system simulator PhysiCell is used (Ghaffarizadeh *et al.*, 2018). In the model, viruses are modelled as a continuously diffusing population that interacts with glioblastoma cells. The model's evolution is driven by the biological assumptions detailed below for the vein cell characteristics, glioblastoma cell characteristics and virus model.

10.2.1.1 *Vein cell characteristics*

Tumour vasculature can play a major role in tumour growth and therapeutic efficacy (Section 2.2.2). In this work, static vein cells are established to simulate the influence of the vasculature on tumour tissue formation and treatment delivery. These vein cells put force on the surrounding proliferating tumour cells, but are unable to move or proliferate. Normally cells that create blood vessels and line the veins, such as endothelial cells, are highly proliferative in the tumour microenvironment (Section 2.2.2). How-

ever, it is assumed that these cells are static as the core function of the vein cells is to simulate the arrival of intravenously injected treatment.

To reduce the computational time of the simulations, a 2-dimensional framework was chosen for the simulations. Since this limits the possible geometry of the vascular system, two vein shapes were considered: triangular and circular, see Fig. 10.2. These shapes are chosen based on a roughly conical tumour vasculature. Initially, all cells were placed in a hexagonal pattern. Cells were then designated either vein cells or glioblastoma cells based on whether they were in the region chosen to be a vein or not.

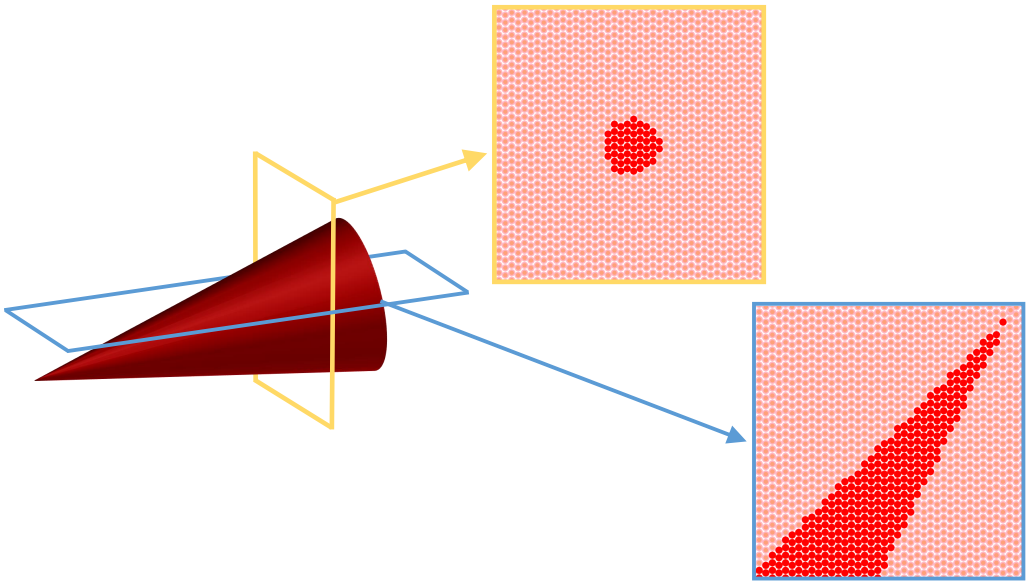

Figure 10.2: Illustration of the two vasculature cross sections considered for the simulations in this chapter.

10.2.1.2 *Glioblastoma characteristics*

Glioblastomas are incredibly heterogeneous tumours, made up of a range of different glial cells (Inda *et al.*, 2014). For the purpose of this work, glioblastoma heterogeneity is not considered to play a major role in TRAIL-mediated apoptosis or viral-induced lysis (Kim *et al.*, 2006a). As such, only a single homogeneous population of glioblastoma cells is considered. These cells proliferate rapidly to form a crowded disorganised tissue layer that reflects a typical section of a glioblastoma. To investigate the efficacy of the oncolytic adenovirus expressing secretable TRAIL on tumour growth at the cell level, only a small section of tumour tissue is modelled.

In Chapter 8, the quiescent cell population and the influence of nutrient diffusion was investigated in detail see Fig. 8.11-8.12. For now, only a section of tumour tissue is considered and the influence of nutrient presence on the growth of tumour cells is assumed to be uniform across the 2-D cross-section. Future extensions of this preliminary work could investigate this on a larger scale. Additionally, since the virus is not modified to express immunostimulatory cytokines, the effects of immune cells are not considered. The initial set up of the vein and glioblastoma cells can be seen in Fig. 10.3.

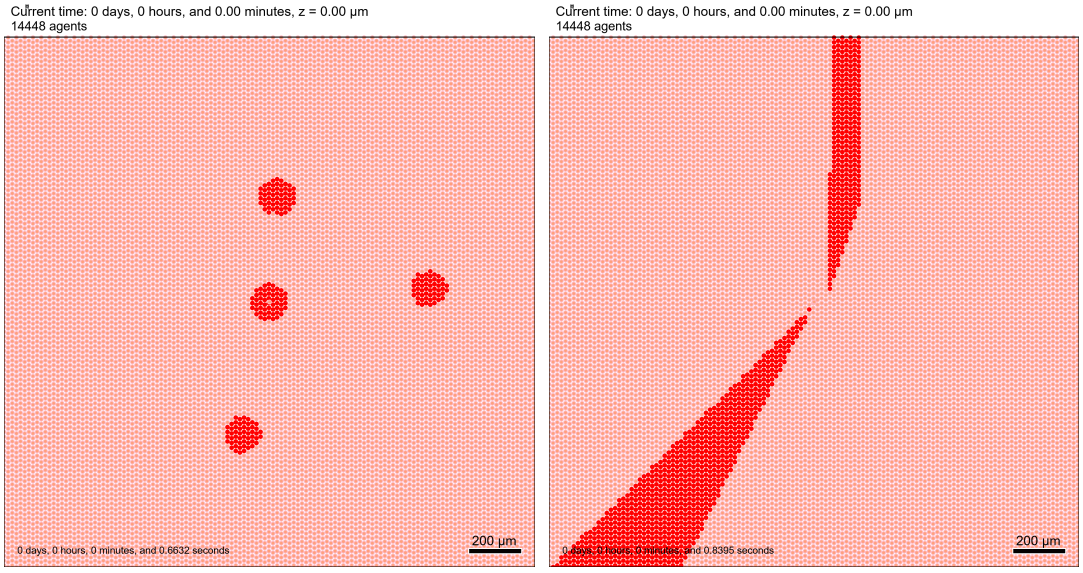

(a) **(b)**

Figure 10.3: Initial setup of vein and glioblastoma cells. Glioblastoma cells are coloured pink and vein cells are coloured brown. (a) is an example of the circular vein cross section and (b) the triangular vein cross section.

10.2.1.3 *Adenovirus expressing secretable TRAIL model*

Similar to the work in Chapters 5-8, Ad-TRAIL virus particles infect glioblastoma cells, replicate inside them, and then lyse the infected cells. To investigate whether the intracellular replication of the virus influences the TRAIL-based virotherapy, intracellular virus replication is explicitly modelled. Intracellular virus particles start replicating only after enough particles have infected the cell. This results in a delay in the start of virus replication similar to that considered in Chapter 4, see Fig. 4.3. This also allows for some stochasticity in the start time of replication amongst the infect cell popula-

tion. The likelihood of lysis occurring is a function of the number of intracellular virus particles, resulting in a similar dynamic to Fig. 4.3.

During replication of the TRAIL-expressing virus, the cell creates new TRAIL molecules, see Fig 2.3. These molecules are secreted into the microenvironment by the virus-infected cell and induce apoptosis in uninfected tumour cells. This occurs by TRAIL binding to the receptors on the cell surface and signalling the apoptosis cascade. TRAIL can induce apoptosis in infected cells, but for the number of cells modelled, this is not considered significant. Fig. 10.4 is a schematic for the TRAIL-expressing adenovirus infection life-cycle.

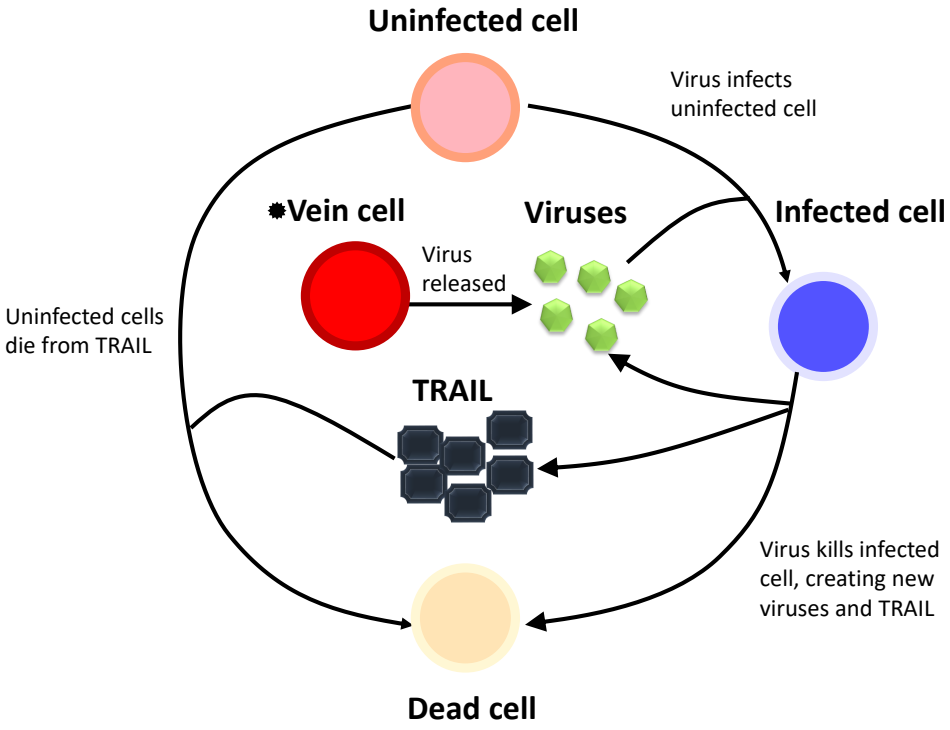

Figure 10.4: Life cycle of oncolytic adenovirus expressing secretable TRAIL. Virus particles infect uninfected cells. Once inside a cell, virus particles undergo replication for a period of time creating both new viruses and TRAIL molecules. Eventually the cell lyses, causing it to die and the viral progeny and TRAIL are released. TRAIL then kills uninfected tumour cells through apoptosis.

10.2.2 *Preliminary results: proposing reasons for TRAIL-secreting virotherapy failure*

After treatment with an oncolytic adenovirus expressing secretable TRAIL, both Kim *et al.* (2006a) and Oh *et al.* (2018) saw a regrowth in the tumour. In this section, initial investigations are conducted into the possible mechanisms inhibiting treatment efficacy at a tissue level. The influence of the TRAIL secretion start time and secretion rate on tumour tissue are simulated. Perturbations of different parameters is also used to further understand the failing regimes of this treatment. The results in this section illustrate the usefulness of the chosen modelling framework and motivate the need for future, more extensive, investigations. The model used in this section is detailed extensively in Appendix C and D. The PhysiCell setup for virus and TRAIL diffusion along with cell movement and proliferation is given in Appendix C. The models developed for virus replication, TRAIL creation and cell apoptosis from either viruses or TRAIL particles is all detailed in Appendix D.

10.2.2.1 *Influence of TRAIL release mechanism on treatment dissemination*

There are two variable characteristics in the model for TRAIL release (Eq. (D.7)): the length of time cells wait after replication has started before they begin secreting TRAIL s_τ, and the rate TRAIL is secreted from the cell s_T. These characteristics control whether TRAIL is primarily released during replication or when the cell lyses (which occurs δ minutes after infection), see Fig. 10.5. To investigate the influence of the TRAIL release mechanism, the number of tumour cells over 4 days is plotted in Fig. 10.6 for variations in s_T and s_τ. The remaining parameter values were taken from Table D.1, where the choice of each parameter has also been given in Appendix section D.1.0.4.

Since the virus arrives in the tumour tissue through the veins, the analysis was conducted for triangular Fig. 10.6(a) and circular Fig. 10.6(b) vein cross sections. A similar trend is observed in the case of circular vein cross sections, where a slower TRAIL secretion rate, improves the treatment most significantly. The geometry of the vein appears to play an important role in the diffusive spread of the virus, where it is clear that multiple small circular veins allow for treatment to spread more effectively than triangular veins. In Fig. 10.7 and 10.8 are simulations with the triangular veins

and in Fig. 10.9 and 10.10 are the corresponding simulations for the circular veins. In these figures the vein cells, uninfected and infected cells and dead cells are denoted in Fig. 10.7 and Fig. 10.9 and the density of TRAIL and the virus are given in Fig. 10.8 and Fig. 10.10.

In Fig. 10.6 there are clearly two very different dynamics depending on the secretion rate and release time of TRAIL. In the case of triangular vein cross sections, treatment performs best when $s_T = 0.0001$ and $s_\tau = 500$. This is most likely due to the virus spreading further throughout the tissue before the initial onset of TRAIL induced apoptosis. This can be seen by comparing the simulations for $s_T = 0.1$ and $s_\tau = 500$ in Fig. D.6 and D.7 $s_\tau = 500$ in Fig. 10.7 and 10.8, to the simulations for $s_T = 0.0001$ and . Decreasing the secretion rate, appears to allow for more cells to become infected over time.

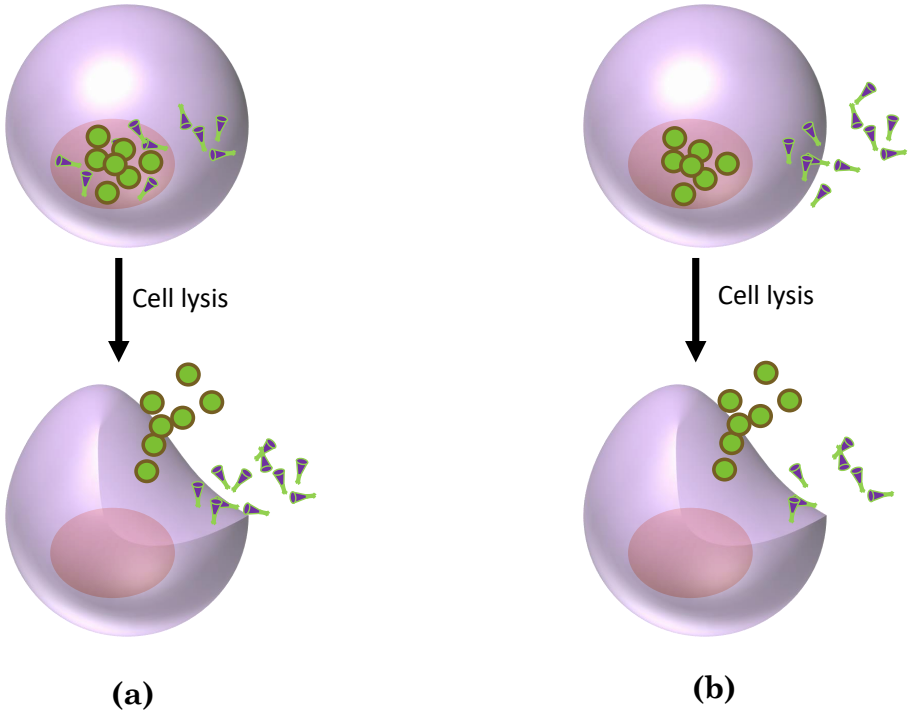

Figure 10.5: Examples of the different TRAIL secretion dynamics that occur with perturbations in s_τ and s_T. (a) TRAIL molecules created through replicated are secreted primarily at time of cell lysis $s_T \approx 0, s_\tau \approx \delta$. (b) TRAIL molecules are secreted whilst the virus is infected $s_T > 0, s_\tau << \delta$.

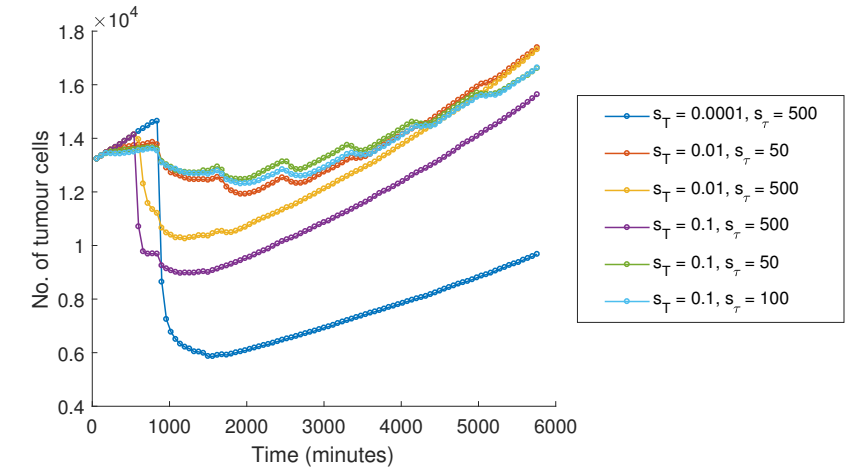

(a)

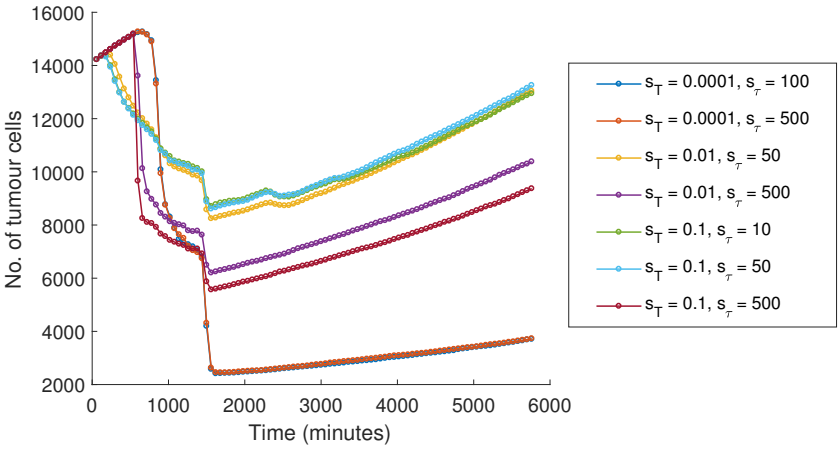

(b)

Figure 10.6: Number of tumour cells over 4 days for perturbations in s_T and s_τ for (a) triangular and (b) circular vein cross sections. Since this is just an initial investigation, a range of different values for s_T and s_τ were chosen that exhibited different dynamics. The remaining parameter values were taken from Tables D.1 and D.2.

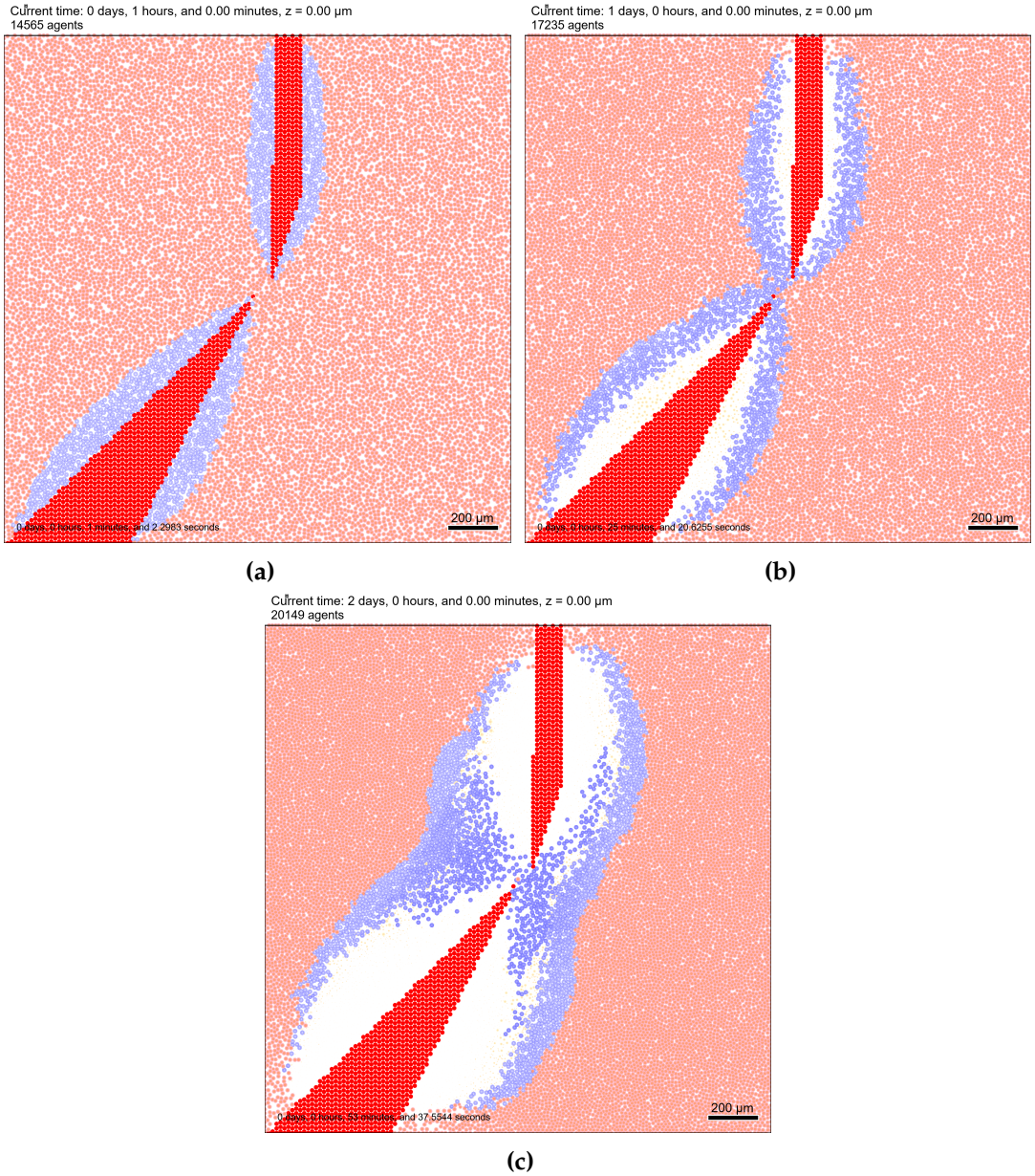

Figure 10.7: Simulation for virus infection in a layer of tissue with triangle veins at (a) 60 mins, (b) 1440 mins (1 day) and (c) 2880 mins (2 days). Parameters were fixed to the values in Table D.1 and D.2 with $s_T = 0.0001$ and $s_\tau = 500$. Red cells represent vein cells, these cells secrete virus that infects tissue cells, which are pink cells. Once a cell becomes infected it is coloured purple, with the darker the shade corresponding to the more virus in the cell. The infected cells die turning a pale yellow and eventually disappearing. The remaining parameter values were taken from Tables D.1 and D.2.

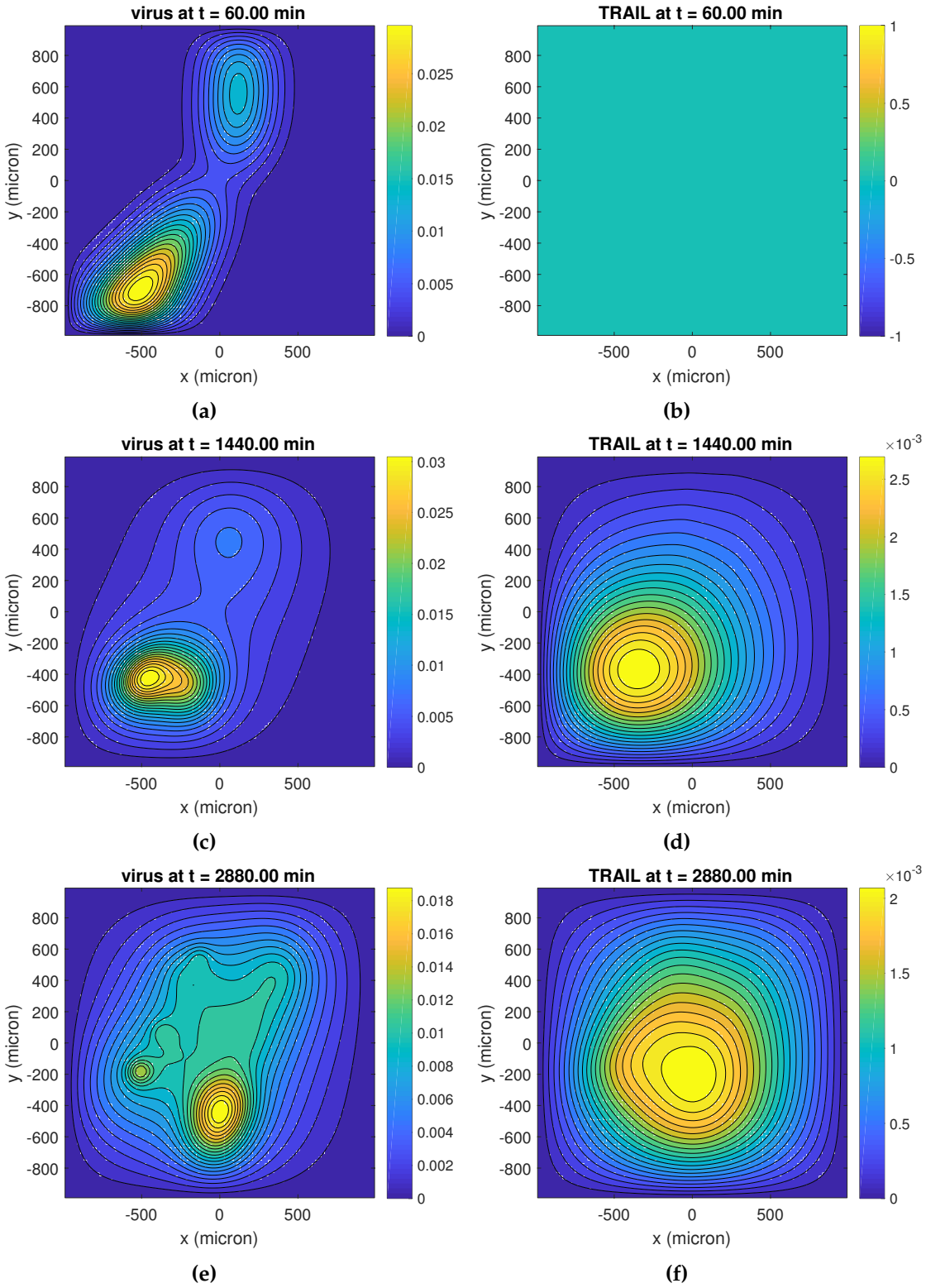

Figure 10.8: Contour plots for the density of virus ((a), (c) and (e)) and TRAIL ((b), (d) and (f)) at 60 mins, 1440 mins (1 day) and 2880 mins (2 days). These plots correspond to the simulations in Fig. 10.7.

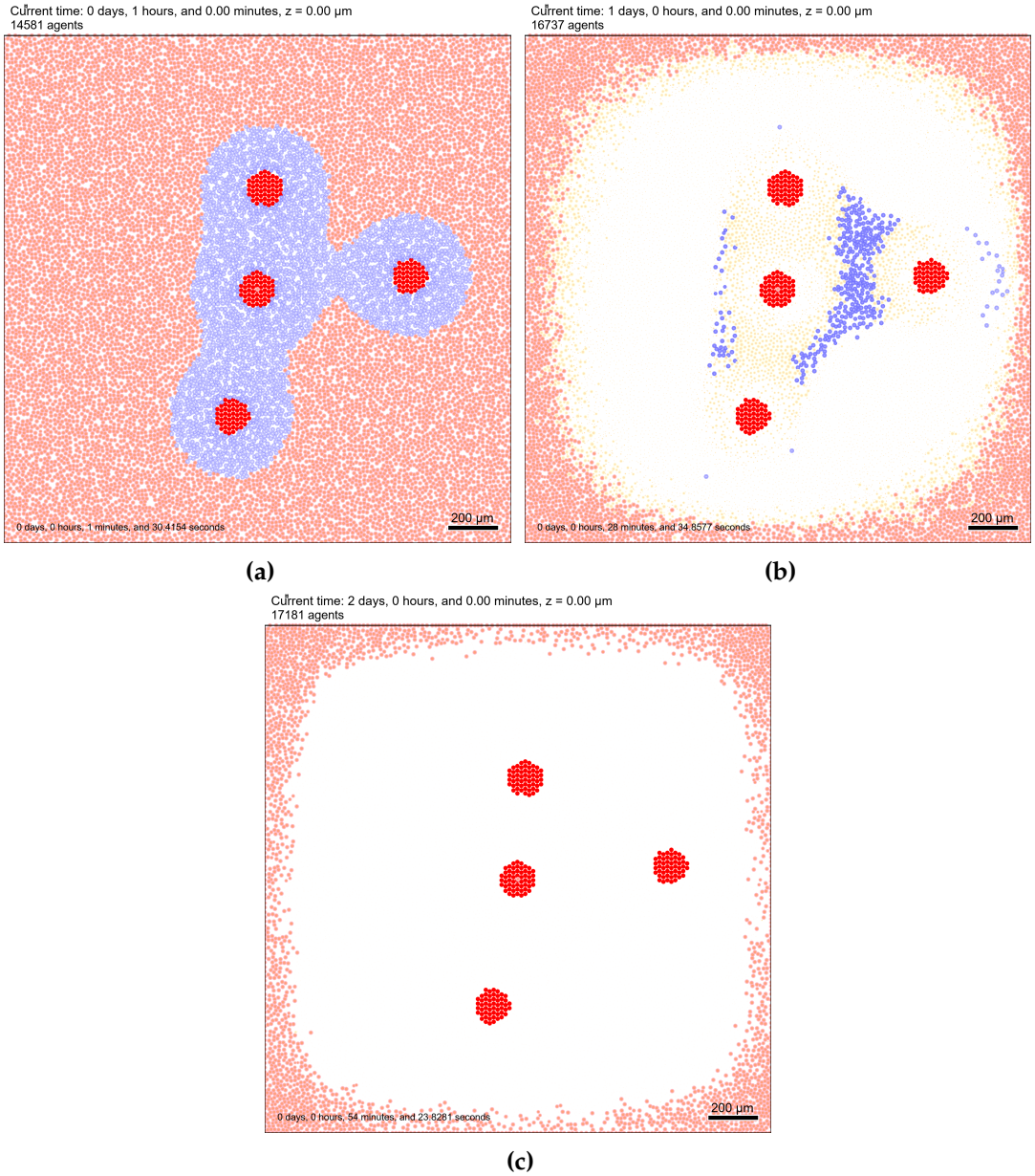

Figure 10.9: Simulation for virus infection in a layer of tissue with circular veins at (a) 60 mins, (b) 1440 mins (1 day) and (c) 2880 mins (2 days). Parameters were fixed to the values in Table D.1 and D.2 with $s_T = 0.0001$ and $s_\tau = 500$. Red cells represent vein cells, these cells secrete virus that infects tissue cells, which are pink cells. Once a cell becomes infected it is coloured purple, with the darker the shade corresponding to the more virus in the cell. The infected cells die turning a pale yellow and eventually disappearing. The remaining parameter values were taken from Tables D.1 and D.2.

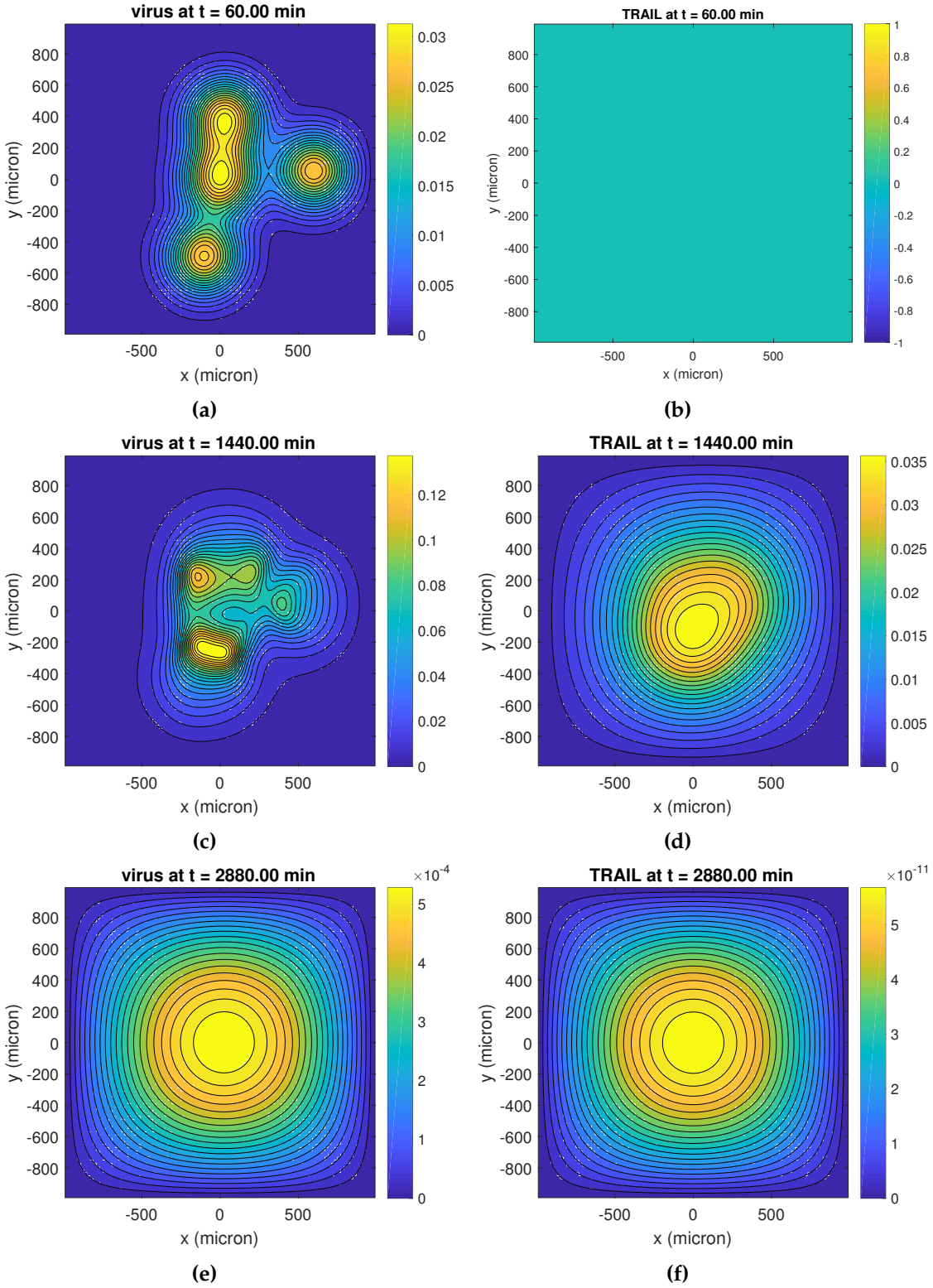

Figure 10.10: Contour plots for the density of virus ((a), (c) and (e)) and TRAIL ((b), (d) and (f)) at 60 mins, 1440 mins (1 day) and 2880 mins (2 days). These plots correspond to the simulations in Fig. 10.9.

10.2.2.2 *Initial parameter sensitivity analysis*

To start to investigate how the treatment's efficacy may depend on other mechanisms, the number of tumour cells has been plotted for different values of the virus diffusion coefficient D_V, the cell uptake rate of virus c_I and the replication rate of TRAIL in the cell c_R, see Fig. 10.11. Specific increases or decreases of these parameters were chosen based on their qualitative impact they had in the model behaviour. Only one parameter was perturbed at a time and the remaining parameters were fixed to the values in Tables D.1 and D.2. The values of s_T and s_τ were fixed to $s_T = 0.1$ and $s_\tau = 500$. They were chosen such that the original simulation predicted tumour cell population increase.

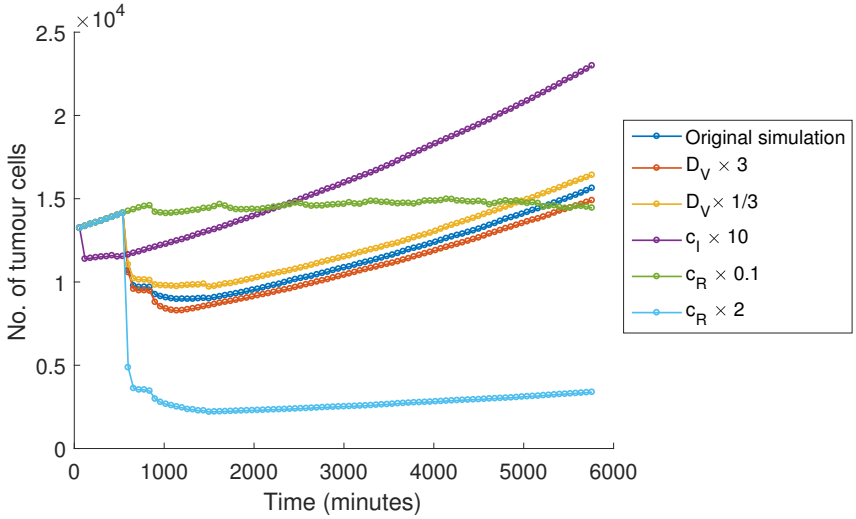

Figure 10.11: Tumour cell number in triangular vein cross section model with parameter perturbations in D_V, c_I and c_R (detailed by the legend). The remaining parameters were fixed to the values presented in Table D.1 and D.2 with $s_T = 0.1$ and $s_\tau = 500$.

10.2.3 *Summary and discussion of initial investigation*

TRAIL-based virotherapies hold significant promise as an effective treatment for glioblastoma. Currently, the treatment is unable to completely eradicate the tumour. Combining intracellular and extracellular modelling from previous chapters, a PhysiCell based model was developed as a platform to investigate the reasons for treatment

failure. Perturbations in the TRAIL release mechanism were shown to influence the dissemination and tumour suppression. An initial parameter sensitivity analysis also predicted parameter regions where success was unobtainable.

The influence of the TRAIL release mechanism can clearly be seen in Fig. 10.6 where the tumour cell population number was plotted as a function of the rate at which cells secrete TRAIL, s_T, and the delay from the start of TRAIL creation to TRAIL release s_τ. It is clear that treatment efficacy depends on the secretion rate of TRAIL. Decreasing the secretion rate significantly decreases the tumour cell population for triangular and circular vein cross sections. This implies that a slower release of TRAIL allows for further treatment spread and tumour cell killing than one large burst at the time of cell lysis. Biologically, this is most likely due to the competition of TRAIL and virus particles for the same uninfected cell population.

Initially, the difference between fast and slow TRAIL release rates is not significant in the spatial time-evolution of the model (Fig. 10.7 and D.6 respectively). It is only at 2 days, that these simulations show qualitatively different dynamics. The infiltration of the virus infection into the tumour tissue is clearly more extensive in the case of the slower TRAIL secretion D.6(c). This suggests that rapid release of TRAIL from infected cells decreases the neighbouring tumour cell population and results in reduced subsequent viral infections.

The 'cross-talk' between cells and the microenvironment can play a significant role in the delivery of viral treatment to the tissue. Oh *et al.* (2018) noted that the blood vessels can function as a limiting factor towards the TRAIL-based virotherapy. As such, the PhysiCell model was simulation for different shaped veins (triangular and circular), see Fig. 10.2.

The tumour cell population responds very differently to treatment arriving through triangular vein cross sections compared to circular vein cross sections, see Fig. 10.6. The triangular shaped veins resulted in a weaker initial outward propagation of the infection region compared to circular veins (Fig. D.6(b) versus D.8(b)). However, as the area of the infected region is smaller, this results in a prolonged effectiveness of the treatment (Fig. D.6(c) versus D.8(c)). This behaviour is most likely an artefact of the assumption that each vein cell starts with an equivalent initial amount of virus that it

then secretes. Biologically, this is reasonable as veins within the tumour are extremely permeable and wider sections of veins would have an increased likelihood of virus particle extravasation (Section 2.2.2). The fact that the shape of the vein seems to have a significant impact on the outcome of the simulations (Fig. 10.6 suggests that further investigation on vein shape is needed.

To begin to explore whether there are other mechanisms that improve TRAIL-based virotherapy treatment, the tumour cell population was simulated for different parameters values, see Fig. 10.11. The TRAIL release mechanism parameters s_T and s_τ were fixed to values that resulted in tumour cell population growth for triangular vein cross sections. Simulations of perturbations in parameter values for the triangular vein cross sections, then showed that it is difficult to improve the treatment efficacy. One interesting result from the simulation in Fig. 10.11, was that reducing the replication rate of TRAIL, was able to stabilise tumour growth.

Increasing the diffusion coefficient for the virus, D_V, had no significant influence on the effectiveness of the therapy. This is likely due to the fact that the secretion rate of TRAIL s_T was high, so TRAIL was still able to infect and kill the neighbouring rim of cells, which was enough to inhibit treatment propagation. Increasing the cells uptake rate of the virus, c_I, initially decreased the tumour cell population by creating more infected cells. However, this in turn increased the number of cells secreting TRAIL and resulted in the tumour cell population increasing significantly.

Interesting behaviour in the tumour cell population was observed with perturbations in the rate TRAIL molecules are created in the cell, c_R, (Fig. 10.11). Decreasing c_R results in a stabilising of the tumour cell number. This suggests that if less TRAIL is created, then the TRAIL molecules and virus particles are able to stabilise the tumour growth. Whereas, increasing the rate of TRAIL generation, is able to significantly reduce the tumour cell number. So if more TRAIL molecules are created, the treatment can be just as effective as if the TRAIL molecules are secreted slower (Fig. 10.6). Overall, Fig. 10.11 suggests that a more extensive parameter sensitivity analysis of the model needs to be conduced so as to truly understand the dynamics.

As this is a preliminary study, there are limitations to the modelling platform and the reliability of the results discussed. The next step of this investigation will be to use

data from the experiments of Kim *et al.* (2006a); Jeong *et al.* (2009) and Oh *et al.* (2018) to inform the parameters in the model that were estimated, see Table D.1 and D.2. To investigate the initial results in Fig. 10.6 and 10.11, the model will be simulated with a set of parameters from a Latin hypercube sampling of the parameter space. This will help to determine whether the treatment outcome depends on the secretion rate of TRAIL, or whether the dynamics in Fig. 10.6 were a result of stochastic fluctuations in the model. Additionally, the defining features of glioblastoma tumours, such as heterogeneous spatial growth and large regions of hypoxia, have not been included in the model and need to be considered.

Preliminary investigations into an oncolytic virus engineered to stimulate the production of TRAIL has further demonstrated the utility of the mathematical frameworks developed in this thesis. While still at an elementary stage, the work in this section is a good representation of the future of mathematical modelling in oncolytic virotherapy.

A

ADDITIONAL INFORMATION FOR CHAPTER 4

The expectation for the total number of viral particles produced from a population of cells over time (Eq. (4.1)) is derived using results from probability theory. The theory behind the derivation is reviewed below, followed by a derivation of the model using the Law of Total Probability and a derivation of the model using the Jacobian matrix transformation.

A.1 PROBABILITY THEORY BACKGROUND

The time at which an individual virus particle starts replicating and the length of time it replicates are random variables. The expected value of a random variable is the long-run average value of repetitions of the experiment it represents. An event is a set of outcomes of an experiment (a subset of the sample space) to which a probability is assigned. Two events are dependent if the outcome or occurrence of the first affects the outcome or occurrence of the second so that the probability is changed. The events of viral start time, τ, and length of time replicating, l, are therefore independent, but the viral start time and end time, $delta$, are dependent. In other words, τ and l are independent events and τ and δ are dependent events, since $\delta = \tau + l$.

When considering the probability of multiple events occurring, a joint probability density function can be useful. The joint probability density function (joint pdf) is a function used to characterize the probability distribution of a continuous random vector. It is a multivariate generalization of the probability density function (pdf) (which characterizes the distribution of a continuous random variable). Given random variables X, Y, that are defined on a probability space, the joint probability distribution for X, Y, is a probability distribution that gives the probability that each of X, Y, falls in any particular range or discrete set of values specified for that variable (DeGroot and Schervish, 2012; Park and Park, 2018), i.e.:

$$f_{X,Y}(x, y) = P(X \leqslant x, Y \leqslant y)$$

The joint probability distribution can be expressed either in terms of a joint cumulative distribution function or in terms of a joint probability density function (in the

case of continuous variables). The joint probability density function $f_{X,Y}(x, y)$ for two continuous random variables is equal to:

$$f_{X,Y}(x, y) = f_{Y|X}(y, x)f_X(x) = f_{X|Y}(x|y)f_Y(y)$$

where $f_{Y|X}(y, x)$ and $f_{X|Y}(x|y)$ are the conditional distributions of Y given $X = x$, and of X given $Y = y$ respectively, and $f_X(x)$ and $f_Y(y)$ are the marginal distributions for X and Y respectively (DeGroot and Schervish, 2012; Park and Park, 2018).

The derivation of the model in Eq. (4.1) is presented in two ways (Section A.2.1 and A.2.2). The first uses the law of total probability and the second uses the Jacobian matrix transformation. The law of total probability states that the probability of X, Y being in the region B, i.e. $P((X, Y) \in B)$ can be written as:

$$\begin{aligned} P((X, Y) \in B) &= \iint_B f_{X,Y}(x, y)dxdy, \\ &= \int P((X, Y) \in B|Y = y)f_Y(y)dy, \end{aligned}$$

where $f_{X,Y}(x, y)$ is the joint density function for X, Y (DeGroot and Schervish, 2012; Zwillinger and Kokoska, 2000). The logic behind the law of total probability is that if $Y = y$ is fixed, then the probability of X, Y being in the region is calculated for all possibly X, Y values by multiplying by the marginal probability distribution $f_Y(y)$ and integrating over all possible values of Y. A schematic illustrating the concept of the joint density function and how it is obtained by integrating over this function, is given in Fig. A.1. Therefore, the probability of $(X, Y) \in B$ is equivalent to calculating the area under the surface $f_{X,Y}(x, y)$ on the set B, i.e.:

$$\iint_B f_{X,Y}(x, y)dxdy$$

The second theory used to derive the model is the Jacobian matrix transformation. That is, if the random vector (X, Y) has PDF $f_{X,Y}(x, y)$ then $g(X, Y)$ has PDF:

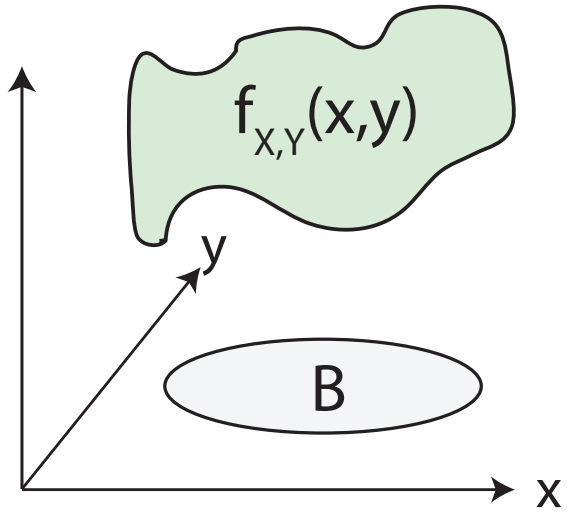

Figure A.1: Illustration for the law of total probability, where $f_{X,Y}(x,y)$ is the joint density function of X, Y and B is the region for which the probability of X, Y in B is being calculated.

$$f_{X,Y}(X,Y)(g^{-1}(x,y))|J_{g^{-1}}(x,y)|$$

where J is the Jacobian matrix (DeGroot and Schervish, 2012).

A.2 THE SETUP AND DERIVATION FOR EQ. (4.1)

Consider an initial number of cells C_0, each containing a single virus particle. Virus particles start replicating at time τ which is a random variable drawn from the distribution $f_\tau(x)$. Virus particles stop replicating after they have replicated for a length of time l (i.e. at time $\tau + l$) which is another random variable drawn from the distribution $f_l(x)$ (whose parameters are not necessarily the same as those of $f_\tau(x)$. Calculating the expected proportion of cells $C(t)$ that have virus particles replicating within them at time t is equivalent to finding the probability of the event t occurring after time τ and before time $\tau + l$, i.e. the region:

$$A = \{t > \tau\} \cap \{t < \tau + l\}.$$

Integrating the joint density function $f_{\tau,\tau+l}(x,y)$ of the random variables τ and l, over the region A can determine the probability for a particle being at t of $t > \tau$ and $t < \tau + l$, i.e. that a virus is replicating. There are two ways to derive this probability, both of which are outlined below. The first method uses the law of total probability and the second uses a Jacobian transformation.

A.2.1 *Law of total probability model derivation*

The expression for the joint density function $f_{\tau,\tau+l}$ can be derived using the law of total probability. The probability that $t > \tau$ and $t < \tau + l$ is equivalent to writing:

$$P(\{\tau < t\} \cap \{t < \tau + l\}) = \int_0^\infty P(\{\tau < t\} \cap \{t < \tau + l\} | \tau = x) f_\tau(x) dx$$

where f_τ is the PDF of τ. Now since $\tau = x$, if $x > t$ then the probability is zero. This simplifies the above to

$$P(\{\tau < t\} \cap \{t < \tau + l\}) = \int_0^t P(\{t < \tau + l\} | \tau = x) f_\tau(x) dx$$

which can be simplified further to

$$P(\{\tau < t\} \cap \{t < \tau + l\}) = \int_0^t P(\{t < x + l\} | \tau = x) f_\tau(x) dx = \int_0^t P(l > t - x) f_\tau(x) dx$$

which is equal to

$$P(\{\tau < t\} \cap \{t < \tau + l\}) = \int_0^t \int_{t-s}^\infty f_l(z) f_\tau(x) dz dx \tag{A.1}$$

where f_l is the PDF of l. With the change of variables $y = z + x$, Eq. (A.1) can be rewritten for the proportion of cells with virus particles undergoing replication inside them at any time t as:

$$C(t) = \int_0^t \int_t^\infty f_\tau(x) f_l(y-x) dy dx. \tag{A.2}$$

From this, the change in the total virus (both intracellular and extracellular), v, at any point in time, t, is the cumulative number of cells actively producing virus multiplied by the rate at which the virus replicates:

$$\frac{dv}{dt} = kC = kC_0 \int_0^t \int_t^\infty f_\tau(x) f_l(y-x) dy dx \tag{A.3}$$

where k is the mean viral replication rate, across the cell population of C_0 cells. Here it is assumed that each cell is not actively producing virus until time τ, chosen from the distribution f_τ, and that they then produce for a period, l, chosen from the distribution f_l. At time t, the number of cells with virus replicating within the nucleus is equal to the proportion of cells that have reached time τ minus the proportion that have reached time $\tau + l$.

A.2.2 *Jacobian matrix transformation model derivation*

Alternatively, to obtain the joint density function $f_{\tau,\tau+l}$, a Jacobian matrix transformation can be used. Let the linear transformation $u : \mathbb{R}^2 \to \mathbb{R}^2$ be defined by:

$$u(x, y) = (x, x + y).$$

Now the density function $f_{\tau,\tau+l}(x, y)$, is the density of $u(\tau, l)$. Then using the Jacobian matrix transformation, if the random vector (X, Y) has PDF $f_{X,Y}(x, y)$ then $g(X, Y)$ has PDF:

$$f_{X,Y}(g^{-1}(x, y))|J_{g^{-1}}(x, y)|$$

where $J_{g^{-1}}$ is the Jacobian matrix for g^{-1}. Calculating g^{-1} and $|J_{g^{-1}}|$, also using the fact that τ and l are independent (i.e. $f_{\tau,l}(x,y) = f_\tau(x)f_l(y)$, where $f_{\tau,l}(x,y)$ is the joint density function of (τ, l)) and substitute $g^{-1}(x,y)$ to obtain

$$f_{\tau,\tau+l}(x,y) = f_\tau(x)f_l(y-x)$$

Therefore, the probability of a cell having a virus replicating inside of it, is the same as the proportion of cells that have replicating virus within them at any point t in time is given by:

$$C(t) = \int_0^t \int_t^\infty f_{\tau,\tau+l}(x,y)\,dy\,dx \tag{A.4}$$

where $f_{\tau,\tau+l}(x,y)$ is the joint density function for τ and $\tau + l$ and substituting (10) into (7) the proportion of cells with virus particles undergoing replication inside them at any time t:

$$C(t) = \int_0^t \int_t^\infty f_\tau(x)f_l(y-x)\,dy\,dx$$

which is equivalent to the equation derived above, Eq. (A.2).

B

ADDITIONAL INFORMATION FOR CHAPTER 8

Typical evolutions of the model for three tumour shapes: circular, rectangular and irregular are presented in Fig. B.1, B.2 and B.3 respectively. Additionally, typical evolutions of the model for circular tumours under treatment with a non-delayed and delayed virus is plotted in Fig. B.4 and B.5.

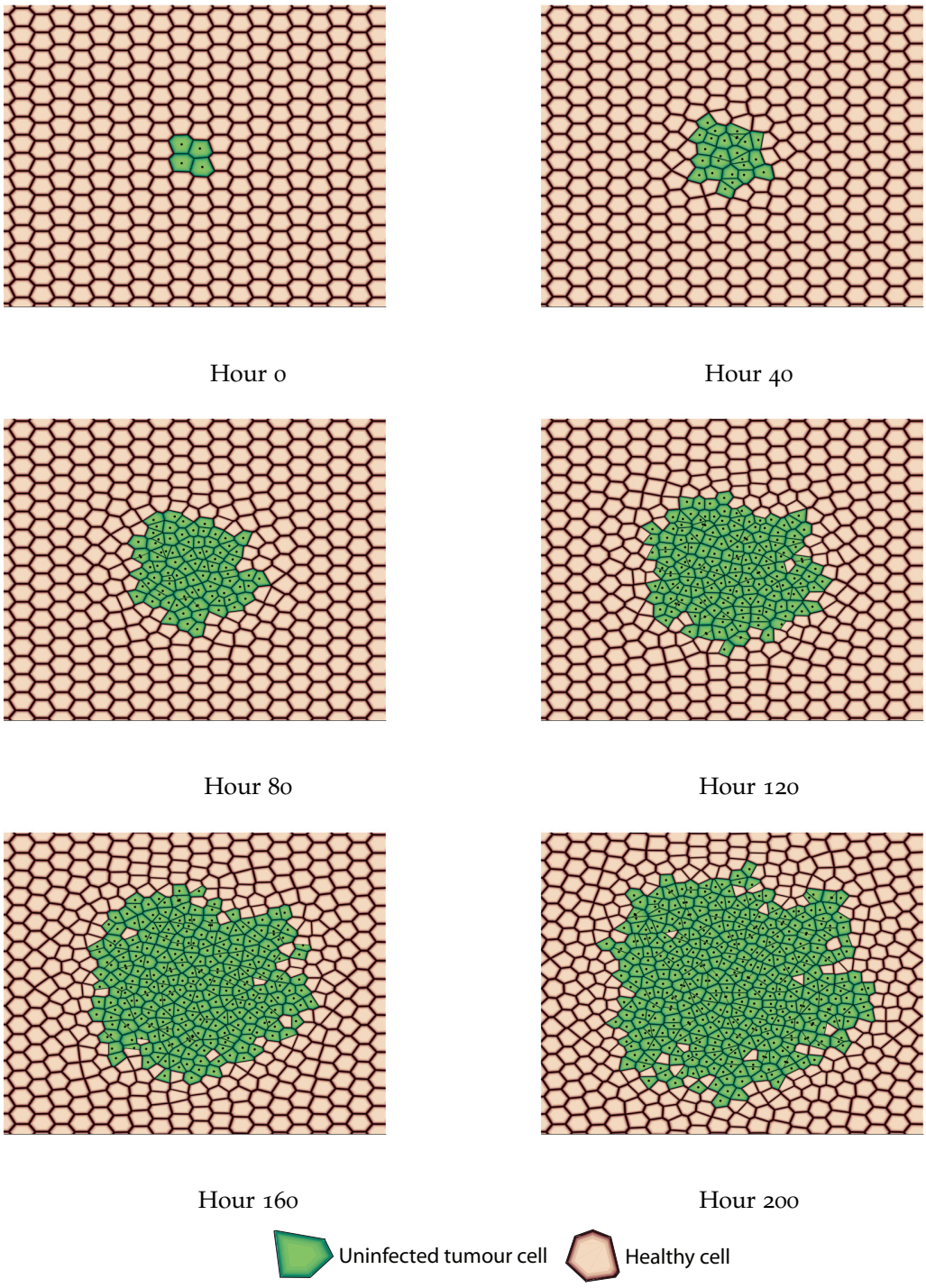

Figure B.1: Typical evolution of the cellular automaton for a circular tumour.

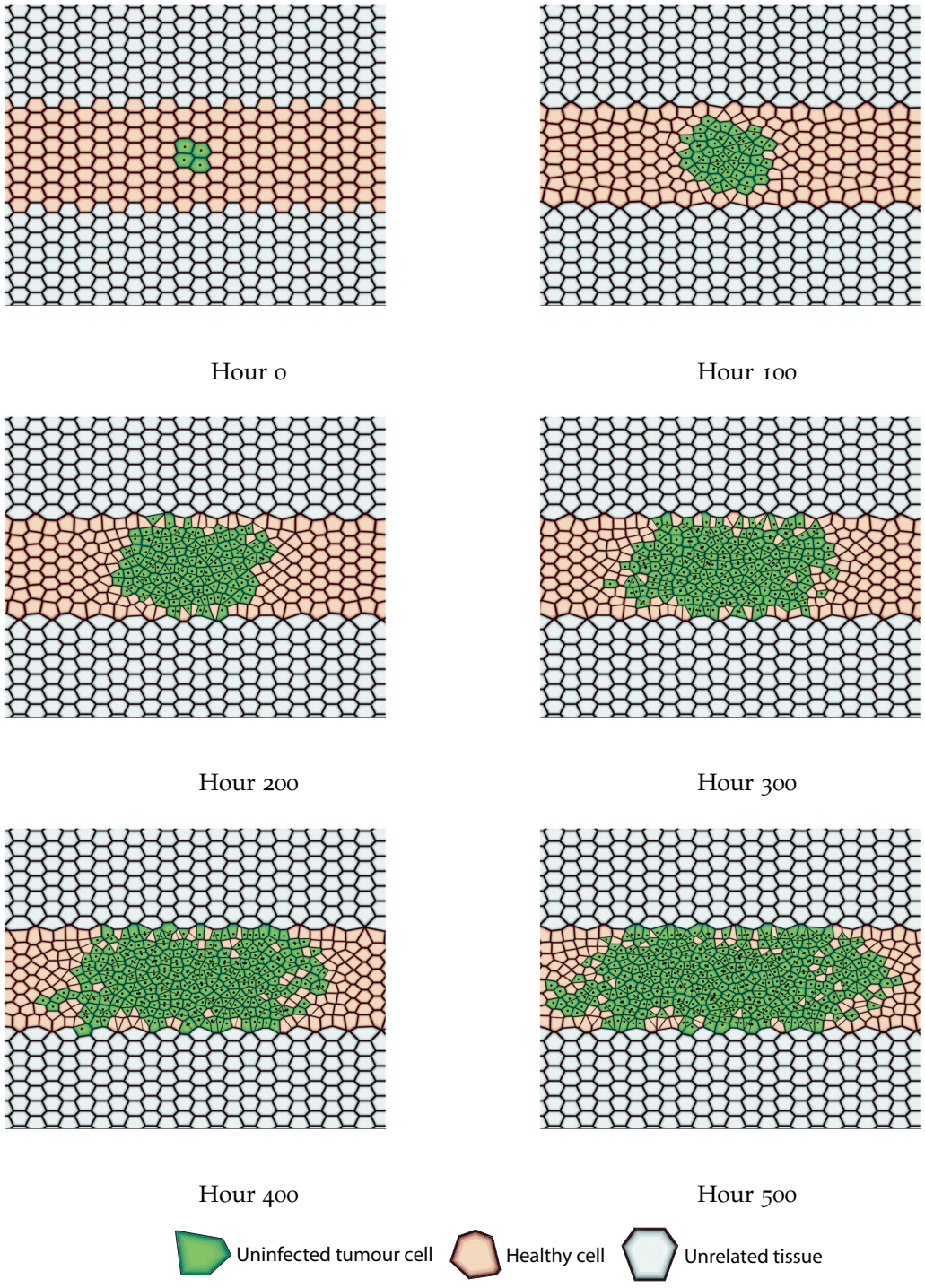

Figure B.2: Typical evolution of the cellular automaton for a rectangular tumour.

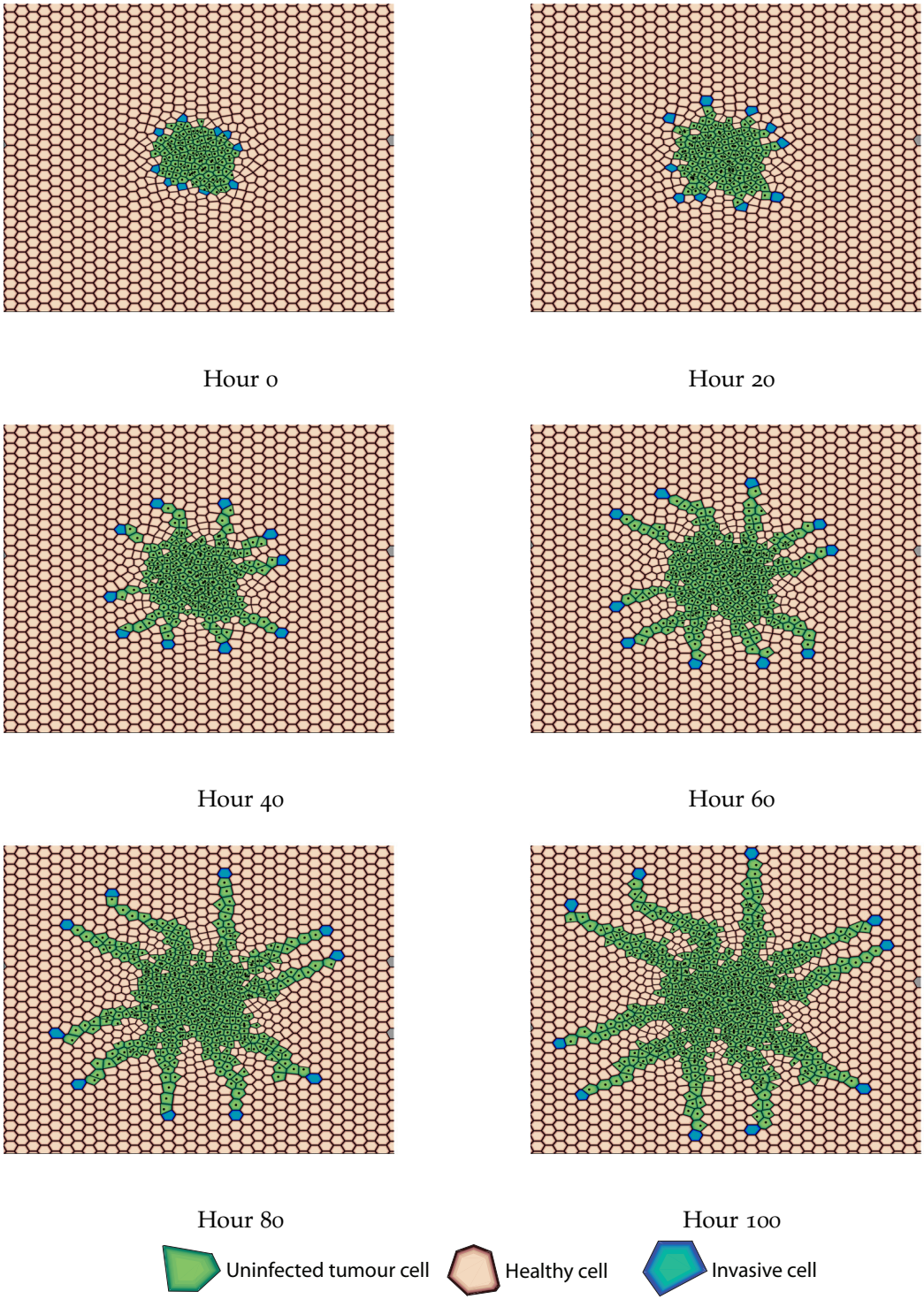

Figure B.3: Typical evolution of the cellular automaton for an irregular tumour.

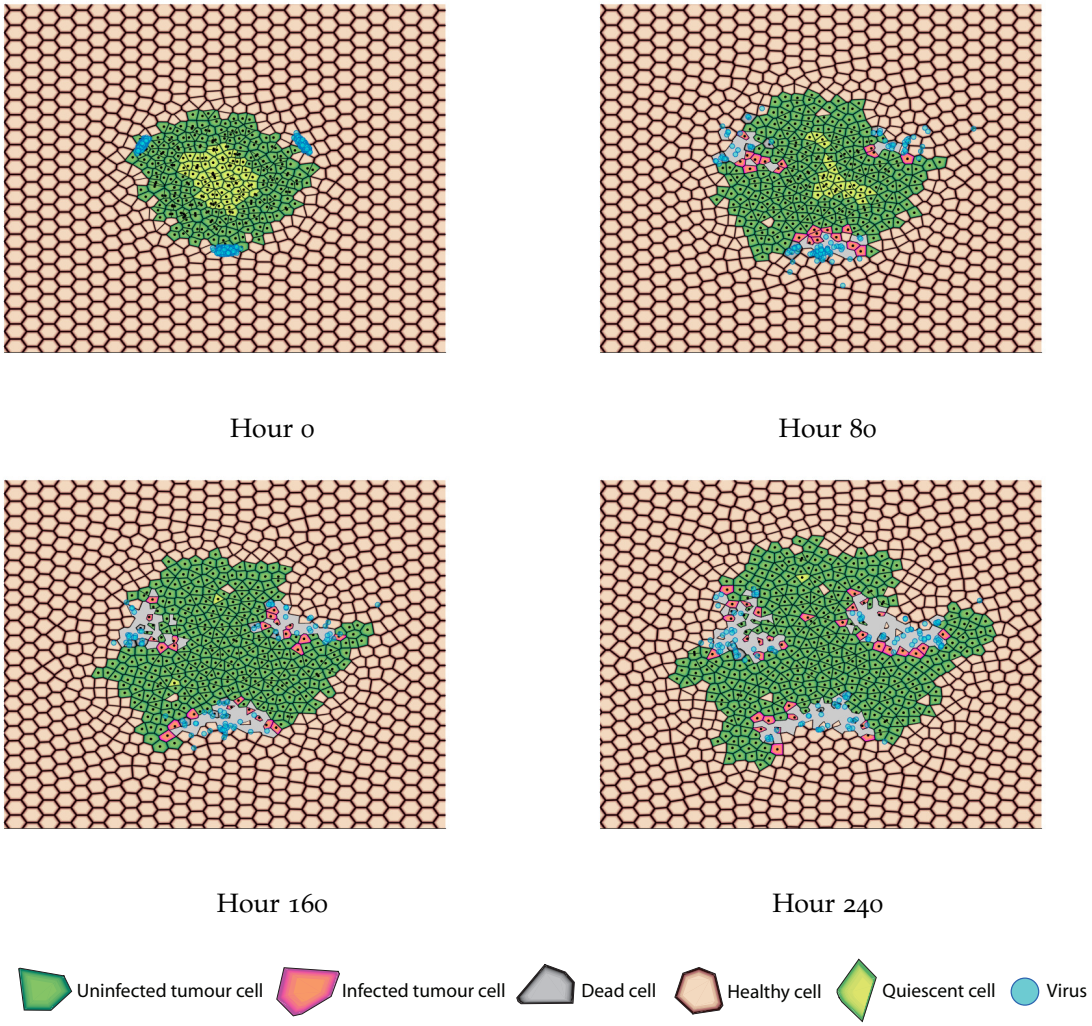

Figure B.4: Typical evolution of the cellular automaton for a circular tumour with a non-delayed viral treatment.

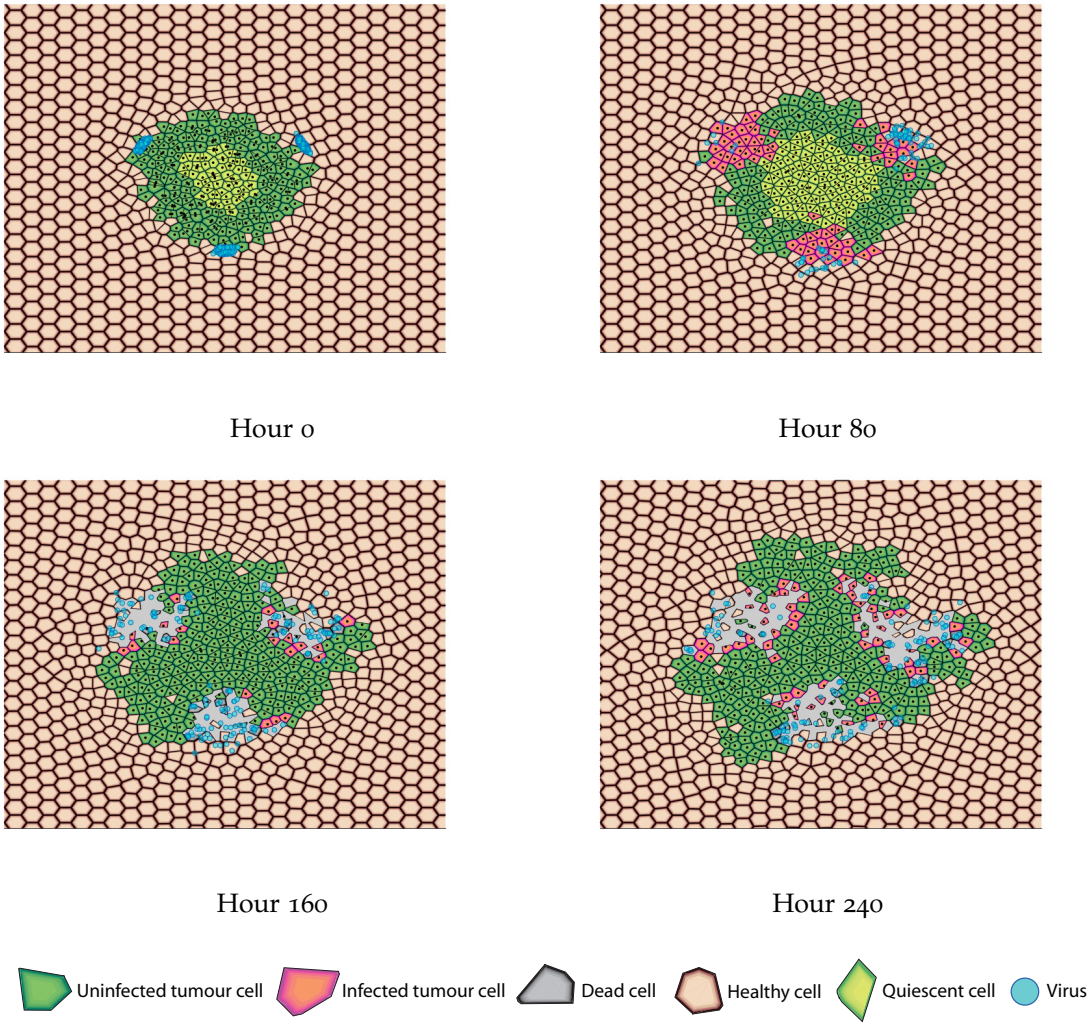

Figure B.5: Typical evolution of the cellular automaton for a circular tumour with a delayed viral treatment.

C

PHYSICELL SETUP FOR WORK DISCUSSED IN CHAPTER 10

C.1 PHYSICELL SETUP

To investigate the efficacy of the TRAIL-expressing adenovirus, a model for the interactions described above are developed in the open-source physics-based multicellular simulator known as PhysiCell (Ghaffarizadeh *et al.*, 2018). PhysiCell provides a robust, scalable C++ code for simulating large systems of cells on standard desktop computers. It allows for biologically realistic modelling of cell cycling, apoptosis, necrosis and cell-volume changes. It includes a standard library of sub-models for cell-fluid and solid-volume changes, cycle progression, apoptosis, necrosis, mechanics and motility. It also allows for specific models describing these characteristics to be user defined. Each cell can dynamically update its phenotype based on its microenvirornmental conditions.

PhysiCell is directly coupled to a biotransport solver known as BioFVM (Ghaffarizadeh *et al.*, 2015). BioFVM simulates many diffusing substrates and cell-secreted signals in the microenvironment. Each cell is able to dynamically update its phenotype based on its microenvironment conditions. Each cell is modelled as a software agent with an independent state, and its own rules to change its behaviour based on local environmental conditions and communication. PhysiCell is an off-lattice modelling platform, meaning that cells can have variable sizes and can move freely without grid artifacts. Below is a brief overview of PhysiCell's inbuilt substrate model (BioFVM), cell mechanics and motion setup, cell proliferation and time scale. For a more extensive and in-depth explanation see (Ghaffarizadeh *et al.*, 2018).

C.1.1 *Substrate modelling*

The in-built biotransport solver in PhysiCell is known as BioFVM (Ghaffarizadeh *et al.*, 2015). It can efficiently simulate secretion, diffusion, uptake and decay of multiple substrates in a large 3-D microenvironemnt. BioFVM solves the PDE

$$\frac{\partial \mathbf{p}}{\partial t} = \mathbf{D}\nabla^2\mathbf{p} - \boldsymbol{\lambda}\mathbf{p} + \mathbf{S}(\mathbf{p}^* - \mathbf{p}) - \mathbf{U}\mathbf{p} + \sum_{\text{cells } k} \delta(\mathbf{r} - \mathbf{r}_k) W_k \left[\mathbf{S}_k(\mathbf{p}^* - \mathbf{p}) - \mathbf{U}_k\mathbf{p}\right] \text{ in } \Omega \tag{C.1}$$

with no-flux conditions on $\partial\Omega$. Here Ω is the computational domain with boundary $\partial\Omega$, $\mathbf{p}$ is the vector of substrate densities, $\mathbf{p}^*$ are the substrate saturation densities, $\mathbf{D}$ are the diffusion coefficients, $\boldsymbol{\lambda}$ are the decay rates, $\mathbf{S}$ is the bulk supply rates and $\mathbf{U}$ is the bulk uptake rates. Here $\delta(x)$ is the Dirac delta function, $\mathbf{r}_k$ is the k^{th} cell's position, W_k is its volume, $\mathbf{S}_k$ is its vector of source rates and $\mathbf{U}_k$ it its vector of uptake rates. All vector-vector products are element-wise. Note that the term $p_V^* - p_{VE}$ assumes that intracellular substrates (or molecules) are secreted at a rate proportion to the density difference of the substrate on the exterior of the cell and the saturation density. For more information see (Ghaffarizadeh *et al.*, 2015, 2018).

The PDE in Eq. (C.1) is used to model the diffusion of extracellular virus particles and TRAIL molecules. In other words $\mathbf{p} = [p_V, p_T]$ where p_V is the density of the virus and p_T is the density of TRAIL molecules. In this way, individual viral particles are not explicitly modelled as in the VCBM, saving computational time. Additionally, the saturation densities are specific for viruses and TRAIL molecules, $\mathbf{p}^* = [p_V^*, p_T^*]$. The diffusion coefficient was also substrate dependent, i.e $\mathbf{D} = [D_V, D_T]$.

To model the virus and TRAIL molecules in the microenvironment, the bulk source and uptake rates $\mathbf{S}$ and $\mathbf{U}$ are set to zero, and only the supply and uptake rates of cells S_k and U_k is considered. Supply and uptake rates of cells are specific for viruses and TRAIL molecules, i.e. $\mathbf{S}_k = [S_{kV}, S_{kT}]$ where S_{kV} is the virus secretion rate from a cell, and S_{kT} is the TRAIL secretion rate from a cell, and $\mathbf{U}_k = [U_{kV}, U_{kT}]$. These rates also depend on the cells in the microenvironment, with different functions of S_{kV}, S_{kT}, U_{kV} and U_{kT} for vein cells and glioblastoma cells. Functions for the supply, $\mathbf{S}_k$, and uptake, $\mathbf{U}_k$, of the virus and TRAIL into the microenvironment are developed in the following Section D.1.

C.1.2 *Cell mechanics and motion*

Cell mechanics and motion are modelled using the PhysiCell built-in rules detailed below (Ghaffarizadeh *et al.*, 2018). Cell agents are assumed to bind to one another within a prescribed interaction distance (some multiple of their radius), and they can exert a pushing force on neighbours. Similar to the equations of motion for the VCBM

(Eqs. (8.2)-(8.6)), PhysiCell uses potential functions to implement simple mechanics and motion. Each cell's position $\mathbf{r}_i$ is updated by calculating its current velocity $\boldsymbol{\nu}_i$ based upon the balance of forces acting upon it. For cell i at position $\mathbf{r}_i(t)$ with velocity $\boldsymbol{\nu}_i(t)$ and with a set $N(i)$ of nearby cells (assuming there is no basement membrane interactions), PhysiCell models the cell-cell adhesive, cell-cell "repulisve" forces and drag forces using

$$m_i \frac{d\boldsymbol{\nu}_i}{dt} = \sum_{j \in N(i)} (\mathbf{F}^{i,j}_{cca} + \mathbf{F}^{ij}_{ccr}) + \mathbf{F}^{i}_{drag} + \mathbf{F}^{i}_{loc}, \tag{C.2}$$

where $\mathbf{F}_{cca}$ and $\mathbf{F}_{ccr}$ are cell-cell adhesive and "repulsive" forces, $\mathbf{F}_{drag}$ collects dissipative, drag-like forces, and $\mathbf{F}_{loc}$ is the locomotive forces. PhysiCell models the drag-like forces by

$$\mathbf{F}^{i}_{drag} = -\nu_i \boldsymbol{\nu}_i,$$

where ν is a (fluid) drag coefficient as in (Frieboes *et al.*, 2007; Macklin *et al.*, 2009, 2012).

The same inertialess assumption ($m_i \dot{\boldsymbol{\nu}}_i \approx 0$) used to simplify Eqs. (8.2) in Section 8.2.3 is also used in PhysiCell. This assumes that forces equilibrate at relatively fast time scales relative to the time scales of cell cycling, death, volume changes, and mutlticellular patterning. This assumption allows Eq. (C.2) to be solved for $\boldsymbol{\nu}_i$:

$$\boldsymbol{\nu}_i = \frac{1}{\nu_i} \left(\sum_{j \in N(i)} (\mathbf{F}^{i,j}_{cca} + \mathbf{F}^{ij}_{ccr}) + \mathbf{F}^{i}_{loc} \right).$$

PhysiCell uses potential functions for the adhesive interactions ϕ and repulsive interactions ψ (Ghaffarizadeh *et al.*, 2018). For adhesion, PhysiCell models

$$\nabla \phi_{n,R_A}(\mathbf{r}) = \begin{cases} \frac{\mathbf{r}}{|\mathbf{r}|} \left(1 - \frac{|\mathbf{r}|}{R_A}\right)^{n+1} & \text{if } |\mathbf{r}| \leqslant R_A, \\ 0 & \text{otherwise} \end{cases}.$$

Here, R_A is the maximum adhesive interaction distance, and n is an integer power (typically 1) chosen for the smoothness of the force's behaviour as $r \to R_A$; $n = 0$

gives minimal smoothness: continuity of the force itself, but not of any derivatives (Ghaffarizadeh *et al.*, 2018). For repulsion, PhysiCell models

$$\nabla\psi_{n,R}(\mathbf{r}) = \begin{cases} -\frac{\mathbf{r}}{|\mathbf{r}|}\left(1-\frac{|\mathbf{r}|}{R}\right)^{n+1} & \text{if } |\mathbf{r}| \leqslant R_A, \\ 0 & \text{otherwise} \end{cases},$$

where n is again the smoothness at the edge of interaction (Ghaffarizadeh *et al.*, 2018). Following previous work by Macklin *et al.* (2012) and D'Antonio *et al.* (2013), PhysiCell models cell-cell adhesive force between cells i and j with individual adhesion parameters $R_{i,A}$ and $R_{j,A}$ as

$$\mathbf{F}^{ij}_{cca} = -C_{cca}A_iA_j\nabla\phi_{n_{cca},R_{i,A}+R_{j,A}}(\mathbf{r_j}-\mathbf{r_i}), \tag{C.3}$$

where C_{cca} is the cell-cell adhesion parameter, A_i and A_j are the cells' relative adhesiveness parameters ($0 \leqslant A_i \leqslant 1$), and n_{cca} is the cell-cell adhesion exponent parameter. By default $A_i = 1$ for all cells.

If cells i and j have radii R_i and R_j, respectively, then the cell-cell repulsive force in PhysiCell is modelled by

$$\mathbf{F}^{ij}_{ccr} = -C_{ccr}\nabla\psi_{n_{ccr},R_i+R_j}(\mathbf{r_j}-\mathbf{r_i}), \tag{C.4}$$

where C_{ccr} is the cell-cell repulsion parameter, and n_{ccr} is the cell-cell repulsion exponent parameter.

In addition to the forces due to interaction with other cells, cell may demonstrate a net locomotive force to become motile. A cell changes its migration velocity stochastically between t and $t + \Delta t_{mech}$ with probability

$$\text{Prob}(\text{change } \boldsymbol{\nu}_{mot}) = \frac{\Delta t_{mech}}{T_{per}}.$$

If a cell changes its migration velocity, it chooses a new migration direction $d_{migrate}$. For this model, it is assumed that cancerous cells have completely unbiased random motion. To calculate the contribution $\mathbf{F}_{loc}$ to the cell's velocity, the migration direction

$d_{migrate}$ is normalised and then multiplied by the cell's migration speed, $s_{loc}(\mu m/min)$. This then gives

$$\boldsymbol{\nu}_{mot} = s_{loc}\frac{d_{migrate}}{\|d_{migrate}\|}.$$

Combining all the assumptions above then gives the formulation for the velocity of the ith cell in PhysiCell as

$$\boldsymbol{\nu_i} = \sum_{j\in N(i)}\left(-\sqrt{c^i_{cca}c^j_{cca}}\nabla\phi_{1,R_{i,A}+R_{j,A}}(\mathbf{r_i}-\mathbf{r_j}) - \sqrt{c^i_{ccr}c^j_{ccr}}\nabla\psi_{1,R_i+R_j}(\mathbf{r_i}-\mathbf{r_j})\right)+\boldsymbol{\nu}_{i,mot},$$

where c^i_{cca} and c^i_{ccr} are the ith cell's cell-cell adhesion and repulsion parameters. Note that if cell i and j have identical cell-cell adhesion and repulsion parameters c_{cca} and c_{ccr}, the cell-cell interaction coefficients simplify to the form in Eq. (C.3) and (C.4). Additionally worth noting, the adhesion interaction potential function $\phi_{n,R}(\mathbf{x})$ is zero for $\|\mathbf{r}\| > R$, and approaches zero with smoothness given by n. Similarly, $\psi_{n,R}(\mathbf{r})$ is a repulsion interaction potential function that is zero for $\|\mathbf{r}\| > R$. Thus, cell-cell mechanical interactions occur over finite distances.

The cell's position is then updated in PhysiCell using the second-order Adams-Bashforth discretisation:

$$\mathbf{r}_i(t+\Delta t_{mech}) = \mathbf{r_i}(t) + \frac{1}{2}\Delta t_{mech}(3\boldsymbol{\nu_i}(t) - \boldsymbol{\nu_i}(t-\Delta t_{mech})),$$

where Δt_{mech} is the cell mechanics time scale (see Section C.1.4). For any further background into the derivation or for the parameter values in PhysiCell, see Ghaffarizadeh *et al.* (2018); D'Antonio *et al.* (2013); Macklin *et al.* (2012).

C.1.3 *Cell proliferation*

PhysiCell includes a cell-cycle modeling framework, where each cell cycle model is a collection of phases, transition rates between the phases, and a cell-division phase transition (Ghaffarizadeh *et al.*, 2018). Since glioblastomas are characterised by rapid cell proliferation, each cancer cell in the model follows the PhysiCell cycle model `live`. This model is equivalent to the exponential growth used in Chapter 5 Eqs. (5.1)-(5.3).

For a population of uninfected cancer cells U, the rate of growth for the population is given by

$$\frac{dU}{dt} = rU$$

where r is the proliferation rate. In PhysiCell, the transition rate (or replication rate) is r. Note that birth is a stochastic event for each cell in the model. If such a process occurs at rate r, then between time t and $t + \Delta t$, the probability of the event occurring for that agent is $r\Delta t$.

When a cell divides, all sub-volumes are divided in half and a duplicate of the cell (including all state and parameter values) is made. To determine where to place the cell and its duplicate, PhysiCell calculates the vector $\mathbf{d}$ where

$$\mathbf{d} = \frac{\mathbf{x} - (\mathbf{x} \cdot \boldsymbol{\theta})\boldsymbol{\theta} + ((1-p)(\mathbf{x} \cdot \boldsymbol{\theta}))\boldsymbol{\theta}}{\|\mathbf{x} - (\mathbf{x} \cdot \boldsymbol{\theta})\boldsymbol{\theta} + ((1-p)(\mathbf{x} \cdot \boldsymbol{\theta}))\boldsymbol{\theta}\|}.$$

and $0 \leqslant p \leqslant 1$ is the degree of polarisation, and $\boldsymbol{\theta}$ is the cell's unit orientation vector and $\mathbf{x} \in [-1, 1] \times [-1, 1] \times [-1, 1]$ is a random vectror. Note that if $p = 1$ then $\mathbf{d}$ is a random unit vector perpendicular to $\boldsymbol{\theta}$, and if $p = 0$, then $\mathbf{d}$ is a random unit vector in 3-D space. 2-D simulations should set $\boldsymbol{\theta} = [0, 0, 1]$. Different to the previous work in Chapter 8, cells divide without checking for an open neighbour site, they can just divide and push any neighbours out of the way.

C.1.4 *Time scales in PhysiCell*

There are three time scales in PhysiCell: biotransport Δt_{diff}, cell mechanics Δt_{mech} and cell processes Δt_{cell}. This is to account for diffusive biostransport occurring relatively fast compared to cell mechanics and cell processes (Ghaffarizadeh *et al.*, 2018). The biotransport time step was chosen based on work by Ghaffarizadeh *et al.* (2015), where they showed that $\Delta t_{diff} = 0.01$ min gives stable and accurate results (relative error 5% or less) for diffusion, decay and secretion rates typical of cancer biology. The other time steps were chosen from the work by Ghaffarizadeh *et al.* (2018). They showed that $\Delta t_{mech} = 0.1$ min accurately and stably computes the cell mechanics

(for tissue engineering and cancer biology problems), and $\Delta t_{cell} = 6$ min sufficiently resolves the 1 hour time scales in cell cycling, death and volume changes.

D

MODEL IMPLEMENTATION FOR WORK DISCUSSED IN CHAPTER 10

D.1 MODEL IMPLEMENTATION

The PhysiCell framework described in the previous section is now extended to include models for the growth and treatment of glioblastomas using an oncolytic adenovirus expressing secretable TRAIL. To do this, mathematical models for the amount of intracellular virus in vein cells and glioblastoma cells are developed below. These are used to calculate the secretion rates $\mathbf{S}_k$ and uptake rates $\mathbf{U}_k$ of cells in the BioFVM PDE Eq. (C.1). These models are used to simulate viral secretion from vein cells, viral infection, replication and lysis of glioblastoma cells, and TRAIL generation, section and apoptosis induction of glioblastoma cells.

D.1.0.1 *Vein cell secretion*

The vasculature can play a major role in the efficacy of cancer therapies (Section 2.2.2). To simulate intravenous injections of oncolytic adenovirus, static vein cells are each initially endowed with V_0/N_V virus particles, where V_0 is the total amount of virus injected initially and N_V is the number of vein cells in the model. Vein cells then secrete the virus into the microenvironment, simulating the arrival of an intravenous injection of treatment. The amount of virus secreted becomes part of the density of extracellular virus, which is simulated using BioFVM's PDE formulation in Eq. (C.1). BioFVM models the microenvironment substrates' bulk source/sink terms as decoupled sets of systems of ODEs, where one vector of ODEs is in each computational voxel. A voxel in PhysiCell represents a value on a regular grid in three-dimensional space. Consider $\mathbf{p}_E = [p_{EV}, p_{ET}]$ to represent the density in each voxel of virus, p_{VE}, and TRAIL, p_{TE}.

Let $n_I(t)$ be the amount of virus inside a cell at time t. The vein cells secrete virus at a rate

$$\frac{dn_I}{dt} = -s_v n_I (p_V^* - p_{VE}), \tag{D.1}$$

where s_v is the secretion rate constant, p_V^* is the virus saturation density (see Section C.1.1) and p_{VE} is the density of virus in the voxel containing the vein cell. The rate at which virus leaves the vein cells is proportional to the amount inside the cell n_I and also the difference between the density of virus in the voxel and the saturation

density (see Eq. (C.1)). The density of extracellular virus in the voxel will increase at a rate proportional to volume of the voxel V_{voxel}. Therefore the rate of change of the density of virus in the voxel will be

$$\frac{dp_{VE}}{dt} = s_v \frac{n_I}{V_{voxel}}(p_V^* - p_{VE}),. \tag{D.2}$$

See Fig. D.1 for a summary of the vein secretion model.

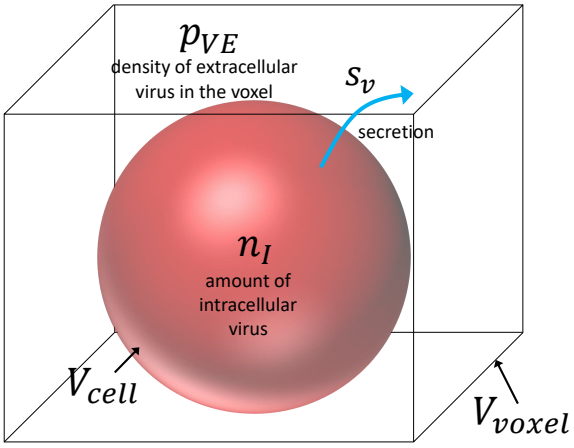

Figure D.1: Schematic for the secretion of virus from a virus-filled vein cell (red). Intracellular virus n_I is secreted with rate constant s_v into the voxel and becomes part of the density of extracellular virus p_{VE}.

To implement this in PhysiCell, the secretion rate in Eq. (C.1) S_{kV} is given by

$$S_{kV} = \frac{1}{V_{voxel}} s_v n_I,$$

as the multiple of $p_V^* - p_{VE}^*$ is already factored into the PDE formulation of BioFVM. For vein cells the uptake rate for virus particles and the secretion and uptake rate of TRAIL molecules are set to 0, i.e. $U_{kV} = 0, S_{kT} = 0$ and $U_{kT} = 0$. The intracellular amount of the virus is approximated using a forward-Euler approximation:

$$n_I(t + \Delta t_{cell}) = n_I(t) - \Delta t_{cell} s_v n_I(t)(p_V^* - p_{VE}).$$

This value is calculated and stored in the cell phenotype as the model iterates.

D.1.0.2 *Glioblastoma cell infection, intracellular replication and lysis function*

The viral infection, replication and lysis of glioblastoma cells is modelled as a three stage process: (1) initial infection, (2) replication and additional infection, and (3) replication and lysis, see Fig. D.2. This is similar to the model developed in Chapter 4 for the intracellular virus replication (see Fig. 4.3). The amount of intracellular virus n_I in a glioblastoma cell is modelled by

$$\frac{dn_I}{dt} = c_I p_{VE} V_{voxel} \left(1 - \frac{n_I}{n_{I,T}}\right)(1 - H(n_I - n_{I,T})) + c_R H(n_I - n_{I*}) \tag{D.3}$$

where c_I is the infection rate, $n_{I,T}$ is the maximum infection capacity, n_{I*} is the minimum amount of intracellular virus needed for replication to commence, c_R is the virus replication and H is the Heaviside function. Virus is assumed to infect at cell at a rate proportion to the amount available to infect, $n_E = p_V E_{voxel}$. The rate at which viruses replicate is assumed to be constant. Once the total intracellular amount of virus has reached $n_{I,T}$ the virus is no longer infected by any extracellular virus. This is to allow for a controlled virus infection, where multiple infections of a single cell can occur.

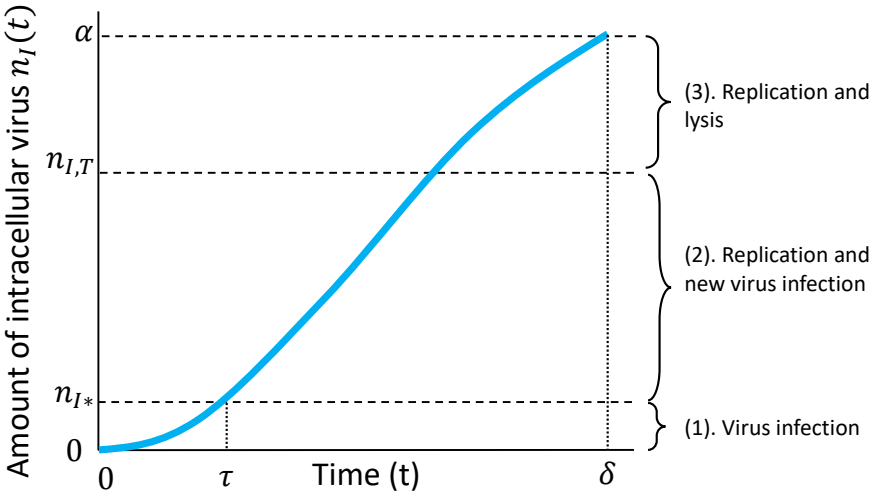

Figure D.2: Illustration of the amount of intracellular virus $n_I(t)$ in a single infected cell. The cell needs to be infected with n_{I*} virus particles before replication can commence. Once replication starts at time τ, new virus particles are still able to infect the cell; however, once the number of intracellular virus reaches $n_{I,T}$, further infection stops. The maximum likelihood of lysis occurring is then reached when the amount of virus exceeds α. Lysis occurs at time δ and can be before $n_I = \alpha$.

Assuming that there is a capacity for the amount of virus, $n_{I,T}$, a particular cell can take up, the rate of uptake can be modelled using a logistic function. The density, p_{VE}, of virus in the voxel outside the virus-infected cell is modelled by

$$\frac{dp_{VE}}{dt} = -c_I p_{VE} \left(1 - \frac{n_I}{n_{I,T}}\right) (1 - H(n_I - n_{I,T})) .$$

To model this in PhysiCell, the uptake rate, U_{kV}, in Eq. (C.1) is given by

$$U_{kV} = c_I \left(1 - \frac{n_I}{n_{I,T}}\right) (1 - H(n_I - n_{I,T}))$$

as the multiple p_{VE} is already factored into the PDE formulation of BioFVM. Similar to the vein wall cells, the amount of intracellular virus is approximated using a forward-Euler approximation:

$$n_I(t + \Delta t_{cell}) = n_I(t) + \Delta t_{cell} \left(c_I p_{VE} V_{voxel} \left(1 - \frac{n_I}{n_{I,T}}\right) + c_R H(n_I - n_{I*})\right) \quad (D.4)$$

Following the ideology of the virus titer modelling in Chapter 4, the lysis rate of virus-infected cells is given by the Hill function

$$a_f(n_I) = \frac{n_I^b}{(\alpha/2)^b + n_I^b}, \quad (D.5)$$

where b is an integer exponent controlling the steepness of the curve ($b \geqslant 1$) and α is the number of new virus particles created through lysis (used in Chapters 6 and 7). A number of studies have characterized biochemical switches from the perspective of steady-state behavior and Hill functions (Ferrell Jr and Xiong, 2001; Ferrell and Machleder, 1998), see the model from de Pillis *et al.* (2005) in Eqs. (3.13)-(3.16). To make sure cells aren't undergoing lysis too early, there are three stages to the lysis cell death considered:

$$a(n_I) = \begin{cases} 0 & n_I < \alpha/5, \\ a_f(n_I) & \alpha/5 < n_I < \alpha, \\ \infty & n_I > \alpha, \end{cases} ,$$

where cells aren't able to die unless they have at least $\alpha/5$ viruses and lyse once they reach α viruses. The time a cell undergoes lysis is δ. When the cell dies, the amount of intracellular virus is secreted instantaneously into the voxel containing that cell, and the density of the virus is updated. If the density in the voxel is close to or above saturation p_V^*, then only an amount of virus that would take the density in the voxel to p_V^* is released and the remainder is released over time. Similar to the model in Chapter 8, death of uninfected tumour cells by causes other than viral lysis is assumed negligible. See Fig. D.3 for a mathematical summary of the viral infection, replication and lysis stages of TRAIL release.

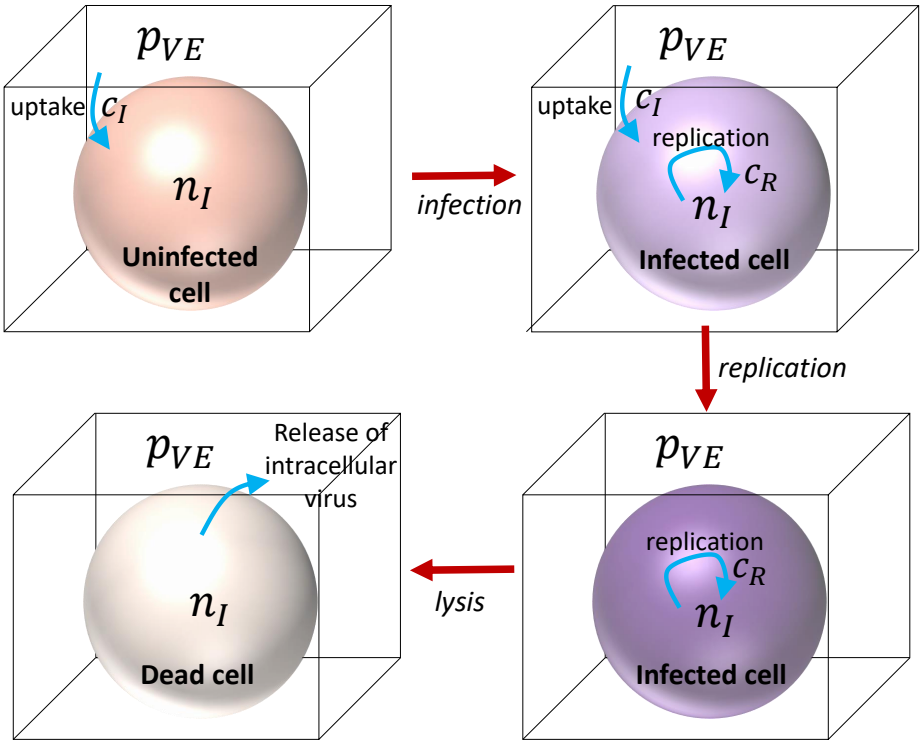

Figure D.3: Schematic for the intracellular and extracellular infection, replication and lysis process. Extracellular virus p_{VE} is taken up by a cell with rate constant c_I. The virus within the cell undergoes replication at a constant rate c_R. The cell then undergoes lysis, releasing its contents back into the extracellular density of virus in the voxel.

D.1.0.3 *TRAIL generation and secretion*

As the oncolytic adenovirus expressing secretable trimeric TRAIL undergoes replication, new TRAIL molecules are created, see Section 2.4.2. TRAIL molecules are created

at the same rate as new virus particles, giving the amount of intracellular TRAIL molecules, T_i, as

$$\frac{dT_I}{dt} = c_R H(n_I - n_{I*}) - s_T T_I H(t - s_\tau)(p_T^* - p_{TE}). \tag{D.6}$$

where C_R is the rate at which TRAIL is created, s_T is the rate of TRAIL secretion, p_T^* is the TRAIL saturation density and p_{TE} is the density of TRAIL in the voxel containing the infected cell. For viral replication to occur, at least n_{I*} virus particles need to be present in the cell (Eq. (D.3)). Trail is secreted from the cell at a rate s_T, proportional to the amount of TRAIL present in the cell. Secretion starts at time s_τ and continues until time δ, at which point the cell undergoes lysis and the remaining viruses inside the cell are released (similar to the model in Chapter 4). Fig. D.4 depicts an illustration of the intracellular TRAIL amount for a single infected cell over time.

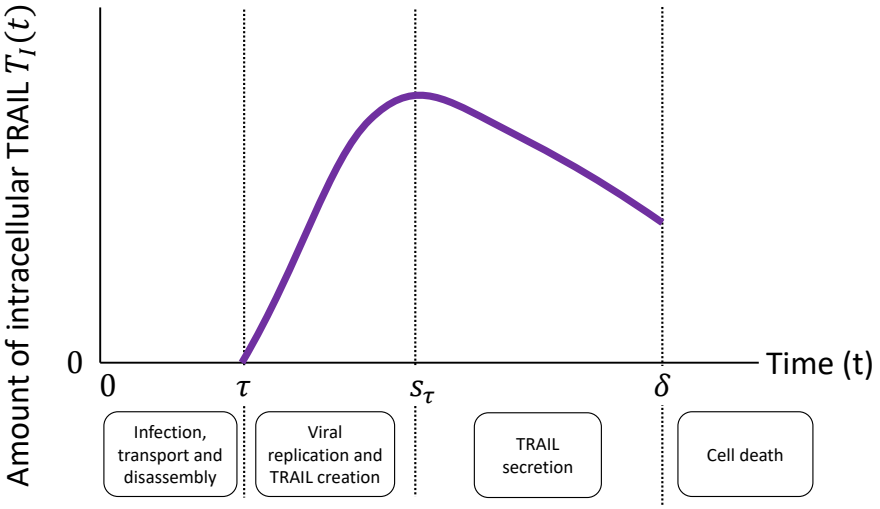

Figure D.4: Illustration of the amount of intracellular virus, $n_I(t)$, in a single infected cell. The cell needs to be infected with n_{I*} virus particles before replication can commence. Once replication starts, new virus particles are still able to infect the cell; however, once the number of intracellular virus reaches $n_{I,T}$, further infection stops. The maximum likelihood of lysis occurring is then reached when the amount of virus exceeds α.

As for the previous intracellular amounts, TRAIL is calculated using a forward-Euler approximation:

$$T_I(t + \Delta t_{cell}) = T_I + \Delta t_{cell} \frac{dT_I}{dt}(p_T^* - p_{TE}).$$

To make sure the value for T_I does not become negative, a condition needs to be imposed on p_T^* such that

$$\begin{aligned} &T_I + \Delta t_{cell}(c_T - s_T T_I(p_T^* - p_{TE})) > 0 \\ &T_I(1 - \Delta t_{cell} s_T(p_T^* - p_{TE})) > 0 \\ &P_T^* < \frac{1}{\Delta t_{cell} s_T} < \frac{1}{\Delta t_{cell} s_T} + p_{TE}. \end{aligned}$$

The secretion rate of the cell for the BioFVM PDE, Eq. (C.1), is

$$\frac{dp_{TE}}{dt} = s_T \frac{T_I}{V_{VOXEL}} H(t - s_\tau)(p_T^* - p_{TE}). \tag{D.7}$$

To model this in PhysiCell, the secretion rate, S_{kT}, in Eq. (C.1) is given by

$$S_{kT} = s_T \frac{T_I}{V_{VOXEL}} H(t - s_\tau),$$

where the term $p_T^* - p_{TE}$ is already factored into the PDE formulation of BioFVM Eq. (C.1). For glioblastoma cells, the secretion rate for virus particles and the uptake rate of TRAIL molecules are set to 0, i.e. $U_{kV} = 0$ and $S_{kT} = 0$. When the cell lyses, it releases the remaining TRAIL molecules until the saturation density of the voxel p_T^*. If more TRAIL is present in the cell then it is released over time, so that the density of TRAIL in the voxel does not exceed p_T^*.

The rate of TRAIL-induced apoptosis for a particular cell depends on the density of TRAIL molecules in the local microenvironment, i.e. $a_T(p_{TE})$. A similar function to that used for the viral lysis is used for TRAIL induced apoptosis:

$$a_T(p_{TE}) = \frac{p_{TE}^b}{M^b + p_{TE}^b}, \tag{D.8}$$

again with the condition that minute traces of TRAIL will not induce apoptosis of cells:

$$a(p_{TE}) = \begin{cases} 0 & p_{TE} < T_{min}, \\ a_f(n_I) & p_{TE} \geqslant T_{min} \end{cases}$$

D.1.0.4 *Parameters and model simulations*

To determine the base line glioblastoma cell replication rate r, measurements for the growth of U-87MG glioblastoma murine tumours by Oh *et al.* (2018) were used. These measurements were obtained using the same method for tumour growth in previous chapters, see Section 2.5.3. Fitting an exponential growth curve to the data gave the fit in Fig. D.5 and Table D.1. The confidence intervals returned were tight and the R^2 value was 0.9996. The growth rate was only fit for the first 9 days as limiting factors (such as carrying capacity) would influence the tumour growth after this time and these are not explicitly modelled.

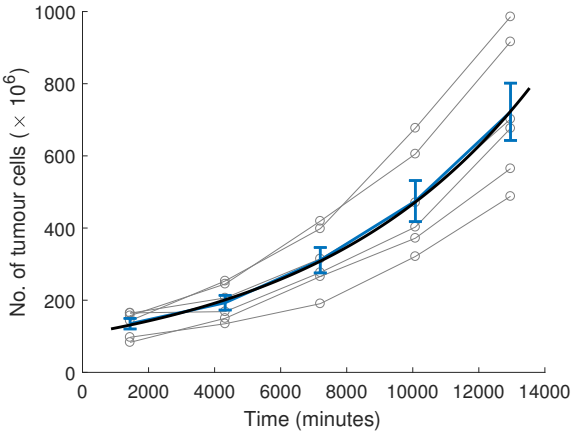

Figure D.5: Output of optimising exponential growth rate r to U87MG glioblastoma tumour growth measurements from Oh *et al.* (2018) for the first 9 days (140000 minutes).

Most of the remaining parameters are estimated based on literature or work in the previous chapters, see Table D.1. The mathematical and experimental work of Dinh *et al.* (2005) is used to estimate parameters relating to the internalisation rate of the virus c_I and the replication rate c_R. They developed an integrative computational framework to model biophysical processes involved in viral gene delivery. Dinh *et al.* (2005) derived the internalisation rate of cells to be $c_I = 0.072$ min^{-1} from kinetic studies of adenovirus trafficking and propagation. The transcription rate in Dinh *et al.* (2005) proposed is 0.033min^{-1}.

The diffusion coefficient of the virus, D_V, was approximated using the work of Yakimovich *et al.* (2012), where the transmission mode of human adenovirus (HAdV)

in monolayers of epithelial cells was analysed by wet-lab experimentation and a computer simulation. Assuming adenoviruses can be approximated as spherical, D_V was estimated to be $243\mu m^2/min$ for particle motion in fibrous tumours. The diffusion coefficient of TRAIL molecules D_T is approximated using the diffusion coefficient of molecules in fibroblast-contracted collagen gel measured by Kihara *et al.* (2013). Since TRAIL has a molecular weight of 40 kDa, the diffusion coefficient of an equivalently weighted molecule, FITC dextrain, is used to approximate TRAIL's diffusion coefficient $D = 2682\mu m^2/min$ (Kihara *et al.*, 2013).

Since all the previous models in this thesis used a viral decay rate that considered not just local intratumoural decay, but also loss to other organs (Chapter 6) and immune clearance (Chapter 8), the decay rates λ_V and λ_T for virus particles and TRAIL are estimated from the literature. The half-life of the adenovirus in tissue was estimated by Ethier *et al.* (2004) to be 318 minutes, using the half-life decay formula this gives the virus decay rate of $\lambda_V = -\ln(1/2)/318 = 0.0022/\text{min}$. TRAIL is known to have an average half-life of 630 minutes (Lim *et al.*, 2011). Using the half-life decay formulas gives the TRAIL decay rate of $\lambda_T = -\ln(0.5)/630 = 0.0011/\text{min}$. This supports what Jeong *et al.* (2009) concluded from their experiments with the ri-Ad-stTRAIL, that viral copies decayed quicker than the TRAIL molecules.

The rate at which virus particles are secreted from vein cells is assumed to be equivalent to the rate determined in Chapter 6, for the rate of transfer of the virus from the blood to the tumour site. As such, this gives $s_\nu = 0.4752/\text{min}$. The initial virus injection was taken from the experiments of Oh *et al.* (2018) who use $V_0 = 5 \times 10^9$ TRAIL-expressing adenovirus particles when treatment murine U-87MG murine tumours.

For some parameters it was not possible to determine their values from the literature, so they have been estimated so that the system is in a qualitatively steady state (i.e. tumour growth and treatment efficacy roughly stablise), see Table D.2. The saturation density of the virus and TRAIL molecules (in other words the density at which the cells stop secreting) was assumed to be equivalent $p^* = 10$. The intracellular virus capacity was set to $n_{I,T} = 100$ to make sure that there wasn't an unrealistic number of viruses infecting cells. The minimum virus replication threshold was $n_{I*} = 10$ to

make sure that any cell that hadn't been sufficiently infected did not start replicating. The integer exponent for the Hill function was set as $b = 3$, so that both apoptosis rates $a_f(n_I)$ Eq. (D.5) and $a_T(p_{TE})$ Eq. (D.8) resembled a sigmoidal curve with a clear switch between non-apoptotic and apoptotic states.

Evolution of the model for the parameters in Table D.1 and D.2 is plotted in Fig. D.6 for triangular vein cross sections and Fig. D.8 for circular vein cross sections. The corresponding virus and TRAIL densities for each simulation is plotted in Fig. D.7 and Fig. D.9. In the following section, all simulations are presented as the average of five model simulations. For the same parameter set, the model simulations didn't show significant stochasticity in the tumour cell population.

Table D.1: Parameters based from literature values for the PhysiCell simulations in this chapter

	Parameter	Units	Description	Value	Source
Literature	D_V	$\mu m^2/min^{-1}$	virus diffusion coefficient	243	Yakimovich *et al.* (2012)
	D_T	$\mu m^2/min^{-1}$	TRAIL diffusion coefficient	2682	Kihara *et al.* (2013)
	λ_V	min^{-1}	virus decay rate	0.0022	Ethier *et al.* (2004)
	λ_T	min^{-1}	TRAIL decay rate	0.0011	Lim *et al.* (2011)
	r	min^{-1}	replication rate	0.0001482	Fit to data from Oh *et al.* (2018) (Fig. D.5)
	s_ν	min^{-1}	secretion rate of virus from vein cell	0.4752	Fit to data from Kim *et al.* (2011a) (Table 6.7 and Fig. 6.9)
	V_0	virus	initial amount of virus in injection	5×10^9	(Oh *et al.*, 2018)
	c_I	min^{-1}	rate at which cell uptakes virus	0.072	Dinh *et al.* (2005)
	c_R	min^{-1}	intracellular replication rate	0.033	Dinh *et al.* (2005)
	α	virus	size when lysis rate is the maximum	3500	Chen *et al.* (2001)

Table D.2: Estimated parameter values for the PhysiCell simulations in this chapter

	Parameter	Units	Description	Value
Estimated	p_V^*	virus	virus saturation density (density at which the cells stop secreting)	10
	p_T^*	TRAIL	TRAIL saturation density (density at which the cells stop secreting)	10
	n_{I*}	virus	minimum virus replication threshold	10
	b	-	integer exponent for hill function	3
	M	$\mu m^2/min^{-1}$	density when apoptosis rate is maximum	10
	T_{min}	$\mu m^2/min^{-1}$	minimum TRAIL density required for apoptosis	10^{-2}

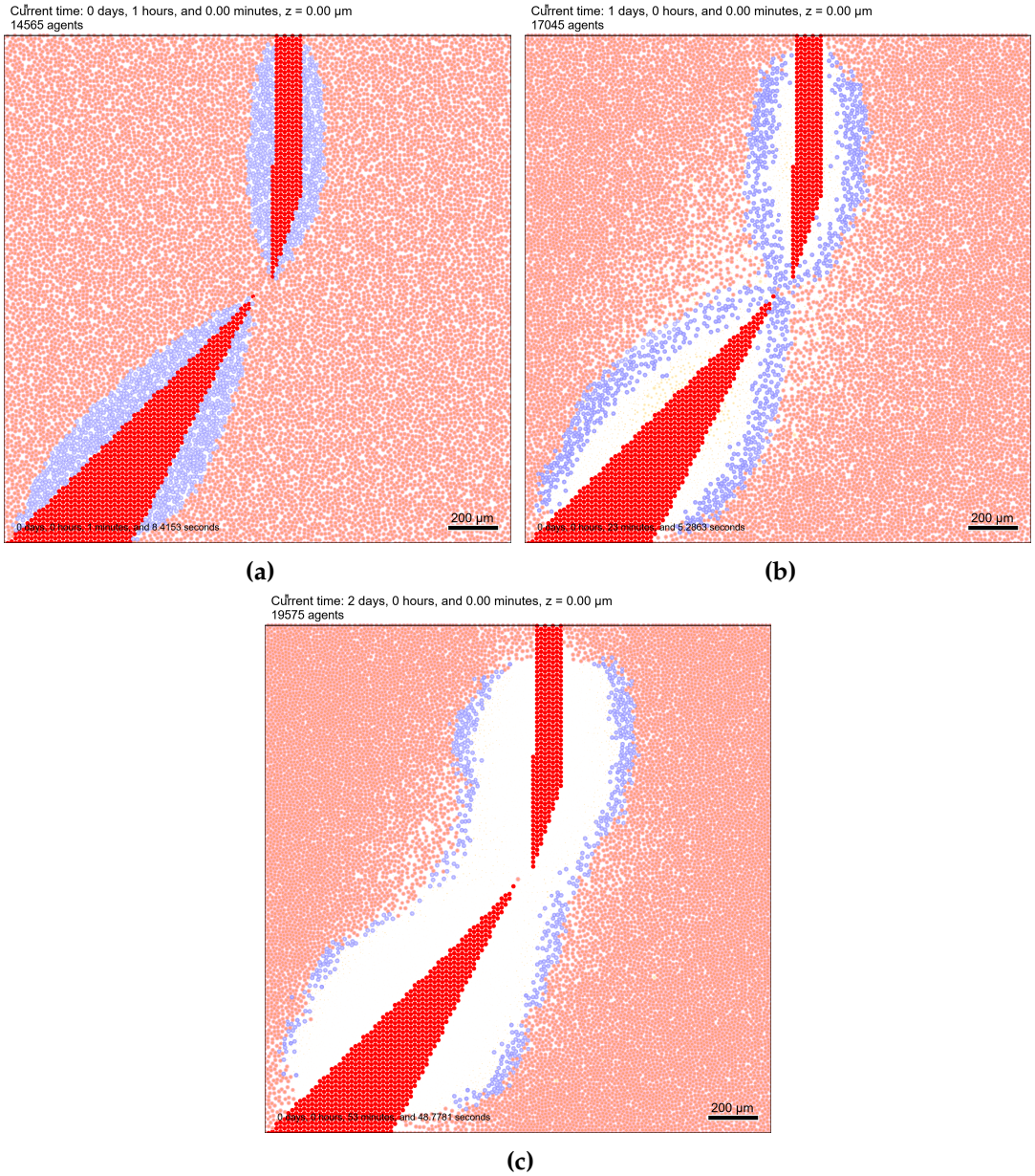

Figure D.6: Simulation for virus infection in a layer of tissue with triangle veins at (a) 60 mins, (b) 1440 mins (1 day) and (c) 2880 mins (2 days). Parameters were fixed to the values in Table D.1 and D.2 with $s_T = 0.1$ and $s_\tau = 100$. Red cells represent vein cells, these cells secrete virus that infects tissue cells, which are pink cells. Once a cell becomes infected it is coloured purple, with the darker the shade corresponding to the more virus in the cell. The infected cells die turning a pale yellow and eventually disappearing.

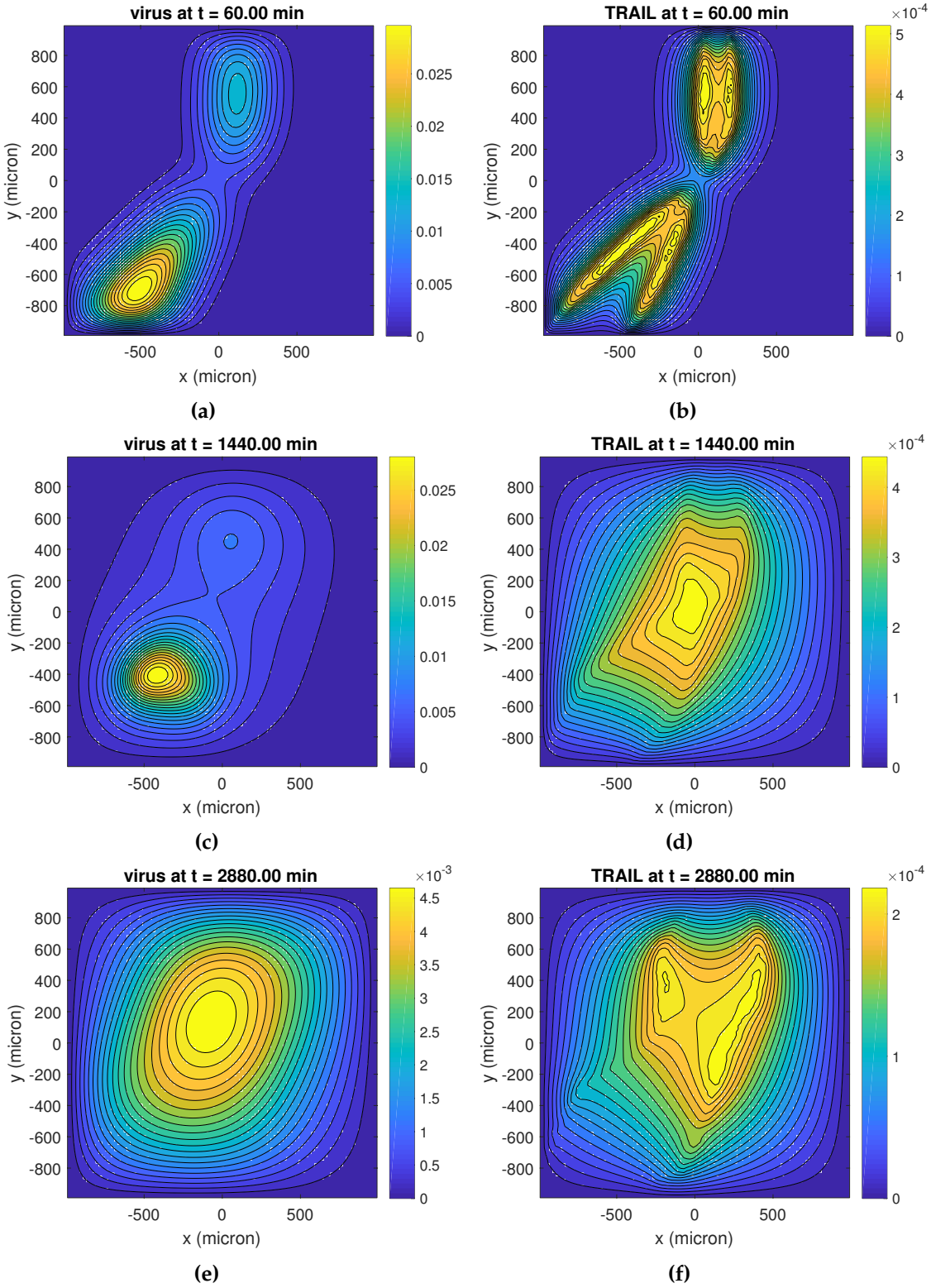

Figure D.7: Contour plots for the density of virus ((a), (c) and (e)) and TRAIL ((b), (d) and (f)) at 60 mins, 1440 mins (1 day) and 2880 mins (2 days). These plots correspond to the simulations in Fig. D.6.

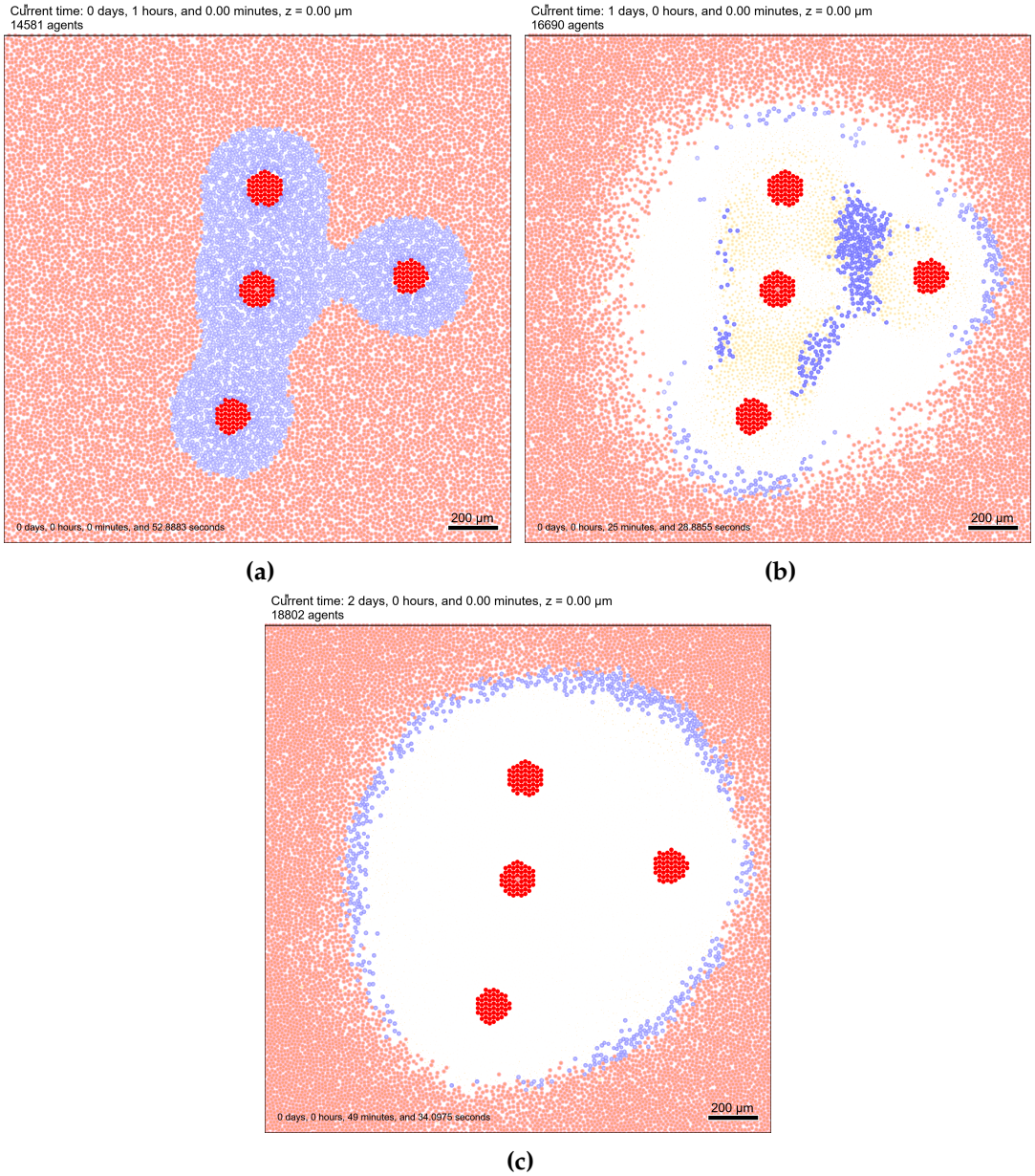

Figure D.8: Simulation for virus infection in a layer of tissue with circular veins at (a) 60 mins, (b) 1440 mins (1 day) and (c) 2880 mins (2 days). Parameters were fixed to the values in Table D.1 and D.2 with $s_T = 0.1$ and $s_\tau = 100$. Red cells represent vein cells, these cells secrete virus that infects tissue cells, which are pink cells. Once a cell becomes infected it is coloured purple, with the darker the shade corresponding to the more virus in the cell. The infected cells die turning a pale yellow and eventually disappearing.

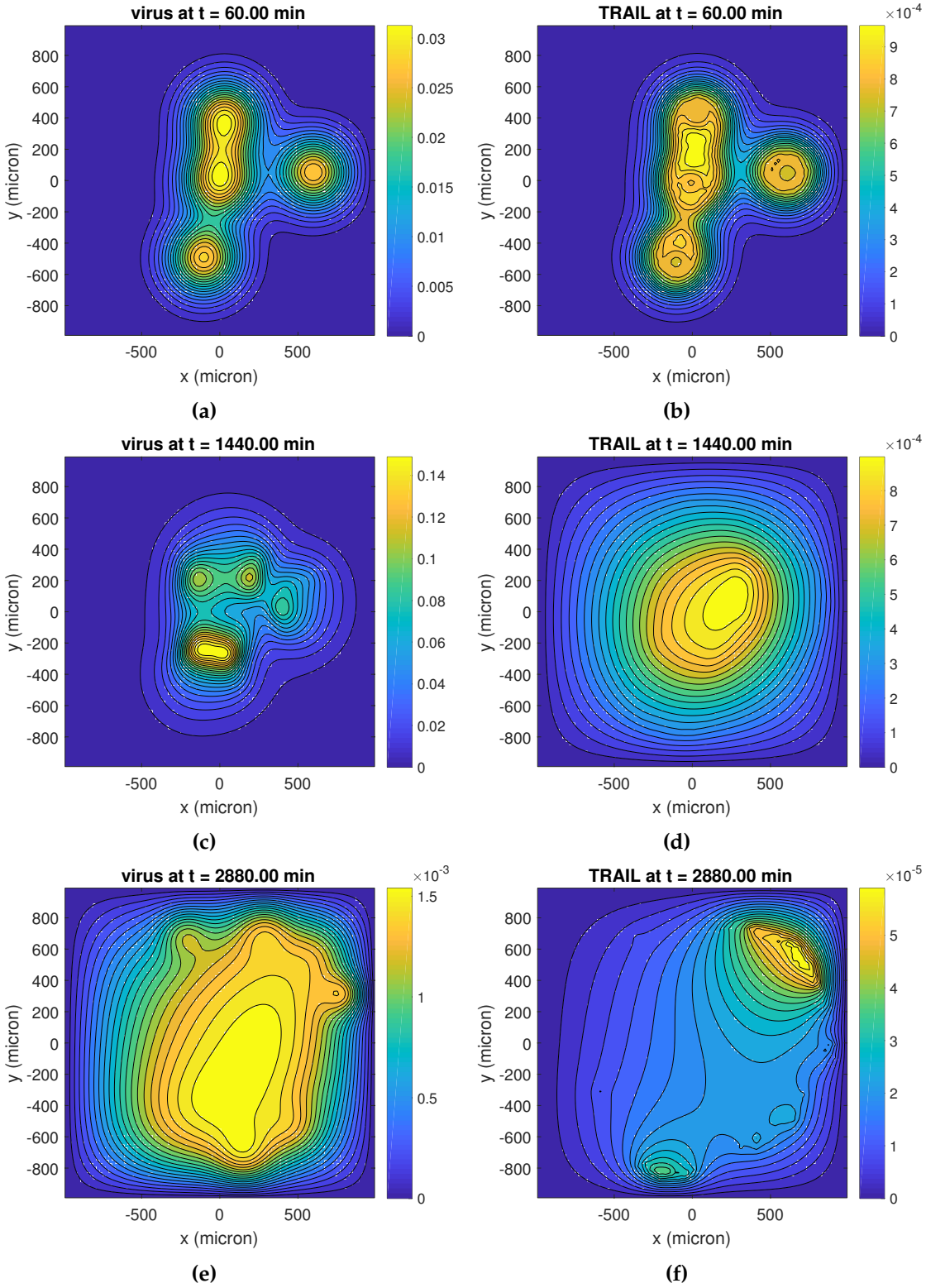

Figure D.9: Contour plots for the density of virus ((a), (c) and (e)) and TRAIL ((b), (d) and (f)) at 60 mins, 1440 mins (1 day) and 2880 mins (2 days). These plots correspond to the simulations in Fig. D.8.

BIBLIOGRAPHY

Adam, J. A. (1986). A simplified mathematical model of tumor growth. *Mathematical Biosciences*, **81**(2), 229–244. (Cited on page 29.)

Alarcón, T., Byrne, H. M., and Maini, P. K. (2003). A cellular automaton model for tumour growth in inhomogeneous environment. *Journal of Theoretical Biology*, **225**(2), 257–274. (Cited on page 38.)

Alberts, B., Bray, D., Hopkin, K., Johnson, A. D., Lewis, J., Raff, M., Roberts, K., and Walter, P. (2013). *Essential cell biology*. Garland Science. (Cited on page 9.)

Alemany, R. (2014). Oncolytic adenoviruses in cancer treatment. *Biomedicines*, **2**(1), 36–49. (Cited on page 17.)

Althaus, C. L., De Vos, A. S., and De Boer, R. J. (2009). Reassessing the human immunodeficiency virus type 1 life cycle through age-structured modeling: life span of infected cells, viral generation time, and basic reproductive number, Ro. *Journal of Virology*, **83**(15), 7659–7667. (Cited on page 48.)

Anderson, A. R., Chaplain, M. A., Newman, E. L., Steele, R. J., and Thompson, A. M. (2000). Mathematical modelling of tumour invasion and metastasis. *Computational and Mathematical Methods in Medicine*, **2**(2), 129–154. (Cited on page 29.)

Appert, J., Raynor, P. C., Abin, M., Chander, Y., Guarino, H., Goyal, S. M., Zuo, Z., Ge, S., and Kuehn, T. H. (2012). Influence of suspending liquid, impactor type, and substrate on size-selective sampling of ms2 and adenovirus aerosols. *Aerosol Science and Technology*, **46**(3), 249–257. (Cited on page 206.)

Ariffin, A. B., Forde, P. F., Jahangeer, S., Soden, D. M., and Hinchion, J. (2014). Releasing pressure in tumors: what do we know so far and where do we go from here? A review. *Cancer Research*, **74**(10), 2655–2662. (Cited on page 76.)

Baccam, P., Beauchemin, C., Macken, C. A., Hayden, F. G., and Perelson, A. S. (2006). Kinetics of influenza A virus infection in humans. *Journal of Virology*, **80**(15), 7590–7599. (Cited on page 75.)

Baer, A. and Kehn-Hall, K. (2014). Viral concentration determination through plaque assays: using traditional and novel overlay systems. *JoVE (Journal of Visualized Experiments)*, (93), e52065. (Cited on page 23.)

Bagga, S. and Bouchard, M. J. (2014). Cell cycle regulation during viral infection. *Cell Cycle Control: Mechanisms and Protocols*, pages 165–227. (Cited on page 193.)

Bajzer, Ž., Carr, T., Josić, K., Russell, S. J., and Dingli, D. (2008). Modeling of cancer virotherapy with recombinant measles viruses. *Journal of Theoretical Biology*, **252**(1), 109–122. (Cited on pages 2, 17, 31, 32, and 112.)

Banks, H., Bortz, D., and Holte, S. (2003). Incorporation of variability into the modeling of viral delays in hiv infection dynamics. *Mathematical Biosciences*, **183**(1), 63–91. (Cited on pages 35 and 56.)

Barber, G. (2001). Host defense, viruses and apoptosis. *Cell Death & Differentiation*, **8**(2). (Cited on page 134.)

Berezovskaya, F., Karev, G., and Arditi, R. (2001). Parametric analysis of the ratio-dependent predator–prey model. *Journal of Mathematical Biology*, **43**(3), 221–246. (Cited on page 110.)

Berezovskaya, F. S., Novozhilov, A. S., and Karev, G. P. (2007). Population models with singular equilibrium. *Mathematical Biosciences*, **208**(1), 270–299. (Cited on pages 32 and 110.)

Blythe, S., Nisbet, R., and Gurney, W. (1984). The dynamics of population models with distributed maturation periods. *Theoretical Population Biology*, **25**(3), 289–311. (Cited on page 56.)

Bommareddy, P. K., Shettigar, M., and Kaufman, H. L. (2018). Integrating oncolytic viruses in combination cancer immunotherapy. *Nature Reviews Immunology*, **18**(8), 498. (Cited on pages 2 and 22.)

Bonhoeffer, S., May, R. M., Shaw, G. M., and Nowak, M. A. (1997). Virus dynamics and drug therapy. *Proceedings of the National Academy of Sciences*, **94**(13), 6971–6976. (Cited on page 30.)

Boondirek, A., Triampo, W., and Nuttavut, N. (2010). A review of cellular automata models of tumor growth. In *International Mathematical Forum*, volume 5, pages 3023–3029. Citeseer. (Cited on page 38.)

Brewer, P. D., Habtemichael, E. N., Romenskaia, I., Mastick, C. C., and Coster, A. C. (2014). Insulin-regulated glut4 translocation membrane protein trafficking with six distinctive steps. *Journal of Biological Chemistry*, **289**(25), 17280–17298. (Cited on page 41.)

Buijs, J. O. d., Musters, M., Verrips, T., Post, J. A., Braam, B., and Van Riel, N. (2004). Mathematical modeling of vascular endothelial layer maintenance: the role of endothelial cell division, progenitor cell homing, and telomere shortening. *American Journal of Physiology-Heart and Circulatory Physiology*, **287**(6), H2651–H2658. (Cited on page 192.)

Byrne, H. M., King, J. R., McElwain, D. S., and Preziosi, L. (2003). A two-phase model of solid tumour growth. *Applied Mathematics Letters*, **16**(4), 567–573. (Cited on page 29.)

Carnaffan, S. and Kawai, R. (2017). Solving multidimensional fractional fokker–planck equations via unbiased density formulas for anomalous diffusion processes. *SIAM Journal on Scientific Computing*, **39**(5), B886–B915. (Cited on pages 194 and 195.)

Chaffer, C. L. and Weinberg, R. A. (2011). A perspective on cancer cell metastasis. *Science*, **331**(6024), 1559–1564. (Cited on page 11.)

Chaplain, M. A., McDougall, S. R., and Anderson, A. (2006). Mathematical modeling of tumor-induced angiogenesis. *Annu. Rev. Biomed. Eng.*, **8**, 233–257. (Cited on page 29.)

Chard, L. S., Maniati, E., Wang, P., Zhang, Z., Gao, D., Wang, J., Cao, F., Ahmed, J., El Khouri, M., Hughes, J., *et al.* (2015). A vaccinia virus armed with interleukin-10 is a promising therapeutic agent for treatment of murine pancreatic cancer. *Clinical Cancer Research*, **21**(2), 405–416. (Cited on page 22.)

Chattopadhyay, J., Sarkar, R., and El Abdllaoui, A. (2002). A delay differential equation model on harmful algal blooms in the presence of toxic substances. *Mathematical Medicine and Biology*, **19**(2), 137–161. (Cited on page 56.)

Chen, Y., DeWeese, T., Dilley, J., Zhang, Y., Li, Y., Ramesh, N., Lee, J., Pennathur-Das, R., Radzyminski, J., Wypych, J., *et al.* (2001). Cv706, a prostate cancer-specific adenovirus variant, in combination with radiotherapy produces synergistic antitumor efficacy without increasing toxicity. *Cancer Research*, **61**(14), 5453–5460. (Cited on pages 119 and 292.)

Chen, Y.-C., Lou, X., Ingram, P., and Yoon, E. (2011). Single cell migration chip using hydrodynamic cell positioning. In *International Conference on MicroTAS*, pages 1409–1411. (Cited on page 202.)

Chiocca, E. A., Abbed, K. M., Tatter, S., Louis, D. N., Hochberg, F. H., Barker, F., Kracher, J., Grossman, S. A., Fisher, J. D., Carson, K., *et al.* (2004). A phase I open-label, dose-escalation, multi-institutional trial of injection with an E1B-attenuated adenovirus, ONYX-015, into the peritumoral region of recurrent malignant gliomas, in the adjuvant setting. *Molecular Therapy*, **10**(5), 958–966. (Cited on pages 19 and 21.)

Choi, I.-K., Li, Y., Oh, E., Kim, J., and Yun, C.-O. (2013a). Oncolytic adenovirus expressing IL-23 and p35 elicits IFN-γ-and tnf-prostate cancer- specific adenovirus variant-co-producing t cell-mediated antitumor immunity. *PloS one*, **8**(7), e67512. (Cited on page 22.)

Choi, J., Kang, E., Kwon, O., Yun, T., Park, H., Kim, P., Kim, S., Kim, J., and Yun, C. (2013b). Local sustained delivery of oncolytic adenovirus with injectable alginate gel for cancer virotherapy. *Gene therapy*, **20**(9), 880. (Cited on pages 213 and 214.)

Choi, K. J., Zhang, S. N., Choi, I. K., Kim, J. S., and Yun, C. O. (2012a). Strengthening of antitumor immune memory and prevention of thymic atrophy mediated by adenovirus expressing IL-12 and GM-CSF. *Gene Therapy*, **19**(7), 711–723. (Cited on pages xxvii, 12, 13, 15, 16, 147, 148, 151, 152, 153, 156, 158, 160, 166, 167, 168, 179, 180, and 182.)

Choi, K.-J., Zhang, S.-N., Choi, I.-K., Kim, J.-S., and Yun, C.-O. (2012b). Strengthening of antitumor immune memory and prevention of thymic atrophy mediated by adenovirus expressing IL-12 and GM-CSF. *Gene Therapy*, **19**(7), 711–723. (Cited on page 22.)

Crivelli, J. J., Földes, J., Kim, P. S., and Wares, J. R. (2012). A mathematical model for cell cycle-specific cancer virotherapy. *Journal of biological dynamics*, **6**(sup1), 104–120. (Cited on page 28.)

Culshaw, R. V., Ruan, S., and Webb, G. (2003). A mathematical model of cell-to-cell spread of hiv-1 that includes a time delay. *Journal of Mathematical Biology*, **46**(5), 425–444. (Cited on pages 35, 36, and 56.)

Cushing, J. (1977). Integrodifferential equations and delay models in population dynamics, lect. *Notes in Biomath*, **20**. (Cited on page 56.)

D'Antonio, G., Macklin, P., and Preziosi, L. (2013). An agent-based model for elasto-plastic mechanical interactions between cells, basement membrane and extracellular matrix. *Math Biosci Eng*, **10**(1), 75–101. (Cited on pages 277 and 278.)

De Boer, R. J., Hogeweg, P., Dullens, H. F. J., De Weger, R. A., and Den Otter, W. (1985). Macrophage T lymphocyte interactions in the anti-tumor immune response: a mathematical model. *The Journal of Immunology*, **134**(4), 2748–2758. (Cited on page 33.)

De Boer, R. J., Oprea, M., Antia, R., Murali-Krishna, K., Ahmed, R., and Perelson, A. S. (2001). Recruitment times, proliferation, and apoptosis rates during the CD8+ T-cell response to lymphocytic choriomeningitis virus. *Journal of Virology*, **75**(22), 10663–10669. (Cited on page 137.)

De Pillis, L. G. and Radunskaya, A. (2001). A mathematical tumor model with immune resistance and drug therapy: an optimal control approach. *Computational and Mathematical Methods in Medicine*, **3**(2), 79–100. (Cited on pages 9 and 13.)

de Pillis, L. G., Radunskaya, A. E., and Wiseman, C. L. (2005). A validated mathematical model of cell-mediated immune response to tumor growth. *Cancer Research*, **65**(17), 7950–7958. (Cited on pages 29, 33, 34, 41, 45, 137, 182, and 285.)

DeGroot, M. H. and Schervish, M. J. (2012). *Probability and statistics*. Pearson Education. (Cited on pages 261, 262, and 263.)

Del Monte, U. (2009). Does the cell number 109 still really fit one gram of tumor tissue? *Cell Cycle*, **8**(3), 505–506. (Cited on page 202.)

Delgado-SanMartin, J. A., Hare, J. I., de Moura, A. P., and Yates, J. W. (2015). Oxygen-driven tumour growth model: a pathology-relevant mathematical approach. *PLoS Computational Biology*, **11**(10), e1004550. (Cited on page 29.)

D'Halluin, J. C. and Milleville, M. (1984). Initiation rate of adenovirus DNA synthesis in infected cell. *Biochimica et Biophysica Acta (BBA)-Gene Structure and Expression*, **782**(1), 67–75. (Cited on page 241.)

Dingli, D., Cascino, M. D., Josić, K., Russell, S. J., and Bajzer, Ž. (2006). Mathematical modeling of cancer radiovirotherapy. *Mathematical Biosciences*, **199**(1), 55–78. (Cited on page 32.)

Dingli, D., Offord, C., Myers, R., Peng, K.-W., Carr, T., Josic, K., Russell, S. J., and Bajzer, Z. (2009). Dynamics of multiple myeloma tumor therapy with a recombinant measles virus. *Cancer Gene Therapy*, **16**(12), 873–882. (Cited on pages 2, 29, 32, 101, 111, and 112.)

Dinh, A.-T., Theofanous, T., and Mitragotri, S. (2005). A model for intracellular trafficking of adenoviral vectors. *Biophysical journal*, **89**(3), 1574–1588. (Cited on pages 289 and 292.)

Doedel, E. J. (2007). Auto-07p: Continuation and bifurcation software for ordinary differential equations. Technical report, Concordia University, Canada. (Cited on page 100.)

Dormann, S. and Deutsch, A. (2002). Modeling of self-organized avascular tumor growth with a hybrid cellular automaton. *In Silico Biology*, **2**(3), 393–406. (Cited on page 39.)

Dowling, M. R., Milutinović, D., and Hodgkin, P. D. (2005). Modelling cell lifespan and proliferation: is likelihood to die or to divide independent of age? *Journal of The Royal Society Interface*, **2**(5), 517–526. (Cited on page 48.)

Drasdo, D., Kree, R., and McCaskill, J. (1995). Monte carlo approach to tissue-cell populations. *Physical review E*, **52**(6), 6635. (Cited on page 198.)

Elaiw, A. (2012). Global dynamics of an hiv infection model with two classes of target cells and distributed delays. *Discrete Dynamics in Nature and society*, **2012**. (Cited on page 36.)

Elsedawy, N. B. and Russell, S. J. (2013). Oncolytic vaccines. *Expert Review of Vaccines*, **12**(10), 1155–1172. (Cited on page 22.)

Enderling, H. and AJ Chaplain, M. (2014). Mathematical modeling of tumor growth and treatment. *Current pharmaceutical design*, **20**(30), 4934–4940. (Cited on page 2.)

Ermentrout, B. (2002). *Simulating, Analyzing, and Animating Dynamical Systems a Guide to XPPAUT for Researchers and Students*. Society for Industrial and Applied Mathematics (SIAM), Philadelphia, PA, 1st edition. (Cited on page 101.)

Ethier, C. R., Wada, S., Chan, D., and Stamer, W. D. (2004). Experimental and numerical studies of adenovirus delivery to outflow tissues of perfused human anterior segments. *Investigative ophthalmology & visual science*, **45**(6), 1863–1870. (Cited on pages 290 and 292.)

Ferrell, J. E. and Machleder, E. M. (1998). The biochemical basis of an all-or-none cell fate switch in xenopus oocytes. *Science*, **280**(5365), 895–898. (Cited on page 285.)

Ferrell Jr, J. E. and Xiong, W. (2001). Bistability in cell signaling: How to make continuous processes discontinuous, and reversible processes irreversible. *Chaos: An Interdisciplinary Journal of Nonlinear Science*, **11**(1), 227–236. (Cited on page 285.)

Folkman, J. and Hochberg, M. (1973). Self-regulation of growth in three dimensions. *Journal of Experimental Medicine*, **138**(4), 745–753. (Cited on page 10.)

Frank, S. A. (2009). The common patterns of nature. *Journal of evolutionary biology*, **22**(8), 1563–1585. (Cited on page 194.)

Frascoli, F., Hughes, B. D., Zaman, M. H., and Landman, K. A. (2013). A computational model for collective cellular motion in three dimensions: general framework and case study for cell pair dynamics. *PloS one*, **8**(3), e59249. (Cited on pages 39 and 40.)

Frascoli, F., Flood, E., and Kim, P. S. (2016). A model of the effects of cancer cell motility and cellular adhesion properties on tumour-immune dynamics. *Mathematical Medicine and Biology: a journal of the IMA*, **34**(2), 215–240. (Cited on page 38.)

Frieboes, H. B., Lowengrub, J. S., Wise, S., Zheng, X., Macklin, P., Bearer, E. L., and Cristini, V. (2007). Computer simulation of glioma growth and morphology. *Neuroimage*, **37**, S59–S70. (Cited on page 276.)

Friedman, A., Tian, J. P., Fulci, G., Chiocca, E. A., and Wang, J. (2006). Glioma virotherapy: effects of innate immune suppression and increased viral replication capacity. *Cancer Research*, **66**(4), 2314–2319. (Cited on pages 190 and 229.)

Galanis, E., Okuno, S. H., Nascimento, A., Lewis, B., Lee, R., Oliveira, A., Sloan, J. A., Atherton, P., Edmonson, J., Erlichman, C., *et al.* (2005). Phase I-II trial of ONYX-015 in combination with map chemotherapy in patients with advanced sarcomas. *Gene Therapy*, **12**(5), 437. (Cited on pages 19 and 21.)

Galle, J., Loeffler, M., and Drasdo, D. (2005). Modeling the effect of deregulated proliferation and apoptosis on the growth dynamics of epithelial cell populations in vitro. *Biophysical journal*, **88**(1), 62–75. (Cited on page 198.)

Ganesan, L. P., Mohanty, S., Kim, J., Clark, K. R., Robinson, J. M., and Anderson, C. L. (2011). Rapid and efficient clearance of blood-borne virus by liver sinusoidal endothelium. *PLoS Pathogens*, **7**(9), e1002281. (Cited on page 128.)

Ganesh, S., Edick, M. G., Idamakanti, N., Abramova, M., VanRoey, M., Robinson, M., Yun, C.-O., and Jooss, K. (2007). Relaxin-expressing, fiber chimeric oncolytic adenovirus prolongs survival of tumor-bearing mice. *Cancer Research*, **67**(9), 4399–4407. (Cited on page 188.)

Ganly, I., Mautner, V., and Balman, A. (2000). Productive replication of human adenoviruses in mouse epidermal cells. *J. Virol*, **74**, 2895–2899. (Cited on page 151.)

Ghaffarizadeh, A., Friedman, S. H., and Macklin, P. (2015). Biofvm: an efficient, parallelized diffusive transport solver for 3-d biological simulations. *Bioinformatics*, **32**(8), 1256–1258. (Cited on pages 274, 275, and 279.)

Ghaffarizadeh, A., Heiland, R., Friedman, S. H., Mumenthaler, S. M., and Macklin, P. (2018). Physicell: An open source physics-based cell simulator for 3-d multicellular systems. *PLoS Computational Biology*, **14**(2), e1005991. (Cited on pages 39, 200, 243, 245, 274, 275, 276, 277, 278, and 279.)

Gibbons, D. L., Byers, L. A., and Kurie, J. M. (2014). Smoking, p53 mutation, and lung cancer. *Molecular cancer research*, **12**(1), 3–13. (Cited on page 13.)

Gombotz, W. R. and Wee, S. (1998). Protein release from alginate matrices. *Advanced drug delivery reviews*, **31**(3), 267–285. (Cited on page 214.)

Goodbourn, S., Didcock, L., and Randall, R. (2000). Interferons: cell signalling, immune modulation, antiviral response and virus countermeasures. *Journal of General Virology*, **81**(10), 2341–2364. (Cited on page 134.)

Gray, C. W. and Coster, A. C. (2016). The Akt switch model: is location sufficient? *Journal of Theoretical Biology*, **398**, 103–111. (Cited on page 41.)

Guckenheimer, J., Holmes, P., and Slemrod, M. (1984). Nonlinear oscillations dynamical systems, and bifurcations of vector fields. (Cited on pages 44 and 103.)

Haroske, G., Dimmer, V., Steindorf, D., Schilling, U., Theissig, F., and Kunze, K. D. (1996). Cellular sociology of proliferating tumor cells in invasive ductal breast cancer. *Analytical and Quantitative Cytology and Histology*, **18**(3), 191–198. (Cited on pages 38 and 188.)

Hawkins, C. J. (2004). Trail and malignant glioma. In *Vitamins & Hormones*, volume 67, pages 427–452. Elsevier. (Cited on page 244.)

Henson, S., Macaulay, R., Kiani-Alikhan, S., and Akbar, A. (2008). The use of the inhibitory receptors for modulating the immune responses. *Current pharmaceutical design*, **14**(26), 2643–2650. (Cited on page 234.)

Hertzog, P. J. (2012). Overview. Type I interferons as primers, activators and inhibitors of innate and adaptive immune responses. *Immunology and Cell Biology*, **90**(5), 471. (Cited on page 134.)

Herz, A., Bonhoeffer, S., Anderson, R. M., May, R. M., and Nowak, M. A. (1996). Viral dynamics in vivo: limitations on estimates of intracellular delay and virus decay. *Proceedings of the National Academy of Sciences*, **93**(14), 7247–7251. (Cited on page 35.)

Heystek, H. C., M. G. C. O. R. and Kalthoff, F. S. (2000). Granulocyte-macrophage colony-stimulating factor (GM-CSF) has opposing effects on the capacity of monocytes versus monocyte-derived dendritic cells to stimulate the antigen-specific proliferation of a human T cell clone. *Clinical and Experimental immunology*, **120**(3), 440–447. (Cited on page 16.)

Hoeben, R. C. and Uil, T. G. (2013). Adenovirus DNA replication. *Cold Spring Harbor Perspectives in Biology*, **5**(3), a013003. (Cited on page 18.)

Höfling, F. and Franosch, T. (2013). Anomalous transport in the crowded world of biological cells. *Reports on Progress in Physics*, **76**(4), 046602. (Cited on page 191.)

Horman, S. R., To, J., Orth, A. P., Slawny, N., Cuddihy, M., and Caracino, D. (2013). 3d high-content analysis of spheroids: New methodology shown to improve screening. *Genetic Engineering & Biotechnology News*, **33**(16), 18–19. (Cited on pages x and 11.)

Huang, J.-H., Zhang, S.-N., Choi, K.-J., Choi, I.-K., Kim, J.-H., Lee, M., Kim, H., and Yun, C.-O. (2010). Therapeutic and tumor-specific immunity induced by combination of dendritic cells and oncolytic adenovirus expressing IL-12 and 4-1BBL. *Molecular Therapy*, **18**(2), 264–274. (Cited on page 22.)

Hurwitz, A. (1895). Ueber die Bedingungen, unter welchen eine Gleichung nur Wurzeln mit negativen reellen Theilen besitzt. *Mathematische Annalen*, **46**(2), 273–284. (Cited on page 44.)

Inda, M.-d.-M., Bonavia, R., Seoane, J., *et al.* (2014). Glioblastoma multiforme: a look inside its heterogeneous nature. *Cancers*, **6**(1), 226–239. (Cited on page 246.)

Jain, R. K. (1988). Determinants of tumor blood flow: a review. *Cancer Research*, **48**(10), 2641–2658. (Cited on page 20.)

Jain, R. K. (1997). Delivery of molecular and cellular medicine to solid tumors. *Advanced drug delivery reviews*, **26**(2-3), 71–90. (Cited on page 20.)

Janeway, Jr., C. A., Travers, P., Walport, M., and Shlomchik, M. J. (2005). *Immunobiology : the immune system in health and disease*. Garland Science Publishing, New York, NY, 6th edition. (Cited on pages 8, 14, 15, 16, and 184.)

Janicki, A. and Weron, A. (1993). *Simulation and chaotic behavior of alpha-stable stochastic processes*, volume 178. CRC Press. (Cited on pages 194 and 195.)

Jenner, A., Coster, A. C., and Kim, P. (2016). Mathematical modelling of oncolytic virotherapy: The effects of a PEG-modified adenovirus conjugated with herceptin. *The Australian Mathematical Society*, **43**(5), 297–299. (Cited on pages xvii, xviii, 115, 136, and 140.)

Jenner, A., Yun, C.-O., Yoon, A., Kim, P. S., and Coster, A. C. (2018a). Modelling heterogeneity in viral-tumour dynamics: The effects of gene-attenuation on viral characteristics. *Journal of theoretical biology*, **454**, 41–52. (Cited on pages x, xi, xii, xviii, xix, 47, 50, 52, 54, 56, 57, 60, 62, 63, 64, 146, 150, 154, 155, 157, and 159.)

Jenner, A. L., Yun, C.-O., Kim, P. S., and Coster, A. C. (2018b). Mathematical modelling of the interaction between cancer cells and an oncolytic virus: insights into the effects of treatment protocols. *Bulletin of mathematical biology*, **80**(6), 1615–1629. (Cited on pages xvi, xvii, 115, 119, 122, 124, 126, and 127.)

Jenner, A. L., Coster, A. C., Kim, P. S., and Frascoli, F. (2018c). Treating cancerous cells with viruses: insights from a minimal model for oncolytic virotherapy. *Letters in Biomathematics*, **5**(sup1), S117–S136. (Cited on pages xii, xiii, xiv, 72, 75, 78, 80, 81, 82, 83, 84, 85, 86, and 87.)

Jenner, A. L., Kim, P. S., and Frascoli, F. (2019). Oncolytic virotherapy for tumours following a Gompertz growth law. *Journal of theoretical biology*, **480**, 129–140. (Cited on pages xiv, xv, xvi, 72, 89, 94, 98, 99, 102, 104, 106, and 108.)

Jeong, M., Kwon, Y.-S., Park, S.-H., Kim, C.-Y., Jeun, S.-S., Song, K.-W., Ko, Y., Robbins, P. D., Billiar, T. R., Kim, B.-M., *et al.* (2009). Possible novel therapy for malignant gliomas with secretable trimeric trail. *PloS one*, **4**(2), e4545. (Cited on pages 244, 259, and 290.)

Jiao, Y. and Torquato, S. (2011). Emergent behaviors from a cellular automaton model for invasive tumor growth in heterogeneous microenvironments. *PLoS Computational Biology*, **7**(12), e1002314. (Cited on pages x, 10, 11, 38, 199, and 205.)

Juweid, M., Neumann, R., Paik, C., Perez-Bacete, M. J., Sato, J., van Osdol, W., and Weinstein, J. N. (1992). Micropharmacology of monoclonal antibodies in solid tumors: direct experimental evidence for a binding site barrier. *Cancer Research*, **52**(19), 5144–5153. (Cited on page 20.)

Kaiser, C. A., Krieger, M., Lodish, H., and Berk, A. (2007). *Molecular cell biology.* WH Freeman. (Cited on pages 7 and 8.)

Kansal, A., Torquato, S., Harsh Iv, G., Chiocca, E., and Deisboeck, T. (2000a). Cellular automaton of idealized brain tumor growth dynamics. *Biosystems*, **55**(1), 119–127. (Cited on page 38.)

Kansal, A. R., Torquato, S., Harsh, G., Chiocca, E., and Deisboeck, T. (2000b). Simulated brain tumor growth dynamics using a three-dimensional cellular automaton. *Journal of Theoretical Biology*, **203**(4), 367–382. (Cited on page 199.)

Karev, G. P., Novozhilov, A. S., and Koonin, E. V. (2006). Mathematical modeling of tumor therapy with oncolytic viruses: effects of parametric heterogeneity on cell dynamics. *Biology Direct*, **1**(1), 30. (Cited on pages 32 and 50.)

Kihara, T., Ito, J., and Miyake, J. (2013). Measurement of biomolecular diffusion in extracellular matrix condensed by fibroblasts using fluorescence correlation spectroscopy. *PLoS One*, **8**(11), e82382. (Cited on pages 290 and 292.)

Kim, C., Jeong, M., Mushiake, H., Kim, B., Kim, W., Ko, J., Kim, M., Kim, M., Kim, T., Robbins, P., *et al.* (2006a). Cancer gene therapy using a novel secretable trimeric TRAIL. *Gene therapy*, **13**(4), 330. (Cited on pages 11, 13, 17, 244, 245, 246, 249, and 259.)

Kim, J., Cho, J. Y., Kim, J.-H., Jung, K. C., and Yun, C.-O. (2002). Evaluation of E1B gene-attenuated replicating adenoviruses for cancer gene therapy. *Cancer Gene Therapy*, **9**(9), 725. (Cited on pages x, xi, xxvii, 19, 20, 48, 49, 50, 58, 59, 60, 65, and 68.)

Kim, J., Kim, J.-H., Choi, K.-J., Kim, P.-H., and Yun, C.-O. (2007). E1A-and e1B-double mutant replicating adenovirus elicits enhanced oncolytic and antitumor effects. *Human Gene Therapy*, **18**(9), 773–786. (Cited on page 22.)

Kim, J.-H., Lee, Y.-S., Kim, H., Huang, J.-H., Yoon, A.-R., and Yun, C.-O. (2006b). Relaxin expression from tumor-targeting adenoviruses and its intratumoral spread, apoptosis induction, and efficacy. *Journal of the National Cancer Institute*, **98**(20), 1482–1493. (Cited on pages 189, 190, 229, and 242.)

Kim, P.-H., Sohn, J.-H., Choi, J.-W., Jung, Y., Kim, S. W., Haam, S., and Yun, C.-O. (2011a). Active targeting and safety profile of PEG-modified adenovirus conjugated with herceptin. *Biomaterials*, **32**(9), 2314–2326. (Cited on pages xvii, 12, 13, 22, 109, 115, 116, 117, 118, 128, 129, 130, 131, 133, 135, 140, 141, and 292.)

Kim, P.-H., Sohn, J.-H., Choi, J.-W., Jung, Y., Kim, S. W., Haam, S., and Yun, C.-O. (2011b). Active targeting and safety profile of PEG-modified adenovirus conjugated with herceptin. *Biomaterials*, **32**(9), 2314–2326. (Cited on pages xxii, 188, 202, and 203.)

Kim, P. S. and Lee, P. P. (2012). Modeling protective anti-tumor immunity via preventative cancer vaccines using a hybrid agent-based and delay differential equation approach. *PLoS computational biology*, **8**(10), e1002742. (Cited on pages 39 and 40.)

Kim, P. S., Lee, P. P., and Levy, D. (2011c). A Theory of Immunodominance and Adaptive Regulation. *Bulletin of Mathematical Biology*, **73**, 1645–1665. (Cited on page 151.)

Kim, P. S., Crivelli, J. J., Choi, I.-K., Yun, C.-O., and Wares, J. R. (2015). Quantitative impact of immunomodulation versus oncolysis with cytokine-expressing virus therapeutics. *Math Biosci Eng*, **12**, 841–58. (Cited on pages 34, 35, 41, 45, 88, 149, and 184.)

Kim, Y., Stolarska, M. A., and Othmer, H. G. (2011d). The role of the microenvironment in tumor growth and invasion. *Progress in Biophysics and Molecular Biology*, **106**(2), 353–379. (Cited on page 10.)

Kiss, R., Camby, I., Salmon, I., Van Ham, P., Brotchi, J., and Pasteels, J.-L. (1995). Relationship between dna ploidy level and tumor sociology behavior in 12 nervous cell lines. *Cytometry Part A*, **20**(2), 118–126. (Cited on page 38.)

Knolle, P. A. and Wohlleber, D. (2016). Immunological functions of liver sinusoidal endothelial cells. *Cellular & Molecular Immunology*, **13**(3), 347. (Cited on page 128.)

Komarova, N. L. and Wodarz, D. (2010). ODE models for oncolytic virus dynamics. *Journal of Theoretical Biology*, **263**(4), 530–543. (Cited on pages 2, 31, 77, and 112.)

Kottke, T., Hall, G., Pulido, J., Diaz, R. M., Thompson, J., Chong, H., Selby, P., Coffey, M., Pandha, H., Chester, J., *et al.* (2010). Antiangiogenic cancer therapy combined with oncolytic virotherapy leads to regression of established tumors in mice. *The Journal of clinical investigation*, **120**(5), 1551–1560. (Cited on page 188.)

Kronik, N., Kogan, Y., Vainstein, V., and Agur, Z. (2008). Improving alloreactive CTL immunotherapy for malignant gliomas using a simulation model of their interactive dynamics. *Cancer Immunology, Immunotherapy*, **57**(3), 425–439. (Cited on page 41.)

Kumberger, P., Frey, F., Schwarz, U. S., and Graw, F. (2016). Multiscale modeling of virus replication and spread. *FEBS letters*. (Cited on pages 16 and 17.)

Kuznetsov, Y. A. (2013). *Elements of applied bifurcation theory*, volume 112. Springer Science & Business Media. (Cited on pages 44 and 103.)

Kwok, K., Groves, M., and Burgess, D. (1989). Sterile microencapsulation of bcg in alginate-poly-l-lysine by an air spraying technique. In *Proc Int Symp Control Release Bioact Mater*, volume 16, pages 170–171. (Cited on page 213.)

Laird, A. K. (1964). Dynamics of tumour growth. *British Journal of Cancer*, **18**(3), 490. (Cited on pages 28 and 29.)

Lawler, S. E., Speranza, M.-C., Cho, C.-F., and Chiocca, E. A. (2017). Oncolytic viruses in cancer treatment: a review. *JAMA Oncology*, **3**(6), 841–849. (Cited on page 16.)

Leach, D. R., Krummel, M. F., Allison, J. P., *et al.* (1996). Enhancement of antitumor immunity by ctla-4 blockade. *Science*, **271**(5256), 1734–1736. (Cited on page 234.)

Lee, H., Kim, J., Lee, B., Chang, J. W., Ahn, J., Park, J. O., Choi, J., Yun, C.-O., Kim, B. S., and Kim, J.-H. (2000). Oncolytic potential of E1B 55 kda-deleted YKL-1 recombinant adenovirus: Correlation with p53 functional status. *International Journal of Cancer*, **88**(3), 454–463. (Cited on pages 19 and 49.)

Lee, Y. C., Fullerton, G. D., and Goins, B. A. (2015). Comparison of multimodality image-based volumes in preclinical tumor models using in-air micro-ct image volume as reference tumor volume. *Open Journal of Medical Imaging*, **5**(03), 117. (Cited on page 24.)

Levy, D. E., GarcıÌĄ, A., *et al.* (2001). The virus battles: IFN induction of the antiviral state and mechanisms of viral evasion. *Cytokine & Growth Factor Reviews*, **12**(2), 143–156. (Cited on page 134.)

Li, H., Li, S., Shao, J., Lin, X., Cao, Y., Jiang, W., Liu, R., Zhao, P., Zhu, X., Zeng, M., *et al.* (2008). Pharmacokinetic and pharmacodynamic study of intratumoral injection of an adenovirus encoding endostatin in patients with advanced tumors. *Gene therapy*, **15**(4), 247. (Cited on page 151.)

Li, M. Y. and Shu, H. (2010). Impact of intracellular delays and target-cell dynamics on in vivo viral infections. *SIAM Journal on Applied Mathematics*, **70**(7), 2434–2448. (Cited on page 36.)

Li, M. Y. and Shuai, Z. (2010). Global-stability problem for coupled systems of differential equations on networks. *Journal of Differential Equations*, **248**(1), 1–20. (Cited on page 30.)

Liechtenstein, T., Dufait, I., Lanna, A., Breckpot, K., and Escors, D. (2012). Modulating co-stimulation during antigen presentation to enhance cancer immunotherapy. *Immunology, Endocrine & Metabolic Agents in Medicinal Chemistry (Formerly Current Medicinal Chemistry-Immunology, Endocrine and Metabolic Agents)*, **12**(3), 224–235. (Cited on page 234.)

Lim, S. M., Kim, T. H., Jiang, H. H., Park, C. W., Lee, S., Chen, X., and Lee, K. C. (2011). Improved biological half-life and anti-tumor activity of tnf-related apoptosis-inducing ligand (trail) using peg-exposed nanoparticles. *Biomaterials*, **32**(13), 3538–3546. (Cited on pages 290 and 292.)

Little, M. P., Heidenreich, W. F., and Li, G. (2010). Parameter identifiability and redundancy: theoretical considerations. *PloS one*, **5**(1), e8915. (Cited on page 67.)

Liu, H., Naismith, J., and Hay, R. (2003). Adenovirus DNA replication. In *Adenoviruses: Model and Vectors in Virus-Host Interactions*, pages 131–164. Springer. (Cited on page 18.)

Liu, T.-C., Galanis, E., and Kirn, D. (2007). Clinical trial results with oncolytic virotherapy: a century of promise, a decade of progress. *Nature Reviews. Clinical Oncology*, **4**(2), 101. (Cited on page 188.)

Lobo, E. P. (2014). *Modelling the Role of Interclonal Cooperativity During Early Carcinogenesis*. Ph.D. thesis, University of Sydney. (Cited on pages 38 and 192.)

Lun, X., Yang, W., Alain, T., Shi, Z.-Q., Muzik, H., Barrett, J. W., McFadden, G., Bell, J., Hamilton, M. G., Senger, D. L., *et al.* (2005). Myxoma virus is a novel oncolytic virus with significant antitumor activity against experimental human gliomas. *Cancer Research*, **65**(21), 9982–9990. (Cited on page 22.)

Macatonia, S. E., Hosken, N. A., Litton, M., Vieira, P., Hsieh, C.-S., Culpepper, J. A., Wysocka, M., Trinchieri, G., Murphy, K. M., and O'Garra, A. (1995). Dendritic cells produce il-12 and direct the development of th1 cells from naive cd4+ t cells. *The Journal of Immunology*, **154**(10), 5071–5079. (Cited on page 234.)

Macklin, P., McDougall, S., Anderson, A. R., Chaplain, M. A., Cristini, V., and Lowengrub, J. (2009). Multiscale modelling and nonlinear simulation of vascular tumour growth. *Journal of mathematical biology*, **58**(4-5), 765–798. (Cited on page 276.)

Macklin, P., Edgerton, M. E., Thompson, A. M., and Cristini, V. (2012). Patient-calibrated agent-based modelling of ductal carcinoma in situ (dcis): from microscopic measurements to macroscopic predictions of clinical progression. *Journal of Theoretical Biology*, **301**, 122–140. (Cited on pages 198, 276, 277, and 278.)

Mallet, D. G. and De Pillis, L. G. (2006). A cellular automata model of tumor–immune system interactions. *Journal of Theoretical Biology*, **239**(3), 334–350. (Cited on pages 2 and 39.)

Martuza, R. L., Malick, A., Markert, J. M., Ruffner, K. L., and Coen, D. M. (1991). Experimental therapy of human glioma by means of a genetically engineered virus mutant. *Science*, pages 854–856. (Cited on page 22.)

McKerrow, J. and Salter, J. (2002). Invasion of skin by schistosoma cercariae. *Trends in Parasitology*, **18**(5), 193–195. (Cited on page 20.)

Meineke, F. A., Potten, C. S., and Loeffler, M. (2001). Cell migration and organization in the intestinal crypt using a lattice-free model. *Cell proliferation*, **34**(4), 253–266. (Cited on pages xxviii, 39, 40, 197, 198, and 203.)

Melcher, A., Parato, K., Rooney, C. M., and Bell, J. C. (2011). Thunder and lightning: immunotherapy and oncolytic viruses collide. *Molecular Therapy*, **19**(6), 1008–1016. (Cited on page 22.)

Metzcar, J., Wang, Y., Heiland, R., and Macklin, P. (2019). A review of cell-based computational modeling in cancer biology. *JCO clinical cancer informatics*, **2**, 1–13. (Cited on pages 37, 39, and 189.)

Mittler, J. E., Sulzer, B., Neumann, A. U., and Perelson, A. S. (1998). Influence of delayed viral production on viral dynamics in hiv-1 infected patients. *Mathematical Biosciences*, **152**(2), 143–163. (Cited on pages 36 and 57.)

Miyashita, S., Ishibashi, K., Kishino, H., and Ishikawa, M. (2015). Viruses roll the dice: the stochastic behavior of viral genome molecules accelerates viral adaptation at the cell and tissue levels. *PLoS Biology*, **13**(3), e1002094. (Cited on pages 28, 35, 36, and 227.)

Mok, H., Palmer, D. J., Ng, P., and Barry, M. A. (2005). Evaluation of polyethylene glycol modification of first-generation and helper-dependent adenoviral vectors to reduce innate immune responses. *Molecular Therapy*, **11**(1), 66–79. (Cited on page 116.)

Mok, W., Stylianopoulos, T., Boucher, Y., and Jain, R. K. (2009). Mathematical modeling of herpes simplex virus distribution in solid tumors: implications for cancer gene therapy. *Clinical Cancer Research*, **15**(7), 2352–2360. (Cited on pages 190, 204, and 229.)

Moreira, J. and Deutsch, A. (2002). Cellular automaton models of tumor development: a critical review. *Advances in Complex Systems*, **5**(02n03), 247–267. (Cited on page 38.)

Mumenthaler, S., D'Antonio, G., Preziosi, L., and Macklin, P. (2013). The need for integrative computational oncology: an illustrated example through mmp-mediated tissue degradation. *Frontiers in oncology*, **3**, 194. (Cited on page 200.)

Murphy, J. M., Sexton, D. M., Barnett, D. N., Jones, G. S., Webb, M. J., Collins, M., and Stainforth, D. A. (2004). Quantification of modelling uncertainties in a large ensemble of climate change simulations. *Nature*, **430**(7001), 768. (Cited on page 45.)

Murray, P. J., Edwards, C. M., Tindall, M. J., and Maini, P. K. (2009). From a discrete to a continuum model of cell dynamics in one dimension. *Physical Review E*, **80**(3), 031912. (Cited on page 197.)

Muruve, D. A., Barnes, M. J., Stillman, I. E., and Libermann, T. A. (1999). Adenoviral gene therapy leads to rapid induction of multiple chemokines and acute neutrophil-dependent hepatic injury in vivo. *Human gene therapy*, **10**(6), 965–976. (Cited on page 214.)

Myers, R., Greiner, S., Harvey, M., Griesmann, G., Kuffel, M., Buhrow, S., Reid, J. M., Federspiel, M., Ames, M., Dingli, D., *et al.* (2007). Preclinical pharmacology and toxicology of intravenous MV-NIS, an oncolytic measles virus administered with or without cyclophosphamide. *Clinical Pharmacology & Therapeutics*, **82**(6), 700–710. (Cited on page 16.)

Nakata, Y. (2011). Global dynamics of a cell mediated immunity in viral infection models with distributed delays. *Journal of Mathematical Analysis and Applications*, **375**(1), 14–27. (Cited on page 36.)

Nelson, P. W. and Perelson, A. S. (2002). Mathematical analysis of delay differential equation models of hiv-1 infection. *Mathematical Biosciences*, **179**(1), 73–94. (Cited on pages 35 and 57.)

Nelson, P. W., Murray, J. D., and Perelson, A. S. (2000). A model of hiv-1 pathogenesis that includes an intracellular delay. *Mathematical Biosciences*, **163**(2), 201–215. (Cited on page 35.)

Nemunaitis, J., Cunningham, C., Buchanan, A., Blackburn, A., Edelman, G., Maples, P. a., Netto, G., Tong, A., Randlev, B., Olson, S., *et al.* (2001). Intravenous infusion of a replication-selective adenovirus (ONYX-015) in cancer patients: safety, feasibility and biological activity. *Gene Therapy*, **8**(10), 746. (Cited on pages 19 and 21.)

Nemunaitis, J., Senzer, N., Sarmiento, S., Zhang, Y., Arzaga, R., Sands, B., Maples, P., and Tong, A. (2007). A phase I trial of intravenous infusion of ONYX-015 and enbrel in solid tumor patients. *Cancer Gene Therapy*, **14**(11), 885. (Cited on pages 19 and 21.)

Neusius, T., Sokolov, I. M., and Smith, J. C. (2009). Subdiffusion in time-averaged, confined random walks. *Physical Review E*, **80**(1), 011109. (Cited on page 195.)

Novozhilov, A. S., Berezovskaya, F. S., Koonin, E. V., and Karev, G. P. (2006). Mathematical modeling of tumor therapy with oncolytic viruses: regimes with complete tumor elimination within the framework of deterministic models. *Biology Direct*, **1**(1), 6. (Cited on pages 32, 74, and 110.)

O'Connor, C. M., Adams, J. U., and Fairman, J. (2010). Essentials of cell biology. *Cambridge: NPG Education*. (Cited on page 9.)

Oh, E., Oh, J.-E., Hong, J., Chung, Y., Lee, Y., Park, K. D., Kim, S., and Yun, C.-O. (2017). Optimized biodegradable polymeric reservoir-mediated local and sustained co-delivery of dendritic cells and oncolytic adenovirus co-expressing IL-12 and GM-CSF for cancer immunotherapy. *Journal of Controlled Release*, **259**, 115–127. (Cited on pages xxviii, 2, 21, 147, 148, 160, 162, 166, 167, 168, 170, 171, 172, 173, 175, 179, 180, 182, and 183.)

Oh, E., Hong, J., Kwon, O.-J., and Yun, C.-O. (2018). A hypoxia-and telomerase-responsive oncolytic adenovirus expressing secretable trimeric trail triggers tumour-specific apoptosis and promotes viral dispersion in trail-resistant glioblastoma. *Scientific Reports*, **8**(1), 1420. (Cited on pages xxvi, 244, 245, 249, 257, 259, 289, 290, and 292.)

Osborne, J. M., Fletcher, A. G., Pitt-Francis, J. M., Maini, P. K., and Gavaghan, D. J. (2017). Comparing individual-based approaches to modelling the self-organization of multicellular tissues. *PLoS Computational Biology*, **13**(2), e1005387. (Cited on page 197.)

Paiva, L., Martins, M., and Ferreira, S. (2011). Questing for an optimal, universal viral agent for oncolytic virotherapy. *Physical Review E*, **84**(4), 041918. (Cited on pages 190 and 229.)

Paiva, L. R., Binny, C., Ferreira, S. C., and Martins, M. L. (2009). A multiscale mathematical model for oncolytic virotherapy. *Cancer Research*, **69**(3), 1205–1211. (Cited on pages 38 and 39.)

Parato, K. A., Senger, D., Forsyth, P. A., and Bell, J. C. (2005). Recent progress in the battle between oncolytic viruses and tumours. *Nature reviews. Cancer*, **5**(12), 965. (Cited on page 188.)

Park, C. C., Bissell, M. J., and Barcellos-Hoff, M. H. (2000). The influence of the microenvironment on the malignant phenotype. *Molecular medicine today*, **6**(8), 324–329. (Cited on page 206.)

Park, K. I. and Park (2018). *Fundamentals of Probability and Stochastic Processes with Applications to Communications*. Springer. (Cited on pages 261 and 262.)

Parry, R. V., Chemnitz, J. M., Frauwirth, K. A., Lanfranco, A. R., Braunstein, I., Kobayashi, S. V., Linsley, P. S., Thompson, C. B., and Riley, J. L. (2005). Ctla-4 and pd-1 receptors inhibit t-cell activation by distinct mechanisms. *Molecular and cellular biology*, **25**(21), 9543–9553. (Cited on page 234.)

Pawelek, K. A., Liu, S., Pahlevani, F., and Rong, L. (2012). A model of hiv-1 infection with two time delays: mathematical analysis and comparison with patient data. *Mathematical Biosciences*, **235**(1), 98–109. (Cited on page 35.)

Perelson, A. S. and Nelson, P. W. (1999). Mathematical analysis of HIV-1 dynamics in vivo. *SIAM review*, **41**(1), 3–44. (Cited on page 30.)

Phan, D. and Wodarz, D. (2015). Modeling multiple infection of cells by viruses: Challenges and insights. *Mathematical Biosciences*, **264**, 21–28. (Cited on page 189.)

Potmesil, M. and Goldfeder, A. (1980). Cell kinetics of irradiated experimental tumors: Cell transition from the non-proliferating to the proliferating pool. *Cell Proliferation*, **13**(5), 563–570. (Cited on page 10.)

Powathil, G. G., Adamson, D. J., and Chaplain, M. A. (2013). Towards predicting the response of a solid tumour to chemotherapy and radiotherapy treatments: clinical insights from a computational model. *PLoS Computational Biology*, **9**(7), e1003120. (Cited on pages 2 and 39.)

Prestwich, R. J., Harrington, K. J., Pandha, H. S., Vile, R. G., Melcher, A. A., and Errington, F. (2008). Oncolytic viruses: a novel form of immunotherapy. *Expert Review of Anticancer Therapy*, **8**(10), 1581–1588. (Cited on page 21.)

Puig-Kröger, A., Relloso, M., Fernández-Capetillo, O., Zubiaga, A., Silva, A., Bernabéu, C., and CorbìÀ, A. L. (2001). Extracellular signal–regulated protein kinase signaling pathway negatively regulates the phenotypic and functional maturation of monocyte-derived human dendritic cells. *Blood*, **98**(7), 2175–2182. (Cited on page 234.)

Rao, L., Debbas, M., Sabbatini, P., Hockenbery, D., Korsmeyer, S., and White, E. (1992). The adenovirus E1A proteins induce apoptosis, which is inhibited by the E1B19-kDa and Bcl-2 proteins. *Proceedings of the National Academy of Sciences*, **89**(16), 7742–7746. (Cited on pages 19, 20, and 49.)

Routh, E. J. (1877). *A treatise on the stability of a given state of motion: particularly steady motion*. Macmillan and Company. (Cited on page 44.)

Russell, S. J. and Peng, K.-W. (2007). Viruses as anticancer drugs. *Trends in Pharmacological Sciences*, **28**(7), 326–333. (Cited on page 16.)

Russell, S. J., Peng, K.-W., and Bell, J. C. (2012). Oncolytic virotherapy. *Nature biotechnology*, **30**(7), 658–670. (Cited on pages 2, 21, and 189.)

Ruzek, M. C., Kavanagh, B. F., Scaria, A., Richards, S. M., and Garman, R. D. (2002). Adenoviral vectors stimulate murine natural killer cell responses and demonstrate antitumor activities in the absence of transgene expression. *Molecular Therapy*, **5**(2), 115–124. (Cited on page 214.)

Saltelli, A., Ratto, M., Andres, T., Campolongo, F., Cariboni, J., Gatelli, D., Saisana, M., and Tarantola, S. (2008). *Global sensitivity analysis: the primer*. John Wiley & Sons. (Cited on page 45.)

Schaller, G. and Meyer-Hermann, M. (2005). Multicellular tumor spheroid in an off-lattice voronoi-delaunay cell model. *Physical Review E*, **71**(5), 051910. (Cited on page 38.)

Sharma, S., Khuller, G., and Garg, S. (2003). Alginate-based oral drug delivery system for tuberculosis: pharmacokinetics and therapeutic effects. *Journal of antimicrobial chemotherapy*, **51**(4), 931–938. (Cited on page 213.)

Sherar, M., Noss, M., and Foster, F. (1987). Ultrasound backscatter microscopy images the internal structure of living tumour spheroids. *Nature*, **330**(6147), 493–495. (Cited on page 10.)

Shinners, S. M. (1998). *Modern control system theory and design*. John Wiley & Sons. (Cited on page 44.)

Shiroki, K. and Toth, M. (1988). Activation of the human beta interferon gene by the adenovirus type 12 E1B gene. *Journal of Virology*, **62**(1), 325–330. (Cited on page 134.)

Shu, H., Wang, L., and Watmough, J. (2013). Global stability of a nonlinear viral infection model with infinitely distributed intracellular delays and ctl immune responses. *SIAM Journal on Applied Mathematics*, **73**(3), 1280–1302. (Cited on page 36.)

Slamon, D. J., Clark, G. M., Wong, S. G., Levin, W. J., Ullrich, A., and McGuire, W. L. (1987). Human breast cancer: correlation of relapse and survival with amplification of the HER-2/neu oncogene. *Science*, **235**(4785), 177–182. (Cited on page 12.)

Sompayrac, L. (2008). *How The Immune System Works*. Blackwell Pub, Malden, MA. (Cited on pages 14 and 15.)

Stosich, M. S. and Mao, J. J. (2005). Stem cell-based soft tissue grafts for plastic and reconstructive surgeries. In *Seminars in plastic surgery*, volume 19, pages 251–260. Copyright© 2005 by Thieme Medical Publishers, Inc., 333 Seventh Avenue, New âĂę. (Cited on page 194.)

Syverton, J. T. and Berry, G. P. (1947). Multiple virus infection of single host cells. *Journal of Experimental Medicine*, **86**(2), 145–152. (Cited on page 189.)

Thorne, S. H., Tam, B. Y., Kirn, D. H., Contag, C. H., and Kuo, C. J. (2006). Selective intratumoral amplification of an antiangiogenic vector by an oncolytic virus produces enhanced antivascular and anti-tumor efficacy. *Molecular Therapy*, **13**(5), 938–946. (Cited on page 22.)

Timm, A. and Yin, J. (2012). Kinetics of virus production from single cells. *Virology*, **424**(1), 11–17. (Cited on page 51.)

Titze, M. I., Frank, J., Ehrhardt, M., Smola, S., Graf, N., and Lehr, T. (2017). A generic viral dynamic model to systematically characterize the interaction between oncolytic virus kinetics and tumor growth. *European Journal of Pharmaceutical Sciences*, **97**, 38–46. (Cited on pages 2, 31, 32, 73, 74, 77, and 113.)

Tokarev, A. A., Alfonso, A., and Segev, N. (2009). Overview of intracellular compartments and trafficking pathways. In *Trafficking Inside Cells*, pages 3–14. Springer. (Cited on page 51.)

Urbańska, K., Sokołowska, J., Szmidt, M., and Sysa, P. (2014). Glioblastoma multiforme–an overview. *Contemporary oncology*, **18**(5), 307. (Cited on page 244.)

Van Liedekerke, P., Palm, M., Jagiella, N., and Drasdo, D. (2015). Simulating tissue mechanics with agent-based models: concepts, perspectives and some novel results. *Computational particle mechanics*, **2**(4), 401–444. (Cited on pages 39 and 189.)

van Stipdonk, M. J., Lemmens, E. E., and Schoenberger, S. P. (2001). Naive CTLs require a single brief period of antigenic stimulation for clonal expansion and differentiation. *Nature Immunology*, **2**(5), 423–429. (Cited on page 137.)

Vasey, P., Shulman, L., Campos, S., Davis, J., Gore, M., Johnston, S., Kirn, D., OâĂŹneill, V., Siddiqui, N., Seiden, M., *et al.* (2002). Phase I trial of intraperitoneal injection of the E1B-55-kd-gene–deleted adenovirus ONYX-015 (dl1520) given on days 1 through 5 every 3 weeks in patients with recurrent/refractory epithelial ovarian cancer. *Journal of Clinical Oncology*, **20**(6), 1562–1569. (Cited on pages 19 and 21.)

Veiga-Fernandes, H., Walter, U., Bourgeois, C., McLean, A., and Rocha, B. (2000). Response of naive and memory CD8+ T cells to antigen stimulation in vivo. *Nature Immunology*, **1**(1), 47–53. (Cited on page 137.)

Velcheti, V. and Schalper, K. (2016). Basic overview of current immunotherapy approaches in cancer. *American Society of Clinical Oncology Educational Book*, **36**, 298–308. (Cited on page 22.)

Wagner, E. K., Hewlett, M. J., Bloom, D. C., and Camerini, D. (1999). *Basic Virology*. Blackwell Science Malden, MA. (Cited on pages 17 and 18.)

Wang, Y. and Yuan, F. (2006). Delivery of viral vectors to tumor cells: extracellular transport, systemic distribution, and strategies for improvement. *Annals of biomedical engineering*, **34**(1), 114–127. (Cited on pages 20 and 206.)

Wang, Y., Wang, H., Li, C.-Y., and Yuan, F. (2006). Effects of rate, volume, and dose of intratumoral infusion on virus dissemination in local gene delivery. *Molecular cancer therapeutics*, **5**(2), 362–366. (Cited on page 151.)

Wang, Y., Zhou, Y., Wu, J., and Heffernan, J. (2009). Oscillatory viral dynamics in a delayed hiv pathogenesis model. *Mathematical Biosciences*, **219**(2), 104–112. (Cited on page 35.)

Wares, J. R., Crivelli, J. J., Yun, C.-O., Choi, I.-K., Gevertz, J. L., and Kim, P. S. (2015). Treatment strategies for combining immunostimulatory oncolytic virus therapeutics

with dendritic cell injections. *Mathematical Biosciences and Engineering: MBE*, **12**(6), 1237–1256. (Cited on pages 2, 34, 35, 45, 118, and 184.)

Wee, S., Gombotz, W., and Fanslow, W. (1995). Evaluation of alginate microbeads for intranasal delivery of ovalbumin. In *Proc. Int. Symp. Control. Rel. Bioact. Mater., Control. Rel. Soc*, volume 22, pages 566–567. (Cited on page 213.)

Wein, L. M., Wu, J. T., and Kirn, D. H. (2003). Validation and analysis of a mathematical model of a replication-competent oncolytic virus for cancer treatment: implications for virus design and delivery. *Cancer research*, **63**(6), 1317–1324. (Cited on page 190.)

Weiswald, L.-B., Bellet, D., and Dangles-Marie, V. (2015). Spherical cancer models in tumor biology. *Neoplasia*, **17**(1), 1–15. (Cited on pages 10 and 205.)

Wilkie, K. P. (2013). A review of mathematical models of cancer-immune interactions in the context of tumor dormancy. *Advances in Experimental Medicine and Biology*, **734**, 201–234. (Cited on page 113.)

Wodarz, D. (2001). Viruses as antitumor weapons. *Cancer Research*, **61**(8), 3501–3507. (Cited on page 73.)

Wodarz, D. (2003). Gene therapy for killing p53-negative cancer cells: use of replicating versus nonreplicating agents. *Human Gene Therapy*, **14**(2), 153–159. (Cited on page 31.)

Wodarz, D. (2016). Computational modeling approaches to the dynamics of oncolytic viruses. *Wiley Interdisciplinary Reviews: Systems Biology and Medicine*, **8**(3), 242–252. (Cited on pages 111 and 112.)

Wodarz, D., Hofacre, A., Lau, J. W., Sun, Z., Fan, H., and Komarova, N. L. (2012). Complex spatial dynamics of oncolytic viruses in vitro: mathematical and experimental approaches. *PLoS Computational Biology*, **8**(6), e1002547. (Cited on pages 38, 134, and 190.)

Wu, N. Z., Da, D., Rudoll, T. L., Needham, D., Whorton, A. R., and Dewhirst, M. W. (1993). Increased microvascular permeability contributes to preferential accumulation of stealth liposomes in tumor tissue. *Cancer Research*, **53**(16), 3765–3770. (Cited on page 20.)

Xu, R., Yuan, Z., Guan, Z., Cao, Y., Wang, H., Hu, X., Feng, J., Zhang, Y., Li, F., Chen, Z., *et al.* (2003). Phase II clinical study of intratumoral H101, an E1B deleted adenovirus, in combination with chemotherapy in patients with cancer. *Chinese Journal of Cancer*, **22**(12), 1307–1310. (Cited on pages 19 and 21.)

Yakimovich, A., Gumpert, H., Burckhardt, C. J., Lütschg, V. A., Jurgeit, A., Sbalzarini, I. F., and Greber, U. F. (2012). Cell-free transmission of human adenovirus by passive mass transfer in cell culture simulated in a computer model. *Journal of virology*, **86**(18), 10123–10137. (Cited on pages 289 and 292.)

Yuan, F., Leunig, M., Huang, S. K., Berk, D. A., Papahadjopoulos, D., and Jain, R. K. (1994). Mirovascular permeability and interstitial penetration of sterically stabilized (stealth) liposomes in a human tumor xenograft. *Cancer Research*, **54**(13), 3352–3356. (Cited on page 20.)

Yuan, Z. and Zou, X. (2013). Global threshold dynamics in an hiv virus model with nonlinear infection rate and distributed invasion and production delays. *Mathematical Biosciences and Engineering*, **10**(2), 483–498. (Cited on page 36.)

Zhang, X., De Milito, A., Demiroglu-Zergeroglu, A., Gullbo, J., DâĂŹArcy, P., and Linder, S. (2016). Eradicating quiescent tumor cells by targeting mitochondrial bioenergetics. *Trends in Cancer*, **2**(11), 657–663. (Cited on page 10.)

Zhu, H. and Zou, X. (2008). Impact of delays in cell infection and virus production on hiv-1 dynamics. *Mathematical Medicine and Biology: a journal of the IMA*, **25**(2), 99–112. (Cited on page 35.)

Zwillinger, D. and Kokoska, S. (2000). *Standard Probability and Statistics Tables and Formulae*. Chapman & Hall/CRC. (Cited on page 262.)